UNIVERSITÉ DE STRASBOURG

École doctorale
Mathématiques,
sciences de l'**information**
et de l'**ingénieur** | ED 269
Université de Strasbourg

ÉCOLE DOCTORALE MATHEMATIQUES, SCIENCES DE L'INFORMATION ET DE L'INGENIEUR

Laboratoire ICube, UMR 7357

THÈSE présentée par **/ DISSERTATION** presented by :

Aude LOUMEAUD

soutenue le /defended on : **09 octobre 2025**

pour obtenir le grade de **/** to obtain the grade of :
Docteur de l'Université de Strasbourg / Strasbourg University Doctor

Discipline/Spécialité **/** Discipline/Specialty : Biomécanique

---

Coupling multiscale numerical modeling and MRI elastography to investigate the impact of the Klf10 gene on the extracellular matrix of murine skeletal muscle

---

THÈSE dirigée par / DISSERTATION supervisor :
Pr. GEORGE Daniel   Professeur des universités, Université de Strasbourg, ICube
Dr. BENSAMOUN Sabine F.   Directrice de recherche CNRS, Université de Technologie Compiègne, BMBI

RAPPORTEURS :
Pr. SACK Ingolf   Professeur des universités, Charité - Universitätsmedizin Berlin
Pr. ALLAIN Jean-Marc   Professeur des universités, Ecole Polytechnique, LMS

EXAMINATEURS/ AUTRES MEMBRES DU JURY / OTHER MEMBERS OF THE JURY :
Pr. LAPORTE Sébastien (Président)   Professeur des universités, Institut de Biomécanique Humaine Georges
                                        Charpak, Arts et Métiers
Dr. CARUEL Matthieu   Maître de conférences, Université Paris-Est-Créteil, MSME
Dr. CHATELIN Simon   Chargé de recherche CNRS, Université de Strasbourg, ICube

INVITÉS / INVITED MEMBERS :
Dr. PO Chrystelle   Ingénieure de recherche CNRS, Université de Strasbourg, ICube

Licence attribuée par l'auteur / Licence attributed by the author

Acknowledgments

Warning: this section will be very long due to the large number of people to thank.

They are many people to thank for varied reasons, and I will start with the ones that made this PhD possible. Thus, I would like to thank ICube laboratory directors Pr. Michel de MATHELIN and Pr. Fabrice HEITZ, as well as the RDH team leaders Pr. Bernard BAYLE and Dr. Jonathan VAPPOU, the MMB team leader Pr. Nadia BAHLOULI for welcoming me. This thesis would not have been possible without the funding of the ITI HealthTech, and I extend my gratitude to Pr. Bernard BAYLE, Pr. Florent NAGEOTTE, Dr. Géraldine GAZZO and Mme Nicole KIRSCH for accepting me and supporting me within this program. Furthermore, a PhD is nothing without a management team, therefore I am grateful to my directors Dr. Sabine F. BENSAMOUN and Pr. Daniel GEORGE and my advisor Dr. Simon CHATELIN for these 3 years of hard work together. Finally, I would like to express my deepest appreciation to my jury members Pr. Ingolf SACK, Pr. Jean-Marc ALLAIN, Pr. Sébastien LAPORTE, Dr. Matthieu CARUEL and Dr. Chrystelle PO for the time and attention they dedicated to this project.

Furthermore, I extend my thanks to the BMBI laboratory in Compiègne, and especially to my collaborator Dr. Philippe POULETAUT for his unvaluable attention to small details and scientific precision, and Dr. Yoann TATARENKO and Dr. Alexandra JOSSE for their experimental works.

Additionally, I would like to thank the IRIS platform of the ICube laboratory for their technical support both in 3D printing and the provision of MRI experimental slots, especially Dr. Chrystelle PO and M. Benoît WACH. Many thanks to all the staff of the laboratory animal facility and especially Dr. Aurore DE CAUWER. I'd also like to extend my gratitude to Mme Christelle CHARLES, Dr. Frédérique OSTRE, Mme Adrienne VARGUN, Mme Magali DARRIEU-MERLOU, Mme Peggy RUPP and Mme Marina URBAN for their important administrative support.

I would like to emphasize the importance of one person in this PhD project: my advisor Simon CHATELIN. I heard quite often that you have to carefully consider two criteria before choosing a PhD project: the topic and your supervisors. A good 75% of the reasons that made me choose this topic is my supervisor, which was already supervising me during my master thesis. Simon, thank you very much for your daily support and active supervision. You are the person who is always one step ahead in any administrative work, seeking conferences for me to submit to, pushing me to write articles, abstracts, to collaborate in different projects, to rest, to take vacations… all of that while actively teaching me how to write those articles, how to draw figures, how to make better presentations, and last but not least, securing the funding to make all of this possible. People have been saying that we look like a mother duck and its little duckling walking behind her and I think it is a good summary of the last four years. You are the dream supervisor for all PhD students, the one that pushes one outside of their comfort zone little by little, while caring for their mental health, their well-being and the future of their career. You deserve the Nobel of the best supervisor, and I am very grateful to have met you.

I am deeply indebted to Dr. Chrystelle PO, both in her quality of jury member and close collaborator for our MRI experiments. First as the IRIS platform manager, and as an MRI expert, you have welcomed me and taught me very valuable knowledge in physics. I keep very good memories of our long experimental sessions and animated discussions. Thank you also for your valuable advice throughout the PhD.

6

Finally, I would like to thank my very big family for everything they have done in the past 25 years. I strongly believe that family is the first and foremost support that holds a great influence at any stage of life, and I would like to emphasize how happy I am to have such a wonderful one. Even if no one understood the topic of my PhD, thank you for all these moments we shared together.

Summary

The structure and function of skeletal muscle are of particular interest to biomechanics research. Muscle tissue makes up the majority of the human body, and its biomechanical properties reflect its state of health and certain characteristics, such as age. Studying the behavior of skeletal muscle involves integrating a hierarchical structure with specific components at each scale. Some of these components influence the overall mechanical response of the muscle, resulting in a non-linear viscohyperelastic behavior at the macroscopic scale. This behavior can be directly related to various pathophysiological states, such as the presence of muscle pathology.

The Klf10 (Krüppel-like factor 10) gene, involved in the regulation of metabolic homeostasis in various organs, is a circadian transcriptional regulator of energy metabolism in the liver, and recent findings suggest a similar role in skeletal muscle (Baroukh et al., 2022). Recent *ex vivo* studies in murine animal models have demonstrated the effect of the Klf10 gene on the passive and active mechanical properties of striated skeletal muscle (Kammoun et al., 2021). Klf10 was also shown to significantly affect the passive mechanical properties of specific components at the microscopic (fiber) scale, with no significant variation at the macroscopic (muscle) and submicron (myofibril) scales, suggesting a key role in the regulation of the component called extracellular matrix (ECM) (Tatarenko et al., 2024). This background has led to the identification of two major scientific challenges, presented in turn below, and to the development of a structured approach setting out the various methodological stages of the thesis implemented to address them.

In vivo **mechanical measurements of murine skeletal muscle**. The effects of the Klf10 gene on the various scales of skeletal muscle have been observed exclusively *ex vivo* and have never been confirmed *in vivo*. This observation constitutes one of the two major scientific challenges addressed by this thesis. The corresponding work consists in extending the skeletal muscle mechanical analysis using innovative *in vivo* experimental protocols, and to extract conclusions regarding the *in vivo* influence of the Klf10 gene on murine skeletal muscle biomechanics. Magnetic Resonance Elastography (MRE) is an imaging method based on MRI imaging, which allows to map *in vivo* mechanical properties (Muthupillai et al., 1995). Although widely used in clinical research, MRE has produced very few devices adapted to the small rodent. An innovative MRE setup for small animals at 7T has been developed for mouse skeletal muscle (Loumeaud et al., 2025a). The application of this protocol to control and genetically deficient mice cohorts allowed us, in collaboration with the Institut de Biologie Valrose (Université Nice Côte d'Azur, CNRS, Inserm, UMR 7277 – U1091) and the department of biochemistry and molecular biology at Mayo Clinic (Rochester, MN, USA), to highlight an *in vivo* significative implication of the Klf10 gene on the stiffness in part of the mouse hindlimb skeletal muscles.

Multiscale numerical modeling of murine skeletal muscle. Current experimental tools for assessing the mechanical properties of microscopic scale constituents, primarily muscle ECM, remain extremely limited, impeding our understanding of its functional role and its relationship to the Klf10 gene. Finite element modeling of these components at different scales (Kuravi et al., 2021b; Sahani et al., 2024) is an effective method for investigating behavior, overcoming the limitations posed by experimentation (Binder-Markey et al., 2021). In this context, we developed an original multiscale modeling approach using Finite Element (FE) modeling, based on periodic representative element (RVE) generation and the "*Direct Finite Element Square*" DFE[2] (Tan et al., 2020). Our skeletal muscle numerical model allowed us to develop an original approach to solve the major scientific challenge at the origin of this thesis:

the lack of experimental data regarding ECM, the implicated mechanisms and prediction of muscular response in general, especially in relation to the Klf10 gene expression. Although this modeling remains complex, due to the hierarchical structure of the muscle combining numerous components at different scales, it constitutes a major lever for progress in the analysis of the global mechanical response of striated skeletal muscle (Loumeaud et al., 2024). Our approach using the DFE^2 method allowed us to take into account distribution parameters related to muscle fibers (slow and fast), geometrical parameters, mechanical parameters, while accounting for the organization and the mechanical properties of ECM for both genotypes (Loumeaud et al., 2025b). Using numerical replication of experimental uniaxial extension tests, both at the microscopic (muscle fibers) and macroscopic (muscle) scales, we determined the influence of Klf10 genetic expression on the mechanical muscle behavior. Results show that this influence is mainly exerted on collagen fibers within the ECM, pointing at shifts in their density or their mechanical properties.

Conclusions. Beyond the innovative experimental tools (small animal MRE setup adaptable to multiple organs at 7T) and developed numerical tools (original multiscale approach both at the microscopic scale through its RVE and at the macroscopic scale through the DFE² method), this thesis has demonstrated not only the possibility of investigating murine skeletal muscle *in vivo*, but also of deducing the properties of muscle ECM, which are still largely unknown, through numerical modeling. Furthermore, the link and effects of the Klf10 gene have been clearly identified across different muscle scales, constituting a major step forward in understanding the effects of this gene not only on biomechanics and muscle characteristics, but more broadly on the metabolic homeostasis involved.

Résumé

L'étude du comportement du muscle squelettique implique d'intégrer une structure hiérarchique avec des composants spécifiques à chaque échelle. Certains de ceux-ci influencent la réponse mécanique globale du muscle, qui se traduit par un comportement viscohyperélastique anisotrope non linéaire à l'échelle macroscopique. Ce comportement peut être directement lié à différents états physiopathologiques, comme l'âge ou la présence d'une pathologie musculaire.

Le gène Klf10 (Krüppel-like factor 10), impliqué dans la régulation de l'homéostasie métabolique dans divers organes, est un régulateur transcriptionnel circadien du métabolisme énergétique dans le foie et de récents résultats suggèrent un rôle similaire dans le muscle squelettique (Baroukh et al., 2022). Des études récentes *ex vivo* sur modèle animal murin ont mis en évidence l'effet du gène Klf10 sur les propriétés mécaniques passives et actives des muscles striés squelettiques (Kammoun et al., 2021). Il a été également montré que Klf10 affecte de manière significative les propriétés mécaniques passives de composants spécifiques à l'échelle microscopique (fibre), sans variation notable aux échelles macroscopique (muscle) et submicronique (myofibrille), ce qui suggère un rôle clé dans la régulation de la matrice extracellulaire (MEC) (Tatarenko et al., 2024). Ce contexte à donné lieu à l'identification de deux verrous scientifiques majeurs, présentés successivement ci-après, ainsi qu'à l'élaboration d'une démarche structurée exposant les différentes étapes méthodologiques de la thèse mises en œuvre pour y répondre.

Mesures mécaniques *in vivo* du muscle squelettique murin. Les effets de Klf10 sur les différentes échelles du muscle squelettique ont été observés exclusivement *ex vivo* et n'ont à ce jour jamais été confirmés *in vivo*. Ce constat constitue un des deux verrous scientifiques majeurs auxquels s'attaque ce travail de thèse. Il s'agit donc d'étendre l'analyse mécanique du muscle squelettique via des protocoles expérimentaux *in vivo* novateurs, et d'en extraire les conclusions quant à l'influence *in vivo* du gène Klf10 sur la biomécanique du muscle squelettique murin. L'élastographie par résonance magnétique (ERM) est une méthode d'imagerie basée sur l'IRM permettant de cartographier des propriétés mécaniques *in vivo* (Muthupillai et al., 1995). Bien que largement utilisé en clinique, l'ERM a donné lieu à très peu de dispositifs adaptés au petit rongeur. Un dispositif novateur d'ERM du petit animal à 7T a été développé pour le muscle squelettique de souris (Loumeaud et al., 2025a). L'application de ce protocole à des cohortes de souris contrôles et présentant une déficience du gène Klf10 a permis, en collaboration avec l'Institut de Biologie Valrose (*Université Nice Côte d'Azur, CNRS, Inserm, UMR 7277 - U1091)* et le département de biochimie et de biologie moléculaire de la Mayo Clinic (*Rochester, MN, USA*), de mettre en évidence *in vivo* une implication significative du gène à l'étude sur la rigidité d'une partie des muscles squelettiques des membres antérieurs.

Modélisation numérique multiéchelles du muscle squelettique murin. Les outils expérimentaux actuels permettant d'évaluer les propriétés mécaniques des constituants à l'échelle microscopique, et en premier lieu la MEC musculaire, restent extrêmement limités, ce qui freine la compréhension de leur rôle fonctionnel et de leur rapport au gène Klf10. La modélisation par éléments finis de ces composants à différentes échelles (Kuravi et al., 2021b; Sahani et al., 2024) est une méthode efficace qui permet d'investiguer le comportement, en s'affranchissant des limites posées par l'expérimentation (Binder-Markey et al., 2021). Dans ce contexte, Nous avons développé une approche

originale de modélisation multiéchelles par éléments finis, reposant sur une génération périodique d'éléments de volume représentatifs (VER) et la méthode « Direct Finite Element Square » DFE² (Tan et al., 2020). Notre modélisation numérique du muscle squelettique nous a permis de développer une approche originale pour solutionner l'autre verrou scientifique majeur et principal à l'origine de ce travail de thèse: le manque de données expérimentales sur la MEC, sur les mécanismes impliqués et sur la prédiction de la réponse musculaire d'une façon générale, et tout particulièrement en lien avec l'expression du gène Klf10. Bien que cette modélisation reste complexe, en raison de la structure hiérarchique du muscle combinant de nombreux composants à différentes échelles, elle constitue un levier majeur pour progresser dans l'analyse de sa réponse mécanique globale du muscle strié squelettique (Loumeaud et al., 2024). Notre approche par méthode DFE² nous a permis d'intégrer des paramètres de distribution des fibres musculaires (lentes et rapides), géométriques, mécaniques, tout en tenant compte de l'organisation ainsi que des propriétés mécaniques de la MEC pour un génotype musculaire sain et altéré par l'inhibition du gène Klf10 (Loumeaud et al., 2025b). Grâce à la reproduction numérique d'essais de traction, aux échelles microscopique (fibre musculaire) et macroscopique (muscle), nous avons déterminé l'influence de l'expression du gène Klf10 sur le comportement mécanique du muscle. Les résultats montrent que cette influence s'exerce principalement sur l'agencement, la densité et les propriétés mécaniques des fibres de collagène de la MEC, que nous avons ainsi pu identifier.

Conclusions. Au-delà des outils novateurs expérimentaux (dispositif ERM petit animal à 7T adaptable à de multiples organes) et numériques (approche multiéchelle originale tant à l'échelle microscopique par son VER que par la transition vers l'échelle macroscopique par la méthode DFE²) développés, cette thèse a mis en évidence non seulement la possibilité d'investiguer *in vivo* le muscle squelettique murin, mais également de déduire par la modélisation numérique les propriétés de la MEC musculaire, encore largement méconnue. Plus encore, le lien et les effets du gène Klf10 ont pu être clairement identifiés au travers des différentes échelles musculaires, constituant un pas majeur dans la compréhension des effets de ce gène non seulement sur la biomécanique et les caractéristiques musculaires, mais plus largement sur l'homéostasie métabolique impliquée.

Table of Contents

Contents

Introduction

Knowledge of the structure and function of skeletal muscles is of particular interest to biomechanics research. Muscle tissue makes up the majority of the human body mass, and its biomechanical properties reflect its state of health and certain characteristics, such as age. Biomechanical properties can be studied *ex vivo* or *in vivo*, ranging to palpation by a healthcare professional to the use of mathematical tools to predict muscle response. The chosen tool or methodology is mostly related to the target components. Indeed, a key aspect of skeletal muscle resides in its hierarchical structure, distributed across different scales. The macroscopic scale designates the whole muscle, while at the mesoscopic scale this muscle splits into several fascicles, each of them in turn containing muscle fibers at the microscopic scale. This quick description is not representative of the diversity of the components contained at each scale in the skeletal muscle, which each contribute in their own way to the global structure and function of the organ.

Biomechanical research mostly investigates the structure and mechanical properties of various tissues. Our organ of interest displays a specific anisotropic viscohyperelastic behavior at the macroscopic scale due to its hierarchical structure. Various methods have been employed to perform studies on skeletal muscles; however, they tend to complexify with smaller scales and smaller components. At smaller scales, it becomes increasingly difficult to isolate and manipulate single components, provided that *ex vivo* experiments are possible. A strong dependency on experimental conditions is introduced in the results.

Methods regarding *in vivo* experiments have known recent developments but remain scarce. In this context, numerical methods combining mathematical models and experimental data provide a good compromise to obtain information on components presenting inherent difficulties for *in vivo* and *ex vivo* methods. Particularly, a new family of numerical methods called multiscale models are increasingly used in the literature. They consist in implementing several scales of the skeletal muscle and the related components in the same mathematical model, taking advantage of the proficiency of experimental data at larger scales to obtain information at smaller scales, e.g. through parameter identification.

In the literature, this proficiency of experimental data applies to whole muscles, but also components such as muscle fibers and myofibrils, which have been extensively studied in several species. Although skeletal muscles contain many components, a few of them contribute to most of the resulting mechanical properties: especially, across the different scales, the extracellular matrix (ECM), divided in three different components that are the endomysium (microscopic scale), perimysium (mesoscopic scale) and epimysium (macroscopic scale). Recently, the scientific community's interest has shifted towards ECM, as evidence shows that this component not only greatly contributes to the skeletal muscle mechanical properties but is also implicated in pathological disorders such as Duchenne Muscular Dystrophy (DMD). However, this component is especially difficult to isolate since its volume fraction within the skeletal muscle is small (less than 10%) and it displays continuous linkage to other components such as muscle fibers. Thus, two key research axes recently emerged in the literature: the experimental characterization of ECM, often in combination with chemical muscle digestion; and the use of multiscale modeling to indirectly retrieve information on ECM using experimental data at the whole muscle scale.

The Klf10 (Krüppel-like factor 10) gene, discovered for its implication in human osteoporosis, is involved in the regulation of metabolic homeostasis in various organs. More precisely, it assumes the role of a circadian transcriptional regulator of energy metabolism in the liver and recent findings suggest a similar role in skeletal muscle. Indeed, recent *ex vivo* studies in murine animal models have demonstrated the effect of the Klf10 gene on the passive and active mechanical properties of striated skeletal muscle. Significant variations of both passive and active mechanical properties of muscle fibers at the microscopic scale were induced by the genetic deletion in the animals. At the same scale, significant variations of structure were observed. However, at different scales, like the submicron scale containing myofibrils and also at the macroscopic scale, no significant variations of mechanical properties were observed. These results suggest the existence of a compensation mechanism between scales. It was hypothesized that the genetic deletion could also affect the ECM.

Considering the aforementioned methods to study ECM, it was chosen to develop a multiscale modeling approach which is now described in this PhD manuscript. The PhD focuses on two separate methods to study the effect of the Klf10 gene deletion in mice skeletal muscles:

In vivo **mechanical measurements of murine skeletal muscle**. The effects of the Klf10 gene on the various scales of skeletal muscle have been observed exclusively *ex vivo* and have never been confirmed *in vivo*. Therefore, a bias can be introduced if the observed shift in mechanical properties at the microscopic scale results solely from increased sensitivity to one element of the testing protocol. This observation constitutes one of the two major scientific challenges addressed by this thesis. Aside from the multiscale modeling analysis targeting specifically the ECM, we extend the existing *ex vivo* experimental dataset with *in vivo* measurements at the macroscopic scale. For this purpose, we use an imaging method based on Magnetic Resonance Imaging (MRI), called Magnetic Resonance Elastography (MRE). MRE allows us to obtain maps representing the variation of mechanical wave propagation within the tissue, which are related to mechanical properties variation. Although MRE is widely used in clinical research on human patients, it presents specific additional challenges for smaller species such as rodents. Therefore, very few experimental setups have been developed for small animal MRE. In this thesis, related works include the development of a MRE protocol for murine skeletal study in two distinct positions, allowing to isolate mechanical contributions of flexor and extensor muscles of the hindlimb. This protocol was then applied to two cohorts of mice presenting different genotypes, to investigate *in vivo* implications of the Klf10 genetic deletion on skeletal muscle stiffness for small deformations.

Multiscale numerical modeling of murine skeletal muscle. To investigate the mechanical properties of ECM in *ex vivo* skeletal muscles, we developed an original multiscale numerical model. This new model aims at overcoming current limitations in the literature through an innovative algorithm for Representative Volume Element (RVE) generation combined to a "*Direct Finite Element Square*" method DFE^2 to transition between scales. The RVE generation algorithm provides a custom geometry accounting for structural variations induced by the genetic deletion, thus decoupling these effects from the mechanical parameters to be identified. The geometry incorporates probabilistic data from previous *ex vivo* imaging experimental data regarding muscle fiber type (slow, fast) as well as probabilistic representation of ECM geometry, divided in 2 components: endomysium and its interface with muscle fibers. Furthermore, the chosen method to transition between scales does not only provide an upscaling from microscopic (muscle fibers) to macroscopic (muscle) scale, but also a downscaling to perform investigations on the microscopic scale geometry as well. Using numerical replication of experimental uniaxial extension tests, both at the microscopic and macroscopic scales, the mechanical parameters associated with ECM are identified and provide insights on the *ex vivo* influence of the Klf10 genetic deletion and points at effects on the collagen fibers within the ECM.

The first chapter of this manuscript aims to describe the hierarchical structure of the skeletal muscle and the complex functions of its main components. Navigating through the scales, we portray the biomechanical methods – both experimental and numerical – that can be used to investigate skeletal muscle biomechanical properties. Special attention is dedicated to the ECM component.

In the second chapter, the *in vivo* experimental characterization of murine skeletal muscle is detailed. After briefly introducing the experimental setup, we depict the protocol and postprocessing pipeline, as well as the results of the experimental tests.

The numerical scale transition method, introduced above as DFE^2 method, consists in the focus of chapter 3. Adaptation of the method to the macroscopic skeletal muscle geometry and hyperelastic anisotropic material, as well as benchmarking and simulation optimization are presented.

Switching scales, chapter 4 offers an insight into the algorithm developed for microscopic scale skeletal muscle geometry conception from histological cross-sections and probabilistic distributions related to the different components. It describes the generation of periodic Representative Volume Elements in the FE software, and the different strategies adopted to reduce numerical artifacts at the microscopic scale.

Resulting from the combination of developments presented in chapters 3 and 4, the multiscale skeletal muscle model and its application to Klf10 genetic expression are reported in chapter 5. The study of the soleus muscle in healthy and genetically modified animals and the conclusions are presented, as well as the limitations posed by our current model. This chapter opens the way to scientific discussion about perspectives to overcome the current limits, as well as the interest of our work for the scientific community.

Chapter 1: Skeletal muscle structure and function

Skeletal muscles exhibit a hierarchical architecture divided into several scales, each including several components necessary to the overall muscle function. When a muscle dysfunction is observed, methods providing information at different scales and on different components are needed to firstly explain the dysfunction and secondly assess medical treatment efficiency.

The development of such methods first requires a good understanding of the multiscale architecture and functioning of the skeletal muscle. In this chapter we describe two categories of methods that can be used: experimental methods applied to skeletal muscle samples, and numerical methods that simulate muscle behavior.

In this chapter, we present elements of bibliography regarding skeletal muscle structure and function, as well as experimental and numerical methods related to skeletal muscle investigation; to explain and justify the methods we used during this PhD. As this thesis focuses on healthy and Klf10 genetic deletion in mice, a special focus on mouse skeletal muscle is put throughout the different sections. Finally, the Klf10 gene and its known impact on mouse skeletal muscle prior to this thesis are described.

1.1. Skeletal muscle anatomy

1.1.1. Multiscale descriptions of the skeletal muscle

Skeletal muscles possess a multiscale architecture (Lieber & Binder-Markey, 2021; Mukund & Subramaniam, 2020). One can define the different scales as macroscale, mesoscale, microscale and submicron scale (Pouletaut et al., 2023). To each scale corresponds a specific architecture and the associated components (Figure 1), which not only have an impact on muscle function but also on its biomechanical response through these different scales. Some of these components contribute to the active or the passive properties of the skeletal muscle. Each scale of the skeletal muscle presents a geometry with long cylindric structures embedded in a matrix-like material:

At the macroscopic scale (of the order of the centimeter), the muscle is surrounded by a layer of connective tissue or extracellular matrix (ECM) called epimysium and connected to tendons.

At the mesoscopic scale, the muscle is constituted of several adjacent mesoscale fascicles, surrounded by a layer of ECM called perimysium (Csapo et al., 2020; Purslow, 2020). Blood vessels and neurons are located between the fascicles.
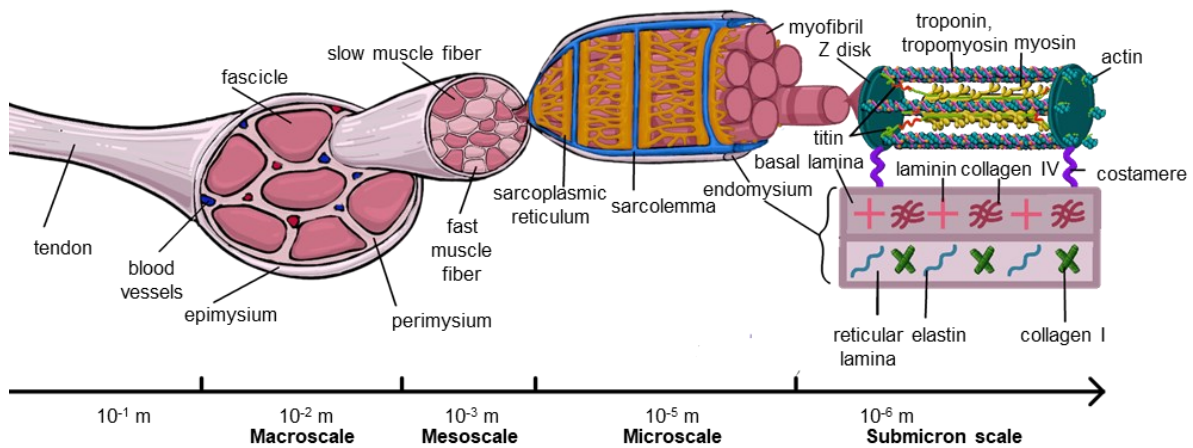
Figure 1. Schematic representation of the multiscale architecture of the striated skeletal muscle (Loumeaud et al., 2024). The different scales defined in this thesis are represented, through the macroscopic (fascicles, blood vessels, perimysium, epimysium), mesoscopic (fascicle), microscopic (fast and slow muscle fibers, endomysium), submicron (myofibrils, sarcoplasmic reticulum, sarcolemma) and nanoscopic (sarcomere from the myofibril, proteins) scales.

At the microscopic scale, the fascicles contain blood vessels, neurons and muscle fibers, surrounded by another layer of ECM called endomysium. These groups of tightly packed muscle fibers or muscle cells (from 10 to 100 µm in diameter) constitute the microscale. Muscle fibers can be arranged in different architectures within the muscle depending on the muscle's function in the body (Roberts et al., 2019) (Figure 2).
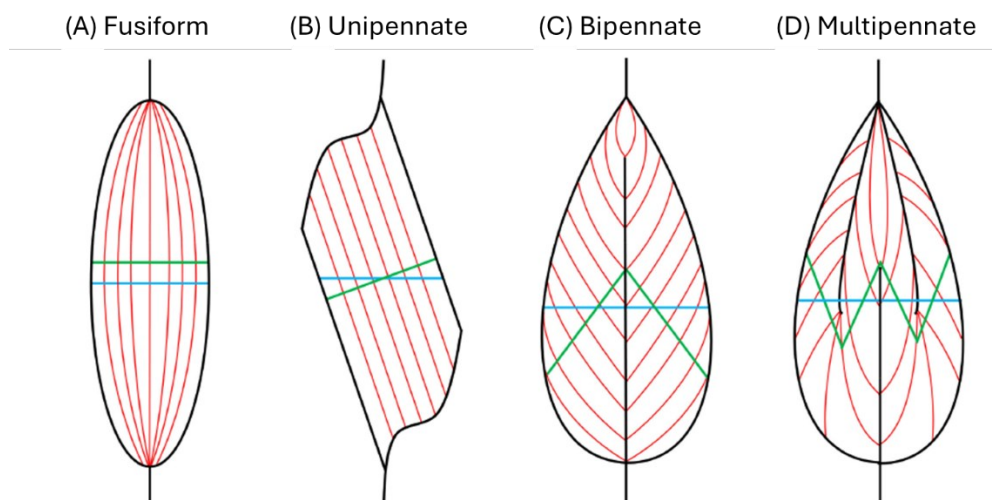
Figure 2. Various pennation angle arrangements of the fascicles/muscle fibers in skeletal muscle. Blue lines indicate the plane for the anatomical cross-sectional area (CSA) (i.e., the CSA that runs perpendicular to the longitudinal axis of the muscle), and green lines indicate the plane for physiological CSA (i.e., the CSA that runs perpendicular to the longitudinal axis of the fascicles/muscle fibers). Adapted from (Jorgenson et al., 2020).

At the submicron scale, a muscle fiber is delimited by a plasma membrane called the sarcolemma, which possesses invaginations within the cell called transverse tubules. The transverse tubules are associated with an organelle called the sarcoplasmic reticulum that pumps and stores calcium ions. These features allow muscle activation. The muscle fiber also contains several nuclei, and other organelles; however, around 60% of the muscle fiber's volume is occupied by myofibrils (Terzolo et al., 2022), and 40% by the muscle fiber's cytoplasm called sarcoplasm (Cooper & Valentine, 2015). Muscle fibers are usually classified according to their color, contractile properties, fatigue resistance and major

source of energy supply (Table 1). This classification distinguishes two main types: type 1 (red slow oxidative) and 2 (white fast glycolytic); however four different types of muscle fibers are recognized (Cooper & Valentine, 2015; Lloyd et al., 2023). Their proportion and dimensions vary in the different muscles.

Table 1. Description of the different histochemical muscle fiber types.

	Type I	Type II A	Type IIX	Type IIB
Contractile properties	Slow twitch	Fast twitch	Fast twitch	Fast twitch
Fatigue resistance	Resistant	Resistant	Intermediate	Fatigable
Source of energy supply	oxidative	oxidative	glycolytic	glycolytic
Diameter	-	+	+++	+++
Role	Endurance	Compromise between strength and endurance	Strength	Strength

Under the submicron scale, myofibrils (from 1 to 2 μm in diameter) constitute in active and passive components. Each myofibril is an assembly in a series of contractile components called sarcomeres. The sarcomeres contain proteins such as actin, titin and myosin. Other relevant submicron cellular components include the sarcoplasmic reticulum, that propagates neural signal as a chemical potential up to the sarcomeres. The sarcomeres are physically connected to extracellular structures through costameres (Humphrey et al., 2014; Peter et al., 2011). Costameres are made of transmembrane proteins such as dystrophin. Transmembrane proteins provide a link from the muscle fibers to the ECM, which at this scale consists in collagen and elastin fibers embedded in a matrix of proteoglycans.

1.1.2. Description of the extracellular matrix (ECM)

Following the multiscale description above and its implication in both passive and active properties of the skeletal muscle, it is essential to detail a fundamental set of components that are still poorly understood from a mechanical point of view, but whose importance for muscle function is increasingly highlighted in the literature: the ECM.

The ECM, also named Intra Muscular Connective Tissue (IMCT), as well as the aponeurosis and the fascia, is an ensemble of connective tissues that can be found in many organs, playing different roles (Muiznieks & Keeley, 2013). In the skeletal muscle, ECM exists in three different layers, namely the epimysium, the perimysium and the endomysium (Figure 3). Those layers exhibit different structures and functions in the muscle (Purslow, 2020). They are constituted of proteins (Table 2) such as collagens and elastin forming different patterns, embedded in a matrix of proteoglycans. Figure 4 presents a multiscale description of ECM including a description of each of the three layers, with a focus on mouse ECM.
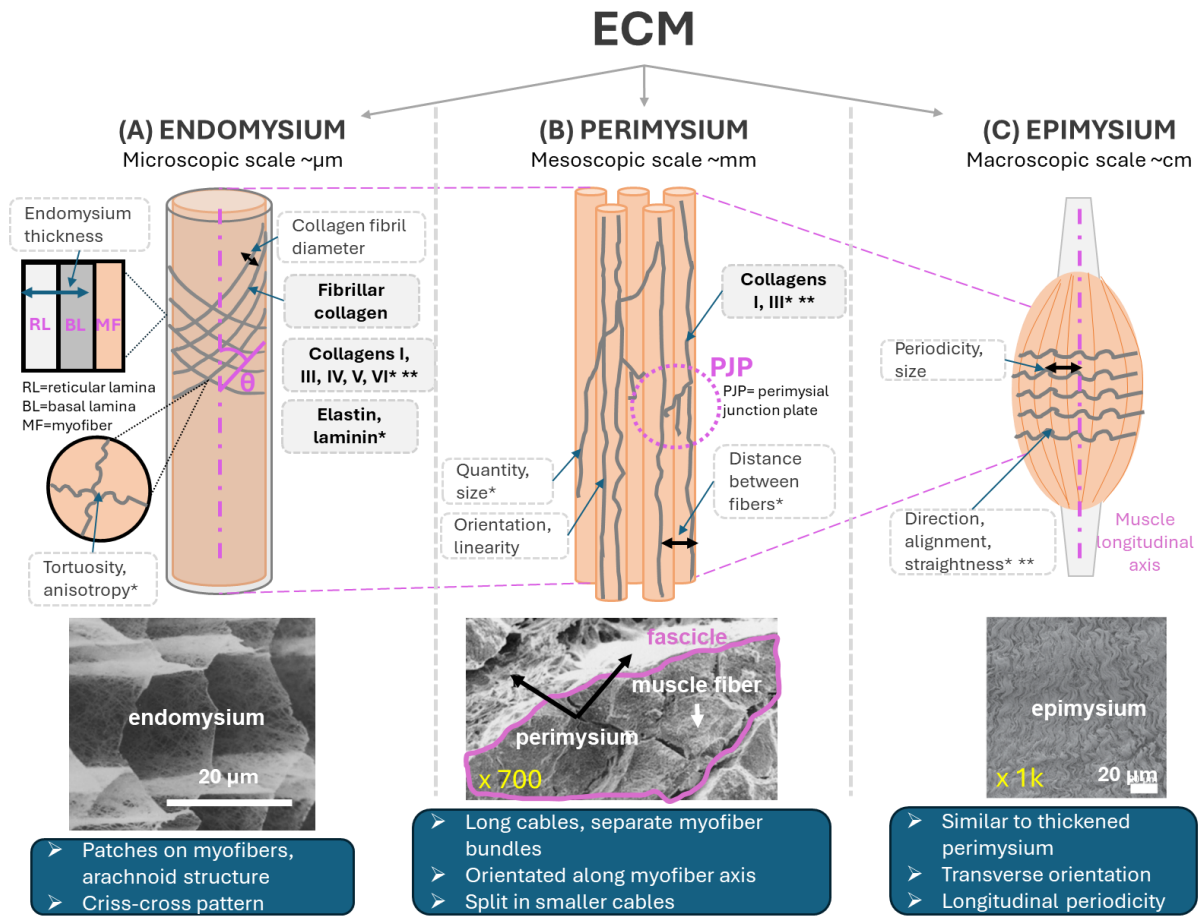
Figure 3. Multiscale architecture of mouse Extracellular Matrix with focus on the influence of age (*) and disease (**) on the measurable geometry and main components highlighted by studies on murine models. Illustrations show Scanning Electron Microscopy images adapted from (A) (P. P. Purslow & Trotter, 1994) on decellularized bovine muscles (B) (Järvinen et al., 2002) on porcine muscles and (C) (Sahani et al., 2022) on murine muscles.

The epimysium layer surrounds the muscle and attaches to the tendons. Purslow (2010) reports different collagen fiber networks arrangements for epimysium in calf muscles. Wavy collagen fibers sets or families can form an angle with the muscle longitudinal axis or run parallel to it. This shape and the epimysium thickness depend on the muscle's architecture.

The perimysium layer is connected on surface to the endomysium and the epimysium. Perimysium forms a tube-like structure surrounding bundles of muscle fibers, made of two or more layers. Layers are composed of networks of long wavy collagen fibers showing preferred orientations along the fascicle longitudinal axis (Purslow & Delage, 2022). The collagen fibers group in flat bundles and form perimysial cables (Gillies et al., 2017). Cables are shared between adjacent fascicles and divide themselves to delineate smaller fascicles. Small cables form regular and numerous connections with muscle fibers (Passerieux et al., 2006; Purslow & Delage, 2022). In a study on bovine epimysium, Passerieux et al. (2006) named these connections "perimysial junctional plates"(PJP), defined as contact regions between the endomysium and the perimysium. In a later study (Passerieux et al., 2007), the same authors inferred that the perimysium in the rat has the same structure as the bovine one, based on Scanning Electron Microscopy (SEM) graphs.

Table 2. Main components of the ECM involved in muscular structural integrity. RL: reticular lamina.

Component	Localization	Quantity	Aspect, dimensions	Function	References
Collagen I	Epimysium Perimysium Endomysium (RL)	<10% dry muscle weight	Fibrils exhibiting cross banding with a 300 nm period, diameter of the order of a few hundred nm	Tensile strength and rigidity	(Dutov et al., 2016; Gelse et al., 2003; Kovanen, 2002; Muiznieks & Keeley, 2013)
Collagen III	Epimysium Perimysium Endomysium (RL)		Fibrils exhibiting cross banding with a 300 nm period, forming loose meshes	Tissue compliance	(Csapo et al., 2020)
Collagen IV	Basal lamina		Non-fibrillar, helices	Structural integrity	(Sanes, 2003)
Collagen V	Epimysium Perimysium Endomysium (RL)		Fibrils exhibiting cross banding with a 300 nm period	Control of collagen fibrillogenesis	(Sanes, 2003)
Collagen VI	Reticular lamina		Non-fibrillar, fine beaded filaments, segments exhibiting cross banding with a 110 nm period, 3-10 nm diameter	Bind with laminin networks, connecting basal lamina and reticular lamina	(Birk & Bruckner, 2005; Gelse et al., 2003; Sanes, 2003; Schüler et al., 2022)
Laminin	Basal lamina		Network-forming	Mechanical linkage from the basal lamina to the sarcolemma	(Sanes, 2003; Wohlgemuth et al., 2023)
Proteoglycans	Epimysium Perimysium Endomysium			Tissue hydration, collagen fibrillogenesis and orientation	(Mukund & Subramaniam, 2020; Wohlgemuth et al., 2023)
Dystrophin	Endomysium			Mechanical linkage from basal lamina to sarcolemma	(Grounds et al., 2005)
Elastin	Epimysium Perimysium Endomysium	<1% dry muscle weight	Fibrous structure	Tissue elasticity	(Bendall, 1967; Sun, 2021)

The endomysium layer constitutes about 5% of the muscle's volume at the microscale and connects to the muscle fibers. The external layer of the muscle fiber is a 9nm thick plasma membrane (Purslow & Delage, 2022). This layer is linked to the endomysium through structures orthogonal to the muscle fiber axis that connect the sarcomeres in the muscle fibers to the ECM, called costameres. The endomysium itself is constituted of two distinct layers: the endomysial basement membrane or basal lamina, situated next to the plasma membrane, which is surrounded by reticular lamina. The basal lamina is reported to be 50 to 70 nm thick, and contains non-fibrillar collagen, non-collagenous proteins and proteoglycans. The structure of the basal lamina mainly contains distinct networks of triple-helix non-fibrillar collagen IV and laminin, linked by the glycoprotein entactin/nidogen. Transmembrane proteins as integrins, dystrophin and dystroglycans alongside laminin link the basal lamina to the muscle fiber, forming part of the costameres (Mukund & Subramaniam, 2020; Sanes, 2003).

In the reticular lamina, collagenous fibrils are embedded in a proteoglycan ground matrix. The proteoglycans play a role in tissue hydration but also contribute to the formation of collagenous proteins and their organization (Ameye & Young, 2002; Weber et al., 1996). Collagen VI α chains connect the reticular lamina to the basal lamina. This lamina consists of a network of wavy fibrillar collagen embedded in a proteoglycan matrix. Fibrillar type I, III, V and XI collagens alongside non-fibrillar types VI and IX collagens can be found in the reticular lamina, the main represented type being types I and III, as illustrated in Figure 4 by (Mukund & Subramaniam, 2020). Protein elastin is the main contributor to the ECM's elasticity. This reticular lamina is shared between neighboring cells (Purslow & Delage, 2022). Figure 4 describes the organization of these different proteins, highlighting the continuous linkage from the muscle fiber to the endomysium.

Initially described as quasi-random (Trotter, 1990), networks of collagen fibers show preferred orientations along the muscle fiber longitudinal axis (Figure 3). These orientations, as well as

endomysium thickness, change along muscle extension (Purslow & Trotter, 1994). The current literature on skeletal muscles agrees on a mean orientation of ±55° to the main axis of the muscle fibers.
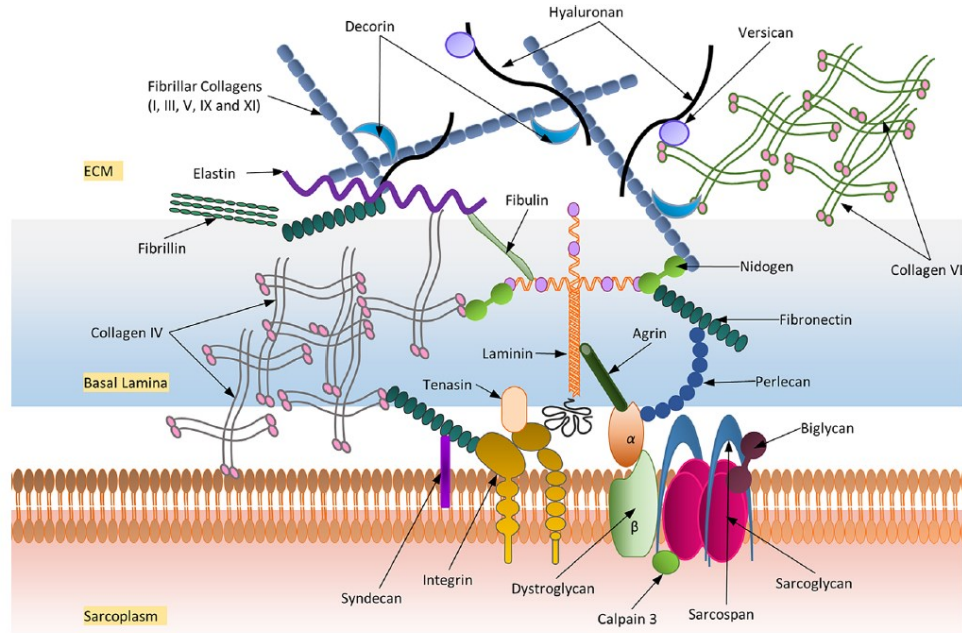
Figure 4. A schematic representation of the main ECM proteins and their approximate localization surrounding skeletal muscle (Mukund & Subramaniam, 2020).

1.1.3. Influence of the ECM on the mechanical properties of the skeletal muscle

Mechanical properties of the smaller scale components result in a global anisotropic viscohyperelastic quasi-incompressible mechanical behavior of the skeletal muscle (Figure 5). Hyperelasticity describes materials that can undergo large deformations without sustaining plastic/permanent deformation. Viscosity expresses the dependency of the mechanical behavior on time, and more specifically the strain rate. Due to its architecture including long fibers aligned in preferential directions at different scales, the skeletal muscle displays anisotropy. Similarly to most biological tissues, the skeletal muscle is mostly composed of water, therefore displaying a quasi-incompressible behavior. Finally, the skeletal muscle exhibits a non-linear stress-strain relationship. When testing muscle activation, two components named respectively passive and active stiffness can be separated, as illustrated in Figure 5. Active tension is obtained when contracting the muscle fibers, with a maximal tension obtained at a muscle fiber length called "optimal length". The muscle can also be stretched, which generates a passive tension within the muscle. Further details and investigations about the experimental mechanical testing of the skeletal muscle are available in the next section of this manuscript (1.2). The different mechanical characteristics briefly described here can undergo changes at different scales in the presence of dysfunctions. Therefore, it is essential to identify the various components, particularly within the ECM, at the smallest scales, which are responsible for this macroscopic passive and active properties of skeletal muscle.
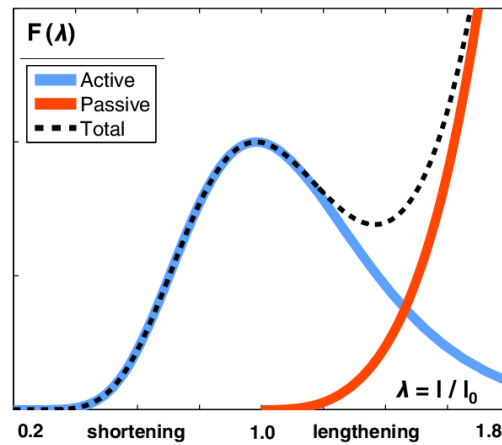
Figure 5. Total muscle force generated as a function of muscle stretch. The total force can be divided into two contributions, the active and the passive force (Wisdom et al., 2015)

Components responsible for passive stiffness

Passive stiffness in the skeletal muscle is attributed to the protein titin in the muscle fibers (Brynnel et al., 2018; Linke, 2023; Prado et al., 2005) and protein collagen in the ECM (Gillies & Lieber, 2011; Lieber & Binder-Markey, 2021; Lieber & Meyer, 2023; Meyer & Lieber, 2011; Sun, 2021). Transmembrane proteins such as dystrophin that belong to the costameres are also believed to contribute to lateral force transmission between muscle fibers and ECM (Grounds et al., 2005; Virgilio et al., 2015).

Components responsible for active stiffness

Because of its function and unlike purely passive organs, skeletal muscles also have active properties that are important to distinguish from the passive properties. To contract skeletal muscles, motor neurons establish communication between the brain and the skeletal muscles at specific sites called the neuromuscular junctions (NMJ) or synapses. At those sites, the electrical signal emanating from the brain is converted into a chemical signal through the release of neurotransmitter acetylcholine (Ach). Ach binds to receptors in the muscle fiber's sarcolemma resulting in a chemical potential called Action Potential (AP), propagated in the muscle fiber through the sarcolemma and down the transverse tubules. This depolarization induces the sarcoplasmic reticulum to release calcium ions into the cytoplasm (MacLennan & Holland, 1975) (Figure 6).

At the submicron scale, this excitation results in changes in the sarcomeres, where active binding sites on the actin protein become exposed. The myosin protein's head attaches to the binding sites, thus forming a cross-bridge, using ATP molecule breakdown as a chemical source of energy. The ATP breakdown provides sufficient energy to cock the myosin head. Afterwards, the myosin head springs from the cocked position, thus pulling on the actin protein. This way, the ATP chemical energy has been converted to mechanical work. Through cross-bridge cycling, the actin and myosin proteins, also called contractile filaments, overlap, attaining full contraction when the overlap is complete. These phenomena are denoted as the sliding filament theory, as reviewed in Powers et al. (2021), and the cross-bridge theory (Huxley, 1957). After the contraction, the calcium ions get transported back in the sarcoplasmic reticulum. In this contraction processus, another important protein is titin. Titin is a giant spring that plays a role in stabilizing the sarcomeres, but is also investigated as a third contractile filament (Herzog, 2018).
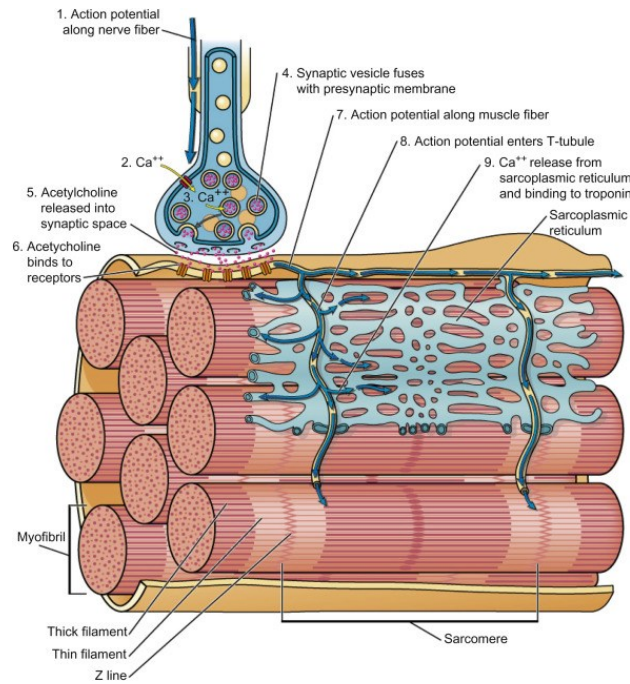
Figure 6. Mechanism of muscle contraction, from AP propagation to calcium ions release in the sarcoplasmic reticulum (Carlson, 2022)

These activation phenomena at the lowest scales ultimately have a direct effect on the mechanical response of skeletal muscle. During muscle activation, the force generation is due to the sarcomere contraction attributed to the binding of proteins actin and myosin, namely the cross-bridge cycling theory (Huxley, 1957; Huxley, 1969). Evidence also suggests an additional active force generated by formation of a bound between titin and actin during activation (Herzog, 2017, 2018), that would be responsible for the residual force enhancement phenomenon first observed in Abbott & Aubert (1952).

Components involved in the lateral force transmission

Passive muscle force mainly originates from the sarcomeres in the muscle fiber, and the ECM. However, costameres connect the interior of the muscle fiber to the ECM, thus leading to a phenomenon called lateral force transmission, where the sarcomeres' active and passive forces are transmitted through shear to the ECM. The ECM network then locally redistributes the loads into the fascicle through endomysium shear (Lieber & Binder-Markey, 2021; Purslow, 2002). P. Purslow (Purslow, 1999; Purslow, 1989) argues that muscle division in fascicles through the perimysium accommodates shear strains during muscle change of shape during contraction and extension, but that perimysium is unsuitable for transmission of contractile force. Perimysium could be a mechanism that prevents over contraction and over extension in a muscle. Moreover, the muscle group compartmenting by fascia pressurizes the compartments and increases muscle contraction efficiency (Purslow, 2002).

ECM seems to bear an increasing fraction of the muscle's load with higher scales and load bearing elements in the ECM are different as a function of scales, either by geometry or composition. Moreover, the degree of collagen cross-linking and the collagen isoform ratio type I /type III are especially considered to be the main indicators of ECM passive stiffness (Lieber & Binder-Markey, 2021).

The multiscale ECM description above groups observations across different species. The prevalence of multilayered ECM was investigated in several species (Sleboda et al., 2020), which are American bullfrog (*Lithobates catesbeianus*), semimembranosus; turkey (*Meleagris gallopavo*), lateral

gastrocnemius; American alligator (*Alligator mississippiensis*), triceps brachii; cane toad (*Rhinella marina*), plantaris; laboratory mouse (*Mus musculus*), lateral gastrocnemius; and common carp (*Cyprinus carpio*), epaxial muscle. All 3 layers of ECM were examined. The results suggest that collagen reinforced ECM is a common feature amongst vertebrate skeletal muscles, with the murine ECM exhibiting no difference compared to the general observations. Moreover, murine hindlimbs present similarities to those of humans, and mice are therefore frequently used as animal models for skeletal muscle studies (Lloyd et al., 2023). In the following sections, we will specifically focus on murine skeletal muscles.

1.2. Skeletal muscle mechanical characterization

In this section, we will briefly make a list of the methods for mechanical characterization of skeletal muscle in the literature at various scales, before highlighting the mechanical particularities associated with experimental investigations on the ECM. Here we will focus exclusively on tests performed on mouse skeletal muscle, which are investigated in our study.

1.2.1. *Ex vivo* experimental methods in small animals at different scales

The mechanical properties of skeletal muscle can be evaluated from characteristic curves derived from standard tests (Tatarenko et al., 2022). Hyperelasticity is displayed in uniaxial tension tests or stretch-release tests (Figure 7B,C), while viscosity can be exhibited through relaxation tests such as incremental stepwise extension (Figure 7A). For both skeletal muscle and muscle fibers, so-called force-length, force-activation and force-velocity relationships can be derived from force-frequency and contraction tests (Figure 7D, E, F, G). The tested sample's orientation influences the results and thus exhibits anisotropic properties.
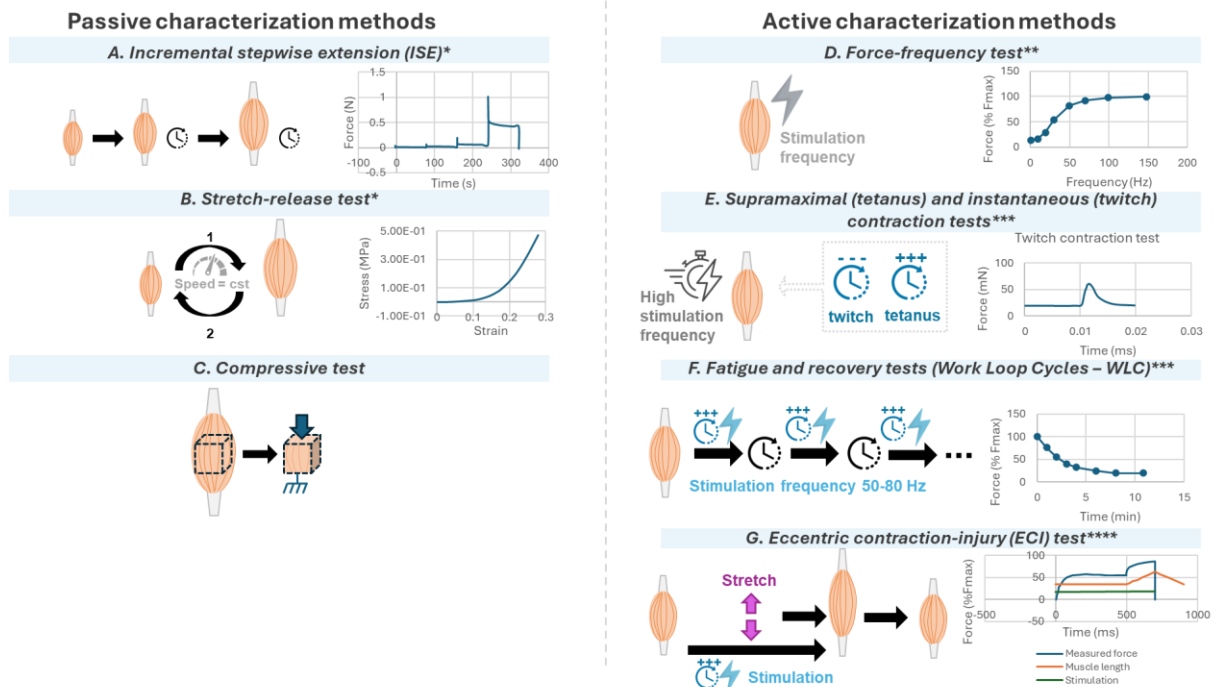
Figure 7. Main passive and active skeletal muscle characterization methods applied to murine muscle. Curves extracted from the literature on whole murine muscles: (*) (Toscano et al., 2010) (**)(Buck et al., 2014) (***) (Tatarenko, 2023) (****) (Liu et al., 2005).

All these methods are applicable to murine skeletal muscles (Tatarenko et al., 2022). Due to the size of muscle, compressive tests are conducted using Atomic Force Microscopy (AFM). Some tests are achievable on the different contractile components up to the submicron scale (Pouletaut et al., 2023), allowing to compare the contributions to the muscle's behavior at the different scales (Figure 8).
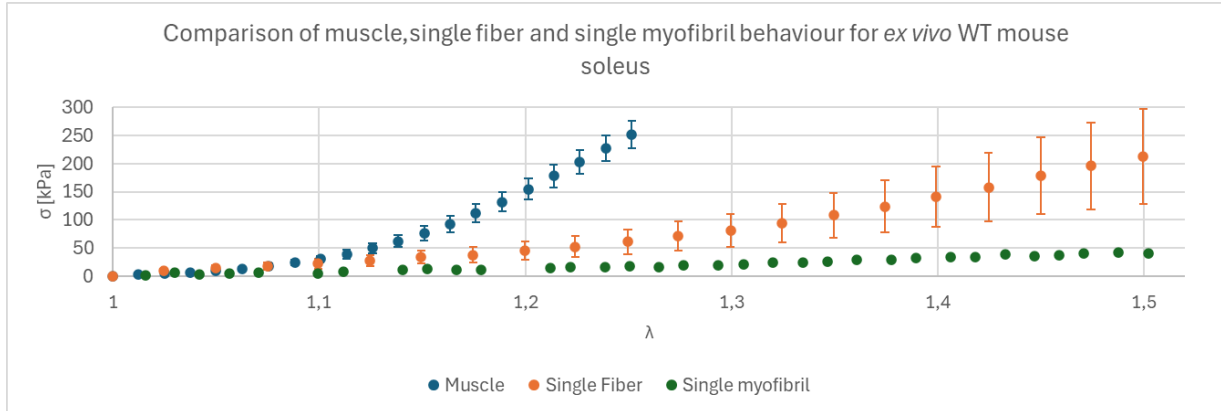
Figure 8. Uniaxial tension response of healthy mouse soleus skeletal muscle components at different scales. Engineering stress is plotted against stretch ratio for each component. Adapted from: (Pouletaut et al., 2023; Tatarenko et al., 2022, 2024).

1.2.2. Elastography in small animals

Elastography is an imaging method that allow to non-invasively assess the *in vivo* mechanical response of a soft tissue (Muthupillai et al., 1995) and has demonstrated clinical diagnosis effectiveness, for instance for cancerous or fibrotic tissues. In particular, dynamic elastography has been developed around 3 successive steps (Figure 9): **(1) Excitation:** non-invasive generation of shear waves within the tissue of interest; **(2) Motion encoding:** encoding of the displacement in medical images (mainly MRI, ultrasounds or optics); **(3) Reconstruction:** estimation of the mechanical properties from the displacement fields using image processing or inverse problem-solving methods.
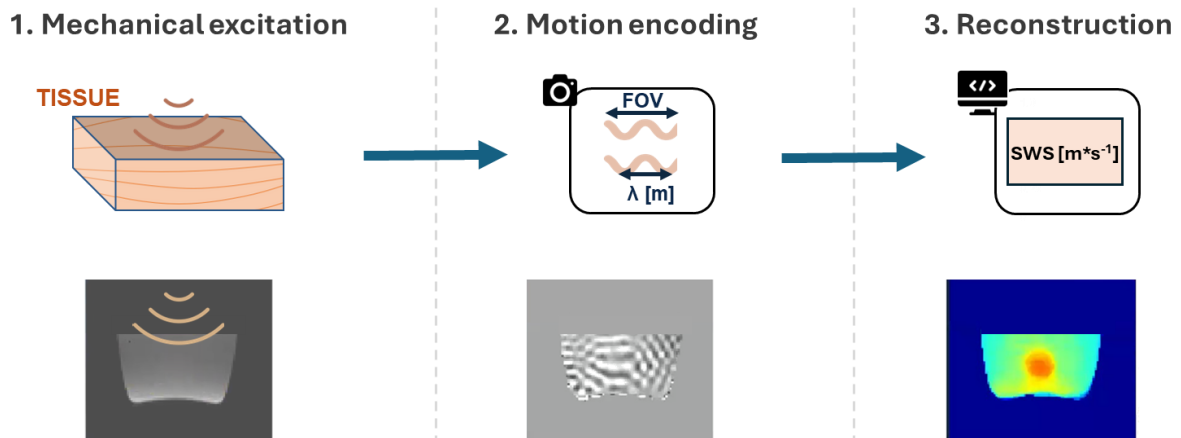
Figure 9. 3 steps of elastography 1) generation of shear waves in the tissue of interest 2) encoding of the displacements through medical imaging and 3) reconstructing the mechanical properties based on the observed local spatial wavelengths within the tissue; image courtesy to J. Vappou.

Murine skeletal muscles have been investigated using different elastography methods: ultrasound (US) elastography (Kammoun et al., 2019; Mele et al., 2016; Sigrist et al., 2017; Suwankanit et al., 2023; Ternifi et al., 2020), Magnetic Resonance Elastography (MRE) (Martins-Bach et al., 2021; Nelissen et al., 2017, 2019; Qin et al., 2014) and optical elastography (Chin et al., 2014; Lloyd et al., 2022) (Figure 9). These techniques allow the *in vivo* imaging of human and murine skeletal muscle mechanical properties in small deformations (Figure 10), with different solicitations used for mechanical excitation (Table 3).

Table 3. Elastography performed on murine skeletal muscles. MRE: Magnetic Resonance Elastography, SWEI: shear wave elasticity imaging, OCT: optical coherence tomography. C57BL/10ScSn-mdx/mdx: Duchenne muscular dystrophy (mdx) mouse model. Tieg1-KO: former designation for Klf10 KO mice.

Study	Mod.	Freq. [Hz]	Mean shear modulus [Pa]	Species	Muscle	Parameter	Ref. on figure 10
Qin et al., 2014	MRE	1000	No value	C57BL/10ScSn-mdx/mdx & C57BL/10ScSn mice	lateral gastrocnemius & plantaris	Anisotropy ratio	-
Martins-bach et al., 2021	SWEI	Pulse	46100	12 month-old DBA/2J mice	Tibialis Cranialis	80° plantar flexion angle	24
	SWEI	Pulse	36000	12 month-old C57Bl/6 mice	Tibialis Cranialis	80° plantar flexion angle	23
	SWEI	Pulse	44100	12 month-old DBA/2J mice	Tibialis Cranialis	60° plantar flexion angle	22
	SWEI	Pulse	34100	12 month-old C57Bl/6 mice	Tibialis Cranialis	60° plantar flexion angle	21
	SWEI	Pulse	30300	12 month-old DBA/2J mice	Tibialis Cranialis	40° plantar flexion angle	20
	SWEI	Pulse	27800	12 month-old C57Bl/6 mice	Tibialis Cranialis	40° plantar flexion angle	19
	SWEI	Pulse	29500	12 month-old DBA/2J mice	Tibialis Cranialis	0° plantar flexion angle	18
	SWEI	Pulse	36000	12 month-old C57Bl/6 mice	Tibialis Cranialis	0° plantar flexion angle	17
Kammoun et al., 2019	SWEI	Pulse	14800	3 month-old WT Mice	hindlimb	Longitudinal	16
	SWEI	Pulse	12033	3 month-old Tieg1-KO Mice	hindlimb	Longitudinal	15
Lloyd et al., 2024	Micro OCT	Quasi-static	15200	24-months-old C57BL/6J mice	Ex vivo quadriceps		14
	Micro OCT	Quasi-static	3633	24-months-old BLAJ mice	Ex vivo quadriceps		13
	Micro OCT	Quasi-static	11067	10-months-old C57BL/6J mice	Ex vivo quadriceps		12
	Micro OCT	Quasi-static	11667	10-months-old BLAJ mice	Ex vivo quadriceps		11
	Micro OCT	Quasi-static	8033	3-months-old C57BL/6J mice	Ex vivo quadriceps		10
	Micro OCT	Quasi-static	8600	3-months-old BLAJ mice	Ex vivo quadriceps		9
Nelissen et al., 2017	MRE	900	4200	3 month-old Sprague-Dawley rats	Tibialis Anterior		8
Nelissen et al., 2019	MRE	900	3290	3 month-old Sprague-Dawley rats	Tibialis Anterior		7
Suwankanit et al., 2023	SWEI	Pulse	2667	4 month-old Wistar rats	Rectus femoris (quadriceps)	Control	6
	SWEI	Pulse	10200	4 month-old Wistar rats	Rectus femoris (quadriceps)	Immobilized	5
	SWEI	Pulse	11033	4 month-old Wistar rats	Vastus medialis (quadriceps)	Immobilized	4
	SWEI	Pulse	2833	4 month-old Wistar rats	Vastus medialis (quadriceps)	Control	3
	SWEI	Pulse	2467	4 month-old Wistar rats	Vastus lateralis (quadriceps)	Control	2
	SWEI	Pulse	10967	4 month-old Wistar rats	Vastus lateralis (quadriceps)	Immobilized	1

In particular, MRE has the great advantage, for the study of a medium as mechanically anisotropic as muscles, of providing 3D information with potential encoding of shear wave fields according to the 3 main directions in space. MRE is typically used with harmonic sinusoidal shear wave propagation, which frequency is limited by the MRI scanner resolution and by the field of view or ROI size. For skeletal muscle, MRE is usually performed around 1000 Hz.
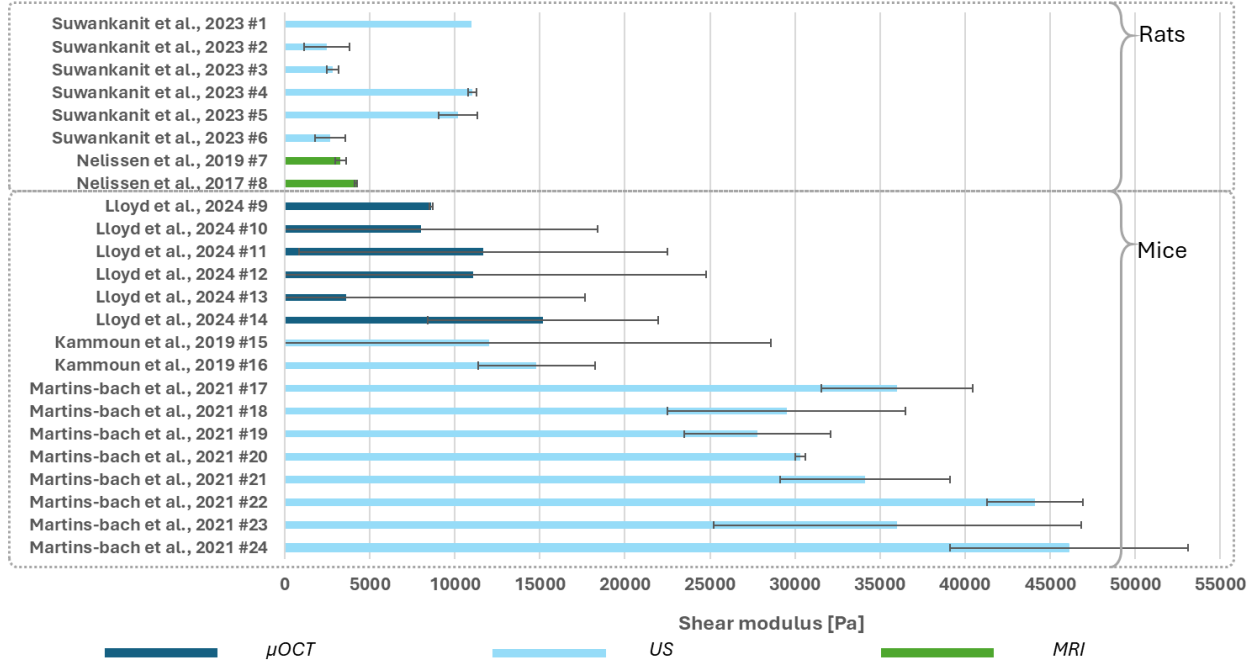
Figure 10. Shear modulus measurements in skeletal muscles of rats and mice using different imaging modalities: optical coherence tomography (OCT), ultrasound imaging (US), magnetic resonance imaging (MRI)

As introduced in the first section, part of the tension within the muscle can be generated through lateral force transmission, with the components involved undergoing shear deformations. Thus, the elastography method is of interest to measure *in vivo* parameters related to those components. **This *in vivo* approach will be developed in the second chapter of this thesis.**

1.2.3. State of the Art of the ECM experimental investigations

In addition to multi-scale experimental tests on whole muscles, muscle fibers and myofibrils, there remains a relatively little-studied element whose importance is now increasingly highlighted: the ECM, a component contributing to the passive stiffness of skeletal muscle. Due to (1) its small volume fraction within the muscle at each scale and (2) its continuous linkages to other components, ECM is difficult to isolate while preserving its structural integrity.

Model of small animals face an additional experimental challenge due to the size of the animal (Tatarenko et al., 2022), that leads to scarcer datasets across the literature. However, animal models presenting pathologies such as Duchenne Muscular Dystrophy (DMD) (Brashear et al., 2021, 2022; DiMario, 2018; Wohlgemuth et al., 2023) or fibrosis (Gillies et al., 2017; L. R. Smith & Barton, 2014) can be studied, at different ages (DiMario, 2018; Gillies et al., 2017; Lieber & Binder-Markey, 2021; Lofaro et al., 2021; Olesen et al., 2022; Sahani et al., 2024; Stearns-Reider et al., 2017; Wood et al., 2014). These studies allow to test hypotheses on ECM behavior and potential medication (Brashear et al., 2022) to treat such conditions.

Investigation methods for ECM remain difficult to implement (Lieber & Binder-Markey, 2021), and focus on characterizing one or other of the following three characteristics of ECM: (1) the ECM

composition, *i.e.* presence and quantity for components; (2) the ECM structure, spatial organization of the components at a given scale; (3) the ECM mechanical behavior at a given scale. Detailed lists of studies characterizing ECM in murine and non-murine species can be found in Appendix A : Experimental characterization of the extracellular matrix at the end of this manuscript.

ECM composition. As introduced in the first section, the ECM composition in the different layers is well-known. Metabolomic analyses allow to test for a variety of genes and proteins specific to ECM (Lofaro et al., 2021). However, analyses focusing on the study of ECM in skeletal muscles often focus on a set of specific components: collagen, laminin, elastin, proteoglycans, and advanced glycation end-products (AGEs). Especially, fibrillar collagen quantity and cross-linking, as well as AGEs content, are investigated using High-Performance Liquid Chromatography (HPLC) (Sanden et al., 2021; L. R. Smith et al., 2021). Light microscopy combined with staining allow to test for elastin (Verhoeff van Gieson staining), collagen III (Herovici staining) and fibrillar collagen (picrosirius red staining) distribution and quantities (Stearns-Reider et al., 2017). Similarly, laminin with collagen distribution and quantities can be investigated using fluorescence microscopy with immunostaining (DiMario, 2018; Lofaro et al., 2021). Mass spectroscopy allows to quantify collagens, proteoglycans and ECM regulators (Lofaro et al., 2021). Overall, the focus is on collagen content. **However, recent studies indicate that although fibrillar collagens are the most important load-bearing components in ECM, their content does not correlate to the whole ECM or whole muscle mechanics (Brashear et al., 2021; Sahani et al., 2024). Thus, the ECM structure is increasingly studied, especially in pathological states such as Duchenne myopathy (Sahani et al., 2022) or cerebral palsy (Smith et al., 2021).**

ECM structure. Although muscle fibers have been extensively studied, the ECM layers surrounding them, and especially their structure, still are not fully understood. Their structure was revealed by a few Scanning Electron Microscopy (SEM) and Transmission Electron Microscopy (TEM) studies (Trotter, 1990; Trotter & Purslow, 1992). The list of studies referring to ECM investigations using these methods is provided in Annex 1 (Appendix A) regarding non murine-species, and Annex 2 (Appendix A) for murine species. TEM and SEM methods allow visualization of the endomysial layer at the microscopic scale, which is difficult to observe due to muscle fibers and perimysium that surround it. Some authors use skeletal muscle decellularization (Gillies et al., 2011; Kuravi et al., 2021b; Purslow & Trotter, 1994; Rowe et al., 2010; Trotter & Purslow, 1992; Wohlgemuth et al., 2023, 2024) as to digest the muscle fibers, leaving empty sheets of ECM. Different existing decellularization methods (Caralt et al., 2015; Gillies et al., 2011) were compared (Reyna et al., 2020) along with a new method using Triton X-100. The comparison was conducted based on collagen, DNA, actin and myosin content, as well as muscle tensile properties, to investigate the efficiency and the damage caused by such methods. The most efficient method (Gillies et al., 2011) did not damage the ECM according to those criteria, although the microstructure integrity has not been checked. The ECM orientation is also increasingly studied using polarized light microscopy and second harmonic generation (SHG) microscopy (Brashear et al., 2021, 2022; Stearns-Reider et al., 2017; Wohlgemuth et al., 2023, 2024; Wood et al., 2014), as it moderately correlates with the ECM and whole muscle mechanical properties (Brashear et al., 2021; Wohlgemuth et al., 2024).

ECM mechanical properties. As detailed previously, *in vivo* imaging techniques provide insight on mechanical parameters within the muscles, however the imaging resolution of the proposed studies does not allow us to go down to sufficiently low scales to properly characterize the ECM *in vivo*. Nevertheless, a number of approaches have made it possible to characterize the ECM in greater detail, both mechanical properties and, more often than not, physiological and metabolic properties, either directly (by characterizing it in isolation) or indirectly (via its influence on skeletal muscle as a whole).

Direct characterization of ECM

An approach to study ECM is to measure the mechanical behavior of a whole skeletal muscle sample after removal of the non-ECM parts. A few studies (Gillies et al., 2011; Kohn et al., 2021; Kuravi et al., 2021b; Wohlgemuth et al., 2023, 2024) have used decellularized muscle to perform tensile and compression tests on ECM alone. Another approach consists in performing two incisions on a muscle (Figure 11), as to prevent muscle fibers from contributing to muscle stiffness during stretch-release tests (Olesen et al., 2022). This test especially allows to quantify lateral force transmission in the whole skeletal muscle at the macroscale. Recently, the mechanical properties of the endomysium were investigated by comparing uniaxial tension tests on two muscle fibers before and after incising the endomysium between them (Danesini et al., 2024).
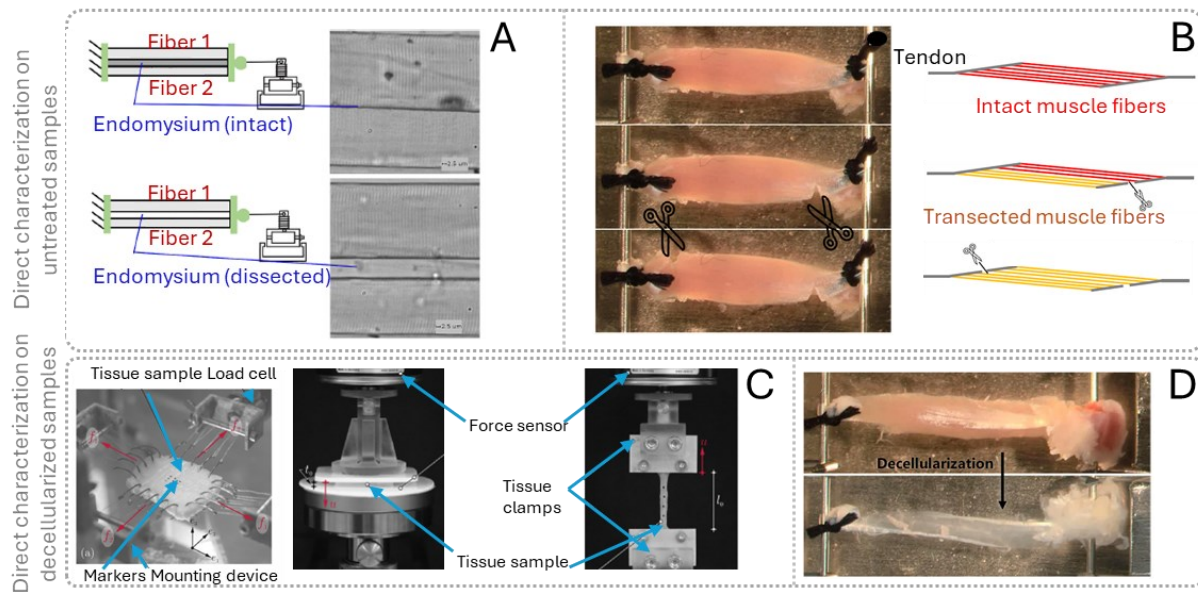
Figure 11. Two approaches allowing to directly investigate ECM mechanical properties in skeletal muscle: A)Uniaxial tension on two muscle fibers with and without incisions in the endomysium between the muscle fibers (Danesini et al., 2024) B) incisions at the middle of the distal aponeurosis and at the middle of the proximal aponeurosis from the opposite side (Olesen et al., 2022); leaving no muscle fibers intact for load bearing as represented schematically. C,D) tests performed on decellularized muscle samples in biaxial tension (Kuravi et al., 2021b), uniaxial tension (Kohn et al., 2021; Olesen et al., 2022) and compression (Kohn et al., 2021)

Indirect investigation of ECM through the mechanical behavior of whole muscle

Tests have been performed on skeletal muscle samples, ranging from fiber (Böl et al., 2019) to whole muscle (Kohn et al., 2021). A few authors have performed experiments at several scales (Table 4), highlighting the non-linearity and evolution of mechanical properties across scales, part of which is attributed to the ECM (Meyer & Lieber, 2011; Ward et al., 2020).

Table 4. Experiments characterizing the mechanical behavior of skeletal muscle at several scales. Scales: (1) macroscopic, (2) mesoscopic, (3) microscopic, (4) submicron.

Study	Solicitations	Muscles	Structures	Species	Scales
Bensamoun *et al.* 2006	Relaxation test, ramp stretch test and stretch release cycle Test	Soleus	Muscle, muscle fiber	Rat	1,3
Meyer *et al.* 2011	Uniaxial tension, relaxation tests	EDL	Muscle fiber, muscle fiber group, muscle fiber bundle	Mouse	2,3
Smith *et al.* 2011	Uniaxial tension	Distal semitendinosus hamstring muscle	Muscle fiber, muscle fiber bundle	Human	3
Wood *et al.* 2014	Uniaxial tension	Tibialis anterior	Single muscle fibers and muscle fiber bundles	Mouse	2,3
Ward *et al.* 2020	Stretch relaxation	Tibialis anterior, EDL, extensor digitorum of the second toe (ED2)	Single muscle fibers, muscle fiber bundles, fascicles, whole muscles	Rabbit	1,2,3
Pouletaut *et al.* 2023	Ramp test and stretch relaxation test	Soleus, EDL	Myofibril (ramp test only), muscle fiber, whole muscle	Mouse	1,3,4

An approach for measuring the mechanical properties of ECM that did not involve muscle fiber digestion was developed, based on comparison of tensile tests with and without presence of ECM (Meyer & Lieber, 2011). The protocol involves stretching and relaxation on mouse EDL single muscle fiber, muscle fiber groups about the size of a muscle fiber bundle, and muscle fiber bundles of 10-20 muscle fibers (Figure 12). Single muscle fiber and muscle fiber groups do not contain ECM between the muscle fibers, contrarily to fiber bundle groups. A nonlinear behavior as well as a significant increase in linear modulus of muscle fiber bundles was reported, likely due to the presence of ECM. This experiment was applied to mice in different studies (Meyer & Lieber, 2011; Wood et al., 2014).
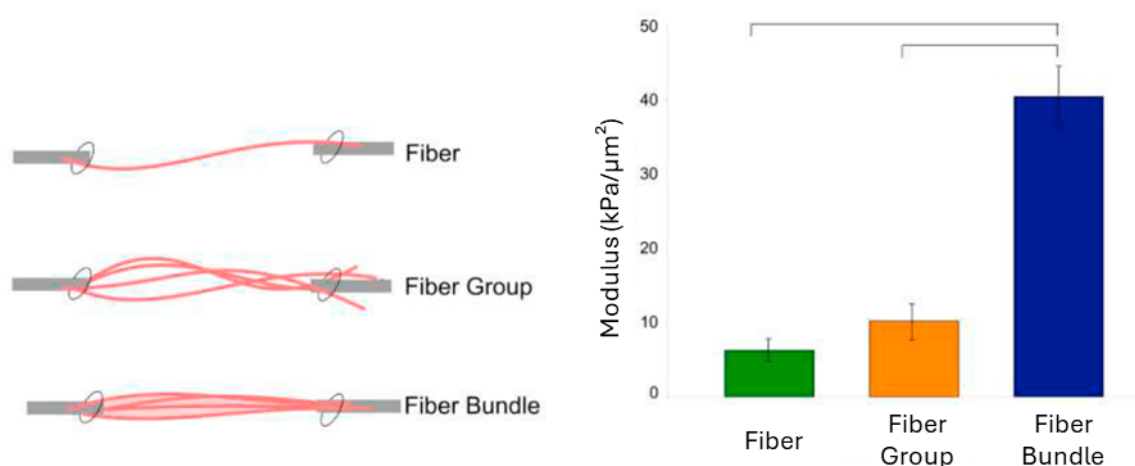
Figure 12. (Left) Schematic illustration of the arrangement of the three specimen types. (Right) Quadratic moduli for fibers, fiber groups and fiber bundles(Meyer & Lieber, 2011).

Similarly, as to identify sources of passive tension within rabbit skeletal muscles, the passive mechanical properties of single muscle fibers, muscle fiber bundles (around 20 muscle fibers), whole fascicles (around 300 muscle fibers delineated by ECM perimysial layer), and whole muscles were measured (Ward et al., 2020) (Figure 13). The macroscale passive modulus was reported as 5 to 10-fold higher than the mesoscale, which in turn was 10 to 100-fold higher than the microscale passive modulus. At the microscale, little difference was observed between muscle fibers and muscle fiber bundles, contrarily to previous observations on mice (Meyer & Lieber, 2011). Moreover, collagen content significantly increased across scales. **The authors concluded that (1) passive modulus is not a constant across scales and (2) passive modulus is nonlinearly increasing across scales in a muscle specific manner, with the ECM's contribution to passive tension increasing across scales.**
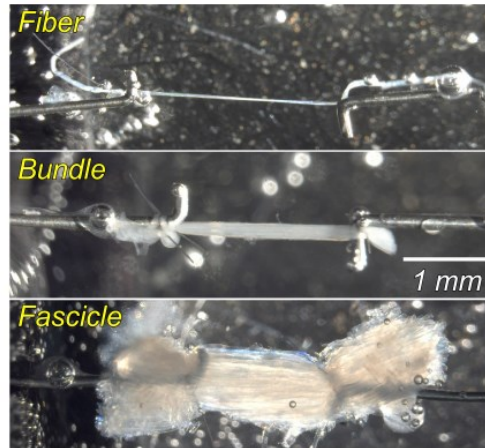
Figure 13. Photomicrograph of samples at the single fiber, fiber bundle (approximately 20 fibers), and fascicle (about 300 fibers, defined by natural ECM divisions) scale.(Ward et al., 2020)

Some authors use such experimental data to identify ECM structural and mechanical parameters in a theorical model. The parameters may not be observable experimentally; hence the model allows new insights on the ECM, but the obtained parameters may not be confirmed by direct experimental observations. These models need a complete dataset to identify the 3D behavior of a skeletal muscle. However, many datasets available in the literature have been obtained from uniaxial tension only, which is not sufficient to identify the transversal properties of the skeletal muscle modeled as a transversely isotropic material (Morrow et al., 2010).

Table 5 presents the publications describing tests performed under 3 configurations or more with the same solicitation mode. Most tests are performed at the macroscopic scale (Böl et al., 2014; Kohn et al., 2021; Mohammadkhah et al., 2016; Morrow et al., 2010; Takaza et al., 2013; Walter et al., 2023). To the best of our knowledge, only one publication reports tests in different configurations at the microscopic scale (Böl et al., 2019). Interestingly, no author has experimented on the same muscle with several configurations at several scales yet.

However, Böl and colleagues have reported experiments with different configurations at different scales for pig muscles in separate publications (Böl et al., 2014, 2016, 2019), as well as tests on decellularized muscles (Kohn et al., 2021; Kuravi et al., 2021b). They especially investigate the possibility to use a rule of mixture on muscle fiber and decellularized ECM experimental data at the microscopic scale to obtain the mechanical behavior of the skeletal muscle at the macroscopic scale (Kohn et al., 2021). They conclude **that the rule of mixture does not allow to reproduce macroscopic scale experimental results, thus exhibiting potential effects of structure and coupling between the muscle fibers and the ECM on the mechanical properties of the whole muscle.**

36

Table 5. Experiments characterizing the mechanical behavior of skeletal muscle in 3 configurations or more. Scales: (1) macroscopic, (2) mesoscopic, (3) microscopic

Study	Solicitations	Muscles	Structures	Species	Scale
Morrow et al. 2010	Longitudinal extension (LE), transverse extension (TE), or longitudinal shear (LS)	EDL	Muscle without aponeurosis (epimysium)	Rabbit	1
Takaza et al. 2013	Tension at different angles (0°, 30°, 45°, 60°, 90°) with respect to the muscle fibers axis	Longissimus dorsi	Muscle samples	Pig	1
Mohammadkhah et al. 2016	Compression and tension in the muscle cross-fibre and fibre directions and at 45° to the muscle fibre direction	Pectoralis	Muscle samples	Chicken	1
Böl et al. 2014, 2016	Semi–confined compression experiments	Biceps femoris	Muscle samples	Pig	1
Böl et al. 2019	Axial tension, axial compression, transversal compression	Biceps femoris	Muscle fibers without endomysium	Pig	3
Kohn et al. 2021	Tension and compression at different angles (0°, 45°, 90°) with respect to the muscle fibers axis	Biceps femoris	Fresh, partly or completely decellularized muscle samples	Pig	1
Walter et al. 2023, Böl et al. 2025	orientation–dependent axial (0°, 45°, 90°) and semi–confined compression experiments	Soleus	Muscle samples	Rabbit	2

All the reported experiments have been performed on *ex vivo* samples, therefore subjected to the effect of *rigor mortis*, which effect on the different skeletal muscle components especially at small scales is not fully understood, and depends on the species, muscles and protocols (Böl et al., 2016). **However, none of the species used for those tests are rodents, as small animals present an additional size challenge for the tested samples.**

Finally, in recent years, many mechanical models have been developed as tools for the study of skeletal muscles. Some mechanical models (Gindre et al., 2013; Sharafi & Blemker, 2011; Virgilio et al., 2015; Zhang et al., 2020) use experimental data at a given scale for characterization of the microstructure. Multiscale models (Bleiler et al., 2019; He et al., 2022; Konno et al., 2021; Kuravi et al., 2021a, 2021b; Lamsfuss & Bargmann, 2022a; Liu et al., 2022; Sahani et al., 2024; Sharafi & Blemker, 2010; Spadoni et al., 2024; Spyrou et al., 2017, 2019; Spyrou, 2020) have been developed as to identify missing experimental data at the microscale, especially on ECM. **It is this latter approach that will ultimately be developed extensively in this thesis.**

Factors influencing the ECM characteristics.

Experimental studies have been performed on diverse pathologic states affecting the ECM: presence of fibrosis in mdx mice (Brashear et al., 2021; Gillies et al., 2017) and in old mice (Wood et al., 2014), cerebral palsy in children (Smith et al., 2021); and abnormalities such as Wooden Breast and Spaghetti Meat chicken (Sanden et al., 2021). Changes in muscle mechanical properties correlate with

pathological states, and these changes may be explained through structural and compositional changes. Some studies (Gillies et al., 2017) and (Brashear et al., 2021) concluded that in mdx mice, collagen architecture rather than collagen content should be investigated for potential therapeutic developments, as the architecture was correlated to the change of mechanical properties. Two studies, (Smith et al., 2021) and (Sanden et al., 2021) reported composition and structural changes. **Collagen cross-linking, fiber quantity, orientation distribution (Brashear et al., 2021; Sanden et al., 2021) and components like type I collagen volume fraction (Smith et al., 2021) were especially pointed at. However authors disagree with the correlation between collagen content and passive muscle stiffness (Brashear et al., 2021; Smith & Barton, 2014). Furthermore, Lieber & Binder-Markey (2021) suggest perimysial collagen cables, which reorganize when strain is applied (Gillies et al., 2017), could be geometrical structures responsible for the difference in load bearing across scales, as exhibited by indirect measurements of the mechanical behavior of ECM.**

1.3. Skeletal muscle modeling

The use of numerical modelling of skeletal muscle and ECM, as mentioned above, will be at the heart of the developments presented in this thesis manuscript around a central point: the effect of a specific gene (Krüppel-like factor 10 or Klf10) on ECM. For this purpose, it is essential to first have a look at the various multiscale mechanical modelling methods for skeletal muscle, and first and foremost at those incorporating information related to the ECM.

To model a multiscale structure, very detailed and complex models including all the components at the different scales (typically in a finite element (FE) framework), can be used. However, this approach is complex to set up and requires extensive resources. Alternatively, multiscale mechanical models are used to link mechanical properties and geometry at different scales. They require a law describing the mechanical behavior for each microcomponent, as to describe the complex global behavior of the multiscale material. Moreover, a multiscale model can also be used to perceive local phenomena happening at smaller scales, when solicitating the material at a larger scale. Considering the specific case of the skeletal muscle, multiscale models have been developed to reproduce the behavior of the whole muscle (Röhrle et al., 2008), but also to identify changes at the microscale due to diseases or thermal therapies (Lamsfuss & Bargmann, 2023; Sahani et al., 2024).

1.3.1. Homogenization methods with their respective hypotheses and limits

Homogenization is currently the most widely used approach for multiscale modeling of skeletal muscle. Homogenization methods have been developed for the study of multiscale materials (Hashin & Shtrikman, 1962, 1963; R. J. Hill, 1965; Reuß, 1929; Voigt, 1889). **These methods consider at a minimum two separate spatial scales: the microscale where the material presents a heterogenous microstructure, and the macroscale, where the material can be supposed homogenous.** Most methods require a strict separation of the scales in terms of dimensions: the microscale must be much smaller than the macroscale, which is the condition for scale separability. Homogenization methods provide a link from the microscale to the macroscale (homogenization) and sometimes an inverse link from the macroscale to the microscale (localization). As we shall see later, it is this particular approach to homogenization methods that is of particular interest to us in the study of ECM.
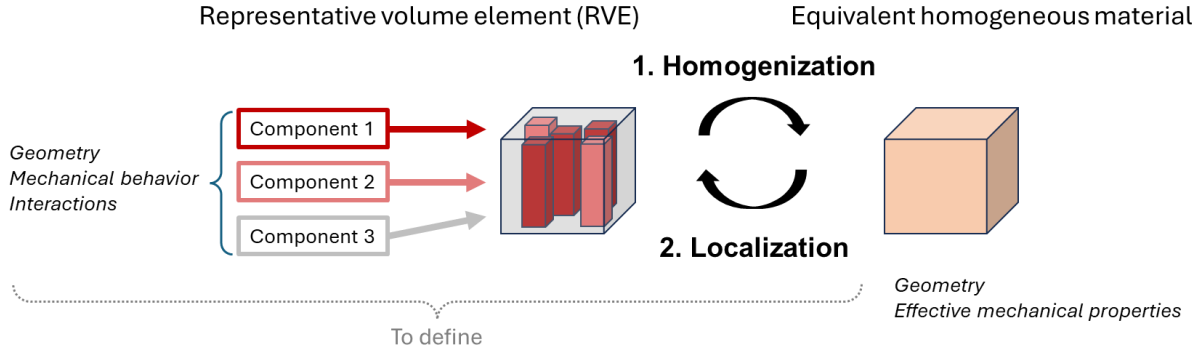
Figure 14. Homogenization of a Representative Volume Element (RVE) to obtain an equivalent homogeneous material

The mechanical behavior at the macroscale is obtained by computing the effective mechanical properties of an equivalent homogeneous material which is representative of the microscopic constituents' behavior (Figure 14). Homogenization methods require specific work on each considered scale. Usually, they allow to link two different scales, namely the macroscale and the microscale. At the microscale, careful definition of the different component's geometry, their interactions, and their behavior is required. Hypothesis regarding the latter characteristics must be formulated in order to use simple models. At the macroscale, it is first and foremost necessary to define a global geometry.

General homogenization approach

Homogenization methods require assumptions and definition of (1) the heterogeneous material's structure distribution at the microscopic scale (RVE), (2) the constituent's constitutive behaviors, and (3) the interactions between the constituents at the microscopic scale.

The first step is the choice of a Representative Volume Element (RVE) which corresponds to the smallest volume representative of the overall behavior. This RVE contains several constituents or phases. The RVE's size should be small enough compared to the macroscopic scale, to ensure a correct separation of scales. Indeed, the variations of mechanical solicitations observed at the RVE scale should be homogeneous at the macroscopic scale. **The second step requires the choice of constitutive behavior for each constituent**. Some homogenization methods are not compatible with complex behavior laws or material anisotropy. Depending on the chosen method, assumptions and simplifications are required. **The third step consists in defining interactions between constituents**. Again, some homogenization methods do not account for interactions, while some others only allow for simple interactions.

As an example, we will describe a simple homogenization approach (Nierenberger, 2013). Let us consider a RVE containing N phases with different volume fractions (Step 1). As many homogenization methods suppose linear elastic materials and small deformations, let us assume each phase i as isotropic linear elastic (Step 2). Let us neglect interactions between the phases (Step 3). The volume fraction of phase i, occupying volume V_i within the RVE, is defined as:

$$f_i = \frac{V_i}{V_{RVE}} \tag{1.3.1.1}$$

By defining $\boldsymbol{\sigma_i}(\boldsymbol{x})$ the stress tensor and $\boldsymbol{\varepsilon_i}(\boldsymbol{x})$ the strain tensor at point x of phase i, the stress-strain relationship within phase i can be defined using $\boldsymbol{C_i}$ the stiffness tensor or $\boldsymbol{Z_i}$ the compliance tensor. The linear elastic behavior within phase $\boldsymbol{i}$ is expressed by the generalized Hooke's law:

$$\boldsymbol{\sigma_i}(\boldsymbol{x}) = \boldsymbol{C_i}\boldsymbol{\varepsilon_i}(\boldsymbol{x}) \; or \; \boldsymbol{\varepsilon_i}(\boldsymbol{x}) = \boldsymbol{Z_i}\boldsymbol{\sigma_i}(\boldsymbol{x}) \tag{1.3.1.2}$$

On the RVE, let us define Σ the mean stress tensor, $\mathbf{E}$ the mean strain tensor, $\mathbf{C}_{eff}$ the homogenized stiffness tensor, and $\mathbf{Z}_{eff}$ the homogenized compliance tensor.

$$\Sigma = \frac{1}{V_{RVE}} \int_{V_{RVE}} \sigma(x)dx = \sum_{i=1}^{N} f_i \mathbf{C}_i \int_{V_i} \varepsilon_i(x)dx \qquad (1.3.1.3)$$

$$\mathbf{E} = \frac{1}{V_{RVE}} \int_{V_{RVE}} \varepsilon(x)dx = \sum_{i=1}^{N} f_i \int_{V_i} \varepsilon_i(x)dx \qquad (1.3.1.4)$$

The RVE should behave according to the following equation:

$$\Sigma = \mathbf{C}_{eff}\mathbf{E} \; or \; \mathbf{E} = \mathbf{Z}_{eff}\Sigma \qquad (1.3.1.5)$$

In a similar way, localization tensors $\mathbf{A}_i$ and $\mathbf{B}_i$ can be defined, and allow to link local quantities $\sigma_i(x)$ and $\varepsilon_i(x)$ to global quantities Σ and $\mathbf{E}$:

$$\varepsilon_i(x) = \mathbf{A}_i(x)\mathbf{E} \qquad (1.3.1.6)$$

$$\sigma_i(x) = \mathbf{B}_i(x)\Sigma \qquad (1.3.1.7)$$

The objective of homogenization methods is to define homogenized tensors $\mathbf{C}_{eff}$ and $\mathbf{Z}_{eff}$, or in an equivalent manner, localization tensors $\mathbf{A}_i$ and $\mathbf{B}_i$.

There exists two main homogenization methods families, namely the numerical computational homogenization methods (Geers et al., 2010; Raju et al., 2021), which require the use of specific simulation tools, and the analytical homogenization methods (Raju et al., 2018). In the following sections, we will refer to these methods as "homogenization" and describe the principles associated with homogenization methods appliable to fiber reinforced composites, that closely correspond to the skeletal muscle microstructure.

Analytical methods: bounds

The Voigt (Voigt, 1889) and Reuss (Reuß, 1929) bounds, also called Rule of Mixture (RoM) models, are amongst the first homogenization methods developed for composites. These formulations give lower bound (Reuss) and upper bound (Voigt) for the effective properties. Both methods are based on the phases' volume fraction, and do not consider the composite's geometry or interactions between phases.

The Voigt formulation assumes isometric strain in the composite, *i.e.* a constant deformation is applied to the composite's boundary. A stiffness tensor is obtained by adding the phases' stiffness tensors pondered by their volume fraction.

$$\mathbf{C}_{eff}^{Voigt} = \sum_{i=1}^{N} f_i \mathbf{C}_i \qquad (1.3.1.8)$$

The Reuss formulation assumes isometric stress in the composite, *i.e.* a constant stress is applied to the composite's boundary; and therefore corresponds to transverse loading. A compliance tensor is obtained by adding the phases' compliance tensors pondered by their volume fraction.

$$\mathbf{Z}_{eff}^{Reuss} = \sum_{i=1}^{N} f_i \mathbf{Z}_i \qquad (1.3.1.9)$$

The bounds provide exact results when the solicitation matches the hypotheses (Figure 15).
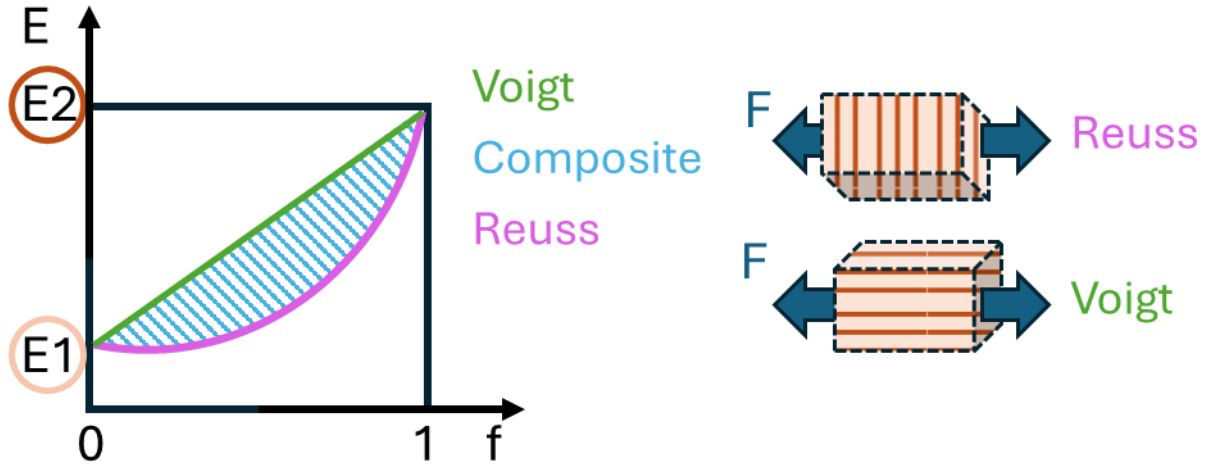
Figure 15. Evolution of a mechanical parameter E as a function of the volume fraction f of component 2 within the material, as computed using the Voigt and Reuss bounds; the exact mechanical parameter is located between the bounds; representation of the assumptions required for each bound.

Analytical methods: Mean Field Homogenization (MFH) methods. The MFH family of methods has been developed from Eshelby's problem (Eshelby, 1959). Eshelby's problem can be expressed as both a homogeneous and a heterogeneous problem that are equivalent (Figure 16). The homogeneous problem considers homogeneous elastic material, which is infinite. Within this infinite geometry, an ellipsoidal region undergoes a uniform deformation, without any constraint applied to it. The heterogenous problem considers an infinite elastic material containing an ellipsoidal inclusion. Moreover, on the boundary of the infinite material, a displacement is applied.
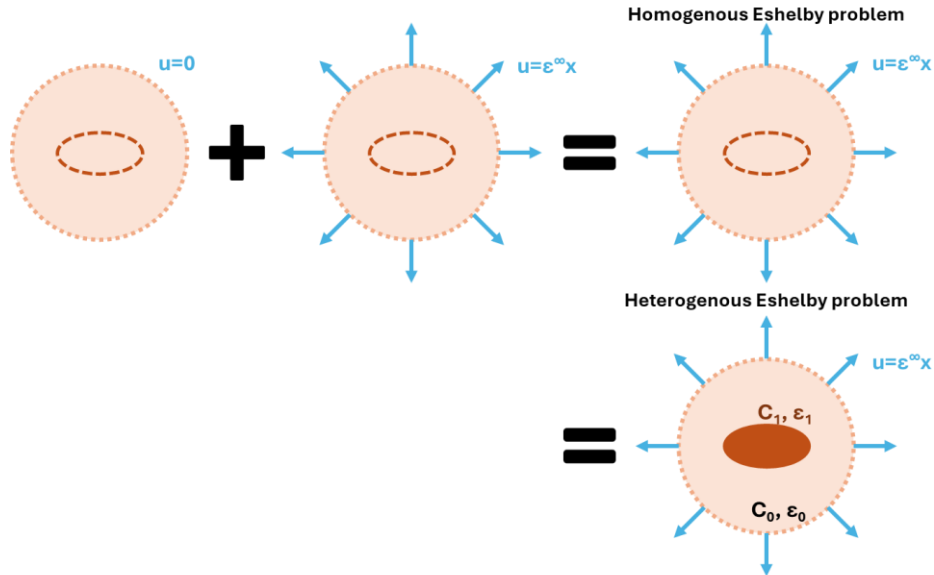
Figure 16. Eshelby's problem

Upon solving this problem, a relationship between the local deformation in the ellipsoidal inclusion ε_1 and the global homogenous free deformation within the material ε_0 is obtained, named the Eshelby tensor. This tensor depends on the infinite material's rigidity and on the inclusion's shape.

$$\boldsymbol{\varepsilon_1} = \boldsymbol{S}\boldsymbol{\varepsilon_0} \qquad (1.3.1.10)$$

Methods based on the solution to Eshelby's problem consider inclusions into an infinite matrix medium (Figure 17), which constitutes the dilute dispersion approximation. Some of them consider

interactions between inclusions (Mori & Tanaka, 1973). Because of the dilute dispersion approximation, inclusion volume fraction should be low. Some MFH methods can be used up to 40% inclusion volume fraction (López Jiménez, 2014).
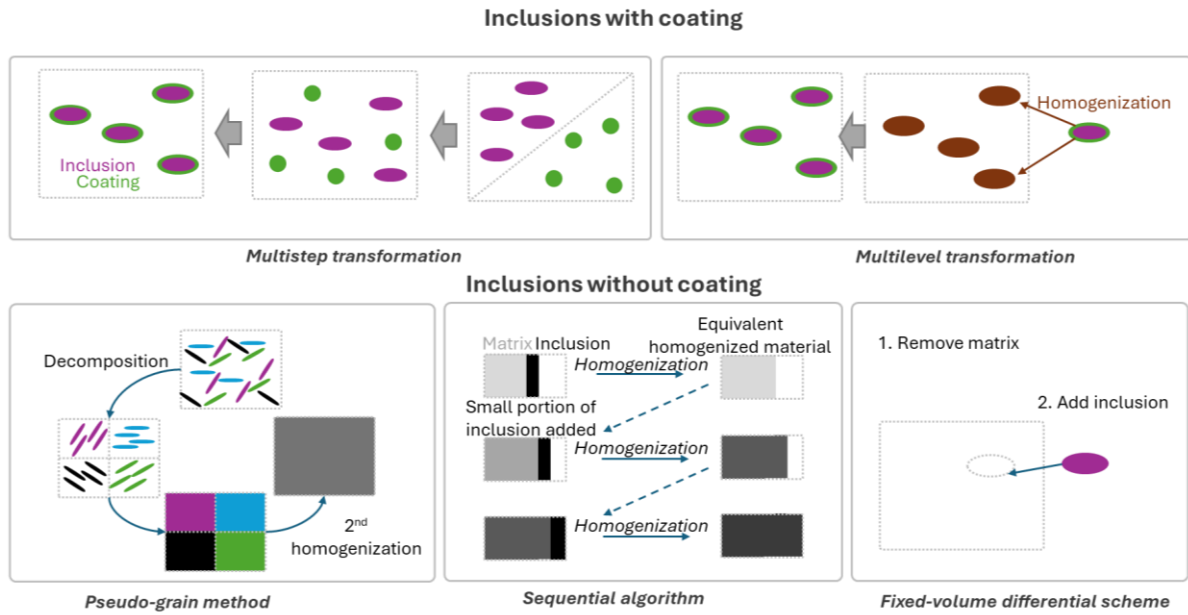
Figure 17. Concept for different homogenization methods based on the Eshelby problem (adapted from (Jain, 2019; Raju et al., 2018))

Analytical methods: asymptotic homogenization.

Asymptotic homogenization was first proposed by Sanchez Palencia in 1983 (Kalamkarov et al., 2009; Sanchez-Palencia, 2006). This method is applied to materials exhibiting periodicity in at least one direction of space. Slow and fast space variables are defined. By using finite series development of the displacement field up to the 2nd order, an equation system is established.

This method considers simple shapes for the inclusions and gives exact results for exact microstructures. However, it will introduce errors if the microstructure is not exactly periodic or if the deformation alters the periodicity hypothesis. For more details on asymptotic homogenization, please refer to (Kalamkarov et al., 2009 ; Potier-Ferry, 2024).

Analytical methods: second order methods.

Most homogenization methods have been developed in the context of linear elasticity. For the analysis of nonlinear materials, the second order methods consider two composites: the actual composite that is being analyzed, and a fictitious composite with the same reference microstructure that exhibits a linear behavior.

This linear behavior is determined for each phase in a way that it represents the linearization of the nonlinear behavior of the actual composite's phase (Bleiler et al., 2021) (Figure 18). They are also called "second-order homogenization scheme" (López Jiménez, 2014). All second order methods are based on suitably chosen linear comparison composites (LCC).
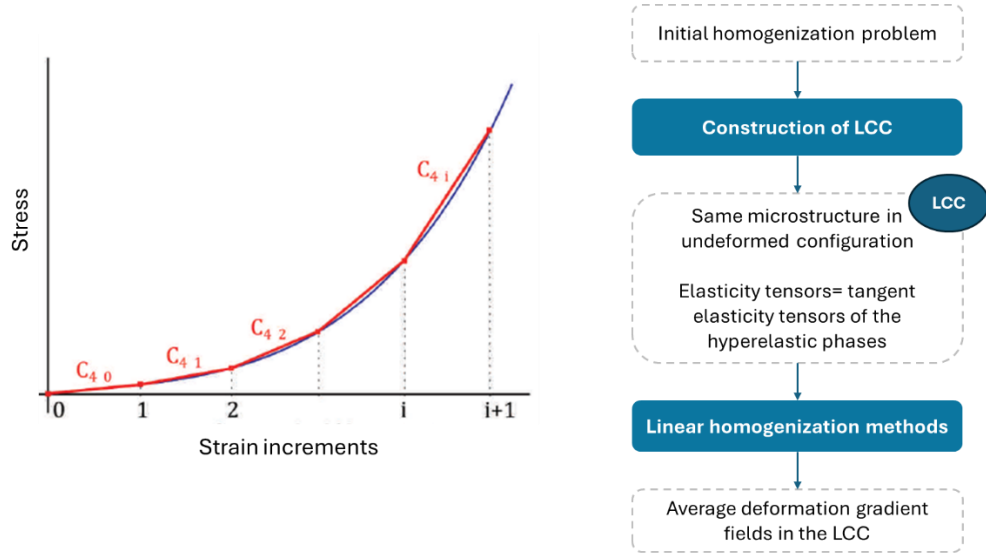
Figure 18. Concept of second order homogenization: the phase's behaviors are considered linear in between two strain increments, thus tangent elasticity tensors are defined (adapted from Nierenberger, 2013)

This approach requires the use of small strain and stress increments otherwise the effective behavior starts diverging from the actual behavior. In the specific case of fiber reinforced composites, such as can be considered for skeletal muscles, several methods (Agoras et al., 2009; Brun et al., 2007; deBotton et al., 2006; Lahellec et al., 2004; Lopez-Pamies & Idiart, 2010) were proposed, as summarized in Table 6. Additional to these methods, a new tangent second order estimate for the behavior of skeletal muscle, considering anisotropic and incompressible muscle fibers and ECM was developed (Bleiler et al., 2021).

Table 6. Second order methods applied to fiber reinforced composites

Study	Hypothesis on material	Method
Lahellec et al., 2004	Periodic microstructures with cylindrical fibers and incompressible phases	2nd order estimates
Brun et al., 2007	Periodic microstructures with cylindrical fibers and compressible phases	2nd order estimates
Agoras et al., 2009	Isotropic phases with generalized Neo-Hookean (I1 based) strain energy functions	Accurate 2nd order estimates
deBotton et al., 2006	Composites with isotropic Neo-Hookean phases	Estimate based on the sequentially laminated (SL) homogenization procedure
Lopez-Pamies & Idiart, 2010	Composites with isotropic Neo-Hookean phases + additional J4 fiber energy contribution	Generalized results of deBotton et al. 2006

Numerical methods: Introduction to FE mechanical modeling

The finite element problem, or Poisson's problem in 1D is given as a simple example to apprehend the Finite Element Method (FEM) (Figure 19). It is formulated on the interval [0;1] and, given $f(x)$, consists in finding $u(x)$ such as:

$$\begin{cases} u''(x) = f(x) \ \forall x \in [0; 1] \\ \quad\quad u(0) = 0 \\ \quad\quad u'(1) = 0 \end{cases} \quad\quad (1.3.1.11)$$

43
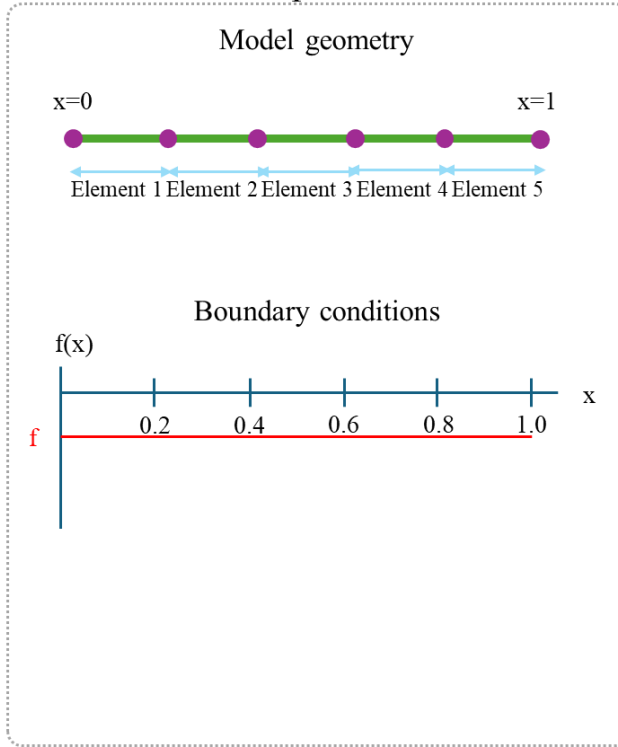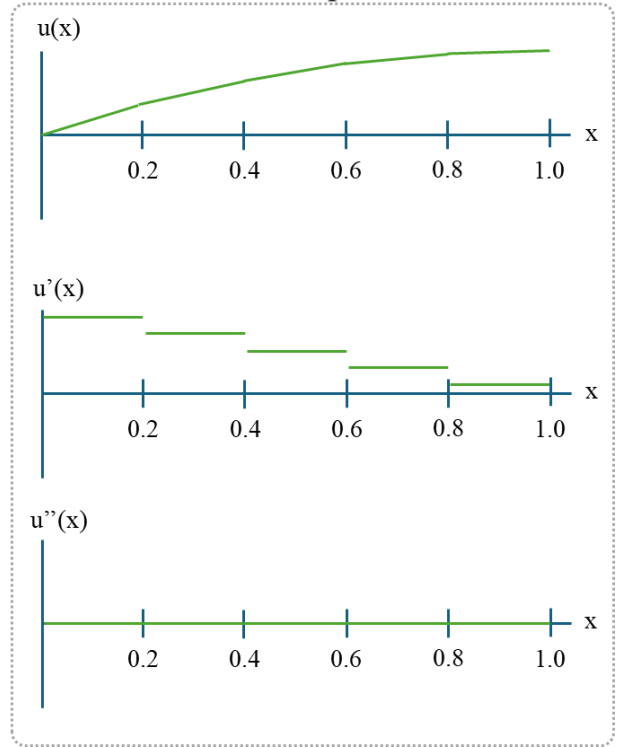
Figure 19. 1D Poisson problem with constant function f(x) defined on five bar elements connected in series, and associated displacement field and its derivatives.

The strong formulation of the problem is so-called because it poses strong hypotheses on u. However, due to the discretized formulation, $u'(x)$ is piecewise constant and $u''(x)$ is null (Figure 19). Let us introduce a test function called v. As multiplying both sides of the equation by v won't change solution u, *i.e.*:

$$u''(x)v(x) = f(x)v(x) \ \forall x \in [0; 1] \tag{1.3.1.12}$$

The following relations, called the weak formulation, can be written:

$$\begin{cases} \int_0^1 u'(x)v'(x)dx = -\int_0^1 f(x)v(x)dx \ \forall v \ with \ v(0) = 0 \\ u(0) = 0 \\ v(0) = 0 \end{cases} \tag{1.3.1.13}$$

In FEM, it is assumed that $u(x)$ is unknown on a finite number of points of interest called nodes. Suppose in this example we have 6 nodes (Figure 19). Between those nodes are elements and, on these elements, it is assumed that $u(x)$ can be described by predefined functions called "shape functions" such that:

$$u(x) = \sum_{i=0}^5 u_i N_i(x) \tag{1.3.1.14}$$

For each node i of a model, the globally defined shape function is:

$$N_i(x) = \begin{cases} 1 \ at \ node \ i \\ 0 \ at \ each \ other \ node \end{cases} \tag{1.3.1.15}$$

44

Then the FE problem is discretized as follows.

Let us introduce the discretized functions u and v and the shape functions at the corresponding nodes (The same goes for v):

$$u(x) = \sum_{i=0}^{5} u_i N_i(x) \tag{1.3.1.16}$$

$$u'(x) = \sum_{i=0}^{5} u_i N_i'(x) \tag{1.3.1.17}$$

$$U = \begin{bmatrix} u_0 \\ u_1 \\ u_2 \\ u_3 \\ u_4 \\ u_5 \end{bmatrix} ; V = \begin{bmatrix} v_0 \\ v_1 \\ v_2 \\ v_3 \\ v_4 \\ v_5 \end{bmatrix} ; N(x) = \begin{bmatrix} N_0(x) \\ N_1(x) \\ N_2(x) \\ N_3(x) \\ N_4(x) \\ N_5(x) \end{bmatrix} ; N'(x) = \begin{bmatrix} N_0'(x) \\ N_1'(x) \\ N_2'(x) \\ N_3'(x) \\ N_4'(x) \\ N_5'(x) \end{bmatrix} \tag{1.3.1.18}$$

The discretized form of the weak formulation can be written as:

$$\int_0^1 V^T N'(x) N'^T(x) U dx = -\int_0^1 f(x) V^T N(x) dx \tag{1.3.1.19}$$

$$V^T \int_0^1 N'(x) N'^T(x) dx \, U = V^T \int_0^1 -f(x) N(x) dx \tag{1.3.1.20}$$

$$V^T K U = V^T F \tag{1.3.1.21}$$

For all V with $v_0 = 0$ and $u_0 = 0$.

The final equation to solve is:

$$KU = F \tag{1.3.1.22}$$

Here K is the stiffness matrix, and F the vector of nodal forces. Although this explanation is simple, this is not how the computations are done in practice.

Shape functions and integration points. FEM uses reference elements (Figure 20). A reference element has its own natural coordinate axes ranging from -1 to 1. The interest in such a coordinate system is the exact computation by a computer of integrals between -1 and 1. To apply the FE method, a need for a mapping Φ_e between this reference element and the actual element arises. This is done using shape functions. The isoparametric concept is the use of the same shape functions in a reference element and in a deformed element, to compute the position of a point within the element.

On a bar element, the shape functions are defined as (Figure 20):

$$\mathcal{N}_0(\xi) = \frac{1}{2} - \frac{1}{2}\xi \tag{1.3.1.23}$$

$$\mathcal{N}_1(\xi) = \frac{1}{2} + \frac{1}{2}\xi \tag{1.3.1.24}$$

$$x = \Phi_e(\xi) = \frac{1}{2}(a+b) + \frac{1}{2}(b-a)\xi = \frac{1}{2}(1-\xi)a + \frac{1}{2}(1+\xi)b = \mathcal{N}_0(\xi)a + \mathcal{N}_1(\xi)b \tag{1.3.1.25}$$
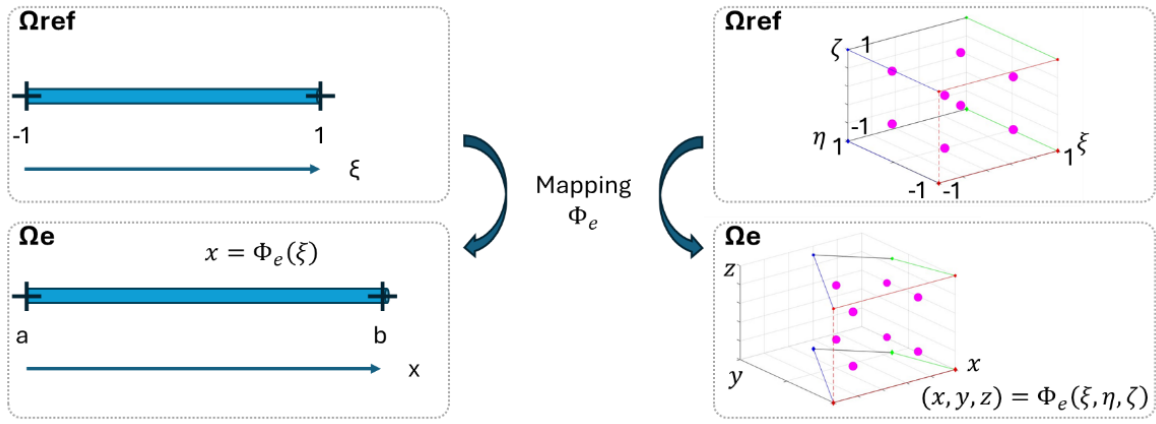
Figure 20. Concept of shape functions in finite element modeling.

Thus the stiffness matrix K, and the vector of nodal forces F can be recomputed as:

$$K_{ij}^e = \int_{-1}^{1} \frac{\partial \mathcal{N}_i(\xi)}{\partial \xi} \left(\frac{\partial \Phi_e(\xi)}{\partial \xi} \right)^{-1} \frac{\partial \mathcal{N}_j(\xi)}{\partial \xi} \left(\frac{\partial \Phi_e(\xi)}{\partial \xi} \right)^{-1} \frac{\partial \Phi_e(\xi)}{\partial \xi} d\xi \qquad (1.3.1.26)$$

$$F_i^e = \int_{a}^{b} -f(x) N_i^e(x) dx = \int_{-1}^{1} -f(\Phi_e(\xi)) \mathcal{N}_i(\xi) \frac{\partial \Phi_e(\xi)}{\partial \xi} d\xi \qquad (1.3.1.27)$$

These formulations are integrals from -1 to 1 and can be computed using gaussian quadrature.

Gaussian quadrature. This numerical method allows the exact computation of integrals by a computer, by transforming an integral into an equivalent sum. Given a polynomial $P(\xi)$ and a set of Gauss points ξ_i and Gauss weights w_i, the integral of P from -1 to 1 can be computed as:

$$\int_{-1}^{1} P(\xi) d\xi = \sum_{i} P(\xi_i) w_i \qquad (1.3.1.28)$$

The higher the polynomial P, the more Gauss points and weights are needed. In FEM, the Gauss points are called integration points and their coordinates in the reference element are known. Their coordinates in the deformed configuration are computed using the mapping through shape functions (Figure 21).
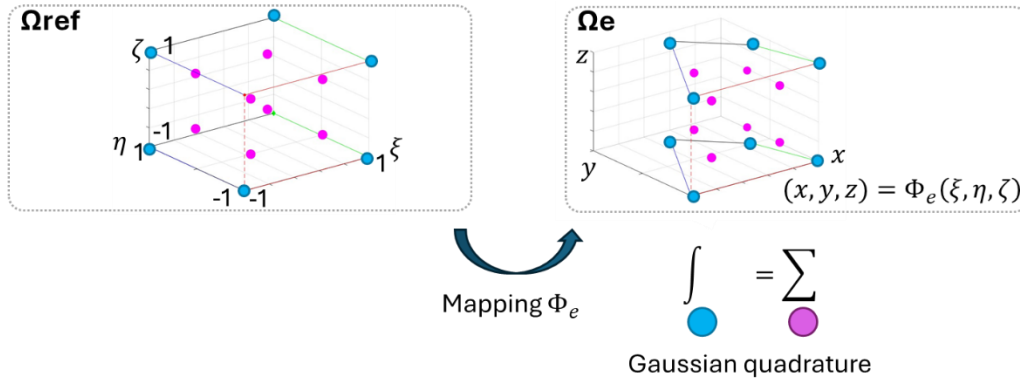
Figure 21. Gaussian quadrature.

Numerical methods: FE²

FE² is a subclass of computational homogenization schemes in which both homogenization and localization are performed. It bears different names and descriptions in the literature (Raju et al., 2021): "*FE²*", "*2 scale FEM simulation in the form of a nested boundary value problem (BVP)*", "*2 scales analyzed or calculated concurrently*", "*Multi-level FEM*" or "*first-order computational homogenization*".

The FE² method computes a single scale's simulation at a given time and passes information from one scale to another, so it is a hierarchical method. Two different FEM simulations representing the two scales are running in a nested manner and passing information to each other (Figure 22). There is one macroscale simulation and there can be several parallel microscale simulations. It uses the deformation gradient and no higher order gradients, which is why it is called a first order computational method.
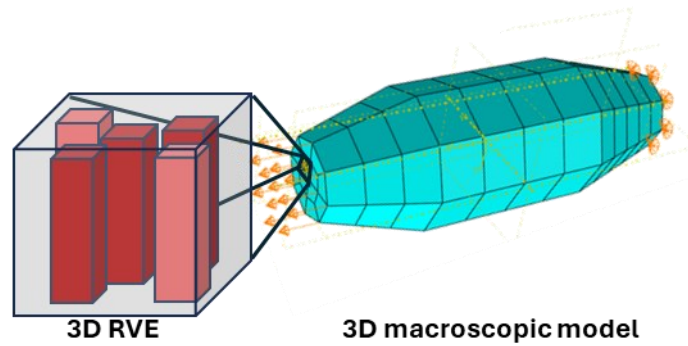
Figure 22. Concept of FE² methods

Each integration point of the macroscale finite elements is associated with its own microscale RVE. The FE² method consists of three main components (Raju et al., 2021):

(1) A geometrical description and a FE model of the unit cell, which is the RVE.

(2) The local constitutive laws describing the response of each component of the composite within the unit cell.

(3) Scale transition relationships that define the connection between the microscopic and the macroscopic fields (stress and strain). These are: (i) a downscaling rule that determines the microscale boundary problem for the RVE given the macroscopic deformation measures; (ii) an upscaling rule for the macroscopic stress given the micromechanical stress state.

Numerical methods: DFE²

In computational homogenization, the different families of FE² methods (Raju et al., 2021) have received increasing interest over the last years. Specifically, a new method called DFE² (Direct FE²) has been proposed in Tan et al. (2020) and applied to the study of porous materials (Liu et al., 2023; Oukfif et al., 2024; Singh Dhari et al., 2023), fiber reinforced materials (Hu et al., 2024; Zhi et al., 2021) and laminates (Zhi, Leong, et al., 2023, 2023). This method is computationally efficient and only requires knowledge of the microstructural mechanical properties. The global approach is illustrated in Figure 23 for the case of laminated thin-shell structures.
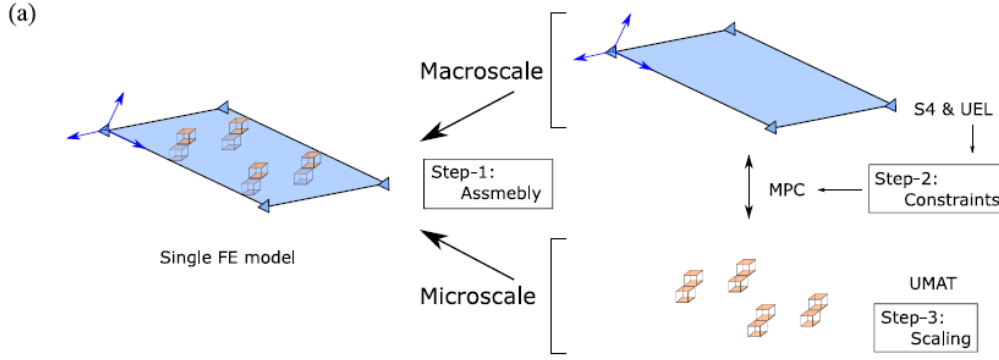
Figure 23. 3 steps for the implementation of DFE² (Zhi, Leong, et al., 2023). Here the RVEs and the macroscopic model belong to the same FE simulation.

There exist more homogenization methods which will not be described in this manuscript due to their irrelevance for long fiber reinforced composites. **The aforementioned methods are all suitable for long fiber reinforced composites under specific hypotheses (Table 7). Thus, only a subset of them have been employed to model skeletal muscles.**

Table 7. Qualitative comparison of the described homogenization methods for long fiber reinforced composites. "+": adapted; "-": not adapted; "?": no information.

Method	High fiber volume fraction	Accounts for the microstructure	Complex microstructure	Additional requirements
Bounds	+	-	-	Loading aligned with the fibers
Mean Field Homogenization	-	+	+	Ellipses or perfect cylinders, up to 40% inclusions due to the dilute dispersion assumption
Asymptotic homogenization	+	+	-	Perfectly periodic microstructure
Second order methods	?	+	?	Depending on the chosen homogenization technique for homogenizing the LCC
FE²	+	+	+	Dependent on the applied boundary conditions

1.3.2. Skeletal muscle multiscale models

The literature review on multi-scale numerical models of the skeletal muscle, as proposed below, has been the subject of a publication to which we invite the reader to refer for further details (Loumeaud et al., 2024). More detailed description of multiscale skeletal muscle models is provided in Annex 3 (Appendix B at the end of this manuscript).

Model geometry

Multiscale modeling implies a definition of a simplified geometry that is representative of the skeletal muscle at the considered scale, based on hypotheses on the anatomical constituents (Bargmann et al., 2018). Here we discuss the implementation of realistic and idealized geometries. Realistic geometries tend to reproduce medical imaging acquisitions (Lauzeral et al., 2019) and are implemented in skeletal muscle multiscale models mostly from microscopy cross section images (Kuravi et al., 2021a; Kuravi et al., 2021b; Marcucci et al., 2017, 2019; Sharafi & Blemker, 2010; Zhang et al., 2020). Kuravi and colleagues propose a 3D realistic geometry obtained from registration and

segmentation protocols on successive histological cross sections, resulting in a 3D reconstruction of a cubic muscle sample at the microscale (Kuravi et al., 2021a; Kuravi et al., 2021b). Realistic geometries can also be AI generated (Virgilio et al., 2015).

However, most multiscale models do not use microscopy images directly, but rather simplified geometries either in 1D, 2D or 3D (Figure 24). 1D elements are used to represent constituents at the submicron scale such as titin represented with springs (Heidlauf et al., 2016, 2017; Schmid et al., 2019), or myofibrils and collagen represented with bars (Terzolo et al., 2022) (Figure 24 A). 1D muscle fibers are modeled at the microscale as springs (Roux et al., 2016, 2021, 2023) and as bars (Heidlauf et al., 2016, 2017; Schmid et al., 2019) (Figure 24 B). At the microscopic scale, some authors assume that muscle fibers are parallel to each other. Thus 2D plane geometries representing a muscle cross section are often extruded alongside the direction orthogonal to the plane, generating a 3D geometry with regular arrangements of parallel muscle fibers such as perfectly circular (Konno et al., 2021; Lamsfuss & Bargmann, 2021, 2022a) (Figure 24 C) or hexagonal (Spadoni et al., 2024; Spyrou et al., 2017; Teklemariam et al., 2019) (Figure 24 D). Perfectly circular arrangements are simple of use especially considering analytical homogenization methods, as these methods often consider elliptical or cylindrical fiber reinforced composites (Jain, 2019). However, the maximum fiber packing or fiber volume fraction (FVF) that can be obtained using this arrangement is 90.7% whereas the muscle fiber FVF in healthy muscles reaches 95%. Moreover, this geometry creates local section variations in the ECM, which are not representative of the real microstructure (Kammoun et al., 2016). Hexagonal muscle fibers overcome these drawbacks, yet they consider fibers with equal geometries and areas, while the real microstructure is more random and contains fibers with different sizes (Kammoun et al., 2017). Thus, an increasing trend is the use of randomized regular arrangements such as Voronoi tessellations (Honda, 1978). Voronoi tessellations or a Voronoi diagram constitute in partitions of a plane into convex regions also called cells. The cells are defined by a given set of points called Voronoi seeds or centroids. Each Voronoi region is defined by a seed. Any point belonging to that region is closer to that seed than to any other seed present in the set. The obtained regions vary in size and shape. Periodic Voronoi tessellations are obtained by duplicating the seeds contained in a 1x1 region into a 3x3 grid and intersecting the obtained Voronoi diagram by a 1x1 bounding box (Figure 24 E). This specific arrangement has been used for periodic numerical homogenization (He et al., 2022; Honda, 1978; Lamsfuss & Bargmann, 2023; F. Liu et al., 2022; Sahani et al., 2024; Spyrou, 2020; Spyrou et al., 2019). Some authors also define curved-edge Voronoi tessellations (Kuravi et al., 2021a; Kuravi et al., 2021b; Liu et al., 2022) using different methods to round up the obtained Voronoi regions, arguing that the realistic geometry does not contain sharp angles. At the mesoscale, fascicles and ECM have been also represented using Voronoi tessellations (Lamsfuss & Bargmann, 2022b). At the macroscale, idealized 3D muscle geometries include rectangular parallelepiped and idealized fusiform muscle shape (Roux et al., 2016, 2021, 2023; Spyrou et al., 2019) (Figure 24 F). Examples of different model geometries implemented in FE softwares are presented in Figure 25.
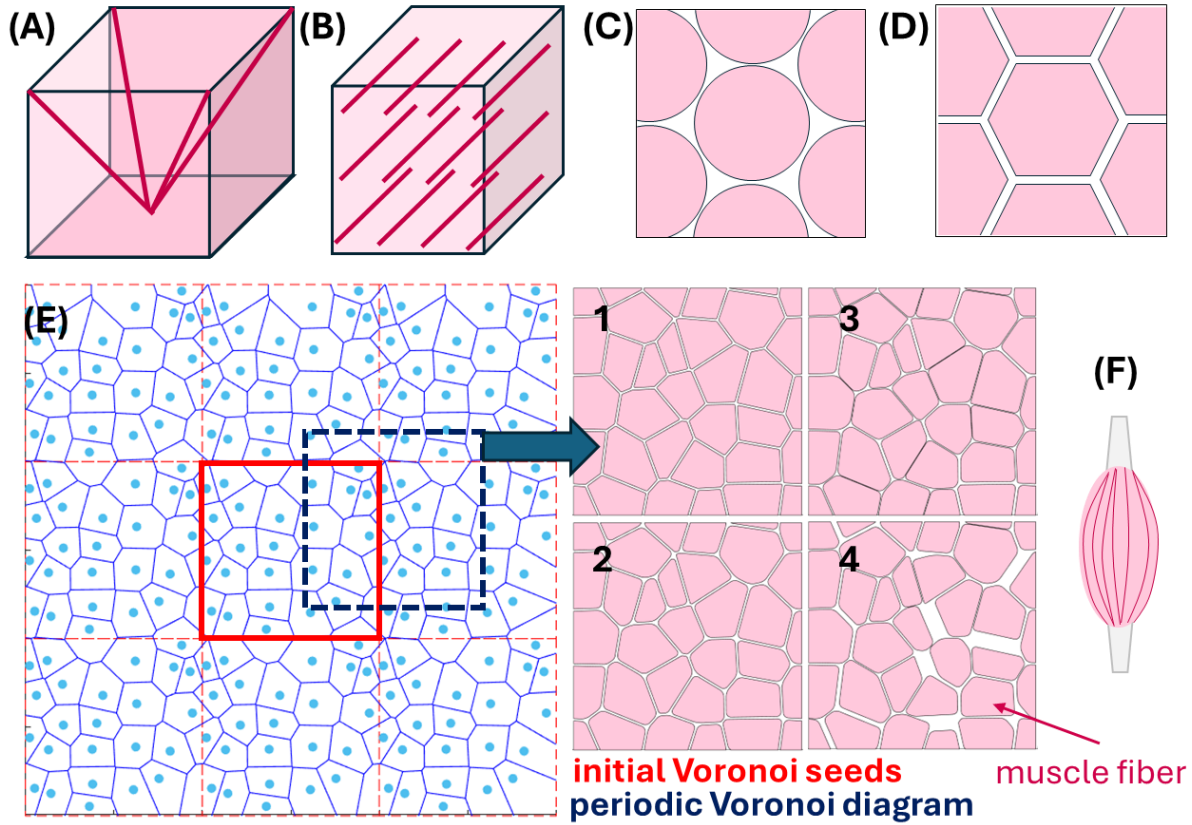
Figure 24. Idealized geometries to represent skeletal muscle: (A) myofibrils represented as trusses in a 3D geometry, (B) parallel 1D fibers embedded in a 3D muscle geometry (C) regular circular arrangement, (D) regular hexagonal arrangement, (E) periodic Voronoi

In the specific context of homogenization, the representative geometry is named unit cell or Representative Volume Element (RVE) (Bargmann et al., 2018; Drago & Pindera, 2007). Recently, tools that can be used to generate RVE in Finite Element software have been developed (Lamsfuss & Bargmann, 2022b; Omairey et al., 2019; Riaño & Joliff, 2019). They allow to automatically generate microscale circular arrangements (Riaño & Joliff, 2019), submicron scale to mesoscale arrangements including Voronoi tessellations (Lamsfuss & Bargmann, 2022b) and periodic boundary conditions (Omairey et al., 2019), that have specific application for numerical homogenization or averaged values scale transitions.
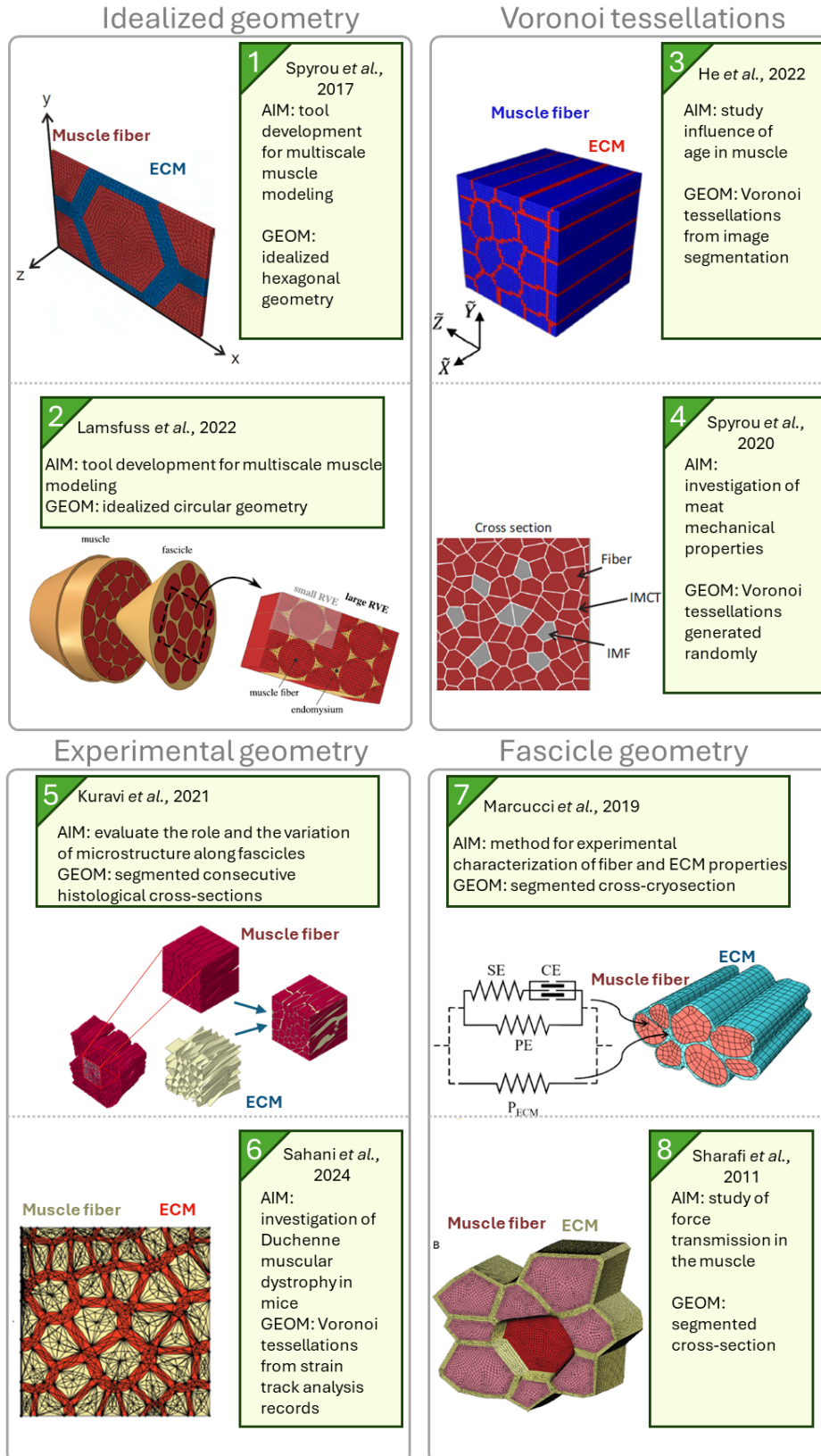
Figure 25. Examples of muscle models and their geometries: idealized hexagonal (Spyrou et al., 2017), circular (Lamsfuss & Bargmann, 2022a) and Voronoi tessellations (He et al., 2022; Spyrou, 2020) geometries, and realistic geometries using Voronoi tessellation- based methods (Kuravi et al., 2021a; Sahani et al., 2024) or muscle cross-section segmentation (Marcucci et al., 2019; Sharafi & Blemker, 2011). For more details, please refer to Appendix B.

Homogenization methods applicable to skeletal muscles

From the submicron scale to the mesoscale, skeletal muscle can be modeled as a fiber reinforced composite, with a Fiber Volume Fraction (FVF) ranging from 90 to 95% for healthy muscles at the microscale. The muscle's microconstituents exhibit an anisotropic behavior (Böl et al., 2019; Kohn et al., 2021; Takaza et al., 2013) but are often assumed transversely isotropic in multiscale models. The aforementioned features constitute a current limitation for the use of most analytical homogenization methods developed for the investigation of fiber reinforced composites.

Amongst these methods **the Mean Field Homogenization (MFH) methods** (Jain, 2019) are based on the so-called dilute dispersion assumption, which considers that the fibers should be contained in dilute quantities in a very large matrix medium, therefore excluding materials with high FVF. Thus, other homogenization methods have been applied to skeletal muscle modeling.

The Voigt and Reuss methods, also named **rule of mixture laws**, provide respectively upper and lower bounds for the behavior of the equivalent homogenous material in the case of a composite reinforced with long parallel fibers (Reuß, 1929; Voigt, 1889). The Voigt method (Voigt, 1889) assumes an isometric strain in the composite and is consequently used for load cases in the direction of the fibers. Its counterpart is the Reuss method (Reuß, 1929) which considers isometric stress in the composite. The advantage of these methods is their simplicity, as they are based only on the FVF, however this implies that they do not take the microscopic geometry into account. Due to this simplicity, homogenized skeletal muscle models often use the Voigt homogenization (Bleiler et al., 2019; Konno et al., 2021; Sahani et al., 2024; Spyrou et al., 2017). However, multiscale experiments on muscle tissue seem to show that the rule of mixture does not allow to capture the multiscale behavior of the skeletal muscle (Kohn et al., 2021).

Another **method based on asymptotic homogenization** (Abdel Rahman et al., 2012; Caillerie et al., 2006) has been used in skeletal muscle modeling (Terzolo et al., 2022). Briefly, asymptotic homogenization assumes that at least one direction of space at the microscopic scale is periodic. The method relies on the displacement field's description at the microscopic scale using fast and slow space variables to account for this periodicity, and then on the application of finite series development to obtain an equation system. Caillerie et al. (2006) developed an estimate for graphite sheets, that corresponds to the linearized behavior of the composite around a pre-stressed configuration. This method provides a better estimate than the Voigt and Reuss methods, at the cost of increased complexity.

One last family of homogenization methods used in the context of skeletal muscle multiscale modeling is the **second order methods**, that have been developed for the modeling of nonlinear elastic composites. Second order methods based on estimates for sequentially laminated composites (López Jiménez, 2014; Lopez-Pamies & Idiart, 2010) have been implemented (Spyrou et al., 2019) and recently developed (Bleiler et al., 2021) for biological materials such as skeletal muscles. Through these methods, high FVF composite including constituents with transversely isotropic behavior can be replicated. Bleiler et al. (2021) developed an estimate considering an anisotropic behavior for all microscopic constituents of a fiber reinforced composite. **However, these methods exhibit great complexity and cannot account for complex geometries at the microscale.**

Numerical or **computational homogenization methods** help overcome the limitations associated with analytical approaches to predict the behavior of heterogeneous materials with complex geometries and solicitations. These homogenization methods are based on simulations of a discretized geometry. They can be separated in two categories, namely hierarchical and concurrent (Raju et al., 2021). **Hierarchical methods** consider different simulations for the different scales, and information is

passed from one simulation to another. Usually, one macroscopic scale simulation is linked to several microscopic scale simulations. The hierarchical approach is implemented through the use of Finite Element Modeling for skeletal muscle homogenization (He et al., 2022; Lamsfuss & Bargmann, 2022a; Liu et al., 2022; Sahani et al., 2024; Sharafi & Blemker, 2010; Spyrou, 2020; Spyrou et al., 2017, 2019), mostly through the use of computational periodic homogenization (Michel et al., 1999) which requires the discretized microscopic scale geometry to be periodic in all space directions.

Conversely, **concurrent methods** consider different scales simultaneously in different subvolumes of the same simulation and these scales may exchange information in hand-shake regions. Some authors also developed a concurrent numerical homogenization method using two different meshes in the same simulation and computing variable interpolation between the two structures (Röhrle et al., 2008) for muscle simulation (Heidlauf et al., 2016, 2017; Röhrle et al., 2012; Schmid et al., 2019). Hierarchical methods can be used to increase the model resolution in the case of damaged areas. However, they do not allow to model Fracture Process Zones (FPZ) to simulate muscle tear for example. This is made possible by concurrent approaches that render a more precise interaction between the scales. Both methods are computationally expensive.

Some multiscale models do not use homogenization methods. Modeling approaches such as Hill's model (Affagard et al., 2015; Carriou et al., 2019; Marcucci et al., 2017, 2019) draw the link between scales as it separates the mechanical contribution of each microscale constituent. Another approach, namely micromechanical modeling, considers large microscale geometries representative of the skeletal muscle and considers the behavior of these composites identical to the macroscale muscle's behavior. This information on the macroscale can be obtained through the average value of stresses and strains over the considered representative volume or surface. This approach is simple and allows a more complex representation of geometry and behavior. This method is used to obtain information on the microstructure, however phenomena happening at the macroscale (*i.e.* FPZ) cannot be modeled with this approach, as it doesn't provide localization.

Passive behavior at different scales

Some of the multiscale mechanical models of skeletal muscle include multiphysics parts, such as chemical (Carriou et al., 2019; Heidlauf et al., 2016, 2017; Schmid et al., 2019; Roux et al., 2021, 2023; Ceelen et al., 2008) or electrical ones (Carriou et al., 2019; Heidlauf et al., 2016, 2017; Schmid et al., 2019; Roux et al., 2021, 2023), to mimic the muscle activation in an active component. It is therefore essential to distinguish, at each scale of skeletal muscle modeling, between passive and active components, both of which will influence the mechanical behavior of the muscle at higher scales. **In our study, we want to develop a multiscale model from our own experimental data. The experimental data at our disposition do not include active data at different scales, and do not provide muscle behavior in large deformations at different speeds. These elements do not allow us to observe the viscous effects in large deformations; therefore viscosity is not included in our model. Consequently, only a passive hyperelastic muscle behavior is considered as a first approach. Since active behavior modeling is not in the scope of this thesis, it will not be detailed in this section.**

At the submicron scale, passive constitutive laws are developed for myofibrils or more specifically titin. Titin is modeled as a linear spring (Heidlauf et al., 2016, 2017; Schmid et al., 2019) or a worm-like-chain model (Gindre et al., 2013). Myofibrils and collagen fibers are modeled as crimped fibrils in an isotropic matrix (Terzolo et al., 2022).

On the scale above, referred to here as microscopic scale, muscle fibers constitutive laws depend on the modeling framework used. In Finite Difference Modeling (FDM), linear springs are used to

represent muscle fibers in traction (Roux et al., 2016, 2021, 2023) and in compression (Roux et al., 2021, 2023). Similarly, using Hill's model, the muscle fiber is represented by three elements, including in series contractile and elastic elements, and a parallel elastic element, using exponential and quadratic hyperelastic formulations (Kammoun et al., 2016; Marcucci et al., 2017). Using Finite Element Modeling (FEM), Reproducing Kernel Particle Method (RKPM) (Zhang et al., 2020), or analytical frameworks, muscle fibers are usually modeled by separate isotropic and anisotropic contributions. The isotropic behavior accounts for cellular components other than myofibrils and is usually represented by simple hyperelastic laws such as Neo-Hookean (Bleiler et al., 2019; Spyrou et al., 2017, 2019; Spyrou, 2020; Lamsfuss & Bargmann, 2021, 2022a, 2023; Ceelen et al., 2008), second order Mooney Rivlin (He et al., 2022), Yeoh models (Konno et al., 2021; Teklemariam et al., 2019), or a quadratic polynomial function (Zhang et al., 2020).

The muscle fiber anisotropic passive behavior is attributed to myofibrils and especially titin proteins. Constitutive laws are expressed as a function of the fiber stretch with a linear (Spyrou et al., 2017, 2019), quasi linear (Terzolo et al., 2022), exponential (He et al., 2022; Zhang et al., 2020) or polynomial (Konno et al., 2021; Teklemariam et al., 2019; Spyrou, 2020) shape, which coefficients are identified on muscle fiber uniaxial tension experimental data (Tatarenko et al., 2024). The fiber stretch is directly related to the Cauchy-Green tensor's invariant I4, thus most models make use implicitly of invariant I4 to model anisotropy. Using a more phenomenological approach, this invariant is explicitly used by Kuravi et al. (2021a and 2021b) following the formulation proposed in Holzapfel et al. (2000). In the same way, Liu et al. (2022) use invariant I4 in combination with invariant I5. The use of invariant I5 is justified by the need to represent shear deformations more accurately (Castillo-Méndez & Ortiz, 2022b). The Criscione invariants (Criscione et al., 2001) have been used to represent shear deformations (Sharafi & Blemker, 2010; Virgilio et al., 2015; Sahani et al., 2024; Sharafi & Blemker, 2011; Blemker & Delp, 2005), as these invariants have a better physiological interpretability than the classical ones, thus leading to more interpretable modeling results. The aforementioned approaches for muscle fibers constitutive modeling are summed up in Figure 26. Some authors introduce corrective coefficients to take age into account (He et al., 2022; Zhang et al., 2020). The titin contribution in the muscle fiber can also be found as a homogenized version of a submicron scale model (Heidlauf et al., 2016, 2017; Schmid et al., 2019). To study rupture in muscle fibers, a model of irreversible deformations and microcracks is proposed in Lamsfuss & Bargmann (2022a).

ECM is represented as a linear elastic material (Roux et al., 2016, 2021, 2023), an isotropic material (Marcucci et al., 2019; Konno et al., 2021; Lamsfuss & Bargmann, 2021, 2022a, 2023) or as a collagen fiber reinforced material (Bleiler et al., 2019; He et al., 2022; Kuravi et al., 2021a; Kuravi et al., 2021b; Spyrou, 2020; Spyrou et al., 2017, 2019). Isotropic depictions of ECM include Yeoh (Konno et al., 2021) and first order Ogden (Lamsfuss & Bargmann, 2021, 2022a, 2023) hyperelastic models. The Hill model (Hill, 1938) has also been extended to separate the muscle fibers and ECM contribution by adding a parallel stiffness to the previous 3D model (Marcucci et al., 2019) representing ECM by means of an exponential formulation.

As a fiber reinforced material, the ECM is modeled as an isotropic matrix reinforced with collagen fibers. As the collagen fibers are wavy and present a specific orientation in the tissue, formulations accounting for the waviness and uncrimping of the collagen fibers in soft tissues have been developed (Gindre et al., 2013; Holzapfel & Ogden, 2015, 2017). The isotropic matrix has been modeled considering a Neo-Hookean behavior (Bleiler et al., 2019; Spyrou et al., 2017, 2019; Spyrou, 2020) or a Mooney Rivlin model (He et al., 2022). Authors use collagen fiber orientations of either ±55° or ±59° relative to the muscle fibers' orientation. Two main families of methods have been described and compared in the literature to model the collagen fibers: the angular integration (AI) approach (Lanir,

1983) and the generalized structure tensor (GST) approach (Gasser et al., 2006). The AI approach considers the mechanical behavior of each collagen fiber and then integrates this behavior over a volume where specific fiber orientation distributions can be defined. On the contrary, the GST approach uses a tensor called generalized structure tensor to represent a fiber family's global orientation, and the mechanical behavior is defined per fiber family. This topic has been reviewed in Holzapfel et al. (2019). The angular integration approach for skeletal muscles ECM is presented in Gindre et al. (2013). More models use the AI approach (Bleiler et al., 2019; He et al., 2022; Sahani et al., 2024; Spyrou, 2020; Spyrou et al., 2017, 2019) than the GST approach (Kuravi et al., 2021a; Kuravi et al., 2021b) as the GST approach is more recent.

Recent ECM models considering collagen cross-linking in the ECM have been developed (Holzapfel & Ogden, 2020; Tian et al., 2016) as this feature directly influences the mechanical properties of ECM (Lieber & Binder-Markey, 2021; Lieber & Meyer, 2023). Moreover, as costameres connect the interior of the muscle fiber to the ECM, this leads to a phenomenon called lateral force transmission, where the fiber's force is transmitted through shear to the ECM. The ECM network then locally redistributes the loads into the fascicle through endomysium shear (Lieber & Binder-Markey, 2021; Purslow, 2002). Consequently, shear modeling in the ECM has gained increasing interest in multiscale models. The previous approaches do not consider shear contribution of the collagen fibers into the extracellular matrix. Recent models aimed at including shear stress related components in ECM constitutive laws. (Kuravi et al., 2021b) developed a specific skeletal muscle ECM behavior law based on the GST approach that also includes a volumetric contribution to penalize volume changes and a structural contribution to model shear. Similarly, Liu et al. (2022) used a passive anisotropic hyperelastic contribution for ECM that includes the Cauchy-Green tensor's invariants I5 and I7, that was developed to better model shear in arteries (Wang & Liu, 2020).

Fat inclusions at the microscale are modeled as an isotropic neo-hookean material (Spyrou, 2020; Virgilio et al., 2015). Transmembrane proteins have also been included at the microscale (Virgilio et al., 2015) as nonlinear springs. The rupture in ECM, muscle fibers, and tendon fibers (Bensamoun et al., 2006) can also be implemented as in Roux et al. (2023).

Very few authors include fascicles as a realistic boundary material in multiscale models. To the best of our knowledge, no specific constitutive laws have been developed for the fascicles in the context of multiscale modeling. A general approach is the use of a rule of mixtures applied to micro constituent behaviors to determine the parameters of a hyperelastic constitutive law (Marcucci et al., 2019; Virgilio et al., 2015). The parameters of a 3D Hill model have been identified by the response of a motor unit (Carriou et al., 2019). They differ from the fascicles as muscle fibers contained in the same motor unit do not necessarily belong to the same fascicle. The skeletal muscle has been represented with motor units grouped in parallel.
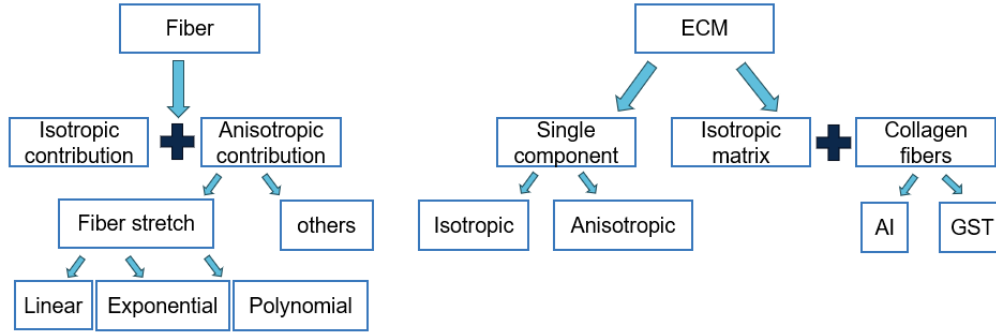
Figure 26. Main approaches to represent muscle fibers and ECM behaviors at the microscale, AI: angular integration, GST: generalized structure tensor

Finite element analysis is increasingly used to analyze the influence of muscle constituents at each scale (such as muscle fibers, fascicles, myofibrils, collagen fibers and others components of the ECM) on the overall mechanical response of the organ (Konno, 2022; Loumeaud et al., 2024; Sahani et al., 2024; Spadoni et al., 2024; Virgilio et al., 2015), allowing for the investigation of pathologies such as neuro-muscular diseases (Konno et al., 2021) or dystrophies (Sahani et al., 2024). However, few of them integrate parameters related to muscle fiber types and geometric characteristics, which can vary through a pathological process (Kammoun et al., 2017; Sahani et al., 2022).

In this thesis, we study the effect of a specific genetic deletion on the mouse skeletal muscle. **Accounting for the Klf10 gene effect and the data previously acquired by our group (detailed hereafter), we chose to develop a passive hyperelastic model using numerical homogenization, including three anisotropic components: muscle fibers, ECM, and the link from ECM to muscle fibers (called transition layer). These components are modeled using a Holzapfel-Gasser-Ogden (HGO) hyperelastic behavior law (Holzapfel et al., 2000) which includes an isotropic contribution with fiber reinforcement using the angular integration approach, and requires only 4 material parameters. To build our model, we do not take into account the viscous properties of the skeletal muscle, which should be considered in future works. As detailed in chapters 3 and 4, our approach provides decoupling of the geometry and mechanical properties, with a genotype-specific microscopic geometry. Therefore we chose to use numerical homogenization with the FE² method which accounts for a complex microstructure. Moreover, the chosen method provides visualization of stress tensorial fields at the microscopic scale.** The next section details the known modifications induced by the Klf10 gene deletion. Particular attention is paid to both structural and mechanical changes observed in different components at different scales, as these elements determine the choice of homogenization method.

1.4. Role of the Klf10 gene on the skeletal muscle

In this thesis, we are focusing on a particular gene, Krüppel-like factor 10 (Klf10), and its influence on multi-scale skeletal muscle mechanical behavior in a mouse model. **We aim to go beyond existing *ex vivo* experimental characterizations at different scales, using two independent approaches: by studying its influence *in vivo*, using the elastography methods described above, and by using multiscale numerical modeling based on homogenization and finite elements to understand its influence on ECM.** But to do this, we first need to properly establish current knowledge of Klf10's impact on the structure and mechanical response of skeletal muscle.

1.4.1. General implication of Krüppel-like factor 10 (Klf10) gene

The Klf10 gene, also called *transforming growth (TGF) factor β-inducible early gene 1* (TIEG1), encodes a protein belonging to the subfamily of zinc finger proteins and the Krüppel-like transcription factor family. These proteins regulate gene transcription for cell development and differentiation (Blok et al., 1995; Subramaniam et al., 2010). The gene was first identified in the context of bone physiology and disease (Subramaniam et al., 1995), as a regulatory gene for growth and function of human fetal osteoblastic cells.

The function and expression associated with the Klf10 gene differ according to the considered organ and the patient's gender (Subramaniam et al., 2010). Due to its role in cell proliferation inhibition and apoptosis induction, the expression of the Klf10 gene is globally linked to immune system reactions and inflammatory processes. In humans, the gene is involved in osteoporosis in female patients. Studies suggest that Klf10 acts as a tumor suppressor in a variety of cancers, and especially in breast cancer (Reinholz et al., 2004; Subramaniam et al., 2010).

To further study these physiological effects, murine models with inhibited expression of the Klf10 gene were developed (Subramaniam et al., 2005), called Klf10-knockout (Klf10 KO). Indeed, the protein sequence of human Klf10 possesses an homologous gene in the murine genome (Subramaniam et al., 2010). Upon inhibiting the Klf10 gene in mice, defects in the skeleton (Subramaniam et al., 2005), heart (Rajamannan et al., 2007) and connective tissue (DiMario, 2018; Gumez et al., 2010) were observed. Some effects are gender-dependent: only female mice develop osteopenic phenotype, while mostly male mice display cardiac hypertrophy (Rajamannan et al., 2007) .

1.4.2. Role of Klf10 gene in the structural and mechanical properties of skeletal muscle

The Klf10 gene is also largely expressed in skeletal muscles (Blok et al., 1995). Thus, the Klf10 KO mouse model was used to investigate potential effects in skeletal muscles. More precisely, different characteristics have been compared between Klf10 KO and Wild Type (WT) mice skeletal muscles, at different scales (Figure 27). **More specifically, the soleus (SO) and Extensor Digitorum Longus (EDL) muscles were studied across different scales (Tatarenko et al., 2024). Soleus is a slow muscle containing mostly slow (type I) muscle fibers, while EDL is a fast muscle containing mostly fast muscle fibers.** Slow-twitch (Type I) fibers rely on aerobic metabolism (oxidative). They possess many mitochondria, a rich blood supply, and high myoglobin content, allowing them to efficiently produce ATP using oxygen. Fast-twitch (Type II) fibers rely on anaerobic metabolism (glycolytic). They have fewer mitochondria and less myoglobin but can generate ATP quickly. However, they build up fatigue more rapidly (Lloyd et al., 2023).
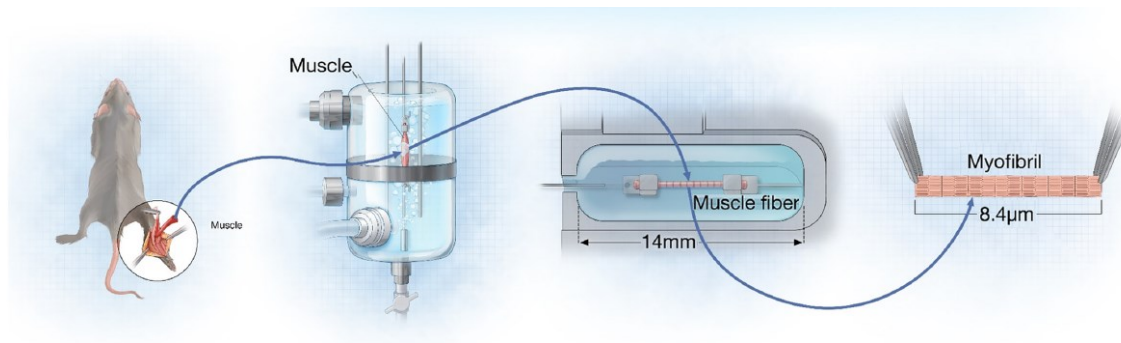
Figure 27. Representation of mechanical tests performed on murine muscles at different scales (Pouletaut et al., 2023).

At the macroscopic scale, murine muscle *ex vivo* and *in vivo* mechanical properties, as well as structural properties have been investigated (Table 8).

Treadmill exercise (Kammoun et al., 2020) performance of the two genotypes was evaluated. Significant differences were found in the total distance run until exhaustion. The two genotypes were also investigated *in vivo* imaging. Both MRI imaging (Kammoun et al., 2017, 2019) and B-mode ultrasound US imaging (Kammoun et al., 2019) on soleus and EDL muscles of Klf10 KO and WT mice allowed to discriminate between the two genotypes based on the texture analysis of the image. However, US imaging, and shear wave US elastography (SWE) (Kammoun et al., 2019) showed no difference in mean echo intensity or coefficient of variation of contrast and mean stiffness, coefficient or variation of contrast. **Thus, at the macroscopic scale, *in vivo* differences could be observed in the structure of the skeletal muscles but not in the mechanical properties.**

Similarly, using mechanical *ex vivo* experiments including stretch-release tests, ramp tests, stretch-relaxation (Tatarenko et al., 2024), no significant differences between the two genotypes were observed.

Table 8. Test applied to SO and EDL muscles at the macroscopic scale for both WT and Klf10 KO genotypes.

Test	Muscles	Animals	Significant differences between WT and KO?	Study
MRI imaging + Texture analysis + Principal Component Analysis on Texture analysis	Soleus, EDL	10 WT, 10 KO	Changes in texture analysis (MRI -TA)	(Kammoun et al., 2017)
MRI imaging + Texture analysis + Principal Component Analysis on Texture analysis	Soleus + EDL + tibialis anterior, plantaris, gastrocnemius lateralis, gastrocnemius medialis	10 WT, 10 KO	Changes in texture analysis (MRI -TA)	(Kammoun et al., 2019)
Shear wave ultrasound elastography + ultrasound imaging and texture analysis, PCA analysis	Soleus, EDL	7 WT, 7 KO	Differences in texture analysis only	(Kammoun et al., 2019)
Treadmill exercise, total distance until exhaustion	Soleus	10 WT, 15 KO	Differences in distance	(Kammoun et al., 2020)
Ramp stretch with a stretch-release cycle (0,167 mm/s speed to 25% L_0 magnitude)	Soleus, EDL	9 SO WT, 9 EDL WT, 6 SO KO, 8 EDL KO	No significant differences	(Tatarenko et al., 2024)
stress-relaxation test using a fast stretch followed by relaxation (5 L_0/s speed to 25% L0 magnitude)	Soleus, EDL	9 SO WT, 9 EDL WT, 6 SO KO, 8 EDL KO	No significant differences	(Tatarenko et al., 2024)

At the microscopic scale, histological analyses (Kammoun et al., 2017) and optical microscopy (Kammoun et al., 2021; Pouletaut et al., 2021, 2023) on WT and Klf10 KO muscle cross-sections revealed **muscle fiber hyperplasia (increase in muscle fiber quantity) and hypertrophia (increase in muscle fiber size) as well as changes in the fiber's type and area distributions (Figure 28).** The fiber type distribution was shifted towards an increase of glycolytic type II muscle fibers to the detriment of oxidative type I muscle fibers.
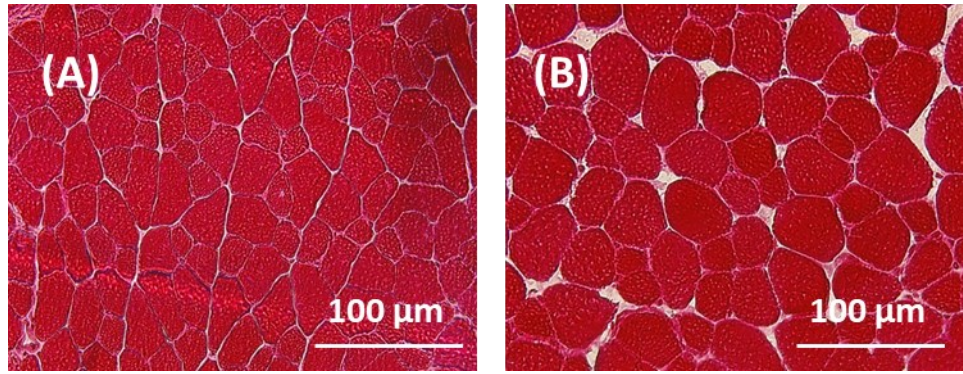
Figure 28. Soleus muscle cross-section observed with optical microscopy with genotype (A) WT and (B) Klf10 KO (Kammoun et al., 2017).

Mechanical tests such as ramp stretch-release , relaxation (Kammoun et al., 2016; Pouletaut et al., 2023; Tatarenko et al., 2022), active tests (Kammoun et al., 2021) and AFM (Kammoun et al., 2019) were performed on isolated muscle fibers (Figure 29**). Muscle-type specific behaviors were observed: Klf10 KO mice display stiffer mechanical properties in the soleus and softer mechanical properties in the EDL compared to WT controls (Tatarenko et al., 2024), thus suggesting a muscle fiber type - dependent effect.**
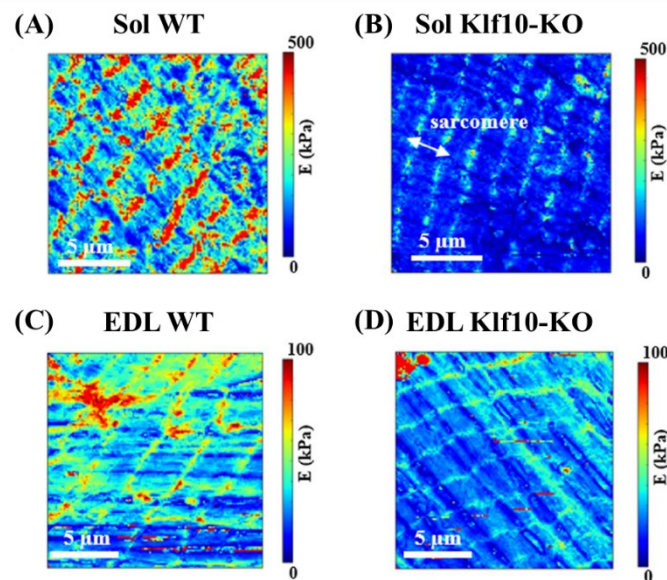
Figure 29. Elasticity maps (15 μm × 15 μm) obtained from AFM for slow (A,B soleus: Sol) and fast (C,D EDL) muscle fibers of wild-type (WT) and Klf10 knockout (KO) mice.(Kammoun et al., 2019)

Submicron scale

Interestingly, **no changes in the passive mechanical properties were observed between WT and Klf10 KO myofibrils at the submicron scale**, upon passive stretch-release on myofibrils (Pouletaut et al., 2021). Moreover, no changes in titin molecular weight were observed between the genotypes. These results suggest that the genetic deletion does not affect titin (Tatarenko et al., 2024). **Thus, the changes in mechanical properties observed at the microscopic scale may be due to other components, potentially transmembrane proteins in the costameres or proteins in the ECM.**

However, TEM analyses exhibited structural differences at the submicron scale (Kammoun et al., 2019, 2020, 2021). Structures like the sarcomeres and the mitochondria are especially affected (Figure 30). Those changes can have a direct influence on the skeletal muscle's active mechanical

properties, as those structures are involved in the contraction processus and energy supply respectively.
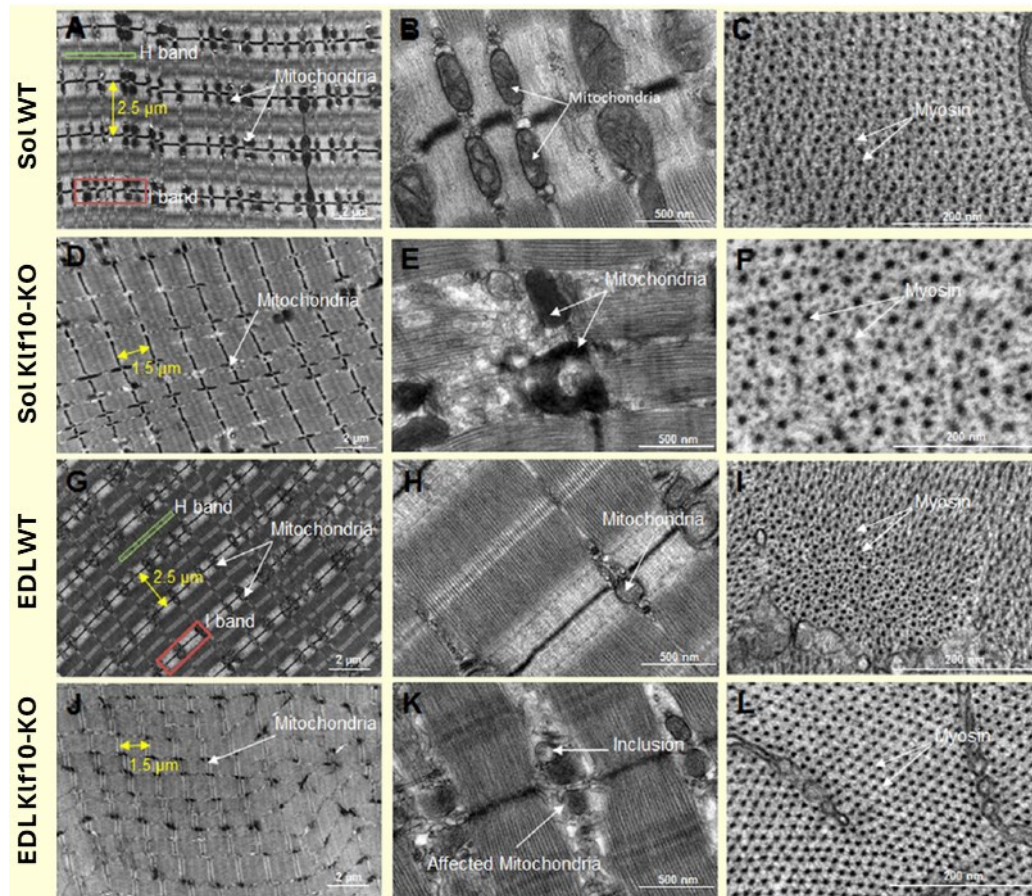
Figure 30. Transmission electron microscopy analyses of Klf10 KO and WT soleus and EDL. Differences were observed in the sarcomere structure, especially the (I and H) bands, as well as the numbers, shape and organization of mitochondria (Kammoun et al., 2020).

Metabolomics

Metabolomics (Baroukh et al., 2022; Kammoun et al., 2020) analyses including enzyme assays, mitochondrial respiration, immunoblotting, MR spectroscopy (Kammoun et al., 2020) were performed. They revealed disorders in the muscle's energy metabolism, with mitochondrial respiration being decreased in Klf10 KO mice. These findings correlate with the enhanced phenotype in soleus muscle, which is a slow oxidative muscle mainly relying on mitochondrial respiration for energy supply, compared to the EDL muscle.

1.4.3. Influence of Klf10 gene in the muscular ECM

Across all scales, 2 observations can be made: (1) although changes in mechanical properties are observed on muscle fibers at the microscopic scale, no changes are observed in myofibrils at the submicron scale or in the muscles at the macroscopic scale (Figure 31, Figure 32); (2) the observed changes are muscle dependent. Altogether, these observations suggest that there exists a compensation mechanism between the microscopic scale and the macroscopic scale, which seems to be muscle dependent. Considering the components which contribute to the skeletal muscle mechanical properties at those scales, it can be hypothesized that this compensation mechanism is due to modifications in the ECM.
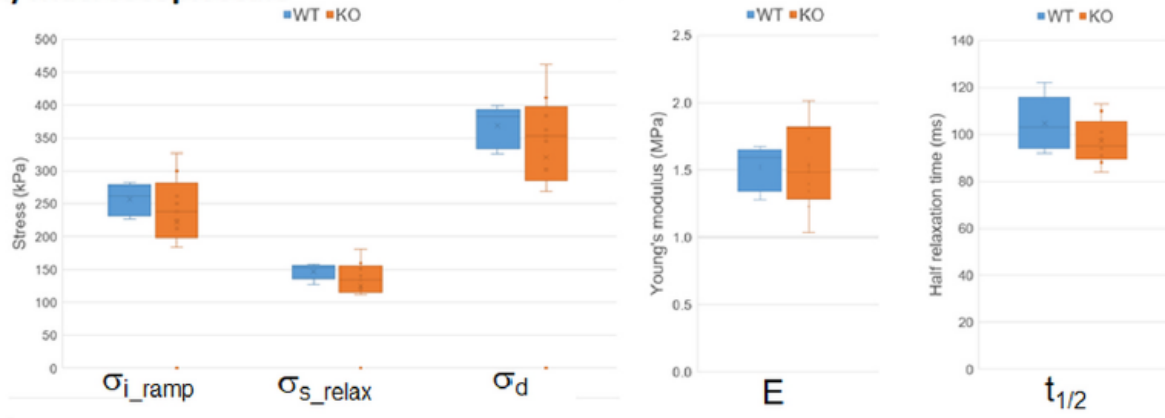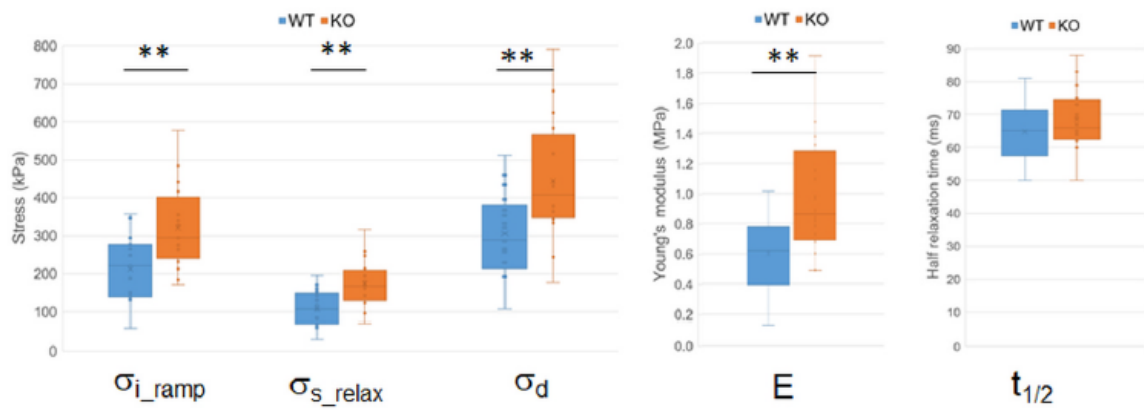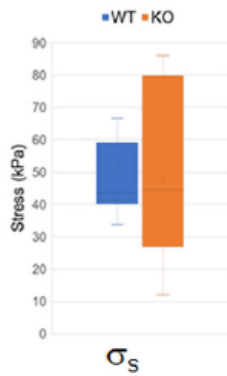
*Figure 31. Multiscale comparison of WT and Klf10 KO mouse soleus muscle's mechanical properties (Tatarenko et al., 2024). Boxplots of instantaneous stress (σi_Ramp), static stress (σs, σs_Relax), dynamic stress (σd), Young's modulus (E) and half relaxation time (t1/2) values of the soleus muscle components at the (A) macro and (B) micro scales, and for the ramp test and the relaxation test. **: p < 0.01 (Mann-Whitney's test).*
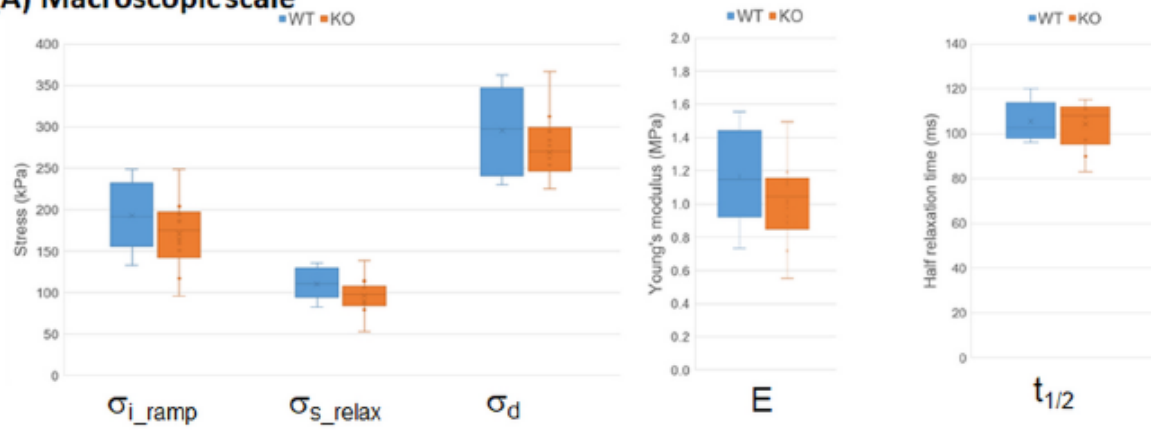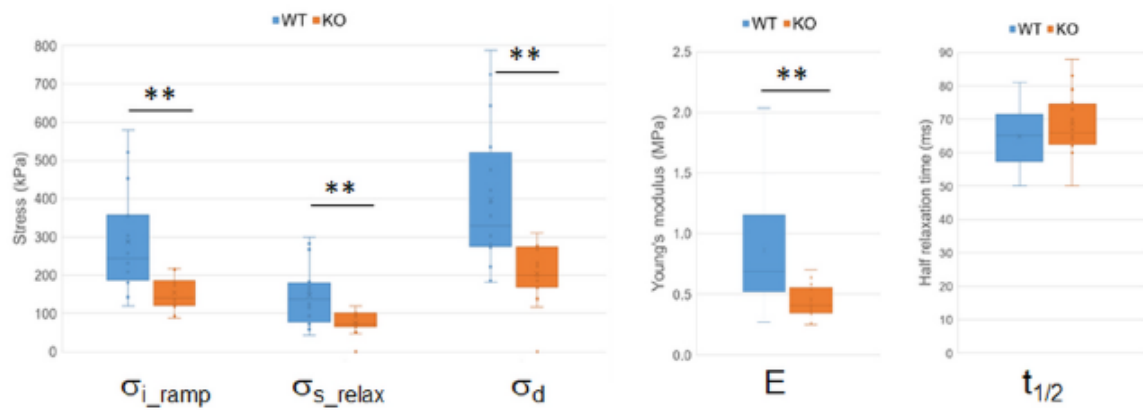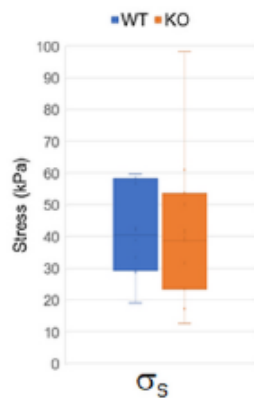
Figure 32. Multiscale comparison of WT and Klf10 KO mouse EDL muscle's mechanical properties (Tatarenko et al., 2024). Boxplots of instantaneous stress (σ_{i_Ramp}), static stress (σ_s, σ_{s_Relax}), dynamic stress (σ_d), Young's modulus (E) and half relaxation time ($t_{1/2}$) values of the extensor digitorum longus (EDL) muscle components at the (A) macro and (B) micro scales, and for the ramp test and the relaxation test. *: $p < 0.05$; **: $p < 0.01$ (Mann-Whitney's test).

1.5. Conclusions

This first chapter allows us to understand the structure and function of skeletal muscles, with a focus on components responsible for mechanical properties. The skeletal muscle structure is hierarchical and can be separated into different scales, which are: the macroscopic scale, the mesoscopic scale, the microscopic scale and the submicron scale. Many experimental methods have been developed to investigate this hierarchical structure, but also its function through the study of the mechanical properties at different scales. Although most studies are performed *ex vivo* and thus subjected to *post mortem* changes due to *rigor mortis,* some methods allow to go beyond those limitations using *in vivo* investigations of skeletal muscle in its physiological environment. Moreover, some experimental methods target specific components that may be involved in pathological processes, such as the Extracellular Matrix (ECM). In the particular case of ECM, experimental characterization methods are scarce and difficult to implement; thus, different approaches have been developed, based on multiscale numerical modeling. Multiscale numerical models of skeletal muscle have been increasingly developed in recent years. They are based on so-called homogenization methods that link different scales. Many of these models are used as tools to investigate the ECM in different conditions: health, ageing, and pathological conditions such as DMD or cerebral palsy.

In this thesis, we study the impact of the Klf10 gene on the skeletal muscle, using a mouse model. In the mouse model, previous experiences have exhibited muscle-dependent alterations in the muscle metabolism, and structural as well as functional alterations at the microscopic scale in muscle fibers *ex vivo*. Interestingly, such alterations are not observed at larger scales such as the macroscopic scale, suggesting a compensation mechanism due to another component. Considering the skeletal muscle structure, the ECM is the first candidate for this mechanism.

Thus, we propose investigating the impact of the Klf10 gene in the mouse skeletal muscle ECM. To do so, we propose using multiscale modeling tools, with the development of a new skeletal muscle model linking the macroscopic and the microscopic scales. This model should include interpretable parameters related to the ECM structure and function and provide insights on a potential compensation mechanism. In this manuscript, we present the development of a passive hyperelastic mechanical model based on *ex vivo* experiments, thus integrating part of the experimental data described in the above section. Moreover, we propose to complete the existing experimental dataset on the mouse skeletal muscle characterization using Magnetic Resonance Elastography to investigate the *in vivo* shear mechanical properties at the macroscopic scale. Given the central role of shear deformation in ECM function, this method offers a unique opportunity to investigate possible compensatory adaptations in this component.

Chapter 2: *In vivo* mechanical properties of the murine skeletal muscle

2.1. Introduction

Skeletal muscle physiology can undergo significant changes due to disease or genetic modifications, affecting processes such as force generation and transmission, among others. Experimenting on the structure and function of skeletal muscle presents specific challenges related to biological scale, tissue components, and testing modalities. For components such as the extracellular matrix (ECM), the scarcity of experimental techniques motivated our decision to pursue an original approach based on multiscale numerical modeling of the murine skeletal muscle. In parallel with this approach, we propose to develop an experimental approach using elastography of murine skeletal muscle, which is currently underutilized but is capable of providing non-invasive, *in vivo* data that closely reflects physiological conditions. More specifically, **we propose to analyze *in vivo* the impact of the Klf10 gene on the murine muscle response via magnetic resonance elastography (MRE)**, the only *in vivo* elasticity imaging approach capable of providing the macroscopic behavior of muscle with data on organ volume and anisotropy, although limited to the macroscopic scale of the organ and to characterization in small deformations.

This chapter presents the experimental developments for investigating the mechanical properties of the murine hindlimb *in vivo*. We begin with a description of the physics and core principles of MRE, followed by a detailed explanation of the custom protocol developed for MRE acquisition in the murine hindlimb. This protocol includes the development of an original mechanical excitation system developed as part of this thesis, as well as MRI sequencing and mechanical reconstruction solutions resulting from collaborations and implemented during this thesis work. Finally, we present and compare experimental results across different genotypes.

In France, research on animals is regulated by specific laws and ethics committees. Therefore, all animal studies performed in this project were approved by the ethical committee (CREMEAS – CE035) and authorized by the Ministry of Higher Education, Research and Innovation (authorization #34518-20211216095932). All procedures complied with Directive 2010/63/EU on the protection of animals used for scientific purposes and were designed to minimize animal suffering in accordance with the 3Rs principle (Replacement, Reduction, and Refinement). For this project, All MRI experiments were performed at the ICube laboratory in the IRIS platform (agreement number E 67-482-041).

2.2. Magnetic Resonance Elastography (MRE) protocol development

As introduced in chapter 1, MRE consists in 3 successive steps: (1) excitation by propagating shear waves in the organ, (2) motion encoding using specific sequences and (3) reconstruction of the mechanical properties. In our case, we want to apply this method to murine hindlimbs in a preclinical 7T MRI system dedicated to small animals. **Preclinical elastography on mice is related to a specific set of constraints for each step. To overcome these constraints, an original experimental setup for excitation was initially designed during my Master thesis (Loumeaud, 2022), and the acquisition protocol was developed as a continuation during the PhD thesis.** Furthermore, through collaborations, specific motion encoding algorithms were written. The aforementioned work is published in Loumeaud et al. (2025a). Finally, a standard reconstruction algorithm was encoded and a postprocessing pipeline was built around this code. Only once this protocol had been developed and

validated on murine skeletal muscle could it be applied to cohorts of control mice and mice with the Klf10 gene inhibited.

2.2.1. Experimental setup development

Requirements. MRE is performed using MRI acquisitions, which provide three-dimensional measurements of tissue magnetization variations due to the joint action of two magnetic fields B_0 and B_1, across a field of view that is divided into voxels (volumetric pixels). For small animals, such as mice, the spatial resolution of standard clinical MRI scanners operating at static magnetic field B_0=1.5T or 3T is typically insufficient, as the standard equipment cannot provide a voxel size under a few cubic millimeters (mm³). To put this into perspective, a 3-month-old mouse weighs approximately 25 g, corresponding to a total body volume of about 25 cm³. A clinical MRI voxel may cover a substantial fraction of the animal, making it unsuitable for localized mechanical property measurements. To address this limitation, preclinical MRI scanners dedicated to small animal imaging are used. They usually operate at B_0 static magnetic field 7T or 9.4T with corresponding gradients to modulate B_0. These systems enable better spatial resolution (with typical voxel sizes on the order of 0.1 mm³) for similar signal-to-noise ratio (SNR) in small field-of-view (FOV) and acquisition times compatible with *in vivo* acquisitions. This allows for accurate MRI imaging and by extension MRE measurements at the scale of individual organs or tissues in small animal models.
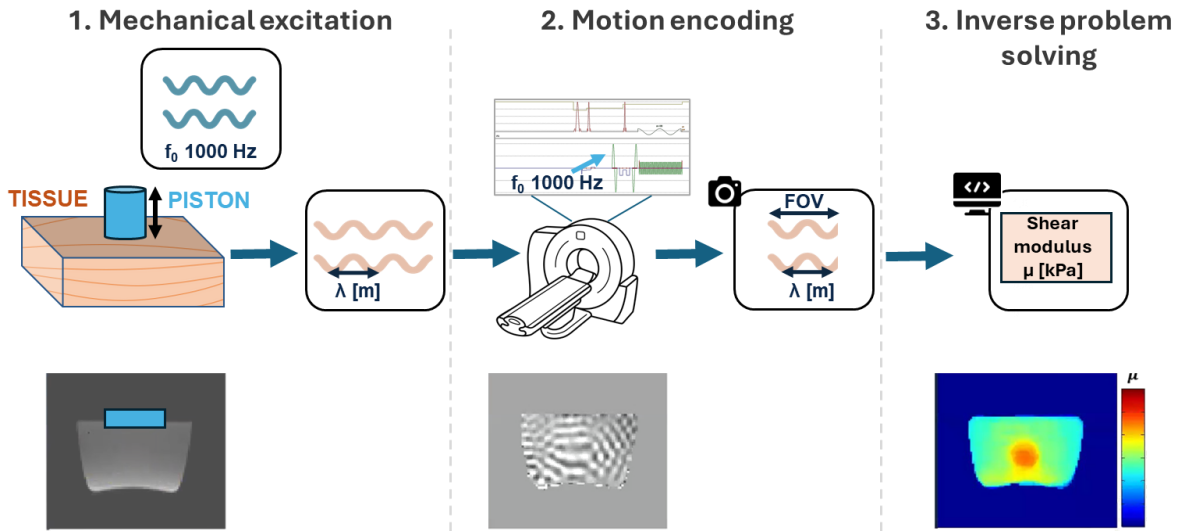
Figure 33. Illustration of the three successive steps in Magnetic Resonance Elastography using harmonic excitation. (1) The piston generates harmonic shear waves within the tissue which (2) are encoded by the MRI scanner into a phase image and (3) are used to reconstruct spatial wavelength maps of the tissue.

In MRE, we aim to generate harmonic shear waves with a unique temporal frequency f_0 in the hindlimb of the mouse and observe their propagation using MRI (Figure 33). As described in more detail in the next section, the spatial wavelength λ of these waves depends on the local mechanical properties of the tissue and the excitation frequency. To reliably measure the spatial wavelength using MRI, at least two voxels per period are required, in accordance with the Shannon sampling criterion. Assuming a linear, elastic, and isotropic medium, and given prior estimates of the tissue's shear modulus μ and density ρ, the spatial wavelength can be estimated by Eq. 2.1.

$$\lambda = \frac{1}{f_0} \cdot \sqrt{\frac{\mu}{\rho}} \tag{2.1}$$

66

Due to this relationship between temporal and spatial frequencies, the admissible range for the excitation frequency f_0 is determined by the ability to image wavelengths λ in a specific tissue and resolution imaging, namely by the number of pixels per wavelength (sampling condition) on the one hand, and by the number of wavelengths in a region of interest (ROI) on the other (observation window condition or wave sampling condition). Considering these constraints (size of a murine skeletal muscle and spatial resolution in the order of 100 µm), the experimental setup should include an MRI-compatible actuator capable of generating harmonic shear waves within an optimal frequency range of 800–1200 Hz for murine skeletal muscles, ensuring both sufficient resolution and tissue coverage. In addition, the amplitude of the shear waves must be high enough to yield an adequate signal-to-noise ratio (SNR) in the MRI phase images. Based on prior works, we hypothesize that a vibration amplitude of approximately 10 µm *in vivo* should be sufficient to meet this requirement.

Moreover, to acquire the MRI signal, it necessary to introduce first a perturbation B_1 in the static magnetic field B_0 of the MRI. This is done using a radiofrequency (RF) coil. As the system comes back to the equilibrium, the variations in the magnetic field are measured through RF coils that convert it into an electrical signal. Therefore, for both signal emission and signal reception, coils are used. Different types of coils can have a great influence on the setup dimensioning and positioning. We use the Biospec 7T small animal MRI system (*Bruker Biospin, Ettlingen, Germany*) in combination with an 86 mm diameter volumetric coil for emission (Figure 34A), and a 10 mm diameter surface reception RF coil (Figure 34C). This means the setup must fit into an 86 mm diameter tunnel and consider the presence of a surface RF coil on the hindlimb of the animal, as well as the animal and its equipment detailed hereafter.

Indeed, these experiments are conducted with living animals. The experimental protocol for our terminal procedure is detailed later in this manuscript. The priority during the experiment is the animal's well-being, which includes two main aspects in the MRI: monitoring the animal's health and providing for the animal's essential needs such as ambient temperature. In addition to this, anesthesia through air mixed with isoflurane gas is used. These aspects require the use of materials such as breathing and body temperature sensors, a heating mattress, survival blanket, and an anesthesia mask (Figure 34A). This also requires experimental positioning with all the aforementioned elements and the vibration setup to be fast, as to prevent hypothermia or extended anesthesia (~4h including the experiment) for the animal. For fast positioning, the setup manipulation must be simple and fast.
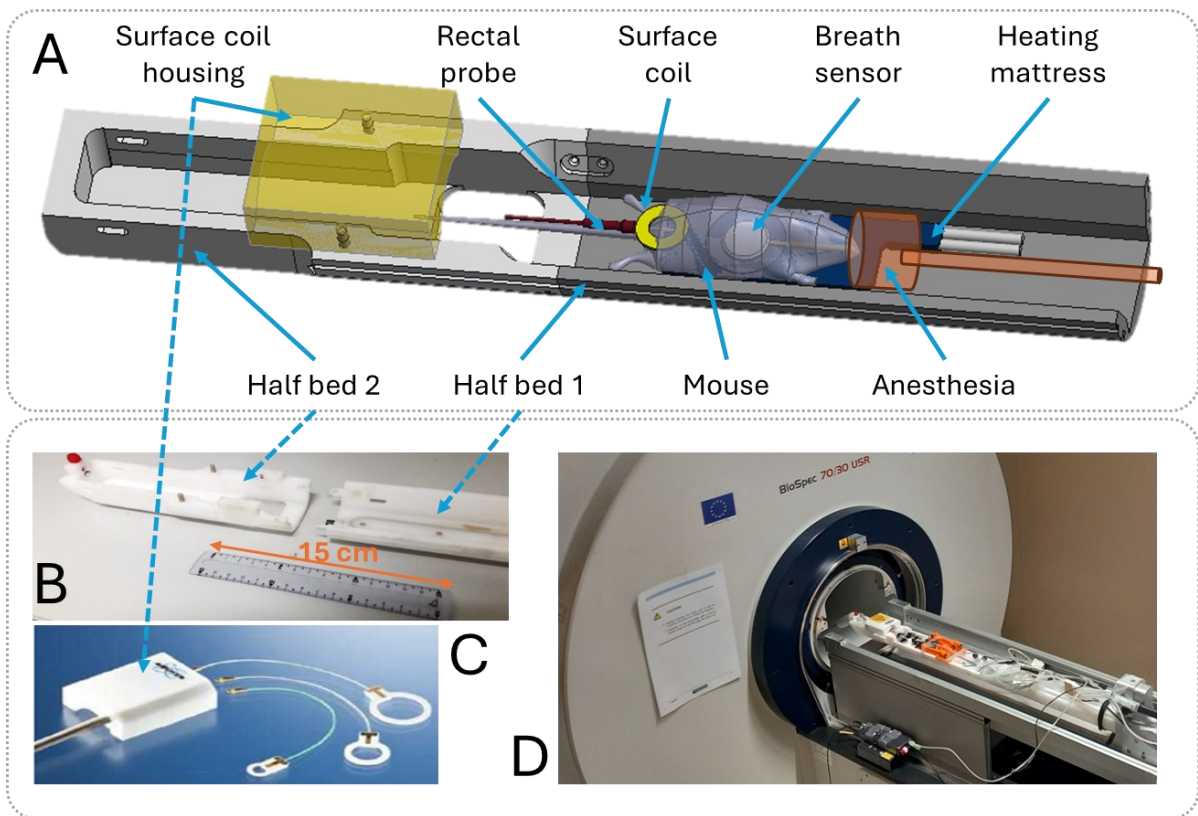
Figure 34. Elements contributing to the system space requirements: (A) elements positioned around the animal, (B) small animal bed, (C) reception coil, (D) overview of the system into the 7T MRI scanner with the volumetric emission coil.

We also would like to avoid causing any physical pain to the animal. MRE can be invasive or non-invasive, the threshold being causing a pain superior or equal to the insertion of a needle in the animal. Indeed, to generate vibrations, an invasive solution would be to insert a vibrating MRI-compatible needle into the hindlimb, while a non-invasive solution would be to put a vibrating object on top of the hindlimb.

Original vibration system. Considering all the requirements listed above, a 3D-printed system that can be positioned on the existing Bruker small animal bed (Figure 34B) has been designed and validated on gelatin phantom gels, then on animals *ex vivo* and finally *in vivo* (Loumeaud, 2022; Loumeaud et al., 2025a). It is composed of different subsystems as illustrated in Figure 35A: some are ensuring the vibration function while others provide an adaptable positioning. (i) *Actuation unit Figure 35B*: the vibration is generated through an MRI-compatible piezoelectric actuator NAC2225 (*CTS Valpey Corporation, Hopkinson, MA, USA*) connected to a piston through a coupling part, allowing for noninvasive vibration generation for a frequency range from 100 to 1200 Hz. The coupling part can be connected to either a plastic screw (noninvasive piston) or a silver needle (invasive piston). The latter allows us to target deeper regions of interest, which is not the case with the hindlimb. Thus, in this thesis, we use a plastic screw as a piston. Overall, pistons of all sizes and shapes can be connected to the coupling, allowing optimal contact for harmonic waves generation in different regions of interest. (ii) *Positioning unit with 3 degrees of freedom (DoF) Figure 35C*: To position the piston, different subsystems of the setup allow a 3D positioning in space through 2 translations and 1 rotation. This feature is especially useful to compensate for the size variation between different animals (*Figure 35D*). The whole setup has been calibrated and abacuses on temperature and displacement as functions of frequency and amplitude have been generated, which allow us to control the experimental conditions.

Finally, long cables allow us to control the actuator from the control room and to synchronize its motion with the MRI sequence using the MRI trigger.
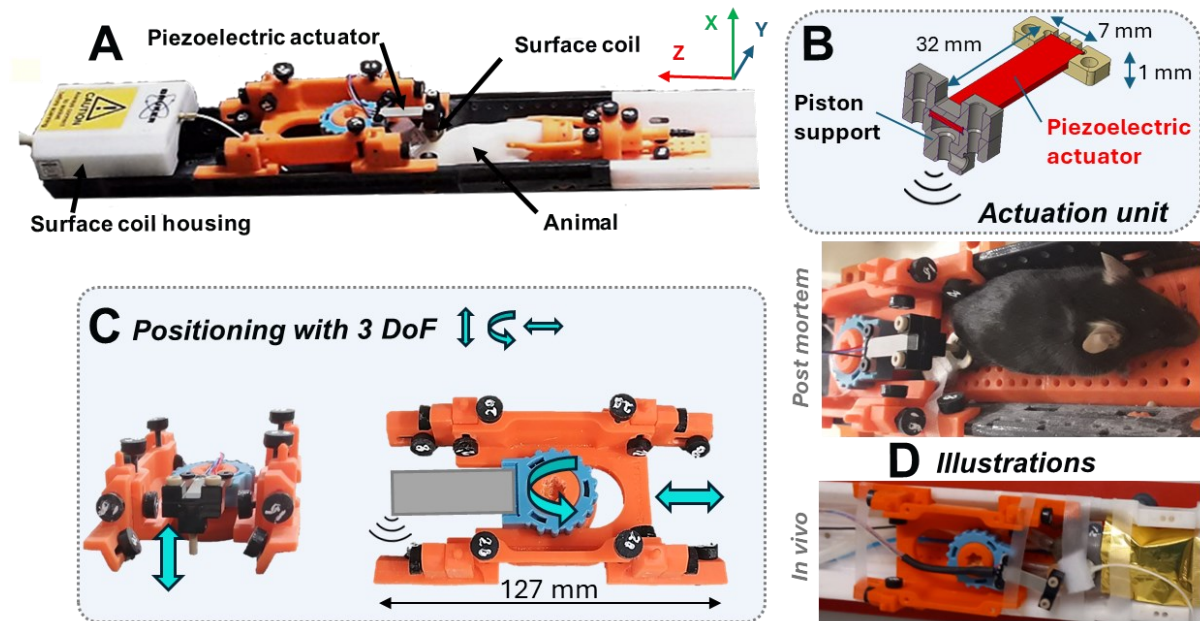
Figure 35. (A) Setup developed for small animal MRE: overview of the system adapted to the small animal MRI bed. The system includes: (B) an actuation unit constituted of a piezoelectric actuator and a coupling part that welcomes a piston; (C) a positioning unit providing 3 degrees of freedom (DoF) constituting in a 40 mm translation along Z axis, a 12 mm translation along X axis and a rotation around X axis axis.(D) Illustration of the setup positioning on a mouse hindlimb postmortem and in vivo.

2.2.2. Data acquisition

To be able to visualize the harmonic shear wave propagation within the mouse hindlimb, a MRE imaging sequence is needed. For this purpose, we collaborated with Dr. P. GARTEISER and Dr. G. PAGÉ from the CRI (*Center for Research on Inflammation, Université Paris-Cité, Inserm UMR 1149, CNRS ERL 8252, Paris, France*), who developed a dedicated imaging sequence for mouse liver MRE. This first sequence is extremely fast. We also collaborated with Dr. P. SANGO-SOLANAS, Dr. D. GRENIER, and Dr. K. TSE VE KOON from the Creatis (*Université Lyon 1, INSA Lyon, CNRS UMR 5220, Inserm U1294, Lyon, France*), who developed another dedicated imaging sequence for mouse liver and brain MRE (Sango Solanas et al., 2021). This sequence allows us to achieve high spatial resolution. In this section, we will describe briefly what an MRI sequence is and the elements to implement for dynamic harmonic MRE, as well as the two sequences introduced above.

Nuclear spin and magnetization. In our context, we want to image spatial displacements in a biological tissue. MRI exploits the magnetic properties of hydrogen atom nuclei, which are abundant in biological soft tissues like skeletal muscles. Hydrogen atom nuclei possess an intrinsic angular momentum which is called "spin". This spin is represented as a vector that rotates. As hydrogen atom nuclei are protons, they carry a positive electric charge. Through their intrinsic rotation, this creates a small magnetic moment aligned on the rotation axis. In the absence of an intense external magnetic field, the magnetic moments of hydrogen atoms in the tissue are randomly orientated, and thus no macroscopic magnetic moment can be observed (Figure 36 Step 1).

Effect of static magnetic field (B_0). Inside the MRI scanner, an intense static magnetic field called B_0 is present. In our case, we use a 7T MRI scanner, meaning the intensity of B_0 is 7T. B_0 aligns the spins of the hydrogen nuclei along its direction. Thus, when the mouse is in the scanner, the magnetic

moments of the protons are all aligned and rotate in a cone around B_0. This phenomenon is called precession. The magnetic moments of the protons precess at a specific frequency known as the Larmor frequency, which is proportional to the strength of the magnetic field. This motion can be decomposed into: a longitudinal component (parallel to B_0) and a transversal component (orthogonal to B_0). It is this transversal component that can be measured with the reception coil. At equilibrium, the spins are not in phase and cancel each other's transverse components out; thus the resulting transversal magnetic component is null (Figure 36 Step 2).
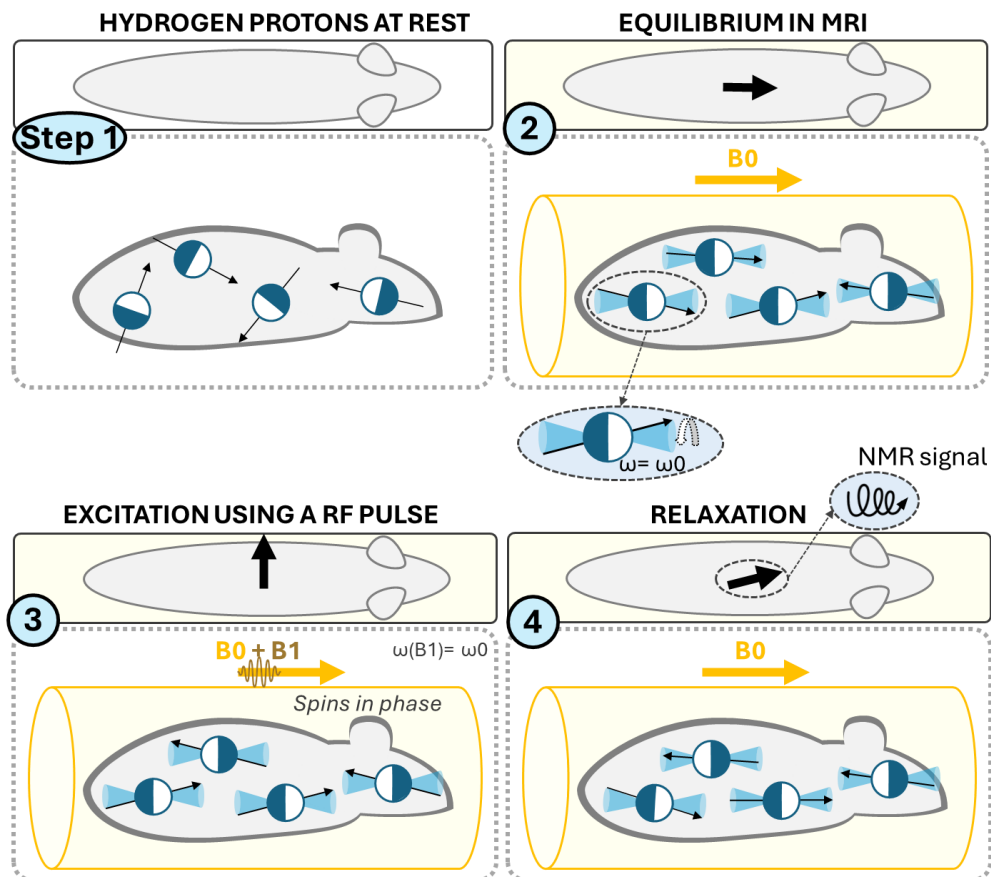
Figure 36. Illustration of MRI physics using two complementary perspectives: a macroscopic view showing the evolution of the net magnetization vector throughout an imaging sequence. The mouse represents one imaging slice, and the sequence is broken down into four key steps: (1) Pre-MRI state: The mouse has not yet entered the MRI scanner; (2) Magnetization alignment in the MRI field; (3) Excitation using a radiofrequency (RF) pulse; (4) Relaxation phase. A more detailed version of this diagram is available in Annex 4.

Nuclear magnetic resonance. If energy is brought to the system (excitation), and this excitation is stopped, the system will restitute this energy to return to its initial state (relaxation). Here energy can be transferred to the mouse's hydrogen nuclei using a radiofrequency (RF) pulse matching the Larmor frequency. A RF coil is used to generate this RF pulse called B_1, which flips the mouse's magnetization vector away from the longitudinal (B_0) axis, generating a measurable transversal component (Figure 36 Step 3). Once the RF pulse is turned off, the hydrogen nuclei relax back until equilibrium (Figure 36 Step 4). The transversal magnetization component during the relaxation phase is non null and induces a signal measurable through a RF coil (receiver coil) (Figure 36 Step 4). The amplitude and phase of this signal depend on the local spin population and their phase coherence.

Imaging sequence. As explained above, the excitation changes the resulting tissue magnetization vector, which is tilted in relation to B_0: the tilt angle depends on the intensity, the duration and the shape of the RF pulse(s), which are defined in the imaging sequence. The imaging sequence also provides encoding of the signal: spatial localization of the NMR signal is guaranteed. The raw NMR signal is a complex signal encoded in a matrix called K-space and must be postprocessed after the acquisition. The encoded components are the intensity, the spatial frequency and the phase of the RF signal. One method to encode the K-space is provided in the imaging sequence.

Spatial encoding and K-space. Spatial localization of the MRI signal is achieved using linear magnetic field gradients along three orthogonal directions. These gradients (slice-select, phase-encode, and frequency-encode) modify the Larmor frequency in a spatially dependent manner, allowing encoding of the signal in a matrix known as K-space. These gradients are generated using gradient coils and are superimposed with the B_0 field. The slice-select gradient slices the mouse volume in successive imaging planes (slices). The phase-encoding gradient imposes a spatially varying phase shift in one in-plane direction and the frequency-encoding (readout) gradient imposes the signal frequency along the other in-plane direction. For each slice, a 2D matrix is encoded in the K-space. The K-space corresponds to a Fourier plane, and the link to the spatial space can be done using a 2D Fourier transform. Usually, two reconstructed images are obtained for each slice: spatial amplitude variation of the signal (amplitude image) and spatial phase variation of the signal (phase image).

Spin Echo Sequences. An MRI imaging sequence can be represented using a diagram, where the temporal organization of the RF pulses and the 3 gradients are represented. In our case, spin echo (SE) sequences are used for MRE. It consists in a series of repeated excitation cycles defined by two key parameters: the repetition time (TR) and the echo time (TE). The series of instructions is repeated after time TR, while for each series the signal is read at time TE. For one repetition, a line of the K space is filled. A SE sequence is characterized by the presence of two RF pulses. Each cycle begins with a 90° RF pulse that tips the net magnetization into the transverse plane. After a delay of TE/2, a 180° refocusing pulse is applied to correct for dephasing caused by static magnetic field inhomogeneities. The spin echo signal is acquired at time TE. The second pulse compensates for constant heterogeneities of the B0 field. During the repetition, different gradients pulses are applied to encode the K-space.
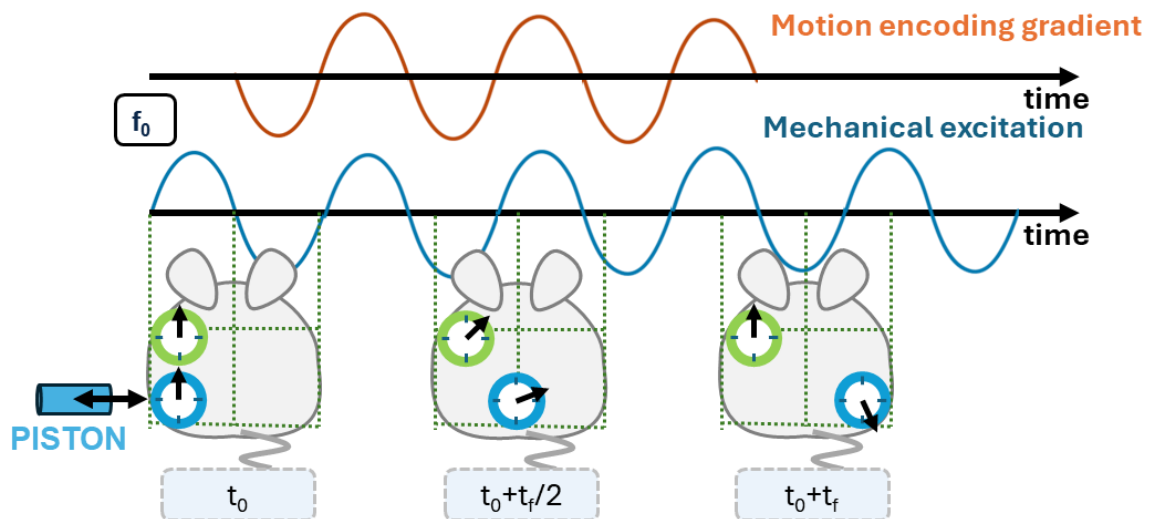
Figure 37. Illustration of phase shifts undergone by hydrogen protons under the Motion Encoding Gradient (MEG): a static proton (green color) total phase shift due to the MEG is null, while a moving proton (blue color) accumulates a non-null phase shift under the MEG.

Dynamic harmonic MRE. In MRE, small tissue displacements are encoded as phase shifts in the MR signal. In our setup, these displacements are harmonic and of small amplitude, allowing the use of linear elasticity approximations. The phase is also sensitive to temperature variations, however in our setup these thermal effects are considered negligible. To capture this displacement, a motion encoding gradient (MEG) synchronized with the mechanical excitation frequency is applied (Figure 37), typically along the read or frequency-encode gradient.
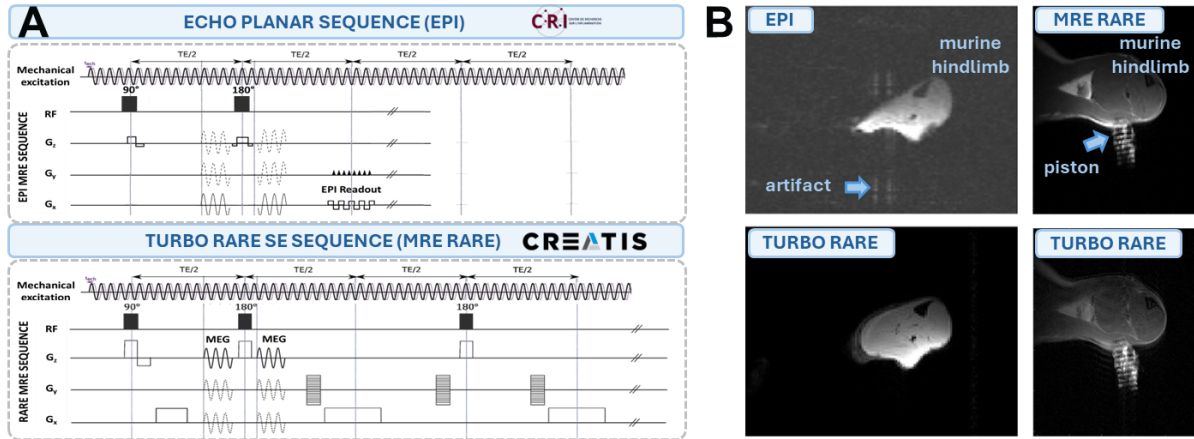
Figure 38. (A) Schematic representation of the two MRE sequences considered for our protocol: a fast EPI sequence and a robust Turbo RARE sequence (Sango Solanas et al., 2021). (B) Comparison of the amplitude images provided by the two MRE sequences with the amplitude images provided by an anatomical T2 TURBO RARE acquisition (Loumeaud et al., 2025a).

For small animal MRE, a compromise must be found between the acquisition duration and the acquisition quality (resolution, signal-to-noise ratio). We especially take into consideration the time spent by the animal under anesthesia. Under these conditions, collaborations were established to exchange expertise and implement this protocol common to several French laboratories (MRESAT project, France Life Imaging ANR-11-INBS-0006), providing the opportunity to implement two distinct MRE sequences developed by partners (Figure 38A):

● To achieve fast acquisitions, we first collaborated with the CRI Paris (*Center for Research on Inflammation, UMR Inserm 1149, Université Paris-Cité, ERL CNRS 8252, Paris, France*) who developed a single shot SE EPI sequence. Using this sequence, only a few seconds are needed for one acquisition. However, the obtained data is noisy and presents artifacts due to tissue heterogeneity in the mouse hindlimb, as illustrated in magnitude images in Figure 38B.
● A second dedicated fast SE RARE (Rapid Acquisition with Relaxation Enhancement) sequence was used in collaboration with the CREATIS Lyon (*Centre de Recherche en Acquisition et Traitement de l'Image pour la Santé, INSA Lyon, Université Lyon 1, CNRS, Inserm, UMR 5220, U1294, Lyon, France*) (Sango Solanas et al., 2021). This sequence allows us to achieve high spatial resolution, in the order of a 100 μm. It is also more robust to artifacts (Figure 38A). However, the acquisition time is in the order of the minute.

2.2.3. Data postprocessing
Image substraction and unwrapping. For each vibration frequency, four time points are acquired during one cycle of the MEG. At each time point, a second image with opposed MEG polarity is acquired and one elastogram is then reconstructed with every phase difference image using the reconstruction method described below. However, phase images are wrapped within the interval $[-\pi, \pi]$. To reconstruct the original phase, an unwrapping process is applied. The resulting unwrapped phase

image undergoes a temporal Fourier transform to remove components unrelated to our harmonic solicitation and then is used as input for further spatial frequency and mechanical parameter estimation using reconstruction algorithms.

Reconstruction method. The obtained data is then reconstructed through the Local Frequency Estimation (LFE) method (Knutsson et al., 1994). This algorithm estimates the spatial frequency of shear waves propagating under the assumption of small deformations, as described hereafter.

In a homogeneous, isotropic, and linearly elastic medium, the mechanical behavior is governed by a linear relationship between the Cauchy stress tensor $\boldsymbol{\sigma}$ and the infinitesimal strain tensor $\boldsymbol{\varepsilon}$, involving the first λ and second μ Lamé coefficients respectively:

$$\boldsymbol{\sigma} = 2\mu\boldsymbol{\varepsilon} + \lambda tr(\boldsymbol{\varepsilon})\boldsymbol{I} \tag{2.2.}$$

$$\boldsymbol{\varepsilon} = \frac{1}{2}(\boldsymbol{\nabla u} + (\boldsymbol{\nabla u})^T) \tag{2.3.}$$

With $\boldsymbol{u}$ the displacement vector, $\boldsymbol{I}$ the second rank identity tensor and $\boldsymbol{\nabla}$ the nabla operator. The dynamic equilibrium equation for wave propagation is then:

$$\rho\frac{\partial^2\boldsymbol{u}}{\partial t^2} = \boldsymbol{\nabla}.\boldsymbol{\sigma} + \rho\boldsymbol{f} \tag{2.4.}$$

With the $\boldsymbol{f}$ external body forces and ρ the medium's density. Assuming no external body forces, this becomes:

$$\rho\frac{\partial^2\boldsymbol{u}}{\partial t^2} = \mu\Delta\boldsymbol{u} + (\mu + \lambda)\boldsymbol{\nabla}(\boldsymbol{\nabla}.\boldsymbol{u}) \tag{2.5.}$$

With Δ the Laplace operator. This equation allows two types of wave solutions (Figure 39A):

• Compression waves are characterized by a motion parallel to the excitation:
$$\boldsymbol{\nabla} \wedge \boldsymbol{u} = \boldsymbol{0} \tag{2.6.}$$

• Shear waves are characterized by a constant volume:
$$\boldsymbol{\nabla}.\boldsymbol{u} = 0 \tag{2.7.}$$

Biological tissues are typically considered quasi-incompressible, and the high velocity (~1540 m.s^{-1}) of compression waves makes them distinguishable from shear waves (~3 m.s^{-1}). In this context, we focus on shear wave imaging. Using the incompressibility assumption ($\vec{\boldsymbol{\nabla}}.\vec{\boldsymbol{u}} = 0$), the wave equation becomes:

$$\rho\frac{\partial^2\boldsymbol{u}}{\partial t^2} = \mu\Delta\boldsymbol{u} \tag{2.8.}$$

Assuming a harmonic wave of angular frequency $\omega = 2\pi f$, the wave equation becomes:

$$\Delta\boldsymbol{u} + \frac{\rho\omega^2}{\mu}\boldsymbol{u} = \boldsymbol{0} \tag{2.9.}$$

And thus the shear wave celerity $c_S = \lambda f$ (λ being the shear wavelength) is given by:

$$c_S = \sqrt{\frac{\mu}{\rho}} \tag{2.10.}$$

73

Therefore, estimating the wavelength and, by the way, the shear wave velocity enables inference of the tissue shear modulus.
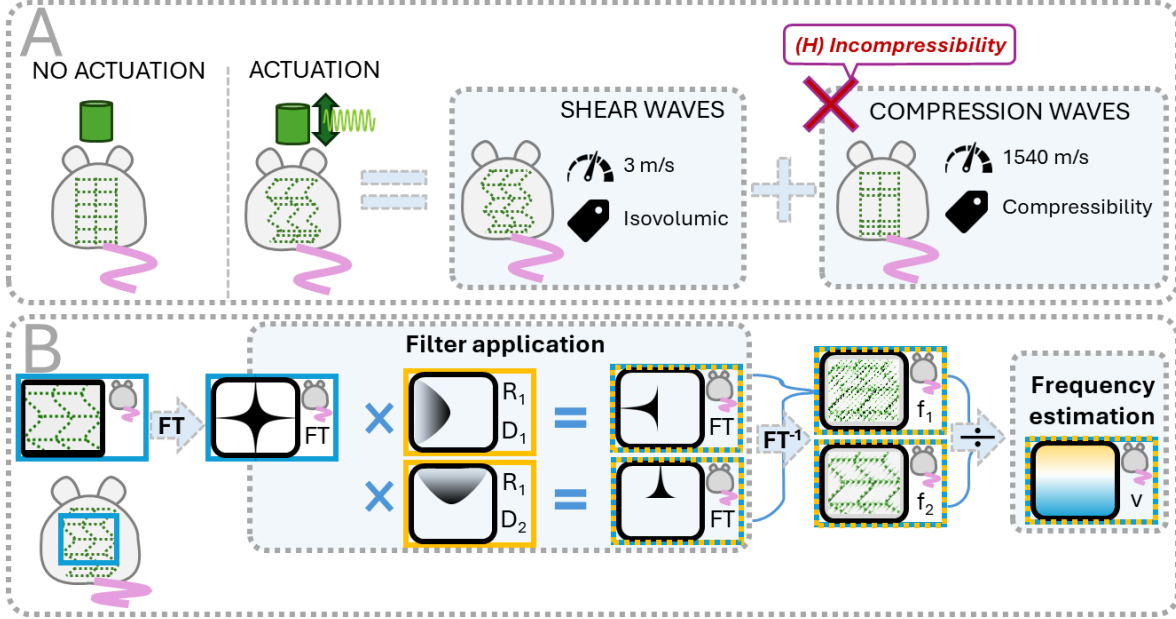
Figure 39. (A) Schematic representation of wave propagation due to harmonical sinusoidal stimulation provided by a piston, which can be decomposed into compression and shear waves. Upon the hypothesis of an incompressible tissue, only shear waves are considered for the reconstruction algorithm. (B) Schematic representation of LFE: after Fourier transform of the phase image, the resulting image undergoes filtering (here one filter is represented) after which an inverse Fourier transform is applied. Resulting images due to two different filtering processus are combined to obtain local frequency estimation.

Local Frequency Estimation. The LFE algorithm estimates the local spatial frequency of shear waves. It does so by applying pairs of lognormal filters to the MRE phase image (Figure 39B). This method is robust to noise, but it requires that the ROI contains at least half a wavelength of the shear wave, which limits the spatial resolution and field of view (Manduca et al., 2001) thus constraining the FOV and the spatial resolution. Therefore, an approximate knowledge of the spatial wavelength is required a priori to appropriately select the filter parameters.

The first step of the algorithm is to transform the phase image containing shear waves into the Fourier space. Assuming local homogeneity, the signal can be treated as locally monochromatic. The local frequency of such a signal is defined as the spatial derivative of the phase of its analytic signal (Boashash, 1992):

$$v_l(\boldsymbol{x}) = \frac{1}{2\pi}\frac{d\phi(\boldsymbol{x})}{d\boldsymbol{x}} \qquad (2.11.)$$

Where:

$$f_a(\boldsymbol{x}) = a(\boldsymbol{x})e^{\phi(\boldsymbol{x})} \qquad (2.12.)$$

Here, $\boldsymbol{x}$ designates the spatial coordinates, f_a the analytical signal with its amplitude a and phase ϕ. By applying suitably chosen lognormal filters with a predefined central frequency and filtering bandwidth, which includes the range of spatial frequencies contained in the shear waves images, those local spatial frequencies can be recovered. Radial filters determine the scale (*i.e.*, frequency band) of analysis. Directional filters determine the orientation at which the frequency is analyzed. By combining these components, the algorithm can isolate wave patterns with specific wavelengths and propagation directions.

For each central frequency ν_i, the image is filtered using a set of directional filters, each tuned to a specific orientation (typically 4–8 directions, evenly spaced in angle). These filters are constructed by combining a radial component $R_i(\nu)$ with multiple directional components D_k. The outputs of these radial-directional filter pairs are summed (or averaged) to obtain a directionally invariant filtered image $F_i(\nu)$ in Fourier space.

The radial component $R_i(\nu)$ is defined as:

$$R_i(\nu) = e^{C_B ln^2\left(\frac{\nu}{\nu_i}\right)} \tag{2.13.}$$

$$C_B = \frac{4}{B^2 \ln(2)} \tag{2.14.}$$

Here, ν designates a spatial frequency, $\boldsymbol{C_B}$ a lognormal scaling constant and B the 6 dB bandwidth of the filter. Considering a unit vector defining the direction of filter D_k, directional components are defined as:

$$D_k(\boldsymbol{u}) = \begin{cases} (\boldsymbol{u}.\boldsymbol{n_k})^2 & if\ \vec{u}.\vec{n_k} > 0 \\ 0 & otherwise \end{cases} \tag{2.15.}$$

Spatial frequency estimation. This process is repeated for a second central frequency ν_j, related to ν_i by:

$$\nu_j = \nu_i e^{\frac{1}{2C_B}} \tag{2.16.}$$

yielding a second directionally invariant filtered image $F_j(\nu)$. The local spatial frequency ν_l is then estimated from the inverse Fourier transforms of these two filtered images f_i and f_j:

$$\nu_l(\boldsymbol{x}) = \sqrt{\nu_i\nu_j} \cdot Re\left(\frac{f_j(\boldsymbol{x})}{f_i(\boldsymbol{x})}\right) \tag{2.17.}$$

In practice, this process is repeated for multiple central frequencies and the resulting frequency maps are averaged to improve robustness and precision.

This reconstruction method was applied successively on homogenous gelatin phantoms (Figure 40A) and heterogenous gelatin phantoms (Figure 40B, C) for validation of our postprocessing pipeline, before being applied to mouse skeletal muscle (Figure 40D).
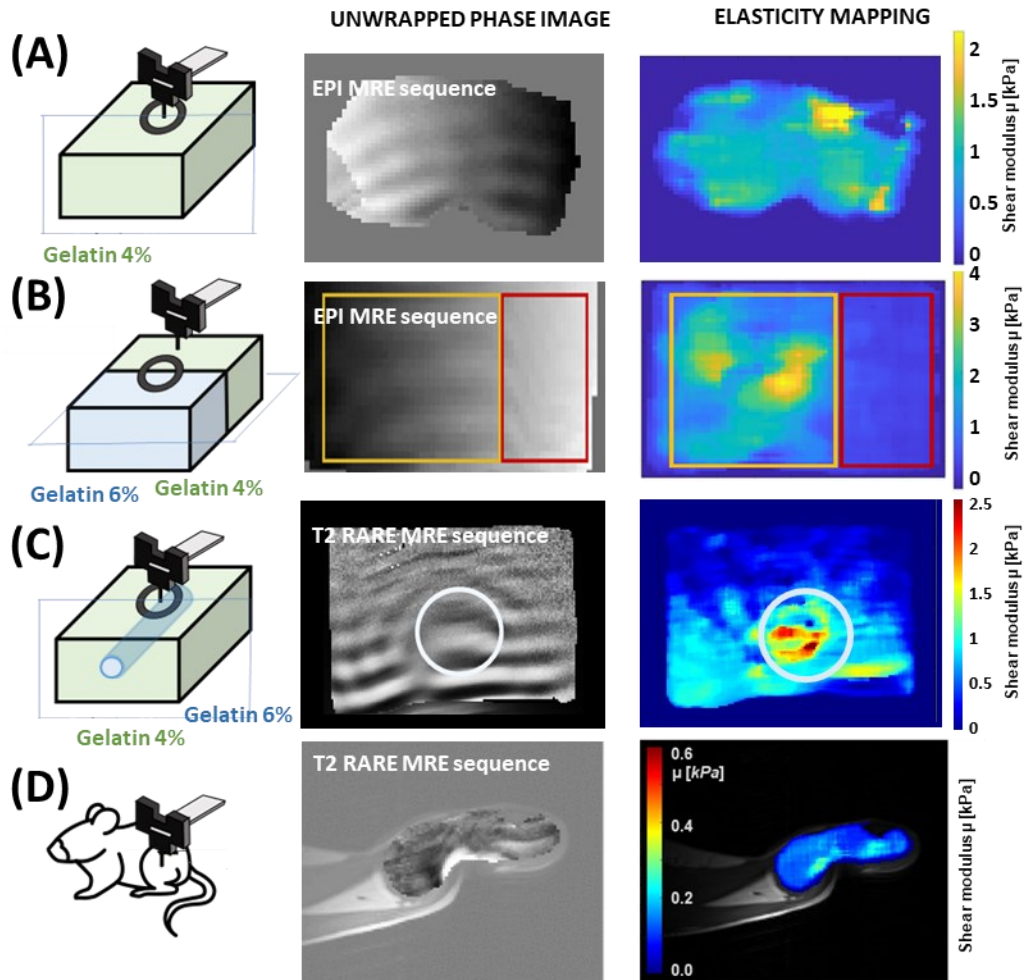
Figure 40. Illustration of unwrapped phase images and reconstructions (shear modulus maps) obtained using two different MRE imaging sequences. The protocol is successively validated on homogeneous (A) and heterogeneous (B)(C) gelatin concentration, before in vivo application for hindlimb mouse skeletal muscles (D).

2.3. MRE analysis of skeletal muscle mechanical properties in the murine hindlimb

2.3.1. Acquisition protocol

Setup installation. The electronic devices and connections shown on Figure 41 were installed prior to the arrival of the animal. A function generator connected to the MRI trigger provides a harmonical sinusoidal signal, transmitted by an amplifier to the piezoelectric actuator. An oscilloscope allows for the visualization of both the input MRI trigger signal and the output sinusoidal signal to monitor their synchronization. 10-meter-long cables connect the amplified and the piezoelectric actuator which are located within two different rooms. Once this connection is achieved, an operator in the control room can adjust the amplitude and frequency of the actuation.

76
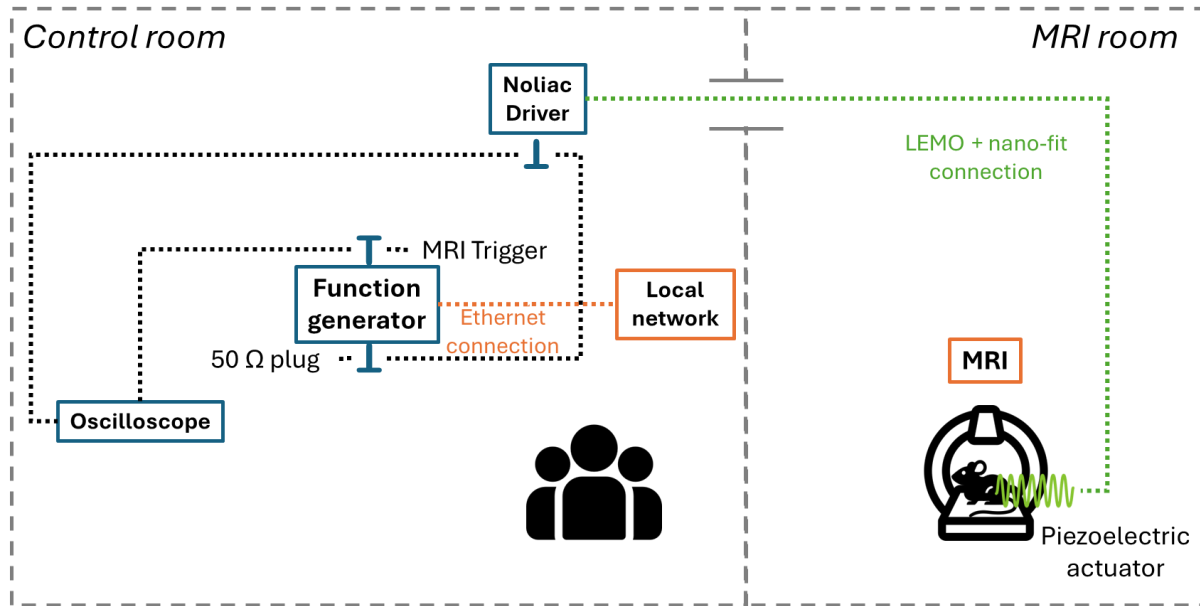
Figure 41. Schematic representation of electronic experimental setup. Devices are separated in two different rooms: the control room that contains all ferromagnetic materials and especially devices controlled by the operators, and the MRI room or Faraday cage that contains the MRI. Black dashed lines represent BNC cables and green dashed lines represent the actuator's cables.

Animal positioning and monitoring. The animal was brought after the verifications and the animal MRI bed preparation (Figure 42A). After weighing, the animal was anesthetized using 2% isoflurane gas. The positioning was then performed. To keep the animal warm, a heating fan was positioned in front of the bed for the duration of the installation. The animal was monitored using a rectal thermometer and a breath sensor. Prior to the installation, they got an injection of saline solution (0.4 mL) in the neck and gel on the eyes to avoid eye dryness. The hindlimb got shaved to allow a better positioning of the setup. Then the animal's body and hindlimb were positioned and fixated as shown in Figure 42B. Two screws were used to position the hips, and a foam provided positioning for the hindlimb. While performing preliminary experiments to calibrate the protocol, a set of questions arose about the mouse positioning. Indeed, the mouse hindlimb muscles contracting differently depending on the current position, therefore affecting their mechanical properties, 2 positions are investigated for each animal, with the aim of subsequently measure the mechanical properties of both flexor and extensor muscles.

The target position on the skin for the piston was marked using a marker pen, which allowed for later repositioning on the same region of interest. Then a survival blanket was placed onto the animal to limit heat losses. Finally, the reception coil and the setup were placed and fixed around the targeted area (Figure 42C). The extremity of the piston in contact with the animal is coated with echography gel, which allows its visualization in the MRI images. We ensured that no contact happened between the piston and the RF coil. The whole bed was then moved into the MRI room. The animal was warmed up by warm water and the sensors were connected to a monitoring program. The whole positioning duration lasts 25 minutes and is very repeatable.
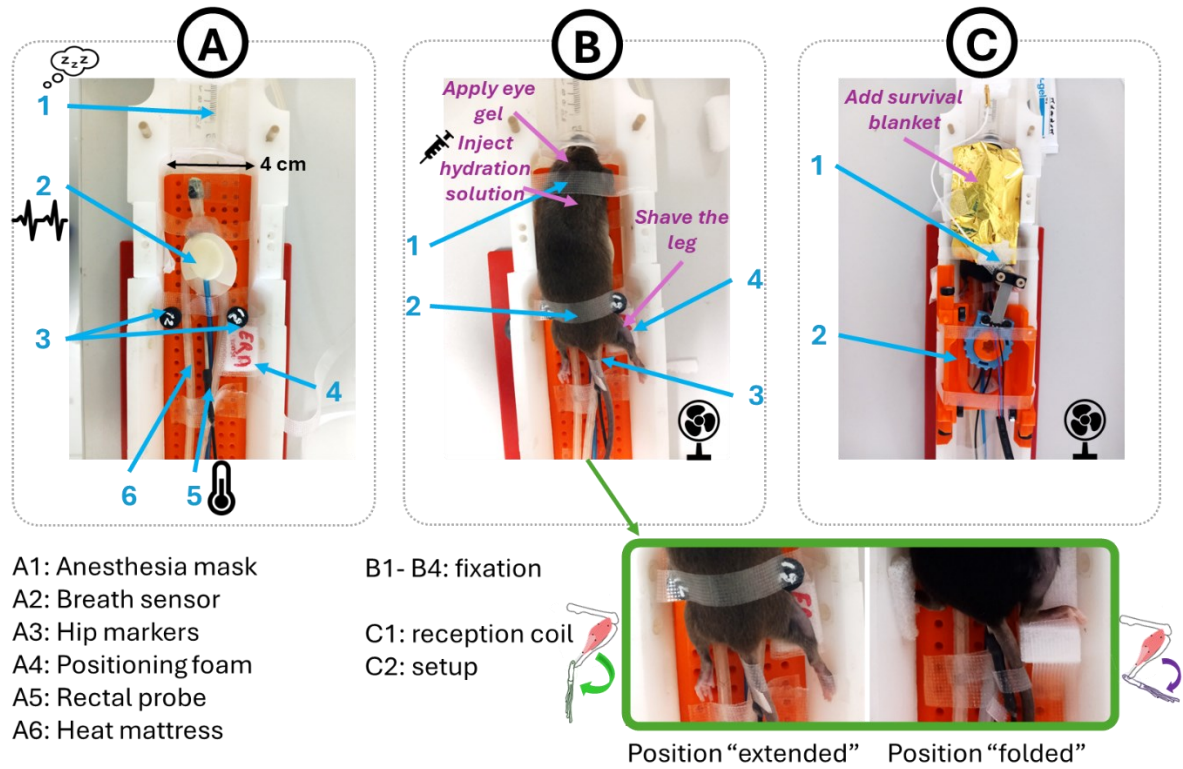
Figure 42. Animal installation in the MRI bed: (A) bed preparation with anesthesia, sensors and positioning items; (B) Mouse positioning and fixation; (C) setup and reception coil positioning over the animal. Items are marked in blue, actions related to the animal's well-being are marked in purple.

MRI acquisitions. For each animal, the following imaging protocol was applied (detail of the sequence parameters are in the Table 9):

- A FLASH sequence allowed to visualize the piston and hindlimb position in the MRI tunnel and center the following acquisitions, slices and field of view around that position.

- T2 TURBO RARE sequence was performed to obtain axial images of the right hindlimb muscles and used to generate manually two 3D ROIs corresponding to ankle extensor and flexor muscles (extensor in green and flexor in red color in the Figure 43).

- RARE MRE sequence at 1000, 1200 and 800Hz to obtain the phase images at 4 time steps and 2 opposite MEG polarities. Once opposite polarity phase images were subtracted two by two and unwrapped, the LFE algorithm allowed to reconstruct shear modulus maps assuming a tissue density of 1060 kg.m^{-3} (Méndez, 1960). It should be noted that since the FOV covers a depth of 12 mm (12 slices, each 1 mm thick), the volume observed is much larger than the area covered by the piston and even exceeds the diameter of the RF receiving coil. Therefore, to calculate the stiffness values, we only keep the 6 slices centered around the piston in post-processing.

- A diffusion tensor imaging (DTI) sequence was performed. This sequence provides information on tissue orientation. The main objective is to ensure that the plane being imaged in MRE and therefore the mechanical properties being mapped are indeed those of the transverse plane, and to evaluate any misalignment (and this in both positions of the leg). This is because we are encoding wave propagation in a single direction of space (according to a single gradient) in MRE slice by slice, rather than in all three directions, due to acquisition times that would otherwise be incompatible with the maximum duration of anesthesia for the animal. These DTI acquisitions are also useful because they could enable the application of reconstruction

methods other than LFE in the future, using transverse isotropic models to analyze the anisotropic mechanical properties of murine muscle *in vivo*. We used a spin echo (SE) based DTI acquisition with six directions and one b value. These results are still being post-processed and will not be presented in this manuscript.

The total duration of such an acquisition block is about 1h30. Afterwards, a quick repositioning of the hindlimb and setup within the MRI room is realized within 5 to 10 minutes, and an identical acquisition block is repeated for the second position of the leg.

At the end of the experiment, the animal was sacrificed using cervical elongation/dislocation without waking the animal. The right and left hindlimb EDL and soleus muscles were then extracted *post-mortem* for histological analysis and SEM imaging. These experiments are still ongoing and will not be presented in this thesis.

Table 9. Acquisition block corresponding to the protocol applied to one position of the hindlimb. For RARE sequences, the RARE factor is set to 4.

#	Sequence	f (Hz)	Time Steps (-)	Directions (-)	MEG Orientation	TR (ms)	TE (ms)	Matrix (-)	FOV (mm²)	Resolution (μm²)	Slices (-)	Slice thickness (mm)	Duration (s)
1	FLASH	-	-	-	-	15	3	192*192	40*40	208*208	15	1	43
2	Turbo RARE	-	-	-	-	2500	33	256*256	20*20	78*78	16	1	160
3	MRE RARE	0	4	-	Axial/slice	2500	10.78	133*133	20*20	150*150	12	1	132
4	MRE RARE	1000	4	-	Axial/slice	1000	10.78	133*133	20*20	150*150	12	1	132
5	MRE RARE	1200	4	-	Axial/slice	1000	10.78	133*133	20*20	150*150	12	1	132
6	MRE RARE	800	4	-	Axial/slice	1000	10.78	133*133	20*20	150*150	12	1	132
7	DTI	-	-	6	-	2000	25	145*111	17*13	117*117	12	1	2352
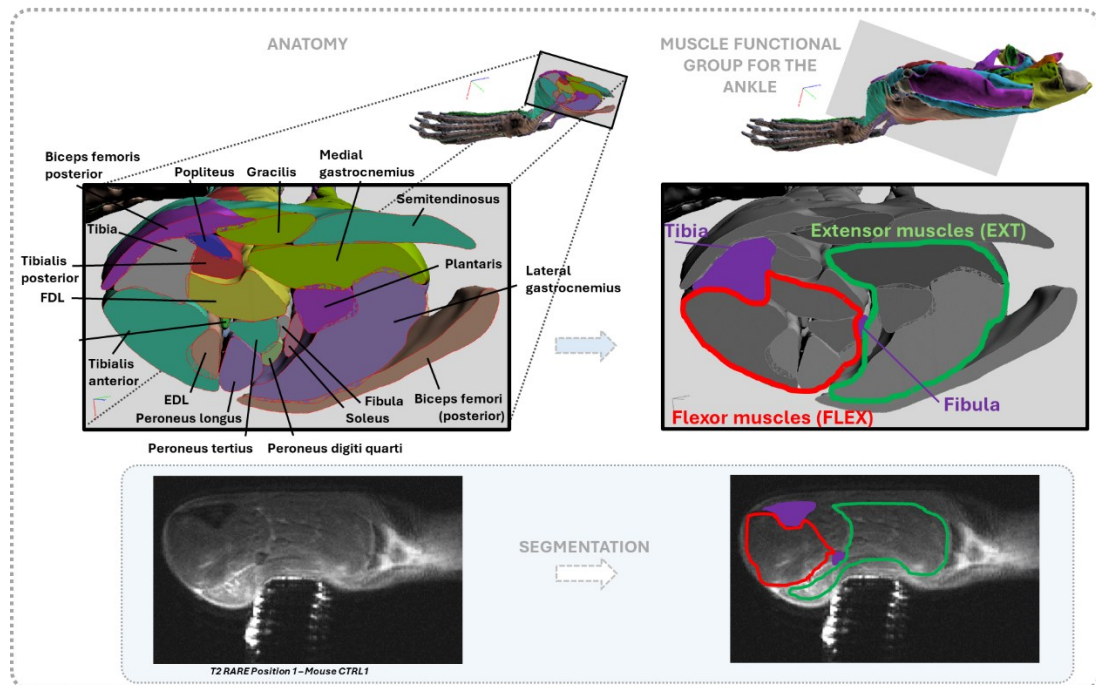
Figure 43. Muscles contained in the leg segment of the mouse hindlimb and their respective functional groups (extensor in green and flexor in red color) with respect to the ankle joint (adapted from: Charles et al. 2016). Segmentation illustration on one acquisition on healthy mouse (CTRL=WT). Bones are highlighted in purple and serve as anatomical markers.

2.3.2. Description of the animals

MRI acquisitions on mice were performed according to the protocol described above approved by local authorities (EU0466 - ICUBE Autor. APAFiS #34518). Three main groups of animals were used to ensure the desired results regarding the influence of Klf10 gene on mechanical properties *in vivo*: one group to study the influence of position, a second to study intra-individual reproducibility, and a third to make a relative comparison between control animals (CTRL or WT) and animals with Klf10 gene inhibition (skmKO) in the skeletal muscles.

First, tests were performed to optimize the protocol and evaluate reproducibility. In total, the following animals were tested as part of these tests (23.6 to 25.0g):

- 3 C57BL/6 WT mice to investigate the effect of and optimize the hindlimb positioning
- 2 C57BL/6 WT mice to investigate the reproducibility of the measurements on the same animal after 48h. One animal being common to the previous protocol: the repeatability of the influence of the position of the hindlimb could thus be tested on this animal.

A new mouse model (skmKO) has recently been developed from the Klf10 KO mice previously used. The originality of this model lies in the fact that the Klf10 gene has been invalidated solely in skeletal muscle, which is of great interest for analyzing the role of this gene in muscle function and physiology more precisely. This conditional deletion allows the muscle phenotype to be linked directly to the absence of the protein in the tissue (unlike the systemic deletion used previously, with the Klf10 KO mice, which does not allow the effects of the mutation in skeletal muscle to be distinguished from those in other organs). It thus makes it easier to identify the regulatory pathways directly dependent on Klf10 for muscle organization and function. It is this skmKO model that is used in this study to investigate the effect of Klf10 gene inhibition:

- 4 skmKO female mice (3-month-old, weighing 22.3g ± 2.1g).
- 4 C57BL/6 female mice (3-month-old control animals, weighing 24.2g ± 0.8g)

We maintained a similar genotype between pathological mice and control mice. The same genetic strain is used here for the 4 female control mice, where the Klf10 gene is expressed normally (non-floxed). All these animals are part of a line developed by Sabine Bensamoun at BMBI at UTC Compiègne and Franck Delaunay and Michèle Teboul at IBV at the University of Nice Côte d'Azur. All these animals are bred at the animal facility in Nice before being sent to the IRIS platform animal facility in Strasbourg, where they are housed for acclimatization for a minimum of two weeks before performing the acquisitions.

2.4. MRE results

This section successively presents the results of the influence of position, intra-individual reproducibility, and skmKO genotype investigation.

2.4.1. Influence of the leg position

In this configuration, ROIs consider the entire muscle, *i.e.*, both the extensor and flexor muscles. Firstly, as can be seen in Figure 44, as a tendency, shear modulus values seem lower when evaluated in position 2 than in position 1. However, in both positions, different groups of muscles are contracted or relaxed. Thus, it confirms the necessity to investigate these properties by separating those muscle groups in the following study of the influence of the Klf10 gene.
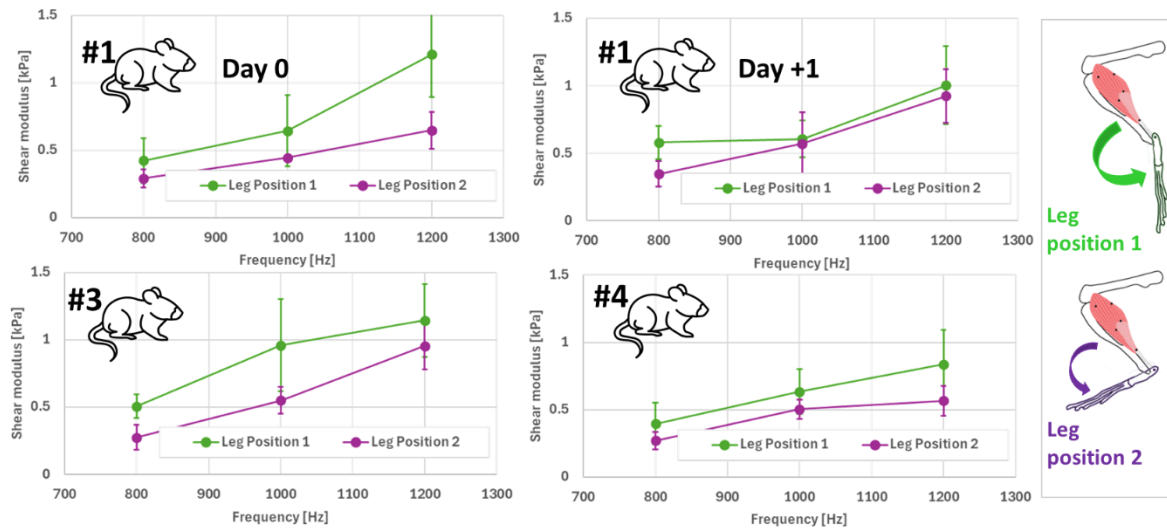
Figure 44. Investigation of leg position influence: mean shear moduli obtained over the hindlimb for each frequency and leg position, separated by individual and date of experiment.

2.4.2. Repeatability

Intra-individual and inter-individual repeatability were evaluated, on one or both positions. Here again, ROIs consider the entire muscle, i.e., both the extensor and flexor muscles. Mean shear modulus within the hindlimb muscles for each individual animal is shown in Figure 45. The measurements are repeatable, and no difference greater than the order of magnitude of the variability and measurement noise can be observed between the repeated acquisitions after 1 or 2 days, whatever the leg position is.
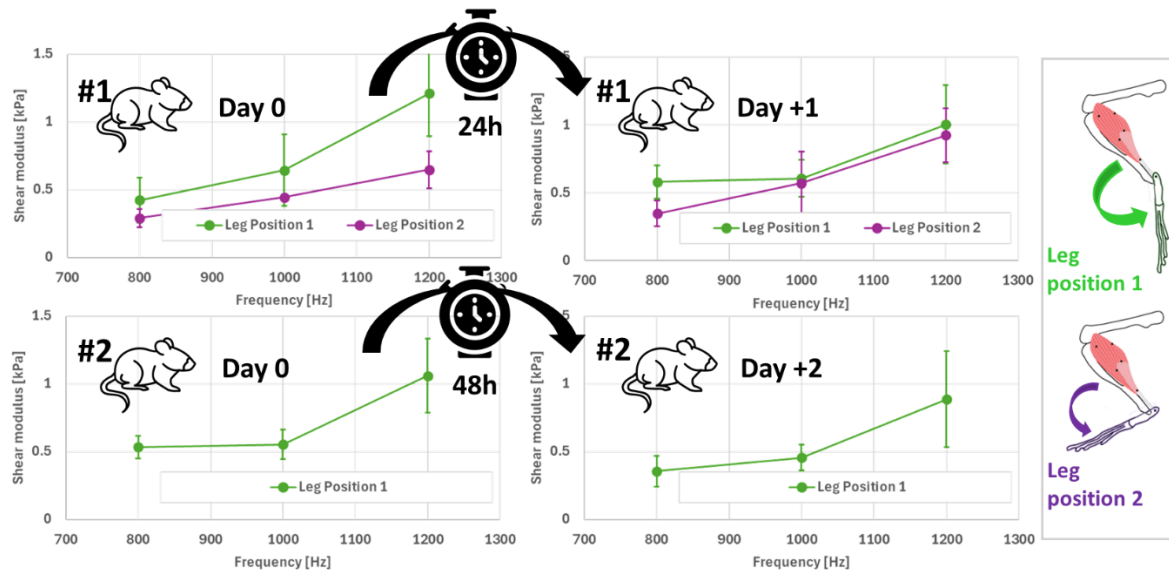
Figure 45. Repeatability investigation: Mean shear moduli obtained over the hindlimb for each frequency and leg position, separated by individual and date of experiment.

It should be noted that changes could also have occurred not because of the protocol itself but because of changes in the animals over the course of one or two days. However, this was not the case during the period under consideration, leaving a certain latency and avoiding the risk of measurement bias between the first and last animals tested subsequently (which may then have been a few days older).

81

2.4.3. Influence of the Klf10 gene

We present here the results obtained with the application of our protocol to the new mouse model (skmKO, n=4) developed from the Klf10 KO mice and healthy controls (Control, n=4).
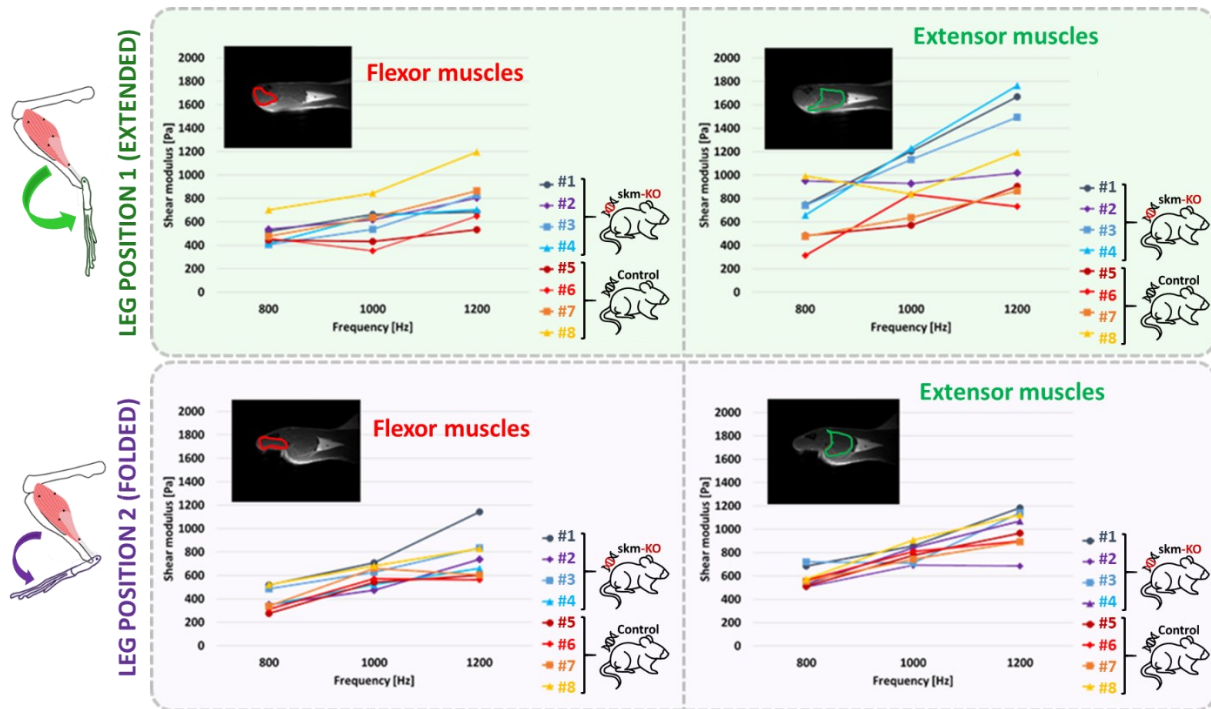
Figure 46. Individual resulting mean shear moduli represented as a function of excitation frequency for each muscle group and each position.

Since the number of animals in each group is low (n=4 per group), it is difficult to establish any statistical test as a whole, even non-parametric, and, in fact, individual results are shown in Figure 46. No effect of genotype is noticeable in position 2, for any muscle group. First, dispersion of values is higher in position 1. No effect is observed for flexor muscles in position 1, however a trend is observable for extensor muscles in position 1, where the average shear modulus is higher for skmKO mice. Overall, no influence of muscle group or position is noticeable for control mice. For skmKO mice, an effect of muscle group can be observed (Figure 47), where the average shear modulus values tend to be higher for extensor muscles regardless of the position.
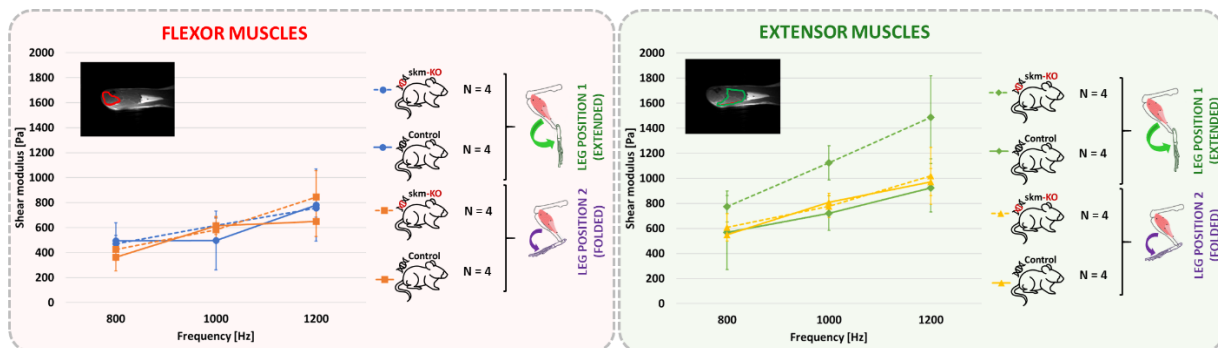
Figure 47. Results averaged over genotypes, presenting mean shear moduli as a function of frequency. Comparison of the two muscle groups.

These experiments point towards a difference of skmKO extensor muscles in elongation. This group of muscles includes the soleus muscle; however, the effect we observe is an average over all the muscles contained in this group and no conclusions can be drawn regarding individual muscles (such as soleus, contained in the extensor muscle group, and EDL, contained in the flexor muscle group). Given the resolution, the size of the organs, and their intertwined architecture, it was impossible to separate the so-called "slow" muscles from the so-called "fast" muscles, as had been done in *ex vivo* tests.

Differences in shear modulus might indicate a remodeling in the structures involved in lateral force transmission. Here the effects of all muscle components are averaged, so no conclusion can be drawn about a particular component.

However, these acquisitions have been performed on a small number of animals (n=8) and do not allow for performing significant statistical analyses of the results. This first series of experiments exhibited potential differences between control and skmKO mice hindlimbs *in vivo* and opened the way for a new series of experiments to be performed before the end of this PhD thesis with the same protocol.

2.5. Conclusion

During this thesis, a protocol for non-invasive *in vivo* MRE of skeletal muscle hindlimb was developed, based on an experimental setup built during the master thesis. The protocol involves collaborations for MRE-specific imaging sequences, and reconstruction methods. Experiments dedicated to the refinement of the protocol were performed and achieved quantification of intra and inter-individual reproducibility, optimization of the protocol duration and refinement of the postprocessing pipeline. **With this protocol, a first *in vivo* investigation of the effect of the Klf10 gene on murine hindlimb was made possible and highlighted potential differences between two genotypes and possible altered pathways in muscle physiology. Investigations of a larger cohort will provide statistically significant results in the near future.** Moreover, this first experiment sets off the path for further *in vivo* MRE experiments on mice.

Chapter 3: Multiscale numerical model

Previously, both in the literature and in chapter 2, important implications of muscle structure on the overall functioning of the organ can be seen at different scales. **In addition, we have highlighted the involvement of some of these components at very specific scales, and in particular the fundamental role of the ECM in overall mechanical behavior. However, the scarcity of methods to mechanically study the ECM has led us, in this chapter 3, to propose an adapted form of an existing multiscale numerical modeling approach (Tan et al., 2020) that allows us to derive the properties of the ECM from the behavior of the other microcomponents and the overall response of the muscle**. More importantly, and in a completely original way, this model has to integrate the mechanical and morphological specificities of the mouse skeletal muscle in relation to the activation or inhibition of the Klf10 gene (numerical application study proposed in chapter 5), notably acquired previously within the BMBI at UTC (Kammoun et al., 2016, 2017; Tatarenko et al., 2024). The approach developed and explained below will be transferable to other multiscale organ studies, but most importantly will provide an accurate description of the mechanical properties of the ECM based on the macroscopic mechanical behavior of skeletal muscle.

3.1. Objectives

To describe the multiscale mechanical behavior of skeletal muscles, several numerical methods have been introduced in chapter 1. They provide different features and limitations, notably on the complexity of the geometry and the materials that constitute the model. Our method must not only be able to consider realistic geometry and mechanical behavior laws that are representative of anterior observations (Tatarenko et al., 2024), but also to provide interpretable information about changes at the microscopic scale (muscle fibers, ECM,…) from the macroscopic mechanical response. This microscopic information can include mechanical parameters with a physical meaning, such as anatomical parameters, mechanical parameters as inputs, but also outputs related to interpretable physical phenomena such as stress concentration. The interest in such an approach is a precise understanding of the modifications induced by the genetic deletion, as to target those modifications with medical equipment in further research stages. Thus, the chosen method should provide both a quantification of an equivalent macroscopic behavior together with a precise knowledge of the local behavior.

Amongst the existing scale transition methods, only numerical homogenization methods allow us to consider a complex microstructure. More specifically, we will here develop a Direct Finite Element Square (DFE²) method. DFE² has first been introduced by Tan et al. (2020) and since then applied to the study of diverse and complex microstructures, such as porous structures (Liu et al., 2023; Singh Dhari et al., 2023), fiber reinforced composites (Hu et al., 2024; Liu et al., 2023; Zhi et al., 2021; Zhi, Leong, et al., 2023; Zhi, Yang, et al., 2023) and laminates (Hu et al., 2024; Zhi, Leong, et al., 2023, 2023). The material behavior laws employed in DFE^2 studies cover a large range, exhibiting plasticity (Hu et al., 2024; Liu et al., 2023; Oukfif et al., 2024; Singh Dhari et al., 2023; Tan et al., 2020; Xu et al., 2022; Zhi et al., 2021; Zhi, Leong, et al., 2023), viscosity (Oukfif et al., 2024; Tan et al., 2020; Zhi et al., 2021; Zhi, Yang, et al., 2023), crack propagation (Singh Dhari et al., 2023; Zhi, Leong, et al., 2023), acoustic (Zhi et al., 2021) and piezoelectric (Li et al., 2024) effects. However, to the best of our knowledge, no anisotropic hyperelastic material has been investigated using a DFE² method. This is what we propose to develop here.

Moreover, DFE² is the only approach that fulfills all our requirements:

- realistic representation of microstructure, notably from personal observations;
- anisotropic mechanical behavior laws corresponding to our experimental observations;
- localization of the microcomponents;
- interpretable information about changes at the microscopic scale from the macroscopic mechanical response.

In this chapter, we will adapt DFE² method to the specific case of skeletal muscle and especially validate the method for hyperelasticity and large deformation models.

3.2. Homogenization method development

3.2.1. DFE^2 Method description

Let us consider a body Ω with boundary conditions Γ. Let us consider a body force $\boldsymbol{b}$ and traction force $\boldsymbol{t}$ applied to Ω. From the principle of virtual work, the weak form of the equilibrium equation is given by Eq. (3.1) and (3.2).

$$\int_\Omega \boldsymbol{\sigma} : \nabla(\delta\boldsymbol{u})d\Omega = \int_\Omega \boldsymbol{b} \cdot \delta\boldsymbol{u}d\Omega + \int_\Gamma \boldsymbol{t} \cdot \delta\boldsymbol{u}d\Gamma \tag{3.1}$$

$$\int_\Omega \delta u_{i,j}\sigma_{ij}d\Omega = \int_\Omega \delta u_i b_i d\Omega + \int_\Gamma \delta u_i t_i d\Gamma \tag{3.2}$$

This equation states that the internal virtual work (left hand side) is equal to the external virtual work (right hand side). Here $\boldsymbol{\sigma}$ is the Cauchy stress tensor, $\delta\boldsymbol{u}$ is the virtual displacement vector, and ∇ the gradient operator. In Finite Element Square (FE²) methods (Raju et al., 2021), the objective is to solve the weak form of equilibrium at the macroscale level using values of stress that are computed at the microscale.

Upon Finite Element (FE) discretization, this equation becomes:

$$\boldsymbol{K} \cdot \boldsymbol{U} = \boldsymbol{F} \tag{3.3}$$

Here $\boldsymbol{K}$ is the stiffness matrix, $\boldsymbol{U}$ is the node displacement vector and $\boldsymbol{F}$ is the node force vector.

Using the Gaussian quadrature, the left side of the weak form of equilibrium can be written as:

$$\int_\Omega \boldsymbol{\sigma} : \nabla(\delta\boldsymbol{u})d\Omega = \sum_e \left[\sum_a w_a J_a (\boldsymbol{\sigma} : \nabla(\delta\boldsymbol{u}))_a \right]_e \tag{3.4}$$

$$\int_\Omega \boldsymbol{\sigma} : \nabla(\delta\boldsymbol{u})d\Omega = \sum_e \left[\sum_a w_a J_a \delta u_{i,j}(x_a)\sigma_{ij}(x_a))_a \right]_e \tag{3.5}$$

Here e denotes the macroscale finite elements and a denotes the integration points within each element. w_a, J_a are the gaussian weight and the Jacobian at integration point a. $(\boldsymbol{\sigma} : \nabla(\delta\boldsymbol{u}))_a$ is the internal virtual work at integration point a.

In the DFE^2 method, both scales are present within the same simulation. The macroscale stress at integration point a is the microscale stress averaged on the RVE volume. Microscale quantities are described using the ~ symbol. These stresses are computed based on a prescribed volume average displacement gradient:

$$\sum_e \left[\sum_a w_a J_a \delta u_{i,j}(x_a) \sigma_{ij}(x_a))_a \right]_e = \sum_e \left[\sum_a w_a J_a \langle \delta \widetilde{u_{i,j}} \rangle_a \langle \widetilde{\sigma_{ij}} \rangle_a)_a \right]_e \tag{3.6}$$

where $\langle . \rangle_a$ denotes the volume averaged quantities over the RVE associated with integration point a and element e.

The Hill-Mandel homogenization condition (Hill, 1963, 1967; Mandel, 1973) requires equality of internal virtual work per unit volume between the two scales:

$$\langle \delta \widetilde{u_{i,j}} \rangle \langle \widetilde{\sigma_{ij}} \rangle = \langle \widetilde{\delta u_{i,j} \sigma_{ij}} \rangle \tag{3.7}$$

According to the Hill–Mandel condition of computational homogenization, the virtual work at an integration point can be calculated from the volume average of the corresponding micro-scale RVE:

$$\left(\boldsymbol{\sigma} : \nabla(\delta \boldsymbol{u}) \right)_a = \frac{\left(\int_{V_a} \widetilde{\boldsymbol{\sigma}} : \nabla(\delta \widetilde{\boldsymbol{u}}) dV \right)}{|V_a|} \tag{3.8}$$

$$\int_\Omega \boldsymbol{\sigma} : \nabla(\delta \boldsymbol{u}) d\Omega = \sum_e \left[\sum_a \frac{w_a J_a}{|V_a|} \int_{V_a} \delta \widetilde{u_{i,j}} \widetilde{\sigma_{ij}} dV \right]_e \tag{3.9}$$

Here $\widetilde{\boldsymbol{\sigma}}$ is the microscale stress tensor and $\widetilde{\boldsymbol{u}}$ is the microscale displacement vector on the RVE. V_a is the spatial domain of the RVE with associated volume $|V_a|$.

We can note that the internal virtual work is equal to a weighted sum of the internal virtual work calculated from the microscale RVEs:

$$\delta W_{int} = \sum_e \left[\sum_a \frac{w_a J_a}{|V_a|} \int_{V_a} \delta \widetilde{u_{i,j}} \widetilde{\sigma_{ij}} dV \right]_e = \sum_e \left[\sum_a \overline{w_a} \int_{V_a} \delta \widetilde{u_{i,j}} \widetilde{\sigma_{ij}} dV \right]_e \tag{3.10}$$

$$\delta \widetilde{W_{int}} = \sum_e \left[\sum_a \int_{V_a} \delta \widetilde{u_{i,j}} \widetilde{\sigma_{ij}} dV \right]_e \tag{3.11}$$

with the scale factor:

$$\overline{w_a} = \frac{w_a J_a}{|V_a|} \tag{3.12}$$

The discretized weak form of equilibrium can then be rewritten as:

$$\widetilde{\boldsymbol{K}} \widetilde{\boldsymbol{U}} \delta \widetilde{\boldsymbol{U}} = \boldsymbol{F} \delta \boldsymbol{U} \tag{3.13}$$

Here $\widetilde{\boldsymbol{K}}$ is the stiffness matrix assembled by the finite elements of all micro-scale RVEs. $\widetilde{\boldsymbol{U}}$ is the nodal displacement vector of the micro-scale RVEs. In DFE[2] method, the material stiffness and density of macro-scale elements is set too a very small value, so that the macroscale elements do not contribute to the stiffness matrix $\widetilde{\boldsymbol{K}}$. For ease of numerical implementation, we set the scale factor to $\overline{w_a} = 1$.

From Eq. (3.13) we would like to eliminate the macroscale nodes displacement $\boldsymbol{U}$. In the DFE[2] method, it is assumed that the microscale displacement is equal to the macroscale displacement $\boldsymbol{u}$ superimposed with a quickly fluctuating microscale displacement $\boldsymbol{u}^*$:

$$\widetilde{\boldsymbol{u}}(\boldsymbol{x}) = \boldsymbol{u}(\boldsymbol{x}) + \boldsymbol{u}^* = \mathcal{N}_i(\boldsymbol{x}) \boldsymbol{u_i} + \boldsymbol{u}^* \tag{3.14}$$

Here x represents the spatial coordinates at a point of interest in a RVE, the macroscale displacement u is calculated from the nodal displacements u_i and the corresponding shape functions $\mathcal{N}_i$ (i ranges from 1 to 8 for 8-node solid elements). When using periodic boundary conditions on the RVEs the rapidly fluctuating field u^* disappears:

$$\tilde{u}(x_{V_a^+}) - \tilde{u}(x_{V_a^-}) = [\mathcal{N}_i(x_{V_a^+}) - \mathcal{N}_i(x_{V_a^-})]u_i \qquad (3.15)$$

where V_a^+, V_a^- represents the two-by-two corresponding boundaries of the RVE (Figure 48).
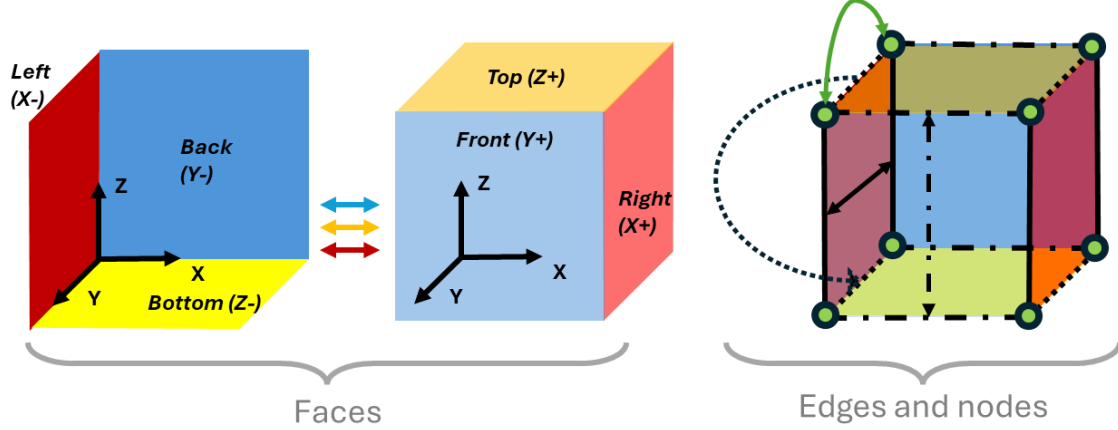
Figure 48. Boundaries of the RVE: for periodic boundary conditions, nodes on opposite faces and edges are linked through equations on their respective degrees of freedom. All faces, edges and corner nodes have to be identified.

Thus, the macroscale and microscale displacements can be related using a linear transformation:

$$U = L\tilde{U} \qquad (3.16)$$

The correlation matrix L does not need to be explicit, because the link is made in the FE software using Multi Point Constraints (MPC). Finally, the discretized form of equilibrium can be written as:

$$\tilde{K}\tilde{U} = LF \qquad (3.17)$$

Here, only the microscale displacements $\tilde{U}$ need to be solved. Thus, knowing the stiffness at the microscale and the boundary conditions at the macroscale, the DFE^2 method solves the displacements at the microscale. Eq. 3.16 provides the displacements at the macroscale.

3.2.2. Adaptation of the method to the skeletal muscle geometry

The DFE^2 method described above has been implemented for 3D solid elements C3D8, which possess 8 nodes and 8 integration points, and which shape functions are linear functions of the coordinates. The full model generation happens in two distinct steps: firstly, geometry generation, and secondly, constraint generation (Figure 49). The geometry is generated from the simulation input files of the macroscale model and the microscale RVE. The information from the input files provides point

clouds for each element. From this data, the position of the integration points within the macroscale model is computed and a RVE is positioned at each integration point.
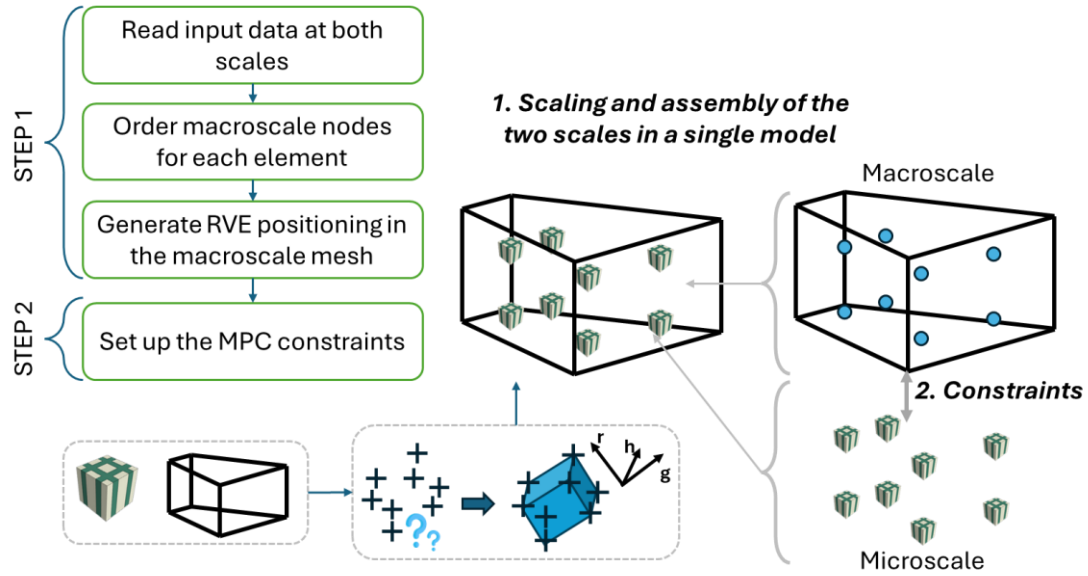
Figure 49. Overview of the DFE² algorithm: two main steps are the geometrical assembly of the macroscale model and the microscale model in step 1, and then the link between scales is provided through MPC in step 2.

As to write the constraints that link the two scales, the method requires to know the shape functions in each element, which require the natural coordinates of every node in each mesh element to be known. In the FE software ABAQUS® SIMULIA (*Dassault Systèmes SE, Vélizy-Villacoublay, France*), a certain convention is used to attribute an order to each node in an element (Figure 50 A). Therefore, one of the first steps in the DFE² script is to recognize the natural coordinates within each element. The DFE² method initially developed makes assumptions about macroscale geometry which do not fit to a muscle geometry (Figure 50 B).
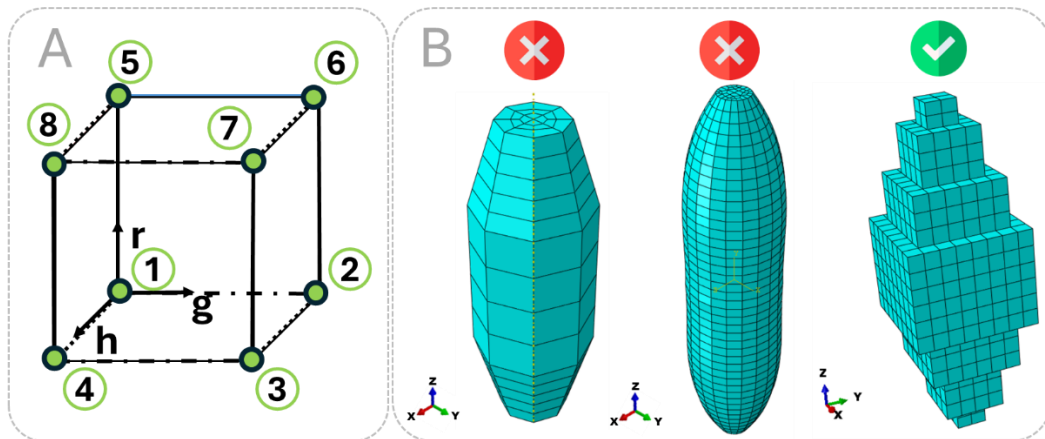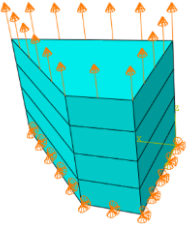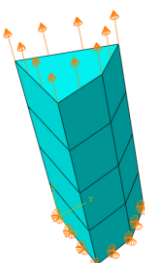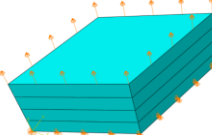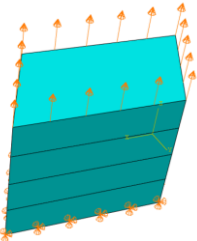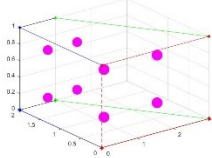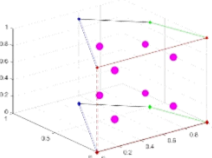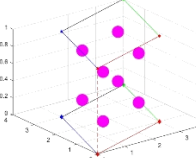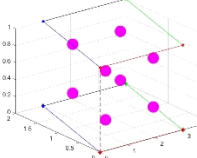
Figure 50. (A) Natural order of the nodes within one 3D solid element and the corresponding natural coordinates; (B) different simplified muscle geometries and their compatibility with the initial DFE² code.

Thus, this part of the method was adapted (Figure 51). It consists in considering the input coordinates of each element and sorting them into two groups of four points. After checking that the groups of points are forming faces, i.e. belong to the same plane, the parallelepiped geometry of the element can be reconstructed and points 1 through 8 identified.

For simplification purposes and considering the geometry of a skeletal muscle, we hypothesize that the mesh elements are roughly aligned along the Z axis. Therefore, the algorithm focuses on finding two faces orthogonal to the Z axis. However, its implementation allows a generalization to any geometry, using K-means or Principal Component Analysis (PCA) to detect clusters of 4 points. K-means clustering is a method that partitions n observations into K clusters, thus we can separate our point cloud into two clusters. Each observation will belong to the cluster with the nearest mean. PCA is a different algorithm aiming at reducing the dimension of the data. Applied to our point cloud, it can output vectors in the direction of the largest variance, and attribute labels to each point according to their relative projection on the PCA vectors. This method can be useful especially when the element is not aligned with the X, Y, and Z axis. As we simplified the skeletal muscle geometry to be roughly aligned along Z, we chose to use K-means.

The developed algorithm has been validated on different geometries aligned with the Z axis, which appear naturally when meshing a muscle cross-section (Table 10). These geometries are right prisms (with and without symmetries), right parallelogramic prisms (with or without alignment with one of the X and Y axes). Each geometry was meshed with four C3D8 elements, i.e. 3D solid elements with 8 nodes and 8 integration points (full integration) using linear shape functions.

Table 10. Simplified geometries tested with both algorithms using simplified FE models, as to be able to compute the positions of integration points and the shape functions.

Prism description	Right prism	Right prism presenting a symmetry	Right parallelogramic prism	Right parallelogramic prism with 1 side aligned with X axis
Simplified FE model				
Position of the integration points within the C3D8 element				
Original algorithm	YES	NO	NO	YES
New algorithm	YES	YES	YES	YES
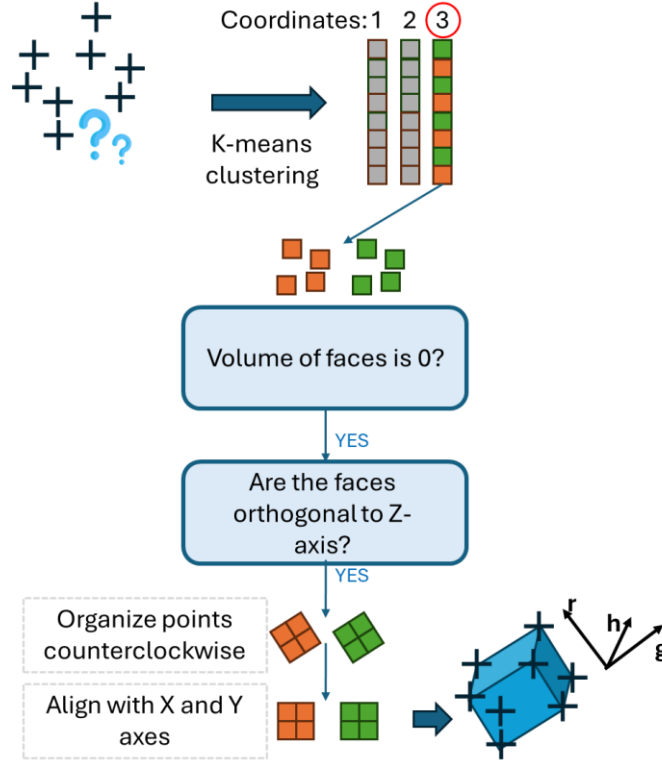
Figure 51. Natural coordinates identification algorithm developed for mesh elements orthogonal to the Y axis.

3.2.3. Adaptation of the method for reduced integration elements

The 3D solid elements available in ABAQUS® provide full or reduced integration, associated with a linear or quadratic interpolation. The difference between those characteristics results in different number of integration points and different expressions for the shape functions. The DFE² method has been developed for full integration first order elements that use 8 integration points. The method described above has only been developed for macroscale full integration first order elements C3D8, a general purpose linear eight-node brick element, fully integrated (2x2x2 integration points). For such elements, the 8 shape functions $\mathcal{N}_i(g,h,r)$ are defined as:

$$u(g,h,r) = \sum_{i=1}^{8} u_i \mathcal{N}_i(g,h,r) \tag{3.18}$$

$$
\begin{aligned}
u(g,h,r) = & \frac{1}{8}(1-g)(1-h)(1-r)u_1 + \frac{1}{8}(1+g)(1-h)(1-r)u_2 \\
&+ \frac{1}{8}(1+g)(1+h)(1-r)u_3 + \frac{1}{8}(1-g)(1+h)(1-r)u_4 \\
&+ \frac{1}{8}(1-g)(1-h)(1+r)u_5 + \frac{1}{8}(1+g)(1-h)(1+r)u_6 \\
&+ \frac{1}{8}(1+g)(1+h)(1+r)u_7 + \frac{1}{8}(1-g)(1+h)(1+r)u_8
\end{aligned}
\tag{3.19}
$$

In an equivalent manner:

$$
\begin{aligned}
\mathcal{N}_i(g,h,r) = & \frac{1}{8}\Sigma_i + \frac{1}{8}g * \Lambda_{i,1} + \frac{1}{8}h * \Lambda_{i,2} + \frac{1}{8}r * \Lambda_{i,3} \\
&+ \frac{1}{8}hr * \Gamma_{i,1} + \frac{1}{8}gr * \Gamma_{i,2} + \frac{1}{8}gh * \Gamma_{i,3} + \frac{1}{8}ghr * \Gamma_{i,4}
\end{aligned}
\tag{3.20}
$$

where:

$$\begin{aligned}
\mathbf{\Sigma_i} &= [+1, +1, +1, +1, +1, +1, +1, +1] \\
\mathbf{\Lambda_{i,1}} &= [-1, +1, +1, -1, -1, +1, +1, -1] \\
\mathbf{\Lambda_{i,2}} &= [-1, -1, +1, +1, -1, -1, +1, +1] \\
\mathbf{\Lambda_{i,3}} &= [-1, -1, -1, -1, +1, +1, +1, +1] \\
\mathbf{\Gamma_{i,1}} &= [+1, +1, -1, -1, -1, -1, +1, +1] \\
\mathbf{\Gamma_{i,2}} &= [+1, -1, -1, +1, -1, +1, +1, -1] \\
\mathbf{\Gamma_{i,3}} &= [+1, -1, +1, -1, +1, -1, +1, -1] \\
\mathbf{\Gamma_{i,4}} &= [-1, +1, -1, +1, +1, -1, +1, -1]
\end{aligned}$$
(3.21)

For computational efficiency, there was an interest in switching to reduced integration first order elements as this divides the model size by a factor of 8. This is done by changing coefficients in the expression of the 8 shape functions:

$$\begin{aligned}
\mathcal{N}_i(g, h, r) = &\frac{1}{8}\mathbf{\Sigma_i} + \frac{1}{4}g * \mathbf{\Lambda_{i,1}} + \frac{1}{4}h * \mathbf{\Lambda_{i,2}} + \frac{1}{4}r * \mathbf{\Lambda_{i,3}} \\
&+ \frac{1}{2}hr * \mathbf{\Gamma_{i,1}} + \frac{1}{2}gr * \mathbf{\Gamma_{i,2}} + \frac{1}{2}gh * \mathbf{\Gamma_{i,3}} + \frac{1}{2}ghr * \mathbf{\Gamma_{i,4}}
\end{aligned}$$
(3.22)

However, to obtain accuracy with such elements, some issues must be addressed. The main issue associated with C3D8R elements is hourglassing.
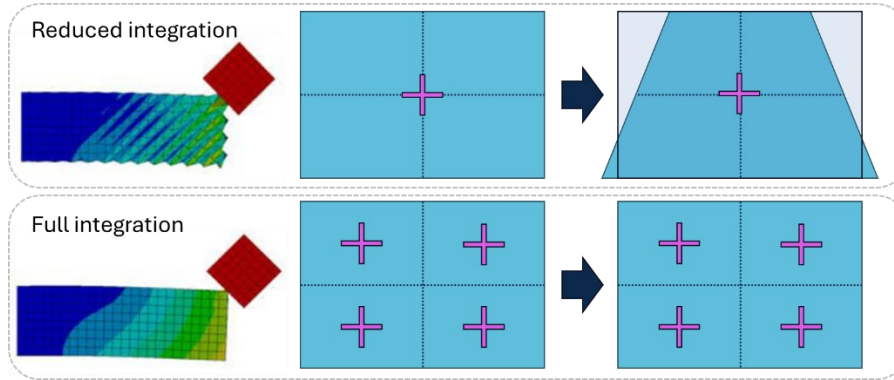
Figure 52. Illustration of the Hourglass phenomenon.

The hourglass phenomenon, illustrated in the Figure 52, is a numerical issue corresponding to a deformation in the mesh in the absence of deformation gradient at the integration point. The deformation pattern exhibits a characteristic wavy appearance, where all the elements are "*hourglass*" shaped. Indeed, one integration point does not provide enough internal constraints within the element to resist some deformation patterns. Thus, the structure deforms without physical forces causing it, what is called artificial zero-energy modes. ABAQUS® provides several methods to mitigate hourglassing, which involve adding artificial stiffness or damping within the element. Using those methods, the obtained results are similar to those obtained with full integration elements, although the problem size has been divided by 8.

The different strategies employed by the FE software to manage hourglassing do not appear within the shape functions. Therefore, their compatibility with the DFE² method must be investigated, as the user cannot access or modify their encoding in the FE software.

92

3.3. DFE² method validation for hyperelastic anisotropic materials

3.3.1. Comparison with an equivalent homogenous model

Since the DFE² method had not yet been implemented for hyperelastic material, the first step was to validate its use in the case of hyperelastic anisotropic material. For this purpose, we generated a RVE with homogenous mechanical properties following the Holzapfel-Gasser-Ogden (HGO) behavior law (Holzapfel et al., 2000) implemented in ABAQUS® for hyperelastic fiber reinforced composites (in this specific case with fibers aligned with a single a direction), defined by the following strain energy function:

$$W_{HGO} = W_{iso} + W_{aniso} + W_{Vol} = C_{10}(\overline{I_1} - 3) + \frac{k_1}{2k_2}\left(e^{k_2(\overline{I_4}-1)^2} - 1\right) + \frac{1}{2}K(J - 1)^2 \qquad (3.23)$$

where J is the determinant of the deformation gradient (*i.e.* the local ratio of volume change) and the invariants of the right Cauchy Green deformation tensor are defined by:

$$\begin{aligned}
\overline{I_1} &= tr(\overline{C}) = tr(J^{-\frac{2}{3}}C) \\
I_3 &= det(C) = J^2 \\
\overline{I_4} &= \overline{C}:(a \otimes a)
\end{aligned} \qquad (3.24)$$

DFE² simulations were implemented on several macroscale geometries with the homogeneous RVE and compared with a standard FE simulation of the macroscale geometry exhibiting the same mechanical properties (Figure 53). These simulations used full integration C3D8 elements.
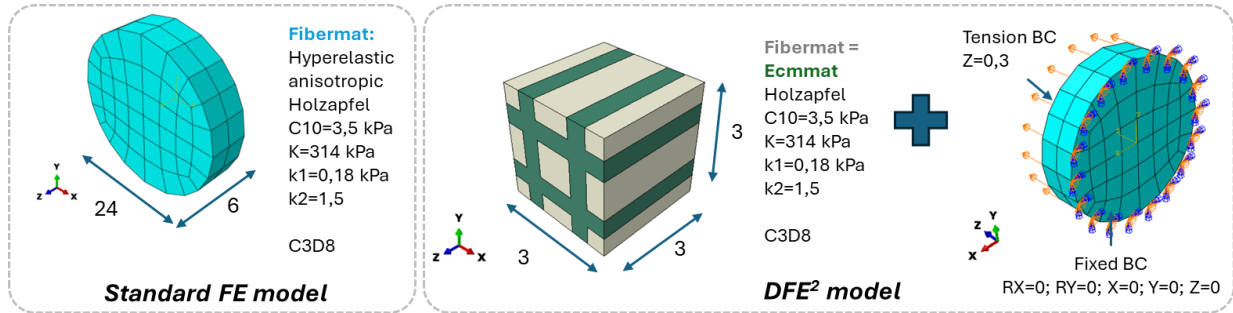
Figure 53. Setup of a pair of models to validate the DFE² method on a muscle slice geometry. BC: boundary condition.

A round muscle slice was generated. Dimensions of the RVE are 0.3*0.3*0.3 mm and were entered as 3*3*3 length units [L] in the Abaqus software to avoid numerical effects due to small edges in this first experiment. Indeed, the Abaqus software being dimensionless, users define their own units within the model. Dimensions of the muscle slice were chosen to obtain mesh elements similar in dimensions to the RVE. An elongation of 10% (tension BC in Figure 53) was imposed on one face of the models, to obtain large deformations and observe the hyperelastic behavior. The opposite face was fixed (fixed BC). Mechanical properties were taken from the literature on muscle multiscale modeling (Liu et al., 2022) from a model using HGO-derived behavior laws (parameters indicated in Figure 53), and fibers were aligned with the Z direction. The internal energy and total strain energy were extracted from both models and used as a means of comparison.

Comparison between FE and DFE². Both standard FE and DFE² models provided the same results in C3D8 elements: the total strain energy, internal energy within the model were the same, as well as the displacements and the stresses repartitions over the model (Figure 54A).

Influence of the geometry. The same result was observed for different geometries (Figure 54B, C).
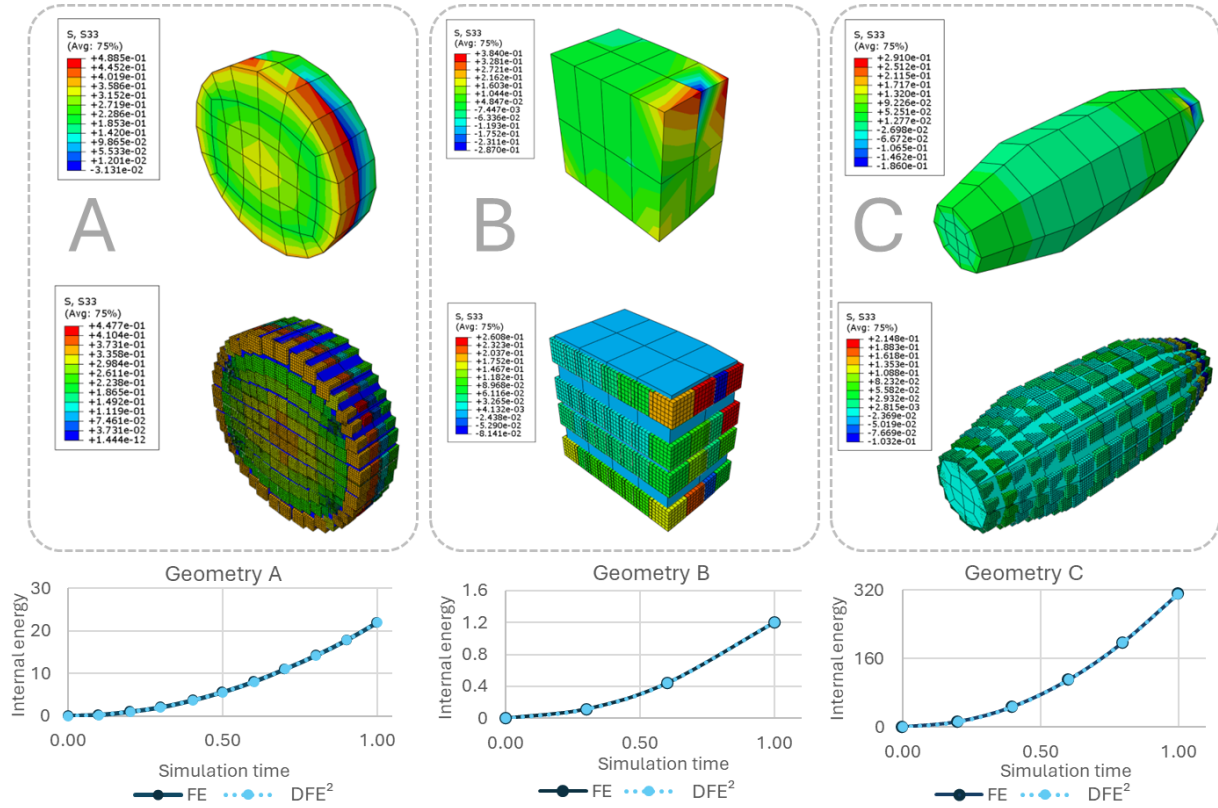
Figure 54. Comparison of FE and DFE² simulations on 3 different geometries: stress field in the Z direction and total internal energy in dJ for both models over simulation time.

Reduced integration. After this validation, the DFE² method adaptation to reduced elements C3D8R was tested. Reduced integration elements provide simulation eightfold less computationally expensive than full integration elements. The counterpart to such a strategy is a numerical phenomenon called hourglassing, as introduced above. In FE software, numerical strategies to control the hourglassing phenomenon can be used.

This effect will be presented in the next section.

3.3.2. Influence and choice of strategy for hourglass control

In ABAQUS®, 3 strategies for hourglassing control are proposed, namely stiffness, enhanced, and viscous hourglass controls. Hourglass stiffness control adds a small artificial stiffness to resist hourglassing modes. It usually is a ratio of the material's shear modulus, controlled by a hyperparameter defining this ratio. The shear modulus is estimated from the material definition. If the ratio value is too low, no hourglassing control happens. When the ratio value is too high, non-physical stiffening occurs. Instead of adding stiffness, enhanced hourglass control uses an energy-based approach to penalize hourglass modes more realistically. This approach is more computationally expensive; however, it does not require a hyperparameter. It is the default option for hyperelastic materials. Viscous hourglass control adds numerical damping instead of stiffness. It is adapted to dynamics analyses rather than static ones, where it can slow convergence.

In our model, we use hyperelastic materials. For tuning the method, a hyperelastic material implemented in ABAQUS® is used. For further analyses developed in the next chapters, UMAT files (user-defined materials encoded by the user), will be provided to the FE solver. Therefore, a few questions arise:

94

- *How do the hourglass controls perform on standard FE models with anisotropic hyperelastic material properties?*
- *Is the DFE² method compatible with the use of any hourglass controls?*
- *Considering that the macroscale model is coupled with RVE, its stiffness is actually much higher than what is defined in the macroscale mechanical properties. What mechanical properties does the software use for the different hourglass controls?*
- *Are the hourglass controls still performing the same when using a user-defined material?*

In the following section, we attempt to answer these questions. In this way, a preliminary study was performed with ABAQUS® HGO material and both stiffness hourglass control and enhanced hourglass control. Viscous hourglass control is not considered as it is not suited to static analyses. Full integration (8 integration points) "FI" and reduced integration (1 integration point) "RI" elements were used on the macroscale geometry (Table 11). Enhanced hourglass control does not require a hyperparameter, contrary to stiffness control. For the latter, recommended values for stiffness ratio in elastic materials range from 10^{-6} to 10^{-3}. The software default being 1, we tested both 10^{-3} and 1 values as well as an intermediary value of 0.3. Similarly to the previous section, a deformation of 10% was imposed on the model (Figure 55) and mechanical properties were taken from the literature on muscle multiscale modeling (Liu et al., 2022). The same RVE was used, and a fusiform whole muscle geometry with 1.9 cm length and 0.7 cm diameter was selected. The simulations were compared based on the force curve in the tension direction Z that was extracted from a reference point "RP" on the model, simulating a uniaxial tension experiment (Figure 56).

Table 11. Simulations performed for a preliminary study on hourglassing controls in hyperelastic and DFE² models: Full integration (FI) or reduced integration (RI) models of homogeneous hyperelastic materials were compared. For the reduced integration models, stiffness and enhanced hourglass controls were investigated. All models simulate the same experiments; the difference in the results was compared based on the resulting force measured at 10% deformation. IP: integration points.

NAME	CONTROL TYPE	STIFFNESS	# IP	FE METHOD	DFE² ERROR (% FE FORCE)	REDUCED INTEGRATION ERROR (%FI FE FORCE)
FI DFE²	/	/	8	DFE²	0.06	0.06
FI FE	/	/	8	Standard	/	0.00
RI Stiffness=0.3 DFE²	Stiffness	0.3	1	DFE²	1.15	32.07
RI Stiffness=1.0 DFE²	Stiffness	1	1	DFE²	0.77	5.28
RI Stiffness=0.001 DFE²	Stiffness	0.001	1	DFE²	1.74	47.89
RI Stiffness=0.3 FE	Stiffness	0.3	1	Standard	/	31.28
RI Stiffness=1.0 FE	Stiffness	1	1	Standard	/	4.55
RI Stiffness=0.001 FE	Stiffness	0.001	1	Standard	/	46.96
RI Enhanced DFE²	Enhanced	/	1	DFE²	12.37	47.89
RI Enhanced FE	Enhanced	/	1	Standard	/	40.54
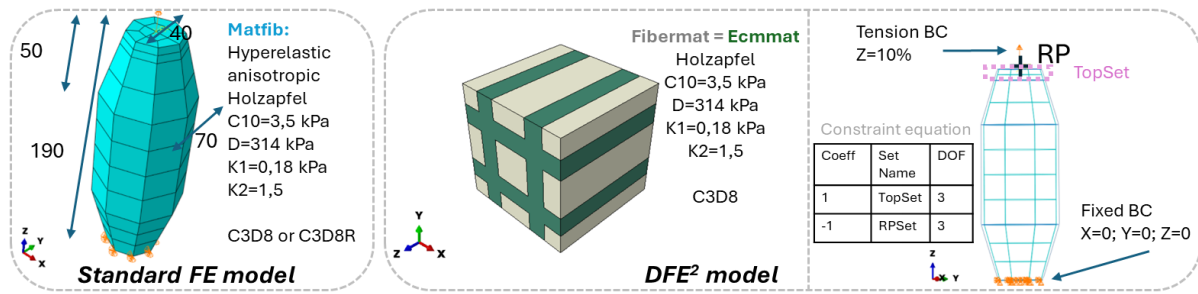
Figure 55. FE models used for a preliminary study on hourglass controls in DFE², featuring a fusiform muscle geometry. The muscle dimensions were chosen to obtain a mesh element size close to the RVE dimensions.

Differences between the standard FE and the DFE² model were observed, and those differences were dependent on the strategy chosen to manage hourglass effects within the model. The results show that the DFE² method using an ABAQUS® defined material is compatible with stiffness hourglass control but not enhanced hourglass control. In the case of stiffness hourglass control, the resulting curves of standard FE and DFE² show a relative error of about 1% in the results at 10% deformation, whereas this error is above 12% using enhanced hourglass control.

However, the reduced integrations simulations show sensitivity to the hourglass stiffness ratio parameter. Results display an error ranging from 5% to 50% relatively to the results obtained with full integration at the final deformation state. This suggests that hourglass stiffness control might be unsuited for hyperelastic materials. As the error is smaller with higher values of hourglass stiffness ratio, we may hypothesize that in our case the hourglass stiffness ratio should be tuned for our model; however, to test this hypothesis we have to make a distinction between physical and non-physical stiffening. Also, this result is obtained on a single geometry; and it might be of interest to generate different geometries, boundary conditions and mesh which would lead to less hourglass energy.
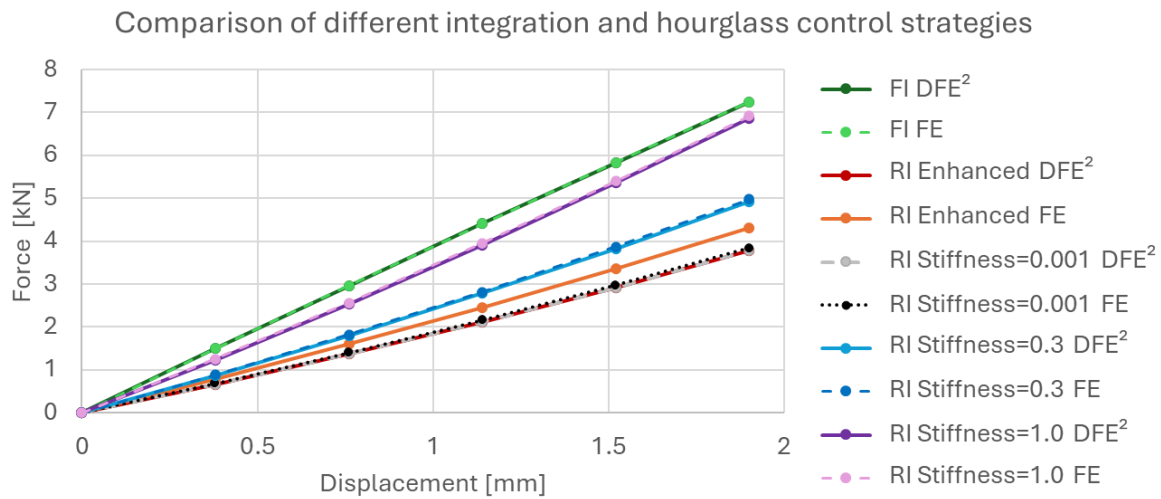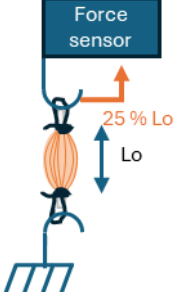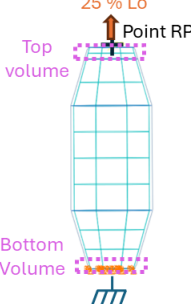
Figure 56. Comparison of full integration (FI) and reduced integration (RI) strategies in hyperelastic standard FE and DFE² models. 3 values were considered for the hourglass stiffness control.

This result leads us to better understand the existence and influence of the hourglass phenomenon, as previously described, and even more so to develop a control strategy to free ourselves from its influence and guarantee the results obtained by our model. Finally, similar results were obtained using a user-defined material (UMAT).

3.3.3. Influence and choice of macroscopic geometry and boundary conditions

Macroscopic model for the muscle geometry. The geometry is different from one muscle to another, and we will focus now on two specific muscles: the *soleus* (slow muscle) and *extensor digitorum longus* (EDL, fast muscle) muscles. A realistic envelope for each muscle can be recovered from anatomical MRI imaging. Ideal fusiform geometry can also be assumed. Finally, the whole muscle can also be assumed to be a cylinder. The chosen geometry must allow the reproduction of the solicitations present in the muscle during uniaxial tension: uniaxial strain but also shear strain that is due to its real geometry. Shear strain is closely linked to the functional properties of the ECM and has been shown to be modified by the Klf10 genetic deletion at the macroscopic (muscle) level in the previous chapter. Thus, a cylindrical geometry cannot be chosen. A fusiform geometry is a simplification of realistic geometry that still allows to reproduce those solicitations; moreover, it exhibits symmetries allowing to decrease the model size by a factor of 8. Thus, this geometry has been chosen. Dimensions have been chosen based on prior works (Tatarenko, 2023).

Table 12. Approaches for modeling the uniaxial tension experiment

-	Experiment (Tatarenko et al., 2024)	Model from Chakouch et al. (2025)	Current approach
Muscle geometry	Real	Cylinder	Idealized fusiform
Nature of geometry constrained in displacement	Complex volumes	Surfaces	Small volumes
Method for result extraction	Force sensor on the lever arm	Force measured on whole model	Resulting force in point RP linked to the displaced top volume through equations
Illustration			

Numerical simulation of experimental protocols. The uniaxial tension was performed by putting a surgeon node with surgical wire on each extremity of a muscle (Tatarenko et al. 2024). The lower extremity was fixed, whereas the upper extremity underwent a displacement of 25% of the optimal muscle length (L_0), and the developed force was measured in the experiment by a piezoelectric actuator connected to the upper extremity (Pouletaut et al., 2023). The same process was simulated in a previous study (Tatarenko, 2023 and Chakouch et al., 2025). We compare the approaches in Table 12.

Considering the experimental setup, we chose to apply constraints on a small volume, and to measure the resulting force on the volume being constrained in displacement. However, a FE model is a discretized approximation of the experiment, therefore constraining volumes might not be the most

effective method to reproduce the experimental setup: indeed, both a constrained volume and a constrained surface impose a displacement to the nodes at the interface with the free volume. Furthermore, this choice can have an impact on the overall model convergence. Thus, a preliminary study was conducted using a simplified muscle RVE and parameters from the literature identical to the previous sections. Simplified muscle models representing one quarter muscle were generated with either surfaces (SURF) or volumes (VOL) constrained on the bottom volume (Figure 57). Additional to this, we investigated the impact of constraining only the Z degree of freedom or all degrees of freedom at once on the bottom of the muscle (Table 13). Tension in the Z direction of 2500 µm corresponding to 25% of the muscle length was applied on the top of the muscle. Macroscopic geometry was meshed with either C3D8 or C3D8R elements. Simulations output force-displacement curves at point RP which are then converted into engineering stress-strain curves.
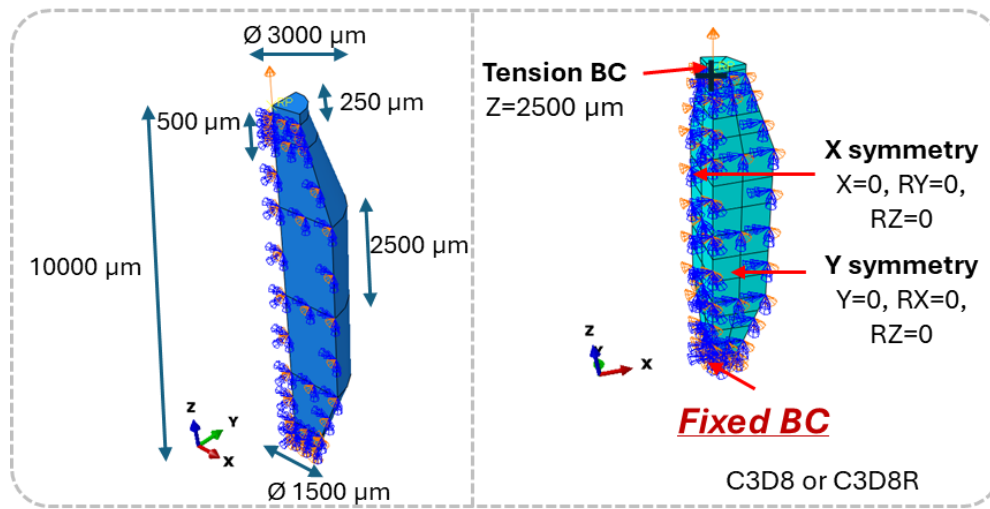
Figure 57. Quarter muscle geometry used to simulate uniaxial tension experiments. A displacement boundary condition was applied on top of the muscle. Another displacement boundary condition was applied at the bottom to remove motion on either a surface or a small volume, either along Z or along all degrees of freedom.

Influence of the macroscopic boundary conditions on the simulations. Figure 58 presents the resulting engineering stress-strain curves for the different boundary conditions. The results show a slight decrease in the measured force when constraining a surface. We assume this decrease is due to the increased length of free muscle volume in this case, which allows a better overall repartition of the imposed deformation. The constrained degrees of freedom had no impact on the force magnitude, however constraining all degrees of freedom made it more difficult for the simulations to converge. Macroscopic element type also had a very strong effect on the convergence, with models using C3D8 elements reaching a deformation below 50% of the performance of the model containing C3D8R elements.

Table 13. Simulation details for the investigation of boundary conditions.

Name	Integration	Geometry for bottom set	Constrained degrees of freedom	Max. normalized time of simulation
RI Vol Z	C3D8R	Volume	Z	1
RI Surf Z	C3D8R	Surface	Z	1
RI Surf XYZ	C3D8R	Surface	X,Y,Z	0,890
RI Vol XYZ	C3D8R	Volume	X,Y,Z	0,801
FI Vol Z	C3D8	Volume	Z	0,413
FI Surf Z	C3D8	Surface	Z	0,459
FI Surf XYZ	C3D8	Surface	X,Y,Z	0,245
FI Vol Z	C3D8	Volume	X,Y,Z	0,243

These conclusions have been drawn for a small parametric study using simplified geometry and only one set of parameters from the literature, and thus only provide hints for the final modeling solution. Moreover, the stress-strain curves in Figure 58 do not display the exponential behavior expected from a skeletal muscle, thus our parameters must be modified for the study of murine muscles. However, it shows the importance of boundary conditions choices on the overall model convergence. Therefore, more analyses have been conducted with a focus on model convergence, through boundary conditions choices, solver parametrization and mesh parametrization.
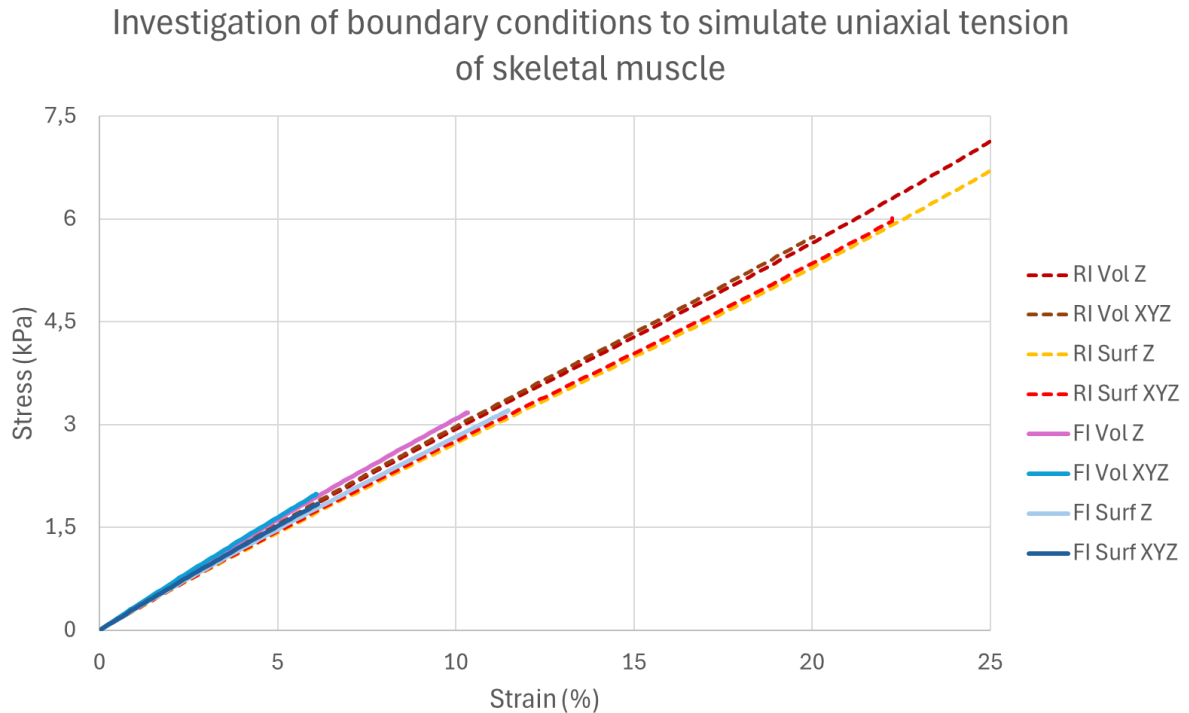
Figure 58. Resulting engineering stress-strain curves for the investigation of boundary conditions. Engineering stress in the tension direction as a function of strain in the tension direction.

3.3.4. Model convergence

The main disadvantage of the DFE² compared to standard FE method is its computational cost. Even using specialized computation stations and diverse strategies to reduce the model's size, the final model still includes many degrees of freedom to solve. Moreover, as anisotropic hyperelasticity is being modelled in this chapter, the resulting behavior is non-linear and behaving following an exponential tendency. These are the main characteristics of the developed model so far.

Every modeling choice will affect the overall model convergence. However, solver parametrization, mesh and behavior law are especially important regarding this matter. The choice of behavior law is conditioned by the available data regarding Klf10 KO and WT (healthy) mouse muscles and will be detailed further in this manuscript. Regarding mesh parametrization, we investigated the element type, the hourglassing control if appliable, and the element overall geometry earlier in this chapter. Thus, the current section mostly focuses on solver parametrization. In solver parametrization, we investigated the technique, the method, and the stiffness matrix storage.

A first parametric study was conducted on the solver parameters. The available **solution techniques** in ABAQUS® are **direct** (by default) and **iterative**. The direct technique solves the global stiffness equation system (Eq. 3.17) by using direct factorization (Lower-Upper or LU decomposition). It is

supposed to be more robust and to handle highly nonlinear problems well; however, it requires more memory. On the contrary, the iterative technique is based on domain decomposition and decomposes the FE model into subdomains where the stiffness equations are solved, with Lagrangian multipliers allowing the continuity between the subdomains. It is more memory efficient but less stable for complex nonlinear problems. Two **methods** are available for solving the stiffness equations: **full newton** and **quasi-newton**. The quasi-newton approximates the stiffness matrix K at each iteration then K is updated progressively, which speeds up the computation time at each iteration, and is useful for large models. On the reverse, the full newton completely recomputes K at each iteration, which provides better stability and a quadratic convergence, which results in less iterations per increment. The **stiffness matrix storage** can be chosen to be **symmetric** or **non-symmetric**. Symmetric storage requires less memory use but some behaviors such as anisotropy or certain types of contact generate asymmetric stiffness matrices, thus introducing convergence issues when using symmetric storage.

Table 14. Impact of solver configuration on the simulation convergence in a case study on simplified skeletal muscle. The solver configuration allowing for best convergence is highlighted in bold.

Method	Technique	Matrix storage	Max normalized simulation time
Direct	Full Newton	Symmetric	0.6975
Iterative	Full Newton	Symmetric	0.6625
Direct	**Quasi-Newton**	**Symmetric**	**0.7984**
Direct	Full Newton	Unsymmetric	0.6763

All the parameters described above are greatly influenced by the FE problem's linearity. As the muscle DFE² presents some non-linearities, however it is difficult to assess the smoothness of the overall FE problem. Therefore, different combinations of the solver parameters have been tested on a simplified DFE² muscle model in a short preliminary study (Table 14). The fusiform muscle geometry is similar to the previous section and is described in Figure 57. These models feature the quarter muscle geometry described in Figure 57, using reduced integration linear elements with hourglassing stiffness parameter of 2. Resulting engineering stress-strain curves are shown in Figure 59. Results indicate that the direct method in combination with the quasi-newton solver and symmetric storage provides the longest simulation time and thus the best convergence in that specific case (Table 14). No divergence of the results was observed in any configuration (Figure 59). The parameter that had the most influence on the convergence was the technique. However, we keep in mind that this is a short study conducted on one set of parameters and one geometry.
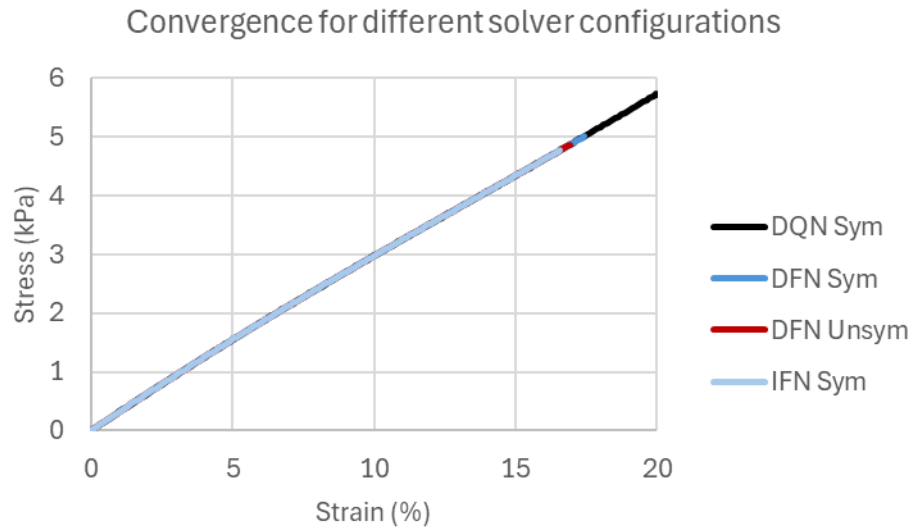
Figure 59. Engineering tress-strain curves obtained for the solver configuration investigation. D: direct; I: iterative; QN: quasi-newton; FN: full newton.

Further parameters were tested for model convergence, both in combination with a simplified and realistic RVE. Relevant parameters here include custom use of the line search algorithm in Abaqus® and custom increment controls. Description of all the tests in an exhaustive manner would be very long; therefore, they are not presented in this manuscript. The final solver configuration is summarized in Table 15.

Table 15. Initial model configuration chosen for the skeletal muscle multiscale analysis in chapter 5.

Chosen parameter	Impact on computation time	Impact on memory usage	Impact on precision	Impact on convergence
Eighth muscle geometry	Divided by a factor 8	Divided by a factor 8	No impact	No impact
C3D8R elements	Divided by a factor 8	Divided by a factor 8	Error linked to hourglass strategy	More stable
Direct method	No impact	Increased use	No impact	More stable
Symmetric stiffness matrix storage	Economy	Decreased use	Depends on the material	No impact
Quasi-newton technique	Economy	Decreased use	Less accurate	Less stable in strongly nonlinear problem

101

3.4. Conclusions of the method

In this chapter, we present the **adaptation of a numerical multiscale method (Tan et al., 2020) to a skeletal muscle geometry and hyperelastic anisotropic material**. We provide evaluation of the method for hyperelastic materials in large deformations. We also investigate the effect of boundary conditions, solver parameters and mesh strategies on the model convergence. **The results provide an overview of the abilities and limits of our modeling strategy, thus characterizing the bias we introduce due to our modeling choices**.

The developed method combines two different scales of a multiscale material in the same simulation, thus providing both information at the macroscale (homogenization) and at the microscale (localization). It is adapted to skeletal muscle geometry at both scales: the macroscale can contain a fusiform muscle geometry, while the microscale can be representative of a sample of skeletal muscle. Particularly, the macroscale model has been adapted as to simulate a uniaxial tension experiment. Moreover, the method has been validated for hyperelastic anisotropic material behavior. Model size reduction strategies and convergence strategies have been implemented and tested on simplified DFE² muscle models. The resulting choices are summarized in Table 15.

The developed method fulfills both of our main objectives: the decoupling of structural and mechanical properties at the microscale, and the need for localization. In this chapter, only the macroscale has been adapted to the skeletal muscle; therefore, a microscale RVE that is representative of the structural properties of mouse skeletal muscle needs to be developed, before combination with the DFE² method as here developed. It is this aspect that we will focus on in the next chapter, with a precise definition of the RVE, its geometry, the distribution of its constituents, and the implementation of behavior laws via an original transition approach. In the final chapter, we will compare the macroscopic aspects discussed here with the application of the resulting global model.

Chapter 4: Modeling the murine skeletal muscle at the microscale

As introduced in chapter 1, the Klf10 gene deletion induces significant morphological and mechanical effects at the microscopic scale (scale of the muscular fibers and ECM), which are not recovered at the macroscopic scale (whole muscle) (Tatarenko et al., 2024). This result suggests a compensation mechanism between those scales. To develop the multiscale model and go through these scales, we introduced in chapter 3 the DFE² method. Based on this method, **we present here the different steps to define the Representative Volume Element (RVE) at the microscopic scale.** We describe the 3D RVE geometry generation, as well as the identification and the assignment of the mechanical behavior of the microcomponents, the generation of a gradient on the mechanical properties between the microcomponents and the definition of the boundary conditions (Loumeaud et al., 2025b). Then, a parametric study is performed to investigate the influence of mechanical gradient properties, muscle fibers geometry and muscle fibers distributions on the response of the 3D RVE in tensile and shear loading.

The microscopic scale has been chosen as the lower scale for our homogenized model. The DFE² method allows to study the multiscale behavior of skeletal muscle, especially by including the influence of the ECM. In this method, the representative volume element (RVE) has to be representative of both the geometry and the mechanical behavior at the muscle microscopic scale. Three elements must be defined: (i) the components included within the RVE, (ii) their geometry, including the RVE boundary conditions, and (iii) their mechanical behavior.

Increasing the number of components at the microscale can be highly beneficial, but it also introduces a larger number of unknowns into the multiscale model, which in turn creates complex interactions between parameters. As a result, reliably identifying the values of all parameters becomes challenging, especially given the limited availability of experimental data. This lack of data constrains our ability to calibrate the model accurately and may compromise predictive reliability. The first step is meant to target components that are the most relevant for the skeletal muscle mechanical behavior by a reasoned choice of components and boundary conditions to take into account. In a second step, a geometry able to represent the changes induced by the Klf10 gene deletion should be defined for each of the previously selected components. Finally, for each component, a mechanical behavior law that includes physically interpretable parameters and corresponds to available experimental data has to be defined. This approach is described below, before carrying out a parametric study to analyze the influence of each of the parameters mentioned.

4.1. Selection of the muscular microcomponents

Components at the microscopic scale. The expression of the Klf10 gene has structural and mechanical effects on the muscle especially at the microscopic scale. Amongst the microcomponents, previously published results using *ex vivo* tests show that the muscle fibers undergo changes both in their structure and their mechanical properties. However, no significant effect of the Klf10 gene has been exhibited on whole muscles. On the contrary, as detailed in chapter 2, preliminary *in vivo* experimental results indicate a change in shear mechanical properties at the macroscale. This information points towards an adaptation of skeletal muscle components such as the ECM and its link

to muscle fibers (costameres). Both components are involved in force transmission at the microscopic scale, which happens through shear deformations in the muscle. Thus, we decided to represent muscle fibers, ECM and its link to muscle fibers (costameres) in our model.

Boundary conditions at the microscopic scale. Then, the boundary conditions between these elements and at the borders of the RVE have to be carefully defined. The former studies investigating Klf10 KO mice using imaging modalities at the microscopic scale exhibited structural changes but no tear or damage. Therefore, we consider here that all of these microcomponents are rigidly bound to each other. However, they may undergo different or excessive solicitations depending on the genotype. To observe microscopic solicitations in skeletal muscles we chose to use the Direct Finite Element Square (DFE^2) method. The DFE² method that we are using for our model is compatible with 3 kinds of boundary conditions (Table 16) at the borders of the RVE (Tan et al., 2020) that we have to take into account:

- Linear displacement boundary conditions, which correspond to the Voigt model, also called homogeneous Dirichlet boundary conditions;
- Traction or constant stress boundary conditions, which correspond to the Hill model, also called homogeneous Neumann boundary conditions;
- Periodic boundary conditions.

As detailed in chapter 1, the Voigt and Reuss methods for a composite provide bounds for the different component's mechanical parameters, independently from the geometry. The advantage from using these bounds in combination with the DFE² homogenization method is the localization. In our case, we want to simulate uniaxial tension experiments aligned with the fiber axis, and the Reuss model does not correspond to this loading configuration. For a uniaxial tension aligned with the fiber axis, the Voigt model provide exact results. However, in our model, although the macroscopic scale (*i.e.* the whole muscles) undergoes uniaxial tension, it results into complex loading at the microscale due to the muscle architecture. Periodic boundary conditions have been increasingly used in the literature for skeletal muscle models, especially combined with a numerical homogenization method (Kuravi et al., 2021a; Lamsfuss & Bargmann, 2022a, 2023; Sahani et al., 2024). It is an estimation and not a bound for the effective mechanical properties. Although it is more complex to set up than the Voigt and Reuss models, it is considered to be the best tradeoff between convergence and accuracy. Therefore, we chose to use periodic boundary conditions.

Table 16. Comparison of the Voigt, Reuss and periodic boundary conditions for the RVE in multiscale modeling.

Criteria/ BC type	Voigt	Reuss	Periodic
Applied quantity	Uniform strain (Dirichlet)	Uniform stress (Neumann)	Periodic displacement and anti-periodic traction
Plane stays a plane	Y	N	N
Applied deformation nature	Affine	Non-affine	Affine + periodic fluctuations
Bias in homogenized stiffness	Overestimates (upper bound)	Underestimates (lower bound)	Balanced
Setup complexity	-	-	+
Degrees of freedom	-	+	0
Solver stability	High	Moderate	Medium-high
Reliability in shear deformations	-	-	+

4.2. Geometry of the RVE

4.2.1. Geometry generation algorithm

The geometry at the microscopic scale is generated in the Finite Element (FE) software ABAQUS® SIMULIA (*Dassault Systèmes SE, Vélizy-Villacoublay, France*). Two successive algorithms are implemented (Figure 60A): firstly, a muscle cross-section image is manually segmented by the user, who also provides probability distributions regarding fiber type and ECM width. The user can also adjust additional input parameters related to the geometry, that will be described further below. A 2D geometry of the RVE is obtained from the manual segmentation (Figure 60B). Secondly, using a second algorithm the 3D geometry of the RVE, material and mesh controls are generated. Mechanical parameters are provided by the user. The geometry is also encoded in Fortran, thus allowing for the localization of each point in the geometry within the FE computation (Figure 60C). This feature is further developed in Section 4.3.4.

The key features of the geometry are: (i) its spatial periodicity, (ii) its rounded fiber corners, and (iii) its components distributions based on experimentally measured probabilistic distributions of the ECM width and the different types of muscle fibers (slow, fast). Lastly, an additional component named "*transition layer*", representing the costameres which separates the fibers and the ECM, is considered.
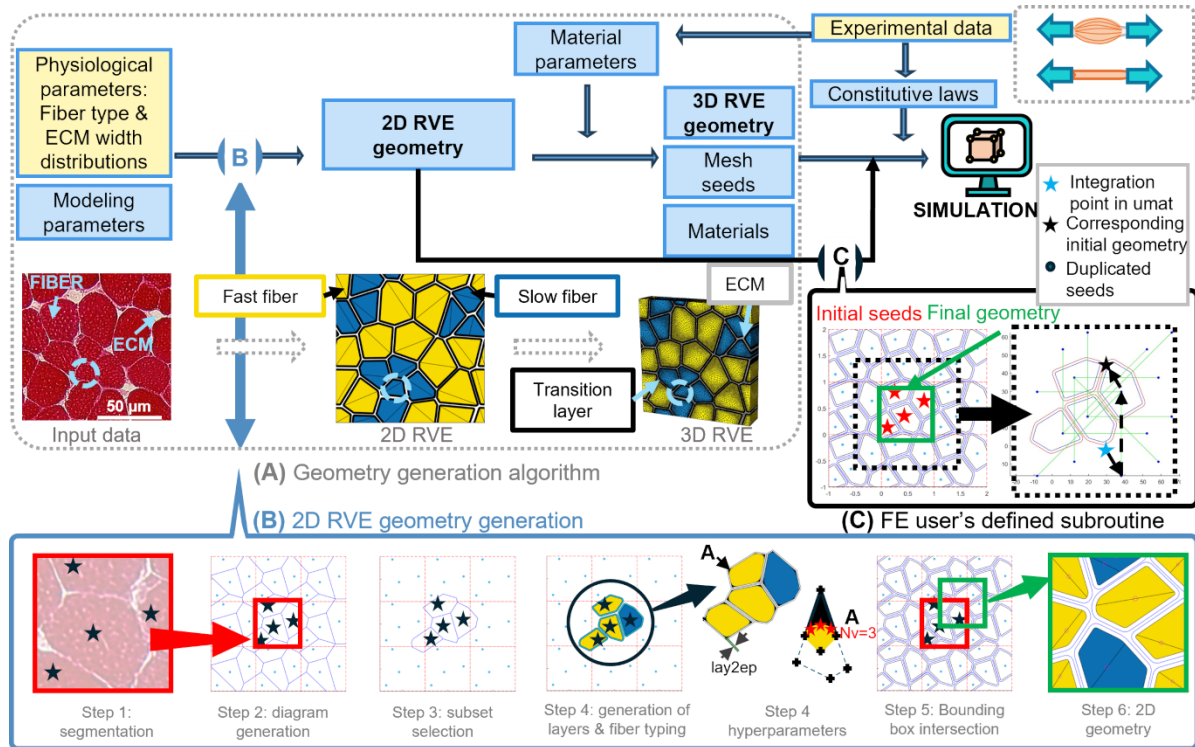
Figure 60. FE model generation: (A) workflow from a microscopic cross-section to a 3D RVE, (B) algorithm for the 2D geometry generation, (C) algorithm for the user subroutine adaptation (Loumeaud et al., 2025b).

The chosen approach consists in considering first a simplified 2D muscle cross-section with the hypothesis that the muscle fibers are locally straight and parallel to each other within the material. Since we chose to use periodic boundary conditions (PBC), the geometry must be periodic, and therefore we cannot directly segment a specific muscle cross-section. However, using a specific cross-section segmentation, it is possible to change the boundaries to obtain such a periodic geometry. To do so, the muscle cross section is assimilated to a Voronoï tessellation (Honda, 1978, 1983).

Considering the metric space $\mathbb{R}^2$ with the Euclidian distance function d, and (e_1, e_2) an orthonormal base, $P_{i,i\in[\![1,n]\!]}$ is a non-empty set of n distinct points in the space $\mathbb{R}^2$, called Voronoi seeds. The Voronoi cell or polygon F_i associated with the seed P_i is the set of all points $X = (x_1, x_2)$ in $\mathbb{R}^2$ whose distance to P_i is smaller than their distance to all seeds P_j different from P_i. The resulting polygons F_i are simple convex. The Voronoi diagram represents the partition of $\mathbb{R}^2$ using polygons F_i (Eq. 4.1).

$$F_i = \{(x_1, x_2) \in \mathbb{R}^2 | d((x_1, x_2), P_i) \leq d\left((x_1, x_2), P_j\right) \forall j \neq i\} \tag{4.1}$$

Restricting the space to a non-empty, convex and continuous part of $\mathbb{R}^2$ the square $[0; 1] \times [0; 1]$ is considered, where a set of seeds S$_i$ is defined. These are referred to as initial seeds. Considering the domain $[-1; 2] \times [-1; 2]$, the initial seeds are duplicated along e_1 and e_2. By computing a Voronoi diagram from the duplicated seeds P_i, a periodic arrangement of the geometry with respect to e_1 and e_2 can be obtained (Spyrou et al., 2019) (Figure 60B Step 2). In the remainder of the article, the polygons are referred to as fibers. The process for the generation of the 2D geometry is implemented based on several successive following steps, all illustrated in the Figure 60B:

Step 1: Segmentation. The first step corresponds to manual segmentation of Voronoi seeds corresponding to the fibers on a cross-section image of mouse skeletal muscle from an experimental histological process. The images used in this study were acquired at magnification x20 on a Leica optical microscope from 10 µm thin cross-sectional slices of mouse muscles (Kammoun et al., 2017). A fraction of this image is manually segmented, corresponding to the domain $[0; 1] \times [0; 1]$. The obtained seeds S$_i$ are duplicated in the domain $[-1; 2] \times [-1; 2]$.

Step 2: Generation of the Voronoi diagram and subset selection. A Voronoi diagram is generated from the duplicated seeds P$_i$ and modified to include the ECM. For this purpose, ECM widths are measured on the muscle image using a custom code developed in Matlab software (*Mathworks, Nattick, USA*).

Step 3: Subset selection. Then a kernel density estimation is applied to these measurements (Kotz & Balakrishnan, 1993) and used as probability distribution to draw values of ECM width for each edge in a specific subset of polygons F$_i$ of the diagram. The selected subset corresponds to the seeds S$_i$ and the step 3 guarantees the diagram's periodicity.

Step 4: Layers generation and fiber typing. The obtained polygons are shrunk individually by a constant value to obtain the transition layer. The polygons are now referred to as fibers and a phenotype (slow or fast) is attributed, from a probability distribution and knowing the area, based on the data published in (Kammoun et al., 2016).

Step 5: Bounding box intersection. At each vertex of the diagram, the geometry is sharp. Sharp angles will affect the convergence and the results of the FE simulation (Schmidt et al., 2009). Thus, these angles need to be rounded up. The round size is controlled by a parameter "$\mathcal{A}$" defining the removed surface from the fiber. The obtained overall geometry is intersected with a bounding box to generate the final periodic geometrical model.

Step 6: Continuity assessment. To be able to apply periodic boundary conditions (Michel et al., 1999) to the 3D model in ABAQUS® (Omairey et al., 2019), edges on the opposite side of the RVE must display the same number of nodes at identical position on the edges. Thus, mesh seed numbers are defined adequately at opposite edges of the RVE boundary.

From these 6 steps, the 3D geometry is generated and scaled (1 unit = 1 μm). Using the mesh seed assignments from the 2D algorithm, sets of edges and periodic mesh seed controls are generated using a specific python script implemented for ABAQUS.

4.2.2. Geometry generation through a probabilistic approach

Since segmentation of microscopic images does not provide a periodic microstructure, we approached the microstructure by positioning one point on each fiber to generate periodic Voronoi tessellations as shown above. On such a diagram, both the ECM width and the fiber type were generated using the probabilistic approach described below.

Fiber type attribution. We consider the data published in Kammoun et al., (2017), which presents the area distribution for each fiber type and the distribution of each fiber type for the skeletal muscles soleus and EDL. An example of both distributions is shown in Figure 61A for the WT soleus. The objective here is to compute the type of a muscle fiber on the Voronoi diagram, knowing its area. The fiber type is a discrete variable that, in our case, takes integer values between 1 and 3. The area of the fibers is a continuous variable that, in our case, takes values between 200 μm² and 2000 μm². We hypothesize that we can discretize the area variable into successive intervals of equal size, that we call *bins*. Let F be the random variable associated with the fiber type. Let A be the random variable associated with the fiber area. Let A_j be the probability of the fiber type being j, where j ranges from 1 to 3. Let A_i be the probability of the fiber area belonging to area *bin i*.

The published data (Kammoun et al., 2017) is the mean area with standard deviation of the fiber area per fiber type, so $P(A|F_j)$ if we consider a normal law.

The objective is to compute the fiber type, knowing the area, using the probabilities $P(F_j|A_i)$. Thus we compute $P(F_j|A_i)$.

$$P(F_j|A_i) = \frac{P(A_i|F_j) \times P(F_j)}{P(A_i)} \tag{4.2}$$

In equation (4.2), we know $P(F_j)$ from the published data (Kammoun et al., 2017). However, we do not know $P(A_i)$, which can be expressed as:

$$P(A_i) = \sum_j P(F_j) \times P(A_i|F_j) \tag{4.3}$$

We can also compute $P(A_i|F_j)$ by postprocessing the published data as follows:

$$P(A_i|F_j) = \int_{Ai} f_j \tag{4.4}$$

Where f_j is the density function associated to the normal distribution of the area associated to each fiber type.
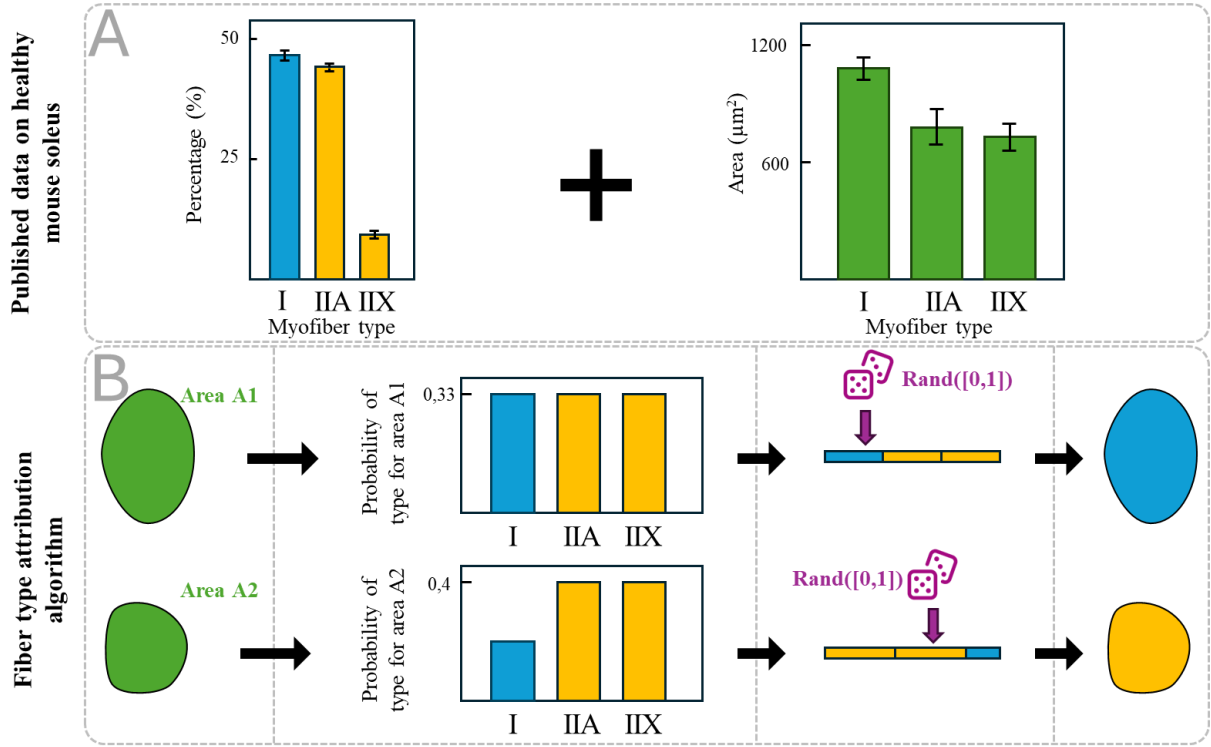
Figure 61. Fiber type attribution algorithm: example of probabilistic data and attribution of a type (I, IIA and IIX) to two different fibers. The probability of the fiber type knowing the area is precomputed. Then, knowing the current fiber's area, a random value is drawn between 0 and 1 (function Rand([0,1]), where each interval is associated to a fiber type.

In the code, we get access to two files containing the list of the *bins* and the associated probability values for each fiber type, knowing the area *bin i.e.* $P(F_j|A_i)$. First the area *bin* corresponding to the fiber is computed. Figure 61B displays an example for two fibers with different areas *A1* and *A2* that correspond to different area *bins*. Therefore, for each of them, a different distribution of fiber type probabilities $P(F_j|A_i)$ was computed. The sum of $P(F_j|A_i)$ over j being 1, a number is drawn between 0 and 1 using the uniform law. The domain $[0:1]$ is divided in 3 continuous domains numbered 1, 2 and 3; each proportional in size to the probability of the corresponding fiber type (Figure 61B). Depending on the subdomain the drawn number belongs to, type 1, 2 or 3 is attributed to that fiber.

ECM width attribution. The ECM width is segmented manually from muscle cross sections published in (Kammoun et al., 2017) (Figure 62). These measurements are divided by 1.5 to account for the portion of ECM represented in the transition layer. Then the variance and the inter-quartile range (IQR) of these series of measurements are estimated. A kernel density estimation is performed on the obtained data using Matlab function "*fitdist*" with the kernel option (Figure 62A), *i.e.* generating a new probability model to fit the measured data. The kernel option has been chosen as the segmented sample does not correspond to any parametric statistical law.

Several kernel function types are available in Matlab: normal, box, triangle and epanechnikov. The box and triangle kernel function were not chosen as they are less smooth, and the normal function was not chosen as it is continuous over $\mathbb{R}$, meaning that negative values of ECM could be obtained in the model. Finally, an epanechnikov (Bowman & Azzalini, 1997) kernel was used, with associated bandwidth:

$$BW = 0.9 \times \min\left(\sigma^2, \frac{IQR}{1.34}\right) \times size\left(\frac{sample}{1.5}\right)^{-\frac{1}{5}} \qquad (4.5)$$

108

Where BW is the bandwidth of the kernel function, σ^2 is the variance of the sample. This formula is known as the normal distribution approximation, Gaussian approximation, or Silverman's rule of thumb (Silverman, 1986). The limit to this approach is that this formula should be used with caution for densities not close to being normal. Factor 1.5 in Eq. 4.5. accounts for the portion of ECM contained in the transition layer. For each edge in the geometry, a random value is then drawn from the probability distribution, as shown in Figure 62B on two different edges.

Transition layer dimensions. The transition layer displays a constant width calibrated on the ECM width measurements. This width is controlled by parameter ep then computed as:

$$ep = 2 \times mean\left(\frac{sample}{1.5}\right) \qquad (4.6)$$

This guarantees that the ECM and transition layer will have similar dimensions, thus facilitating the 3D meshing of the RVE in the FE software.
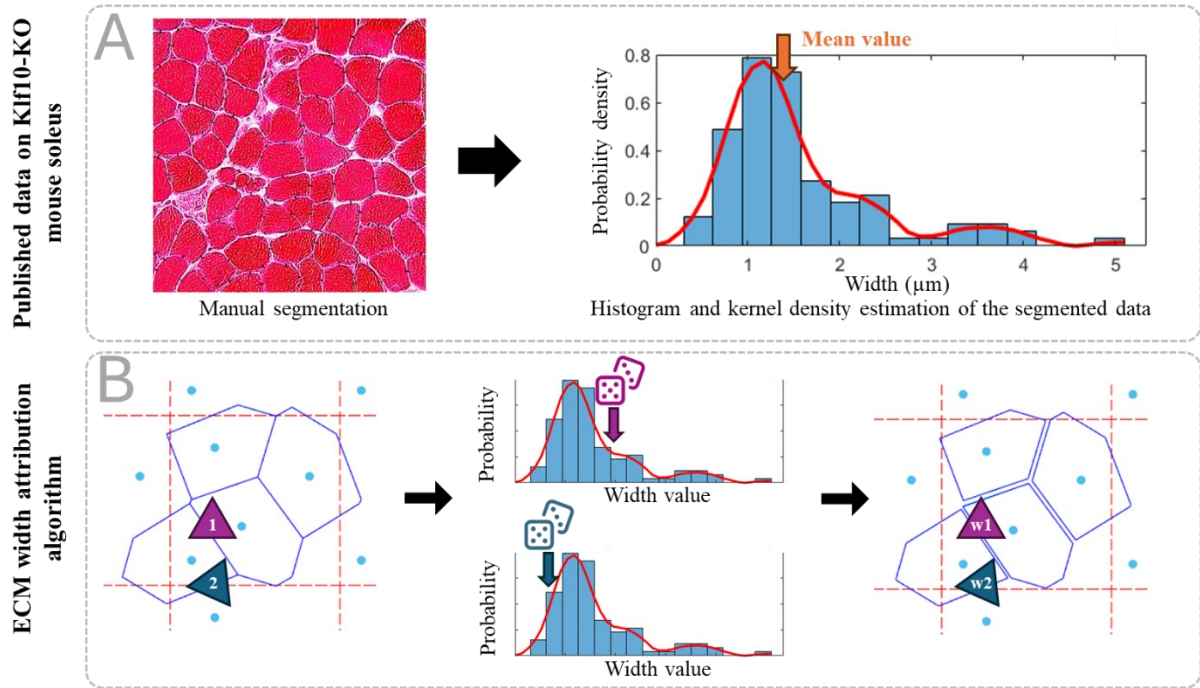
Figure 62. Edgewise ECM width attribution algorithm: example of probabilistic data generation and attribution of a width to two different edges.

4.3. Mechanical behavior laws at the microscale

4.3.1. Continuum framework and requirements for the FE software

Transversely isotropic hyperelastic materials are defined for the different microscopic components of the skeletal muscle. Many hyperelastic constitutive laws are described using the strain energy density functions Ψ, which can be a function either of the coefficients of the deformation gradient $\boldsymbol{F}$, or of the invariants $I_{i,i\in[\![1;8]\!]}$ of the right $\boldsymbol{C} = \boldsymbol{F}^T\boldsymbol{F}$ or the left $\boldsymbol{B} = \boldsymbol{F}\boldsymbol{F}^T$ Cauchy-Green deformation tensor (Chagnon et al., 2015; G. F. Smith & Rivlin, 1997).

When writing a custom User-Defined Material (UMAT) in ABAQUS®, several tensors must be upgraded at each simulation step: the Cauchy stress tensor and the tangent stiffness tensor. The Cauchy stress tensor $\boldsymbol{\sigma}$ is defined as:

$$\boldsymbol{\sigma} = \frac{2}{J} \boldsymbol{F} \frac{\partial \Psi}{\partial \boldsymbol{C}} \boldsymbol{F}^T = \frac{2}{J} \boldsymbol{F} \frac{\partial \Psi}{\partial I_i} \frac{\partial I_i}{\partial \boldsymbol{C}} \boldsymbol{F}^T \tag{4.7}$$

And the tangent stiffness tensor or consistent Jacobian $\mathbb{C}$ is introduced as:

$$\mathbb{C} = \frac{1}{J} \frac{\partial \Delta(J\boldsymbol{\sigma})}{\partial \Delta \boldsymbol{\varepsilon}} \tag{4.8}$$

With Δ being the Laplace operator. Both tensors were implemented in the open source UMAT published in (Castillo-Méndez & Ortiz, 2022a), and adapted for our use during this PhD thesis to the mechanical behavior law described below.

4.3.2. Mechanical behavior laws

Let us define the 1^{rst}, 3rd and 4th invariants of $\boldsymbol{C}$ as:

$$\overline{I}_1 = tr(\overline{\boldsymbol{C}}) \text{ where } \overline{\boldsymbol{C}} = J^{-\frac{2}{3}} \boldsymbol{C} \tag{4.9}$$
$$I_3 = J^2 = \det(\boldsymbol{C}) \text{ with } J = \det(\boldsymbol{F}) \tag{4.10}$$
$$\overline{I}_4^i = \boldsymbol{M}_i . \overline{\boldsymbol{C}} \boldsymbol{M}_i \tag{4.11}$$

$\boldsymbol{M}_i$ is a vector that defines the ith anisotropy directions in the material for $i \in \{1,2\}$.

We use the Holzapfel-Gasser-Ogden (HGO) model developed for fiber reinforced composites (Holzapfel et al., 2000), where the strain energy density function is written as:

$$\Psi = C_{10}(\overline{I}_1 - 3) + \frac{K}{2}(J-1)^2 + \frac{k_1}{2k_2} \sum_{i=1,2} \left(\exp^{\left[k_2(\overline{I}_4^i - 1)^2 \right]} - 1 \right) \tag{4.12}$$

and the Cauchy stress tensor, using the Eq. (4.7) and (4.11), is defined as:

$$\boldsymbol{\sigma} = 2C_{10}J^{-1} \left(\overline{\boldsymbol{B}} - \frac{1}{3}I_1\boldsymbol{I} \right) + K(J-1)\boldsymbol{I} + \frac{2k_1}{J} \sum_{i=1,2} \left((\overline{I}_4^i - 1) e^{\left[k_2(\overline{I}_4^i - 1)^2 \right]} (\overline{\boldsymbol{m}}_i \otimes \overline{\boldsymbol{m}}_i) \right) \tag{4.13}$$

In our case, $\boldsymbol{M}_i$ is computed in the plane $(\boldsymbol{X}, \boldsymbol{Z})$ with an angle $\pm\theta$ with respect to $\boldsymbol{Z}$ (Figure 64). k_1, k_2 are material parameters and $\overline{\boldsymbol{m}}_i = J^{-\frac{1}{3}} \boldsymbol{F} \boldsymbol{M}_i$. The material parameters for skeletal muscle from the literature (Liu et al., 2022) are reported in the next section 4.4.1 for the different components of the model at the microscale: ECM, fast fibers and slow fibers. The use of parameters identified on our own experimental data is considered in chapter 5.

4.3.3. Mechanical properties transition

One of the major originalities of our approach is to propose an "intermediate" transition zone representing the link between muscle fibers and ECM (costameres). We suppose in this manuscript that this component provides a mechanical continuum between the other components, in the shape of a gradient of mechanical properties. Over and above its benefits in terms of stability and continuity in numerical simulations, this transition zone, although still poorly understood in terms of its role in muscle mechanics, does indeed represent structural components of cellular micromechanics, fibrous zones surrounding muscle fibers and in contact with the ECM.

For this transition layer component, the algorithm (i) localizes the integration points in the geometry, and (ii) computes the distance of these points to their corresponding fiber (Figure 60C).

From this distance, a gradient in the mechanical properties is computed and applied to all mechanical parameters in the transition layer following Eq. 4.14 through 4.16 hereafter detailed.

The transition layer was tested with 3 different gradient shapes corresponding to a sigmoid function (Eq. 4.14), a linear function (Eq. 4.15) and a piecewise continuous function (Eq. 4.16). The mechanical properties vary between two bounds that are respectively the fiber and the ECM values, following these functions. The gradient functions belong to different differentiability classes and exhibit different derivatives at the contact points with muscle fibers ($x = 0$) and extra cellular matrix ($x = 1$). To integrate the gradient, an ABAQUS® subroutine was adapted from (Castillo-Méndez & Ortiz, 2022a).

$$P(x) = P_{Fib} - (P_{Fib} - P_{Mat}) * \frac{1}{1 + e^{-5*x}} \tag{4.14}$$

$$P(x) = P_{Fib} - (P_{Fib} - P_{Mat}) * x \tag{4.15}$$

$$P(x) = \begin{cases} \frac{1}{3}P_{Mat} + \frac{2}{3}P_{Fib} \text{ if } x < \frac{1}{2} \\ \frac{1}{3}P_{Fib} + \frac{2}{3}P_{Mat} \text{ if } x > \frac{1}{2} \end{cases} \tag{4.16}$$

In section 4.4, we will analyze which of these transition functions provides the most realistic microscopic mechanical behavior, and what impact this has on macroscopic muscle response.

4.3.4. UMAT adaptation to DFE²

FE software ABAQUS® implements the previously presented behavior law at the level of slow and fast fibers, the ECM and the transition layer, using a "UMAT" (*User-defined MATerial*) subroutine, that we have adapted from the literature (Castillo-Méndez & Ortiz, 2022a). The initial UMAT contained the tangent stiffness tensor and Cauchy stress definition for a fiber reinforced material containing one single anisotropy direction oriented in the (X, Y) plane following the HGO constitutive law described above (Holzapfel et al., 2000). **We implemented several contributions to this code: (i) the integration of a second anisotropy main direction, which is essential to represent the ECM; (ii) the differentiation between the different materials contained in the RVE; (iii) the localization of the integration points into the original RVE geometry** to be able to identify both the closest fiber boundary and its fiber type in the case of the transition layer material. Moreover, as we work with the DFE² method, the internal energy of the RVE has to match the internal energy of the macroscopic integration point. However, in the UMAT, we only have access to the microscopic integration point coordinates and its material name. Thus, there are two different ways to keep the internal energy balance: (1) scale the RVE dimensions for each macroscopic integration point before the simulation, and (2) keep the original RVE dimensions but scale the mechanical properties in the UMAT. Of these two equally effective approaches, the first one was used because of its greater ease of implementation. In practice, we relied on the use of 3D source codes, which we adapted (Zhi, Leong, et al., 2023).

A subroutine was written to identify the position of the integration point in the RVE geometry, and to return the fiber type, distance to the fiber and the dilatation coefficient associated with the RVE. It is articulated around several stages (Figure 63): knowing the position of all RVE in the model, one or several RVE containing the integration point (IP) are identified (Figure 63A). Through translation and dilatation, the subroutine maps the transition layer integration points (IP) to a "registration space", that fully describes the RVE geometry (Figure 63B.i.). From the registration space, the closest fiber to the integration point is identified (Figure 63B.ii.). Then the associated fiber type and distance to the fiber boundary can be retrieved (Figure 63B.iii.). This information is stored in 2 user-defined variables (Figure 63C); thus the integration points only go through the subroutine once, at the beginning of the FE simulation. In the geometrical scaling case, the different RVE in the multiscale model are all dilated in space by a certain scale factor. Thus, they may intersect each other, and this can lead to issues

identifying the RVE to which the integration point belongs, which is taken care of by repeating stage B for each RVE identified in stage A and taking a decision based on an error function in stage C of the implemented subroutine.
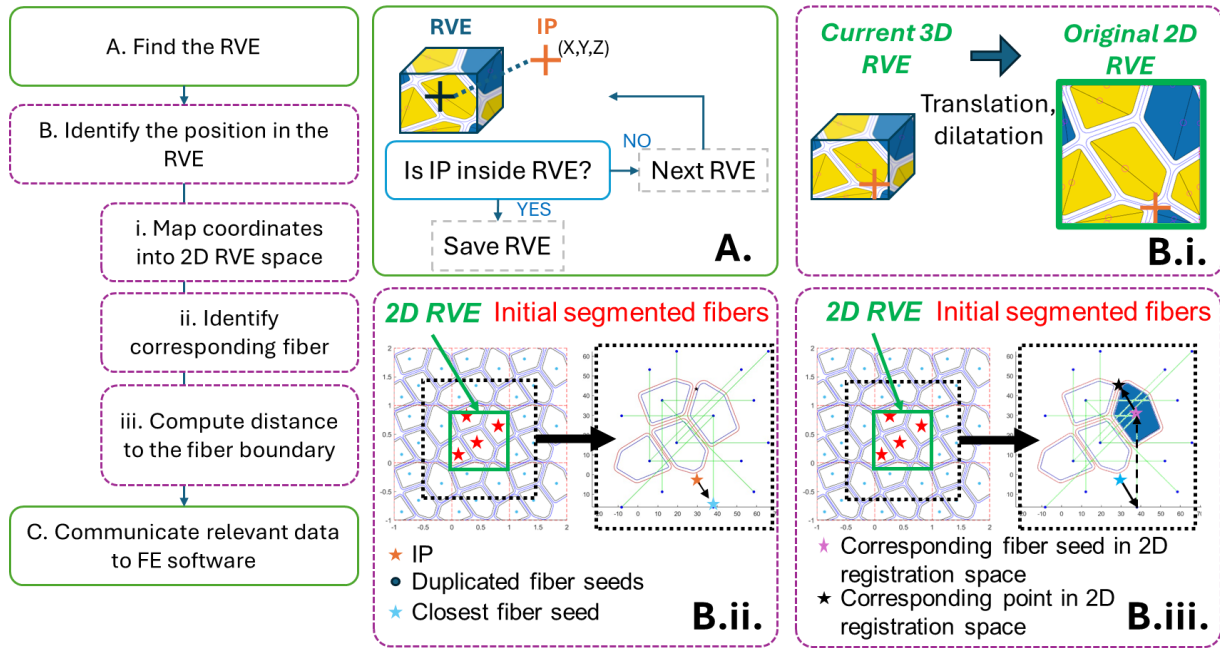
Figure 63. *Overview of algorithm associated with geometrical scaling.*

We have succeeded in implementing a microscale RVE taking into account custom distributions of geometrical features such as fiber geometry, fiber type, and ECM width. We take into account muscle fibers, ECM and its interface with muscle fibers (costameres). We have developed an algorithm allowing to identify the position and orientation of any point in the structure with respect to other components. All components can be modelled using a HGO constitutive law with 2 directions of anisotropy, which parameters can be modulated depending on the components and their orientation in space. This work has been published (Loumeaud et al., 2025b).

We now need to study the parameters and especially hyperparameters contained in all the algorithms and their influence on the behavior of this RVE before considering the transition to the macroscale of the complete muscle (chapter 5).

4.4. Parametric study on the 3D RVE definition

In this section, a parametric study is conducted on small RVEs of healthy soleus skeletal muscle. Indeed, we have introduced many assumptions and parameters to be able to build our RVE. We introduced too many geometrical and mechanical parameters for this parametric study to be exhaustive; however, we study the effects of important parameters, those controlling fiber rounding, the gradient of mechanical properties. Results are provided independently of fiber type, which effect is investigated separately.

4.4.1. Materials and method for the parametric study

Mechanical properties. The material orientations for the different components are defined in Figure 64. The parameters implemented for the different materials are summarized in Table 17. Those

parameters have been identified on porcine skeletal muscle experiments using a HGO-derived modelling framework (Liu et al., 2022). A ratio of 1.43 between fast and slow fibers was used (Tatarenko et al., 2024).

Table 17. Material parameters extracted from the literature for the ECM, fast and slow fibers (Liu et al., 2022) and implemented for multiscale model. (ECM: extra cellular matrix). Parameter C_{10}: Proportional to shear modulus of the proteoglycan matrix. Parameter K: bulk modulus. Parameter k_1: Collagen fiber mechanical behavior. Parameter k_2: Collagen fiber exponential behavior. Parameter ϑ: Angle for defining collagen fiber orientation using vector m_i.

Material	Parameter	Values
ECM	C_{10}^{m}	0.002 MPa
	K^{m}	0.170 MPa
	k_1^{m}	0.001 MPa
	k_2^{m}	1.33
	θ^{m}	±55.0°
Fast fiber	C_{10}^{ff}	0.0035 MPa
	K^{ff}	0.314 MPa
	k_1^{ff}	0.0018 MPa
	k_2^{ff}	1.5
	θ^{ff}	0.0°
Slow fiber	C_{10}^{sf}	0.0025 MPa
	K^{sf}	0.22 MPa
	k_1^{sf}	0.00125 MPa
	k_2^{sf}	1.5
	θ^{sf}	0.0°
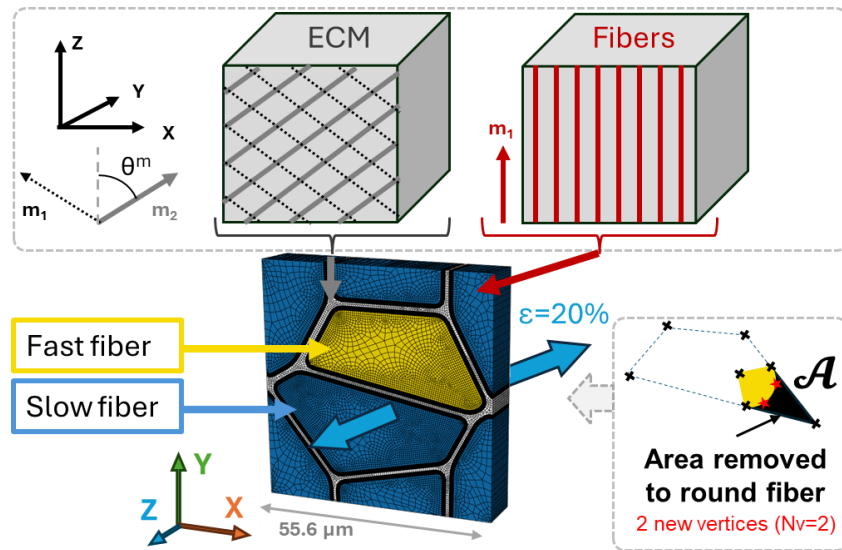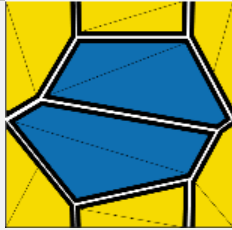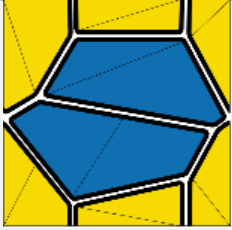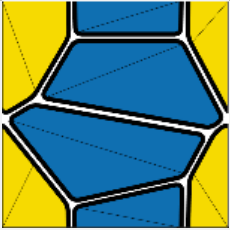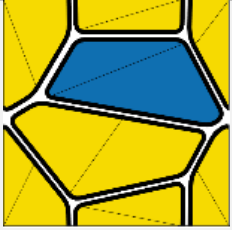
Figure 64. RVE definition: representation of the structural orientation of the materials (ECM, fiber), of the muscle geometry definition and applied loads.

The parametric study investigates successively the influence of:

- fiber area reduction due to rounded edges at the vertices of the Voronoi geometry;
- the interface gradient shape functions between fibers and ECM;
- the presence of multiple fiber types.

Geometry	P1	R1	R2	R3
Representation				
Number of elements [-]	125,460	128,490	112,335	137,655
Normalized area parameter "$\mathcal{A}$" [-]	0.0	0.6 10^{-5}	6 10^{-5}	12 10^{-5}
FVF [%]	94.5	94.5	94.0	93.5

Geometry. For this purpose, 4 variations of a geometry representing a square muscle cross-section with 4 muscle fibers were generated (Table 18). The geometrical distributions associated to the components are representative of a healthy soleus mouse skeletal muscle (Kammoun et al., 2017). Geometry differences were induced by varying the values of parameter "$\mathcal{A}$" (Figure 64) controlling the vertex sharpness. A sensitivity analysis has been conducted prior to the parametric study on the mesh density for elements C3D20R.

Loads and boundary conditions. A uniaxial tension generating 20% deformation is applied along the fiber direction Z (Figure 64). All boundary conditions were implemented using the ABAQUS ® Plugin EasyPBC ® (Omairey et al., 2019) that applies node-wise periodic boundary conditions as described in chapter 3, and prescribes displacements on ABAQUS ® Reference points to simulate uniaxial tension (Figure 65). As a result, surfaces parallel to Z axis both undergo a 10% deformation in the +/-Z directions respectively.
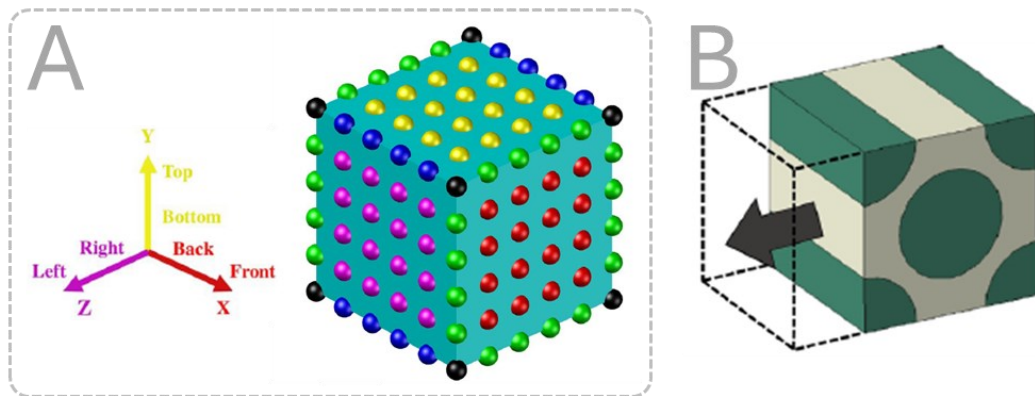
Figure 65. (A) Node sets for periodic boundary conditions and (B) boundary conditions applied for uniaxial tension in the Z direction. Adapted from (Omairey et al., 2019).

114

FE simulations. On each of the 4 geometry variations introduced in Table 18, we can analyze the influence of rounded edges at the vertices of the Voronoi geometry. Moreover, for each variation, we define several FE analyzes using different interface gradient shape functions between fibers and ECM as well as different distributions of fiber types. To study the influence of gradient properties at the interface between fibers and ECM and of parameter "$\mathcal{A}$", all fibers are assimilated to fast fibers, which exhibit harder mechanical properties that slow fibers. The influence of fiber type is analyzed separately, using the parameters that provided the best results in the rest of the study.

Outputs. From the simulation results, displacement at corner nodes was used to perform the mesh convergence study. In the parametric study, we look at the Cauchy stress tensor **S** components S11 and S33, representing the true stress acting on the deformed configuration. They correspond to the normal true stress in the **X** (transverse) and **Z** (axial) directions respectively.

4.4.2. Gradient of mechanical properties at the interface fiber-ECM

To compare different gradient shape functions, the transition layer is assigned different material properties as defined by the 3 gradient shape Eq. 4.14, 4.15 and 4.16, and respectively labeled EXP (exponential), LIN (linear) and PWC (piecewise continuous).

We want to avoid concentration of local mechanical stress. The greater the difference between the mechanical properties of two microcomponents, the greater the potential stress concentration at the interface. In fact, in order to best analyze the improvement brought about by the use of the transition layer, it is advisable to place oneself in the configuration where the latter plays the most important role. In this way, only fast fibers are considered in this section, as they display higher stiffness compared to slow fibers and ECM. These characteristics have a direct influence on mechanical stress concentration.

Differences in the Cauchy stress values and repartition over the RVE due to the gradient function have been observed in the different geometries and are compared on Figure 66. The piecewise continuous gradient created stress concentration and higher mean stresses on the different components in the RVE (Figure 66). Local stress concentration could also be observed using the linear gradient; however, the overall mean stress values (Figure 66B) and repartition over the RVE were not impacted and were similar to those obtained with the exponential gradient and the ECM material.
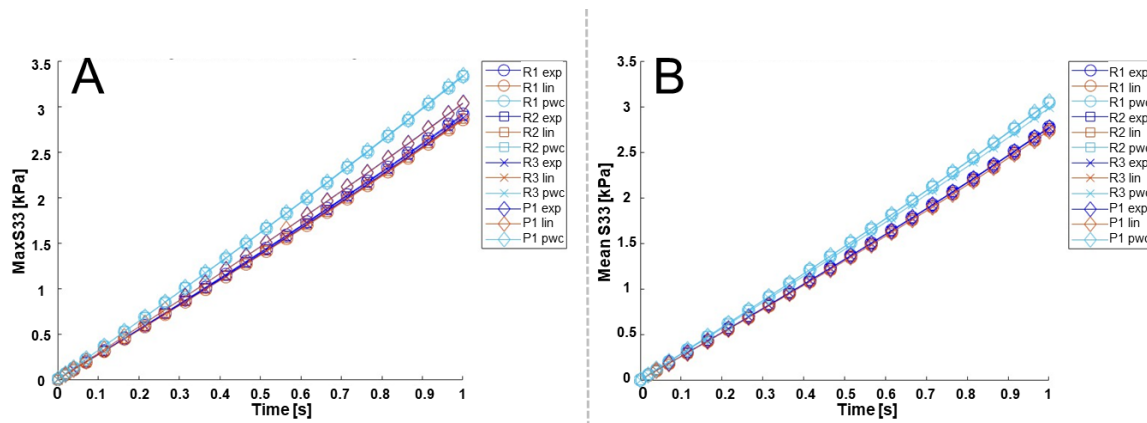
Figure 66. Comparison of the maximum (A) and mean (B) stresses on the ECM component's Cauchy stress S33 along direction Z, for different gradients applied to the different geometries described in Table 18. Four groups of three curves are plotted, representing the four geometries (P1, R1, R2, R3). For each geometry, the results were obtained for each of the three gradients (EXP: exponential, LIN: linear and PWC: piecewise continuous).

On the set of geometries and loads studied, the use of exponential and linear gradients shape functions provided better stress repartition than the simulations without gradients, avoiding non-realistic local stress accumulations. However, the displacement gradient created within C3D20R elements by the piecewise continuous and the linear shape functions seems too high and leads to stress concentration, whereas the exponential function does not have such an effect.

The use of an exponential gradient shape function also allows to decrease stress concentration compared to the same geometry without any gradients. This suggests that using an exponential gradient in the transition layer is an efficient means of decreasing numerical errors due to the transition between different materials. However, these conclusions are highly dependent on the mechanical properties. Another limitation is the use of the gradient on all mechanical properties, including anisotropic fiber reinforcement, whereas the costameres fibrous structure possesses an orientation orthogonal to the muscle axis, contrarily to the other components.

4.4.3. Impact of round geometry

In complement to the effect of interface gradient properties, the effect of rounded vertices was investigated. To this end, the geometries described in Table 18 were compared: geometry P1 has sharp vertices, whereas geometries R1 through R3 display rounded vertices with different values for parameter "$\mathcal{A}$" (Figure 64). Different concentration of constraints can be observed (Figure 67). Geometry P1 displayed slightly higher mean stress values in the RVE components than the rounded geometries. For both P1 and R1 geometries, the observed stress repartition displays stress concentrations. A more regular mesh in the transition layer was observed with higher values of parameter "$\mathcal{A}$", with elements parallel to the local fiber boundary. Higher values of parameter "$\mathcal{A}$" are associated with relaxation of the constraints, regardless of the gradient use. Additional constraint relaxation is also obtained when using the gradient.

Moreover, since the load is aligned with the muscle fiber's axis, the effect of geometrical variation is limited in that direction, however it becomes more important in the transverse direction. Thus, uniaxial tension of 20% in the transverse (in-plane) direction was also tested on all geometries, using the exponential gradient and no gradient, the transition layer being associated to the ECM material in the latter case (Figure 68). Similarly as for out-of-plane tensile test, it can be noted that more stress concentrations can be observed for this loading, and they decrease with increasing value of parameter "$\mathcal{A}$" and the use of exponential gradient.
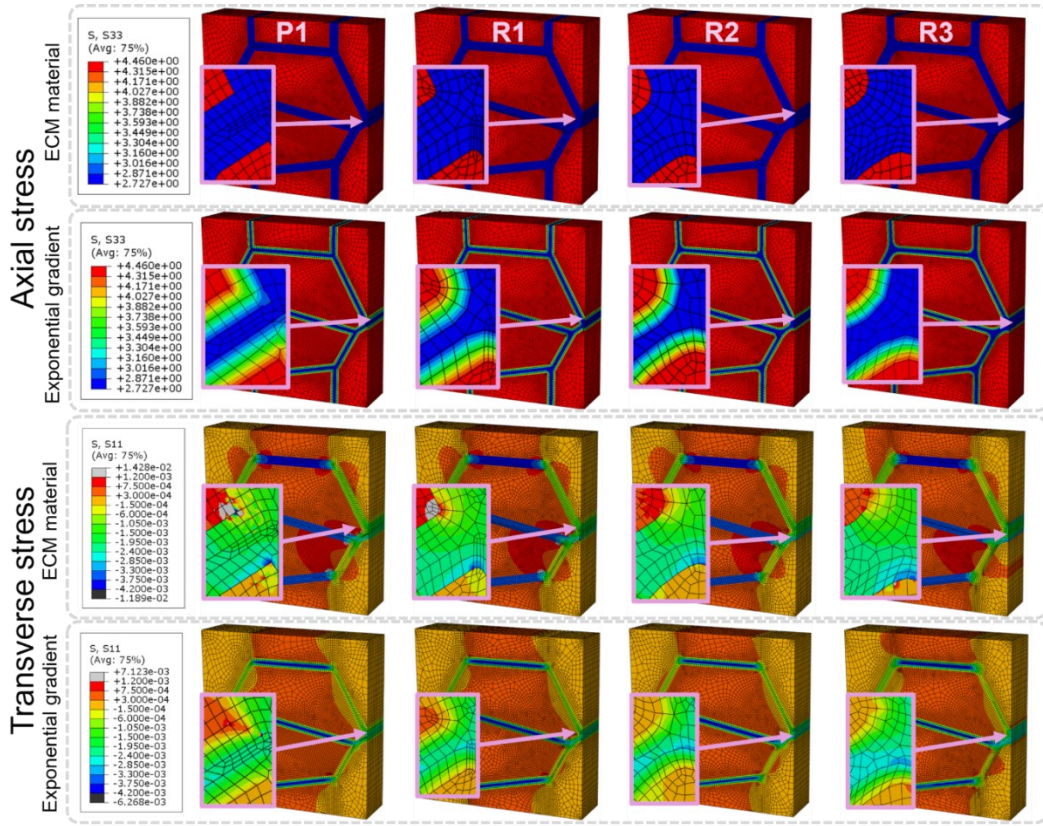
Figure 67. Comparison of the stress values (kPa) in tension (Z) and transverse (X) directions, on the different geometries subjected to axial tension when using an exponential gradient and in the absence of a gradient: grey values on scales indicate unrealistic stress values due to stress concentrations.
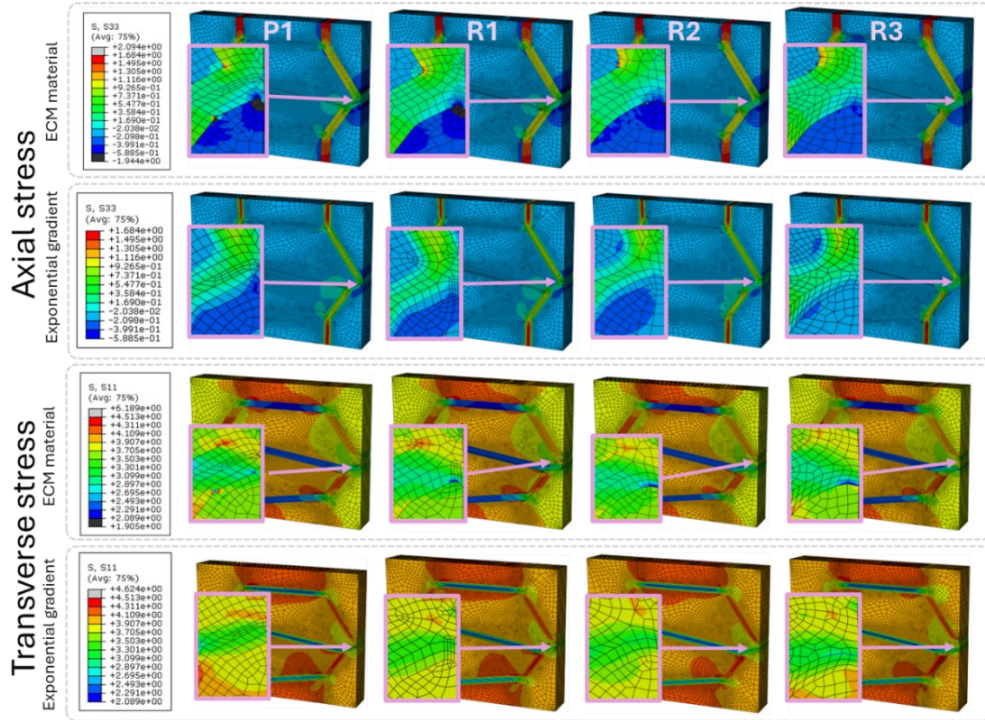
Figure 68. Comparison of the stress values (kPa) in tension (Z) and transverse (X) directions, on the different geometries subjected to transverse (in-plane) tension when using an exponential gradient and in the absence of a gradient: grey values on scales indicate unrealistic stress concentrations.

Thus, the proposed approach provides two ways of reducing numerical errors in the model, using both a rounded-up geometry and a gradient of mechanical properties.

The presented parametric study was performed using geometries whose fiber volume fraction (FVF) corresponds to healthy skeletal muscle. Interestingly, rounding up the geometry does not have a strong effect on the FVF; however it significantly decreases stress concentrations. This effect is predominant in the directions orthogonal to the muscle fiber's axis. Thus, it would be interesting to study these effects further on different loadings, such as out-of-plane shear loadings, which are naturally occurring in skeletal muscles and responsible for force transmission (Lieber & Binder-Markey, 2021).

4.4.4. Influence of fiber type

Finally, different fiber types have been attributed to geometry R3 (Figure 69), as this geometry displays the best results for stress repartition and is thus less sensitive to gradient or geometry-related concentrations of mechanical stress. This muscle is a slow muscle, thus here 3 slow fibers and 1 fast fiber have been generated from the distributions published in Kammoun et al. (2017). This example illustrates the functioning of this RVE generation algorithm in the case of a healthy muscle. An exponential gradient has been used. Smooth stress repartitions and results in agreement with the fiber types are obtained, for both axial (Figure 69) and transverse (Figure 70) loadings.
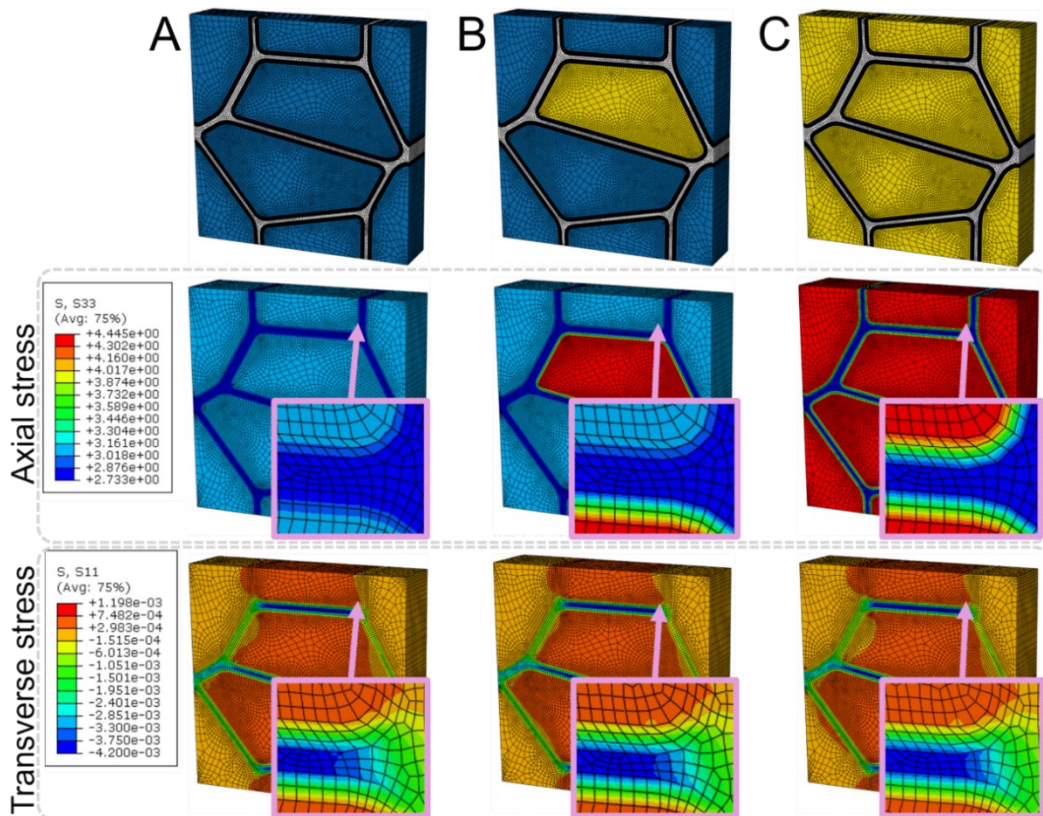
Figure 69. Comparison of the stress values (kPa) in tension (Z) and transverse (X) directions, on geometry R3 subjected to axial tension for different fiber type distributions: (a) 4 slow fibers, (b) 3 slow and 1 fast fibers, (c) 4 fast fibers. Slow fibers are represented in blue and fast fibers in yellow color in the upper scheme.

The algorithm successfully integrates different fiber types, allowing to model different muscle types. No effect of the fiber type was observed on the obtained results. However, no sensitivity study was conducted on the material parameters. In addition, due to a lack of data in the literature, the material

parameters were extracted from porcine experiments whereas the geometry was extracted from murine experiments.
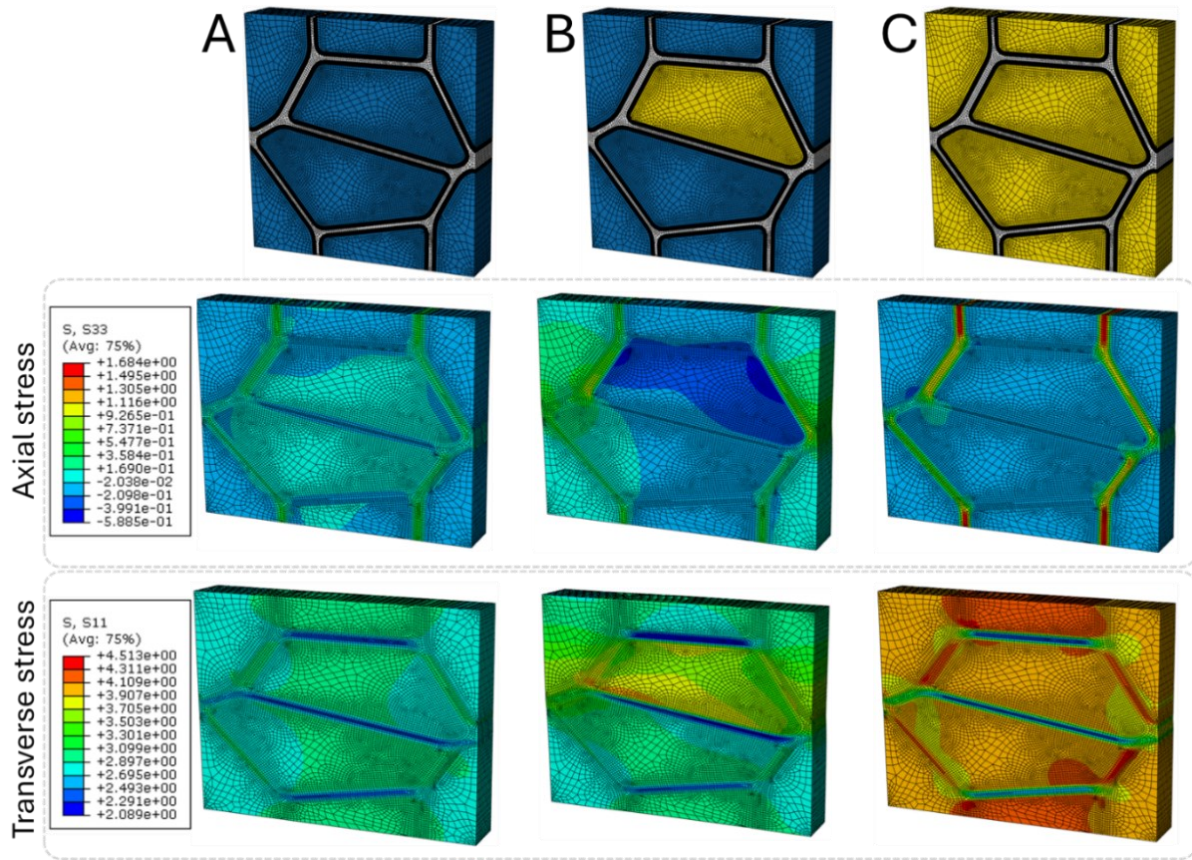
Figure 70. Comparison of the stress values (kPa) in tension (Z) and transverse (X) directions, on geometry R3 subjected to transverse (in-plane) tension for different fiber type distributions: (a) 4 slow fibers, (b) 3 slow and 1 fast fibers, (c) 4 fast fibers. Slow fibers are represented in blue and fast fibers in yellow color in the upper scheme.

4.5. Conclusion on the skeletal muscle model at the microscale

The original geometry generation algorithm introduced in this chapter can output either patient-specific (Sahani et al., 2024; Virgilio et al., 2015) or generic (Konno et al., 2021) muscle geometry, as controlled by a few input parameters. This feature allows the study of different muscle phenotypes. Moreover, the resulting geometry contains an additional component between fibers and ECM which is usually not represented in muscle models (Loumeaud et al., 2024; Virgilio et al., 2015) although being involved in pathological pathways (Sahani et al., 2022; Virgilio et al., 2015).

This algorithm provides 3D periodic RVE generation of skeletal muscle at the microscopic scale, that is compatible with the DFE² approach presented in chapter 3. It includes custom features that allow the representation of different muscle phenotypes, while providing features to address numerical issues. All components are modeled by a HGO behavior law (Holzapfel et al., 2000) which allows to represent fiber reinforced materials and provides structural and interpretable physical parameters. **Based on these results, the next step (chapter 5) is to assemble this RVE into the DFE² muscle model and to apply this to control and Klf10 KO muscles geometries and mechanical properties based on our own experiments (Kammoun et al., 2016, 2017; Tatarenko et al., 2024).**

Chapter 5: Investigation of the muscular ECM mechanical parameters and influence of the Klf10 gene through a multiscale modeling approach

5.1. Introduction

The objective in this thesis is to investigate the influence of the Klf10 gene on the overall multiscale biomechanical response. This primarily involves studying the difference between the two genotypes healthy (WT) and Klf10 KO (KO) within murine skeletal muscles. To this end, we decided, in parallel with the *ex vivo* tests previously carried out and the *in vivo* tests (chapter 2), to first create a multiscale numerical model, which must be able to take into account known experimental behavior (macroscopic for the whole muscle, microscopic for the muscle fibers) to compensate for the lack of data on the extracellular matrix (ECM). After presenting the contributions on the scale transition method (chapter 3) and the microstructure generation (chapter 4), these two aspects are combined to create multiscale muscle models representative of the two genotypes. This methodology allows to decouple geometric considerations from mechanical considerations.

Thus, in this chapter, the numerical investigation of the ECM mechanical parameters is described. We first demonstrate the ability of our approach to reproduce the macroscale behavior of a WT skeletal muscle. Then, we investigate its ability to find patterns in the parameter sets that distinguish the two genotypes (WT and Klf10 KO), allowing us to formulate hypothesis about the effects of the Klf10 gene deletion on ECM. As the model also provides information on the microscale tensorial fields, this step is linked with the analysis of not only the macroscopic but also the microscale stress field under macroscopic muscular solicitations. We expect our model to be able to provide such original features, but also to exhibit some limits and dependencies on hyperparameters as further developed in this chapter. Thus, we also discuss the potential solutions to overcome them.

5.2. Model parameters

As introduced in chapter 1, we base our current work on previously acquired experimental data on whole muscle and isolated muscle fibers (Tatarenko et al., 2024). This allows us to identify the main part of the parameters in our model using uniaxial tension tests on single muscle fibers. The remaining mechanical parameters are linked to the ECM, which is scarcely studied in the literature. Moreover, the existing literature about ECM mechanical properties is very heterogenous.

5.2.1. Muscle fibers parameters

The muscle fibers are considered as a neo-hookean matrix reinforced with one fiber family (the myofibrils), modeled using the HGO model (Holzapfel et al., 2000). All parameters were identified on previously acquired data (Tatarenko et al., 2024) using Nelder-Mead Simplex Method (Lagarias et al., 1998) (*fminsearch* function, *Matlab, Mathworks, Natick, MA, USA*) and we considered an incompressible material for the identification. The C_{10f}, k_{1f} and k_{2f} parameters were initialized with values of 3500 kPa, 180.44 Pa and 1.5043, respectively, as proposed in (Liu et al., 2022) and four constraints were imposed on the identification algorithm to ensure physical meaning and positivity for the parameters, as related in Eq. (5.1) through (5.4). In the end, the parameters given in Table 19 were

identified and implemented for the WT, Klf10 KO fiber FEM for EDL or soleus muscle, in addition to a Poisson's ratio of 0.49 to ensure quasi-incompressibility while allowing numerical compatibility.

$$C_{10f} \geq 1 \tag{5.1}$$

$$C_{10f} \geq \frac{C_{10}^{init}}{k_1^{init}} * k_{1f} \tag{5.2}$$

$$k_{1f} \geq 1 \tag{5.3}$$

$$k_{2f} \geq 0 \tag{5.4}$$

Table 19. Optimized parameters for muscle fibers

Single fiber extracted from slow (SOL) or fast (EDL) muscle	K (kPa)	C_{10} (kPa)	k_1 (kPa)	k_2 (-)
Soleus WT (SOL WT)	3739	37.637	6.00	1.1708
Soleus Klf10 KO (SOL KO)	5460	54.968	8.50	1.2488
EDL WT (EDL WT)	4944	49.774	7.00	1.2500
EDL Klf10 KO (EDL KO)	2666	26.836	3.69	1.1789

Uniaxial tension of single muscle fibers was simulated in Abaqus. The experiment consists in imposing a displacement equal to 50% of the initial's muscle fiber length (Figure 71). The muscle fiber geometry was considered cylindrical and dimensions were taken from (Tatarenko, 2023).
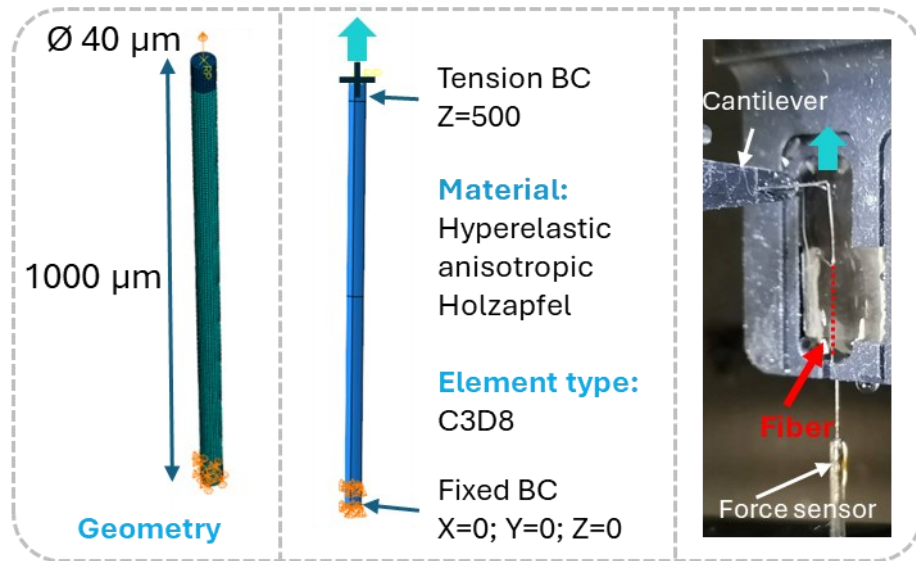
Figure 71. Numerical model and boundary conditions to model muscle fiber uniaxial extension.

As discussed in chapter 1, both soleus and EDL muscles contain fast and slow fibers, despite being respectively a slow and a fast muscle. For further simulations, it is assumed that the parameters obtained for the fibers in this section correspond to slow fibers in soleus and fast fibers in EDL. Moreover we consider a stiffness ratio of 1.43 between the mechanical parameters of fast and slow fibers (Tatarenko et al., 2024). The muscle fiber parameters being fixed, the objective is to identify parameters corresponding to the ECM material.

Final stress-strain curves are presented in Figure 72 for the four combinations of identified parameters for the four fibers configurations (fast and slow, WT and KO), compared with the corresponding experimental curves. Although small discrepancies can be observed beyond 30% deformation, these remain minor compared with experimental measurement errors, and whether for

small or large deformations, the identified behavior laws seem particularly well suited to reproduce the tensile behavior of the muscle fibers in question. This allows us to set the behavior law parameters subsequently used for the microscopic part concerning muscle fibers, based on experimental tests previously developed within our team.
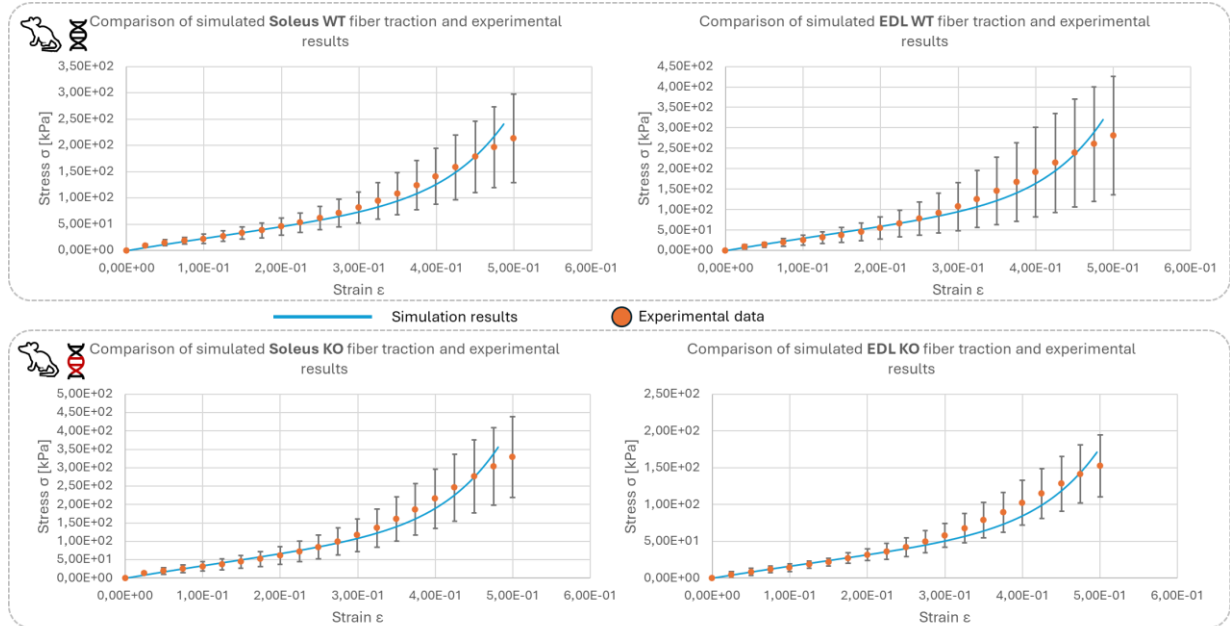
Figure 72. Engineering stress-strain curves representing single muscle fiber uniaxial tension up to 50% of their initial length. Numerical simulations are compared to experimental data for 2 genotypes (WT, KO) and two fiber types (slow: SOL, fast: EDL).

5.2.2. ECM parameters

Here, we seek to establish the orders of magnitude for the ECM parameters and use them as a starting point for initializing their identification by our multiscale model for the cases concerned here.

The constitutive law for the different constituents is the HGO model (Holzapfel et al., 2000), which considers an isotropic neo-Hookean matrix reinforced with two fiber families, representing myofibrils in muscle fibers, and collagen fibers in ECM. The transition layer is supposed to be isotropic and therefore the gradient of mechanical properties (as defined in chapter 3) is only applied to the parameters K and C_{10}. The Poisson's ratio ν has been fixed to a value of 0.49, to provide a tradeoff between quasi-incompressibility and numerical stability. Thus, the bulk modulus K is linked to the shear-related parameter C_{10} through the following equation:

$$K = \frac{4*C_{10}(1+\nu)}{3(1-2\nu)} \tag{5.5}$$

As presented in chapter 1, the parameter θ defining the orientation of the collagen fibers within the ECM in regard to the main muscle axis is admitted to be in range 55° to 59° in healthy muscle, confirming observations ranging from 34° to 55° in compression and 55° to 73° in tension in bovine skeletal muscles (Purslow & Trotter, 1994). Since we only consider uniaxial extension, we chose to vary parameter θ from 55° to 73°.

However, very few studies have quantified the mechanical properties of ECM, even more scarcely using the HGO model parameters (Gasser et al., 2006; Holzapfel et al., 2000; Kailash et al., 2024; Lanzl et al., 2024). These studies and the associated parameters are listed in Table 20. Amongst those studies, even fewer consider murine ECM (Kailash et al., 2024). Since these large deformation models are so underdeveloped, we will rely on these values for the remainder of our study but will adapt them

to those proposed for muscle FEM and using the linear small deformation characterizations of ECM proposed in the literature.

Table 20. Literature review of studies using the HGO models to fit ECM response within biological soft tissues.

Study	Tissue	C_{10} [kPa]	k_1 [kPa]	k_2 [−]	Deformation	Solicitation	Geometry
Gasser et al., 2006	Iliac adventitia (human)	7.64	996.60	524.60	45 %	FE inflation and tension	Parallelepiped
Holzapfel et al., 2000	Rabit carotid adventitia	0.3	0.56	0.71	-15 to 15% shear	inflation and torsion	Cylinder
Holzapfel et al., 2000	Rabit carotid media	3	2.36	0.84	-15 to 15% shear	inflation and torsion	Cylinder
Lanzl et al., 2024	Adipose human ECM	0.00947	0.4293	11.60	15% stretch, 50% shear	FE biaxial tension and simple shear	Parallelepiped
Kailash et al., 2024	6-month-old female mouse elastic artery ASC	8.29-62.1	8.43-62.5	0.10-1.19	50%	Inflation	Cylinder

In muscle multiscale modeling, the ECM is more often considered as an isotropic neo-hookean material. Values for ECM shear modulus span across a large range of values. In the subset of multiscale models considering anisotropic ECM (Bleiler et al., 2019; He et al., 2022; Kuravi et al., 2021a; Kuravi et al., 2021b; Spyrou, 2020; Spyrou et al., 2017, 2019), the values for ECM shear modulus are comprised between 7 and 57 kPa.

ECM Young modulus or shear modulus values have also been measured in the literature (Table 21). The two ranges of values are comparable but span across several orders of magnitude. Regarding this parameter, our group recently published preliminary results of a study in which ECM patches have been indented using an AFM setup (Dupres et al., 2025). The obtained values are coherent with other measurements from the literature (Camman et al., 2023; Lloyd et al., 2022; Pavan et al., 2020). Thus, as a first approach, we consider large ranges of values (Table 22) for the initialization of the identification of our ECM simulation parameters. Afterwards, the obtained parameters for the ECM are compared to the experimental values in literature.

Table 21. Literature review of proteoglycan ECM stiffness values with a focus on skeletal muscle. E: Young's modulus, G: shear modulus, G': storage modulus.

Study/Author	Tissue Type	Param.	Value (kPa)	C_{10} (kPa)	Method
(Pavan et al., 2020)	ECM-derived hydrogels	E	40-650	6.66-108.3	Tensile testing
(Camman et al., 2023)	Hydrogels engineered with variable proteoglycan porosity and anisotropy to mimick skeletal muscle	G'	1–10	0.5-5	Shear oscillatory measurements
(Camman et al., 2023)		E	25.1 ± 9.6	4.21 ± 1.6	Tensile test
(Lloyd et al., 2022)	3D murine skeletal muscle	G	20	10	Quantitative micro-elastography (QME)
Our preliminary results (Dupres et al., 2025)	ECM patches on murine muscle fibers	E	216-1188 (702.2 ± 486.2)	36.2-199.3	Atomic Force Microscopy (AFM)

Table 22. Parameters to be identified using simulations and corresponding initial value ranges.

Parameter	Component	Value range (kPa)	Interpretation
C_{10}	ECM	1.1-200 kPa	Proportional to shear modulus of the proteoglycan matrix
k_1	ECM	0.56-997 kPa	Collagen fiber mechanical behavior
k_2	ECM	0.1-525	Collagen fiber exponential behavior
θ	ECM	55-73	Angle for defining collagen fiber orientation using vector m_i

5.3. Application to the study of ECM in the context of Klf10 gene investigation for soleus muscle

We have seen that the Klf10 gene has implications not only for the biomechanics of muscle fibers and potentially the ECM, but also for the architecture and geometry of these microscopic components. It is therefore essential to take this into account in the model described here before proceeding with the complete simulation of skeletal muscle with or without gene expression.

5.3.1. Geometries

Macroscale geometry. The chosen soleus macroscale geometry is an idealized fusiform muscle geometry (Figure 73) which measurements are adapted from (Tatarenko, 2023). The shape is not cylindrical as to capture potential shear effects in the portions where the muscle section is reduced. Simplification consists in assuming 3 central axes of symmetry, exploited first of all to reduce the model's size (even if the extension to a more realistic geometry from anatomical high-resolution MRI is planned as a further perspective for this work). The model contains 30 C3D8R elements.
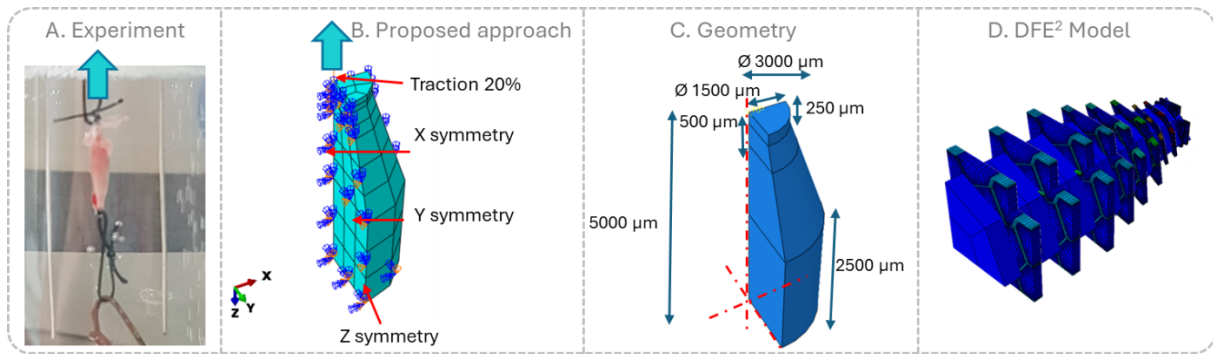
Figure 73. A) Macroscale uniaxial tension experiment on whole muscle, with imposed displacement and resulting force measured using a force sensor. B) Simplified macroscale boundary condition parametrization on C) an idealized muscle geometry resulting in D) a quarter muscle DFE² model.

Microscale geometry. Two pairs of soleus muscle microscale geometries, each containing 1 healthy (WT) and Klf10 KO (KO) geometry, were generated. We refer to these pairs as *set 1* and *set 2*, each containing one WT and one KO geometry. Set 1 was used for parameter set identification, and set 2 was used to perform parameter set evaluation. They were generated using the algorithm introduced in chapter 4 section 4.2. The segmentation was performed manually on randomly chosen microscopic cross-section portions (Figure 74). The final geometries used for investigations in soleus muscle resulted from a compromise between RVE dimension and numerical model size.
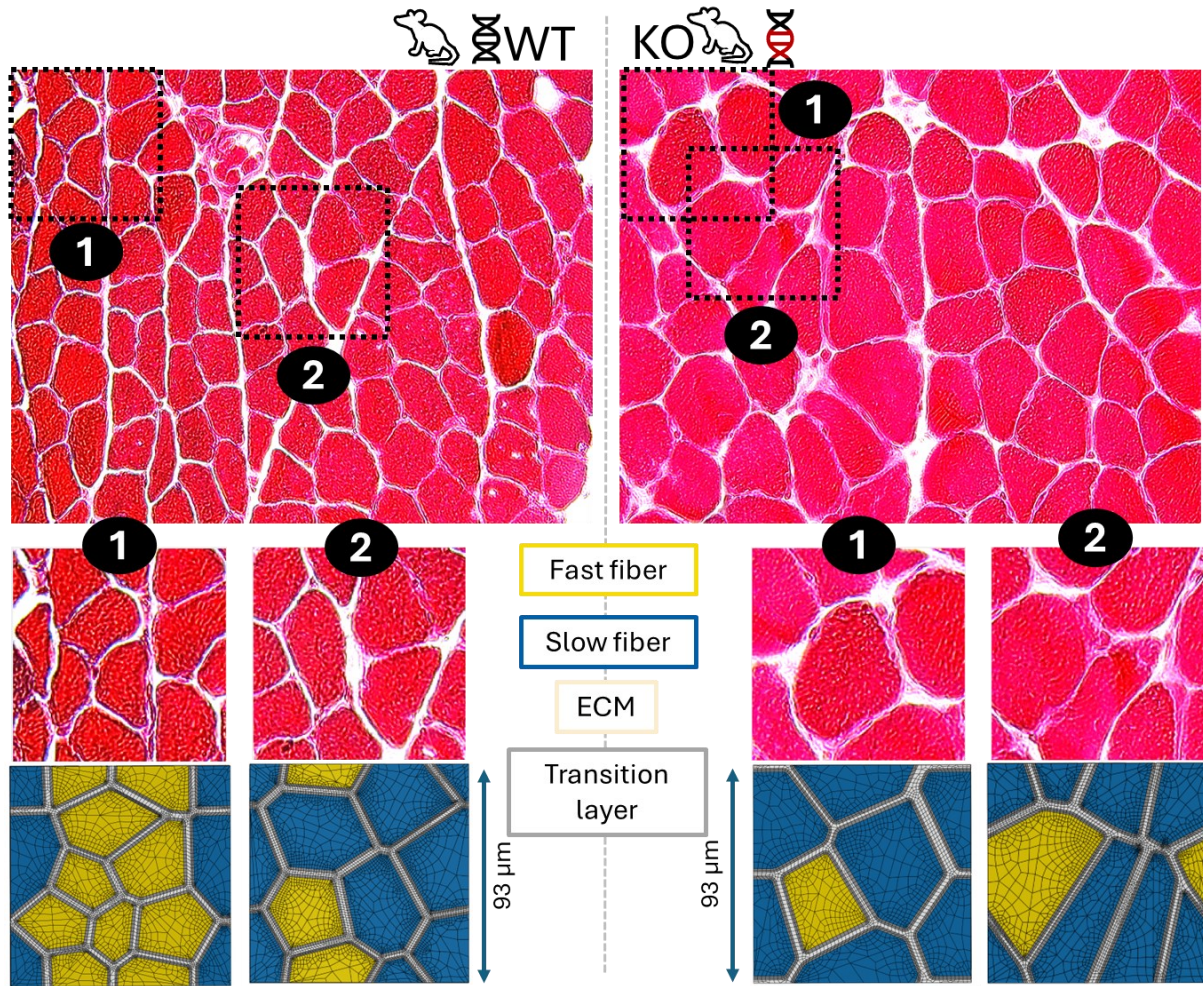
Figure 74. Sets of microscale geometries used for parameter identification.

We considered non-cubic RVE, with a depth representing 10% of its width, thus being closer to the assumption of local parallelism between the fibers. This helped reduce the number of mesh elements with the RVE and thus the global model size. The same physical dimensions of 93*93*9.3 µm were chosen for both Klf10 KO and WT RVE in the two sets, and the geometries were generated using the parameters presented in Table 23. Different parameters were arbitrarily chosen to round up the RVE edges for each genotype (area of 0.052 µm^2 for WT vs 0.26 µm^2 for KO), as Klf10 KO muscles showcase hyperplasia and therefore corresponding RVE contain about twice less muscle fibers than their healthy counterpart. Mesh parameters were the same for all models and adjusted to obtain adequate mesh and convergence results within the Abaqus® software (Figure 75).
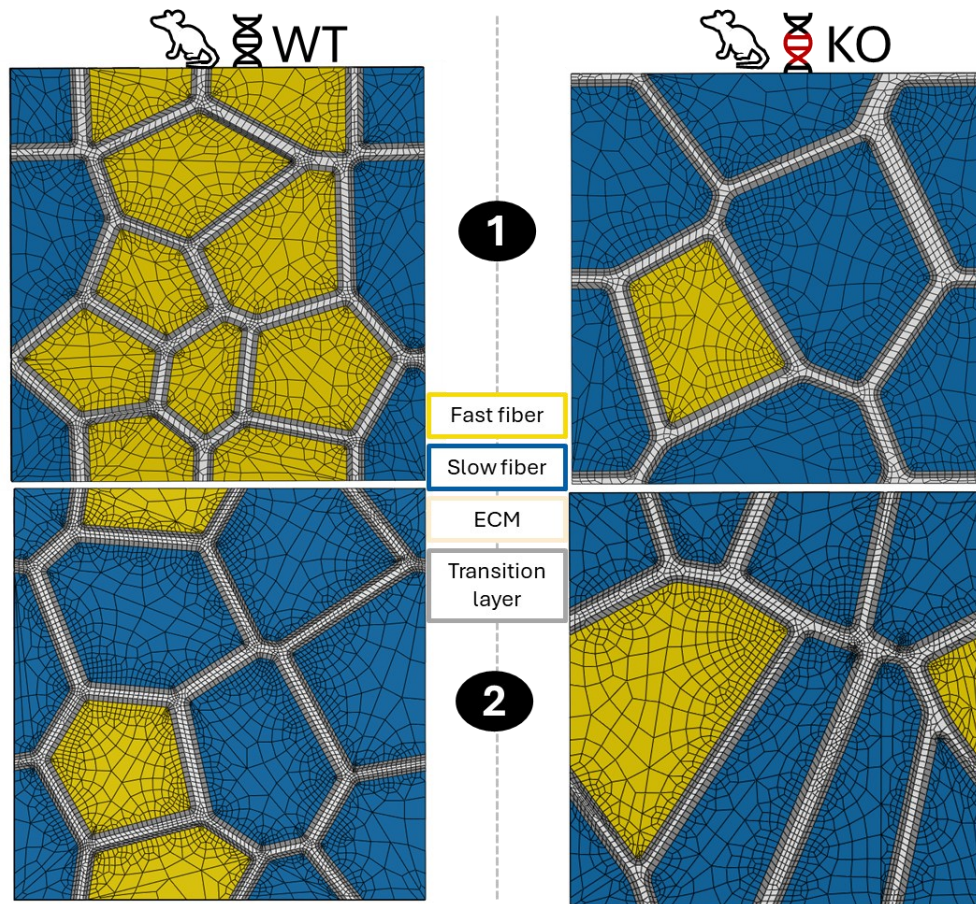
Figure 75. Mesh of both microscale geometries sets.

In Set 1, the KO RVE contains 5 fibers whereas the WT RVE contains 11. Set 2 displays 7 fibers for the WT RVE and 5 for the KO RVE. The repartition of fiber types and ECM is different in both sets; however, the same dimensions were used. The macroscale geometry is unchanged. By using the method developed in chapter 3, both scales are combined in a single model. The model containing the Klf10 KO microscale RVE is referred to as KO model, in opposition to WT model.

Table 23. Characteristics and main parameters for both sets of microscale geometries (further details in chapter 4 section 4.2).

Criteria	RVE WT set 1	RVE WT set 2	RVE KO set 1	RVE KO set 2
Characteristics				
Number of fast fibers [-]	8	2	1	1
Number of slow fibers [-]	3	5	4	4
Number of mesh elements [-]	19790	23755	12780	15930
Fiber Volume Fraction (FVF) [-]	0.90	0.91	0.91	0.91
Parameters for 2D geometry generation				
Area parameter [μm^2]	0.052	0.052	0.26	0.26
Portion of initial image [-]	1/3	1/3	1/3	1/3
Number of additional vertices to form a round	2	2	2	2
Mesh parameters				
Mesh density for ECM and transition layer	30	30	30	30
Mesh density for muscle fibers	18	18	18	18

5.3.2. Identification of the ECM mechanical parameters

Our objective is to evaluate the influence of our various model mechanical parameters related to ECM and identify the sets of values that yield macroscopic mechanical tensile responses similar to those obtained experimentally. To achieve this, beyond initializing these parameters using values from the literature as those obtained by the research team using AFM, they must also be identified through a multiparametric study conducted over fixed ranges and with representative sampling, since these parameters may be interdependent. Thus, in order to optimize the number of simulations required, it is important to use a robust sampling method.

Latin Hypercube Sampling (LHS) is a sampling technique that ensures efficient coverage of the input parameter space (Shields & Zhang, 2016; Stein, 1987). Unlike simple random sampling, which may cluster in some regions and leave others sparse, LHS divides each input variable's range into equal probability intervals and samples once from each interval. The samples are combined in a way that maximizes diversity and parameter space-filling (Figure 76).

The main steps for LHS implementation are: (1) to divide the range of each variable into *n* equally probable intervals; (2) to randomly sample one value from each interval for each variable; (3) to shuffle the sampled values for each variable independently and combine them so each sample has a unique value from every variable's interval. LHS is especially useful for reducing the number of simulations needed while still capturing the variability across all dimensions, thus it is used in design of experiments and sensitivity analysis (Afzal et al., 2017).
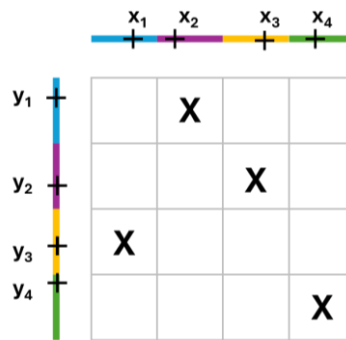
Figure 76. Simplified explanation of LHS using $n = 2$ variables x and y to generate, for instance, 4 sets of parameters.

The LHS method was a good candidate for our model, fulfilling the subsequent requirements:

- Explore the large ranges of parameter values with few simulations,
- Provide insights on local minima of a function which is not explicit, and therefore cannot be subjected to a gradient-descent algorithm,
- Provide parameters sets for the simulations without a nested loop, allowing the user to manually control the simulations and the result post-processing.

We used LHS sampling for manual definition of the parameter ranges concerning the $n = 4$ parameter sets, namely C_{10}, k_1, k_2 and θ (*lhsdesign* function, *Matlab, Mathworks, Natick, MA, USA*).

Error metrics. We consider the curve resulting from simulation of uniaxial tension tests of murine skeletal muscles up to 20% deformation. Three error measurements are computed to compare all simulations, to compare different phenomena occurring within the model. Based on preliminary observations, we arbitrarily decided to separate the curves in three distinct parts (Figure 77), that we name *small*, *medium* and *large* deformations. This separation results from two observations made from preliminary simulations that are not presented within this manuscript: (i) up to 6% deformation, the muscle fibers uniaxial tension curves match the whole muscle uniaxial tension curves, and (ii)

convergence of the model until 12% deformation is attainable, and divergence may occur past this value.

For these reasons, a single mean error is computed and analyzed on each of the three segments independently, to be able to compare all the simulations and investigate the effect of the different parameters on each deformation stage separately. This error is a root mean square error (RMSE) computed on a 3rd degree polynomial interpolation of the simulation results. In case of divergence, we cannot interpolate the values on the missing part of the curve. Therefore, the segment with no simulated values is replaced by a constant value of 200 kPa (above the maximum attainable stress for the muscle) to provide penalty against divergence in the error measure.

Correlation analysis was performed between the simulation parameters and the obtained errors to identify possible influence of a specific parameter on a deformation stage. Heatmaps and correlation coefficients were obtained. The correlation analysis may allow to observe potential relationships between the parameters.
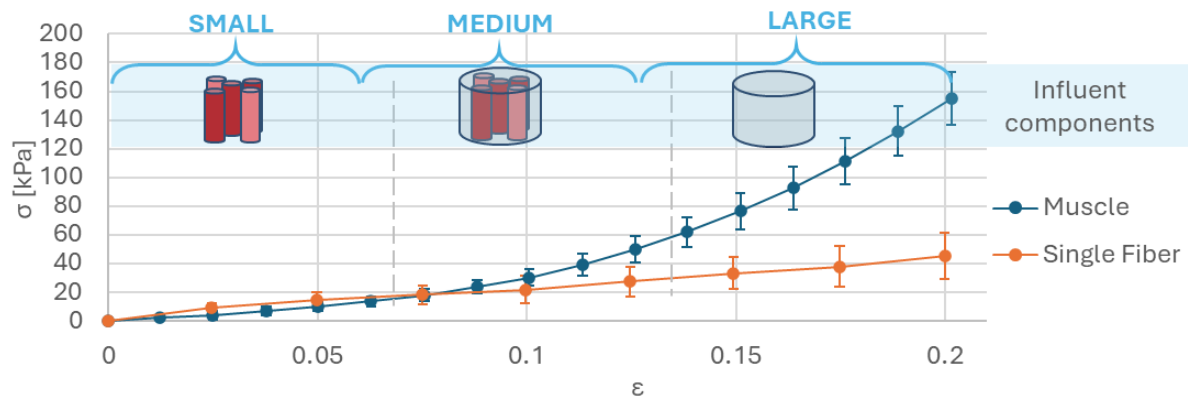
Figure 77. Definition of deformation regions for the error analysis on experimental uniaxial tension data for whole muscle and single muscle fibers up to 20% deformation.

5.3.3. Exploration of the mechanical parameters space

The ECM parameter sets were obtained by progressively exploring the parameter space (Table 22) in order to reduce the range of admissible parameter sets while analyzing the level of influence of each of these parameters and their interconnection. The exploration of mechanical parameter space has been conducted on the first set of geometries. All parameter sets used for this study are shown in Figure 78. We will not present the results of all simulations here, but will rather focus on the interdependency between parameters, and the different local minima resulting from our analysis.
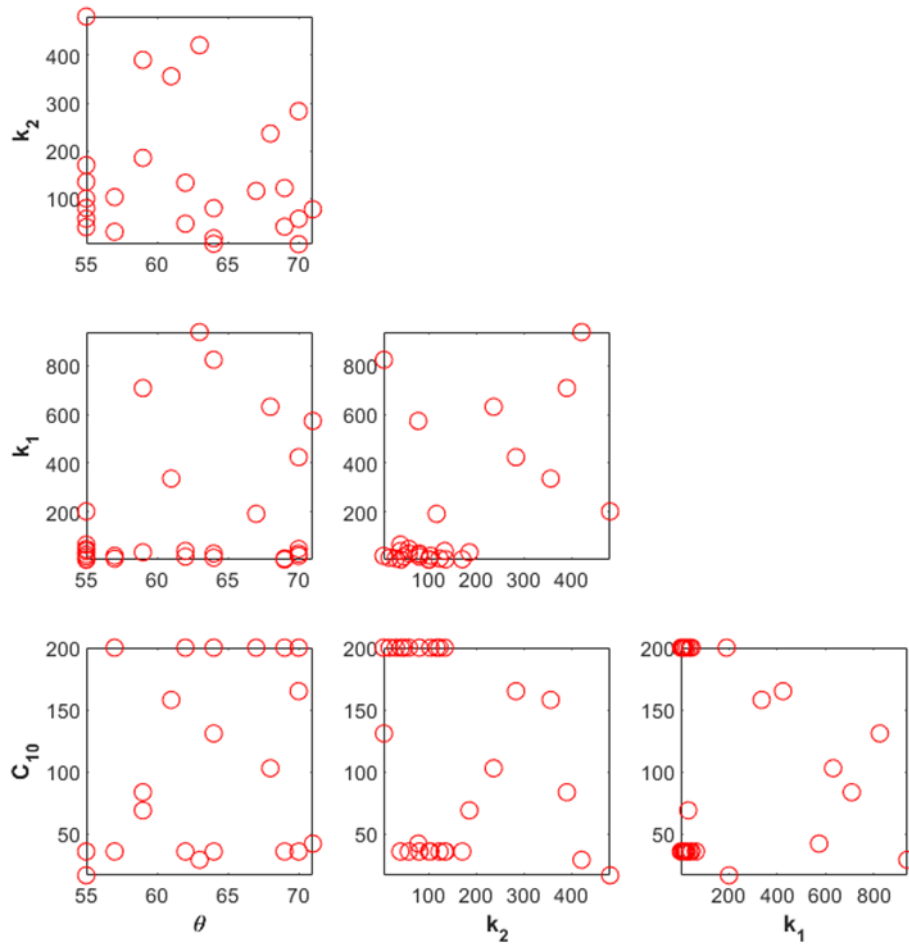
Figure 78. All parameter sets sampled from the parameter space.

Isotropic ECM. 5 parameter sets were generated using LHS sampling on parameter C_{10} value range to investigate the effect of this parameter alone (Table 24), thus making ECM an isotropic material. Therefore, the collagen fibers contain within ECM do not contribute to mechanical properties of the muscle.

Table 24. Mechanical parameter sets and total error in kPa (for the 3 segments altogether) results, for both WT and KO models, considering isotropic ECM.

Small error KO [kPa]	Total error KO [kPa]	Small error WT [kPa]	Total error WT [kPa]	C10 [kPa]	k1 [kPa]	k2 [-]	theta [°]
0.60	101.33	1.50	114.336	16.8	0	0.1	55
0.86	98.70	1.11	110.8521	36.0	0	0.1	55
1.47	94.77	0.72	105.4867	69.1	0	0.1	55
2.71	87.95	1.50	97.2738	131	0	0.1	55
4.12	80.93	2.95	89.0745	200	0	0.1	55

Results show that isotropic ECM does not allow to reproduce our uniaxial tension tests (Figure 79), with a total error being over 80 kPa. However, errors in small deformation range are small (below 5 kPa). With all C_{10} values, the simulated tension test fits within experimental bounds. Therefore the model does not seem to be sensitive to values of C_{10} up to 6% deformation in the case of isotropic ECM. However, this conclusion cannot be extrapolated to the case of anisotropic ECM.
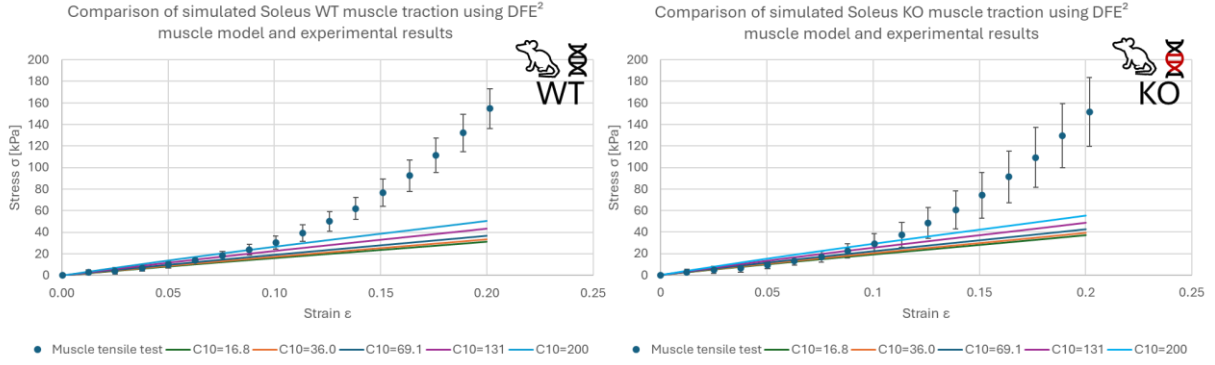
Figure 79. Simulation engineering stress-strain curves compared to experimental data for isotropic ECM. Parameter C_{10} controlling the ECM rigidity was varied between 16.8 and 200 kPa.

Anisotropic ECM: effect of C$_{10}$. After a first random exploration of the parameter space, ranges for collagen-related parameters k_1 and k_2 were restricted to [1;50] kPa and [50;150], respectively. To explore the interaction between parameter C$_{10}$ and other parameters, we randomly generated sets of parameters $\{k_1, k_2, \theta\}$ using LHS sampling, for values of C_{10}=36 kPa and C_{10}=200 kPa corresponding to our experimentally observed bounds (Table 25 and Table 26).
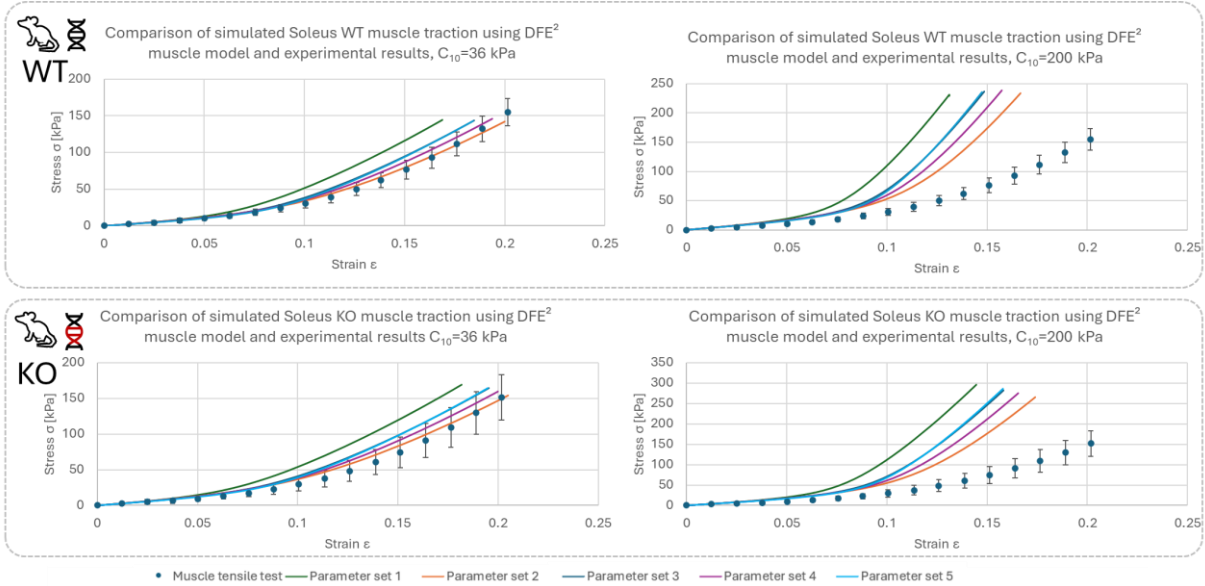
Figure 80. Engineering stress-strain representation of experimental and simulated uniaxial tension for both genotypes with C$_{10}$=36 kPa and C$_{10}$=200 kPa, using anisotropic formulation of ECM.

Results show a rigidification of the muscle behavior and divergence when C_{10}=200 kPa (Figure 80). We can conclude that parameter C_{10} is linked to the other model parameters and cannot be analyzed separately. Interestingly, two of the randomly generated parameters sets, sets 3 and 5 (marked with * and highlighted in blue in Table 25 and Table 26) provide the same macroscopic response. Therefore, we can conclude that independently of parameter C_{10}, at least two of the remaining parameters k_1, k_2, and θ are linked to each other.

131

Table 25. Mechanical parameter sets and results of total error in kPa (for the 3 segments altogether), for both WT and KO models, based on the input range [C_{10} fixed to 36 kPa ; k_1= 1 to 50 kPa ; k_2= 50 to 150; θ=55 to 73°]. RMSE inferior to 30 kPa are indicated in bold values. (*: parameter sets exhibiting similar behavior)

Small error KO	Medium error KO	Large error KO	Total error KO	Small error WT	Medium error WT	Large error WT	Total error WT	k1 [kPa]	k2	theta [°]
4,45	30,05	53,65	88,15	3,14	25,53	44,18	72,84	39,5	133	62
2,11	9,38	5,82	17,31	0,87	4,78	5,82	11,47	47,6	57,6	70
2,20	16,22	24,79	43,21	1,20	11,55	26,17	38,92	19,4*	103*	57*
2,01	12,47	14,52	29,00	0,98	7,88	21,65	30,50	28,6	79,7	64
1,82	15,09	30,94	47,85	1,29	10,38	26,02	37,69	8,45*	122*	69*

Table 26. Mechanical parameter sets and results of total error in kPa (for the 3 segments altogether), for both WT and KO models, based on the input range [C_{10} fixed to 200 kPa ; k_1= 1 to 50 kPa ; k_2= 50 to 150; θ=55 to 73°]. RMSE inferior to 30 kPa are indicated in bold values. (*: parameter sets exhibiting similar behavior)

Small error KO	Medium error KO	Large error KO	Total error KO	Small error WT	Medium error WT	Large error WT	Total error WT	k1 [kPa]	k2	theta [°]
9,67	124,37	92,92	226,96	8,30	105,94	90,84	205,08	39,5	133	62
5,55	45,69	112,69	163,94	4,64	41,77	184,84	231,25	47,6	57,6	70
5,22	76,39	308,42	390,04	4,22	73,03	106,11	183,37	19,4*	103*	57
5,10	60,22	114,65	179,97	4,21	56,35	93,95	154,51	28,6	79,7	64
4,46	76,89	143,44	224,78	3,47	73,42	345,27	422,16	8,45*	122*	69

To complete these observations, a correlation analysis was performed on the parameter set using C_{10}=36kPa. Correlation with all RMSE errors and the input parameters {k_1, k_2 , θ} was plotted (Figure 81), The plot is a heatmap with coefficients varying from -1 to 1, -1 indicating a strong negative correlation and 1 indicating a strong positive correlation. The resulting map shows little correlation between parameter θ and any error measurement. Interestingly, parameter k_2 is strongly correlated to all errors. Only a small correlation between k_1 and the error measurements is obtained. This suggests that our model is strongly dependent to the values of k_2.
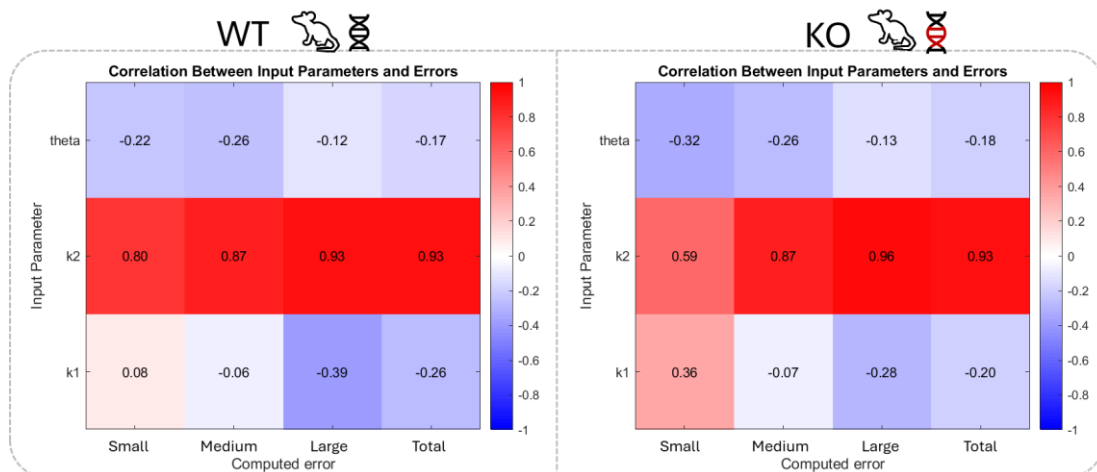
Figure 81. Heatmap of correlation analysis between the parameters k1, k2 and ϑ and errors obtained with the different RMSE metrics. For this dataset, C10=36 kPa. -1 indicates a strong negative correlation and 1 indicates a strong positive correlation.

Finally, three out of the five generated parameters sets provide a macroscopic response that fits to experimental data when combined with C_{10}=36 kPa. We will now focus on the characteristics of the datasets allowing us to fit experimental data, to investigate relationships between parameters.

Relationship between ECM parameters k₁ and k₂. Throughout different LHS sampling of parameter sets using C_{10}=36kPa, we gathered several datasets fitting to experimental data and plotted parameters $\{k_1, k_2, \theta\}$ against each other (Figure 82). Here, we can suppose that there is a linear relationship between parameters k_1 and k_2. The two simulations with the lowest error for WT were then used to compute the following relationship:

$$k_1 = -1.001 * k_2 + 105.5 \tag{5.6}$$
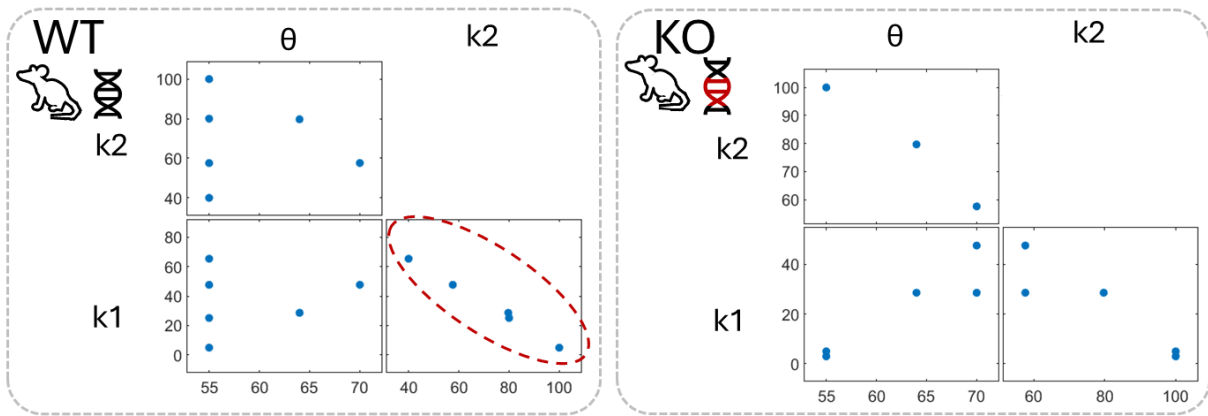
Figure 82. Matrix plot of the parameter sets extracted from series LHS1 and LHS2 fitting to experimental data. Highlight of a possible relationship between parameters k1 and k2.

Additional simulation sets were added assuming this relationship (Table 27) and results shown in Figure 83 tend to confirm this relationship that we have now to take into account.
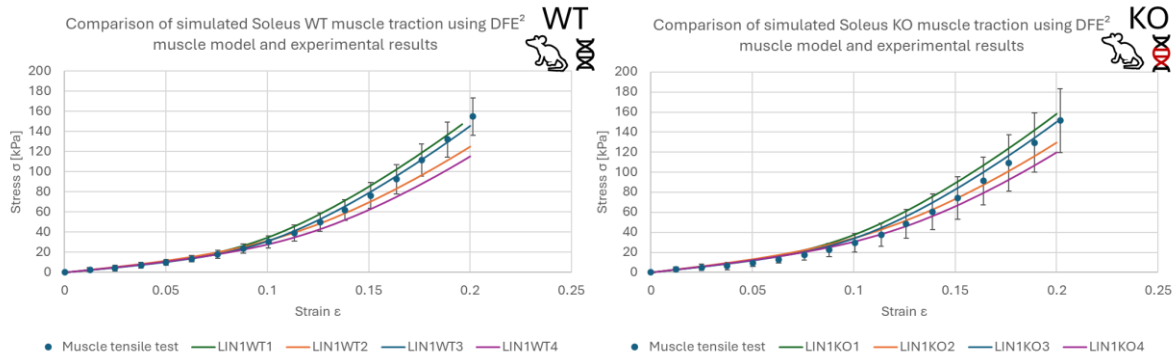
Figure 83. Macroscopic behavior obtained for series exploring linearity between parameters k1 and k2 with C₁₀=36 kPa, and ϑ=55°, in comparison with the experimental data.

Table 27. Mechanical parameter sets and results of total error in kPa (for the 3 segments altogether), for both WT and KO models, obtained for series exploring linearity between parameters k1 and k2 with C₁₀=36 kPa, and ϑ=55°.

Small error KO [kPa]	Medium error KO (kPa)	Large error KO [kPa]	Total error KO [kPa]	Small error WT [kPa]	Medium error WT [kPa]	Large error WT [kPa]	Total error WT [kPa]	k1 [kPa]	k2 [-]
2,00	11,02	14,07	27,08	0,93	6,92	6,35	14,20	25,1	80
2,58	5,06	10,37	18,00	1,02	2,19	17,51	20,72	65,3	40
1,43	7,02	7,16	15,62	1,01	3,01	3,52	7,53	15,1	80
1,88	2,87	18,49	23,25	0,40	5,09	25,98	31,47	39,2	40

Exploration of an optimized restricted parameter space. Following results regarding previous series, one question can be formulated: does there exist a combination of parameters θ, k_1 and k_2 that allows to fit the experimental data using C_{10} = 200 kPa? To answer this question, a parameter space with lower bounds for parameters k_1 and k_2 was sampled including 5 parameter sets (Table 28), with the parameter C_{10} fixed to a value of 200 kPa. Results show that a fitting parameter set can indeed be found (Figure 84), thus hinting at the existence of a relationship between parameters k_1, k_2 and C_{10}.

Table 28. Mechanical parameters and total error results for test LHS3, for both WT and KO models. [C_{10} fixed to 200 kPa ; k_1= 1 to 20 kPa ; k_2= 0.1 to 57; θ=55 to 73°]. RMSE inferior to 30 kPa are indicated in bold values.

Reference of the parameter set	C_{10} [kPa]	k_1 [kPa]	k_2 [-]	θ [°]	Total RMSE WT [kPa]	Total RMSE KO [kPa]
LHS4-SET1	200	15.9	47.3	62	97.0	105
LHS4-SET2	200	19.1	4.40	70	80.3	72.64
LHS4-SET3	200	8.13	30.3	57	26.8	19.4
LHS4-SET4	200	11.7	17.0	64	61.4	53.7
LHS4-SET5	200	3.89	41.1	69	22.2	24.4
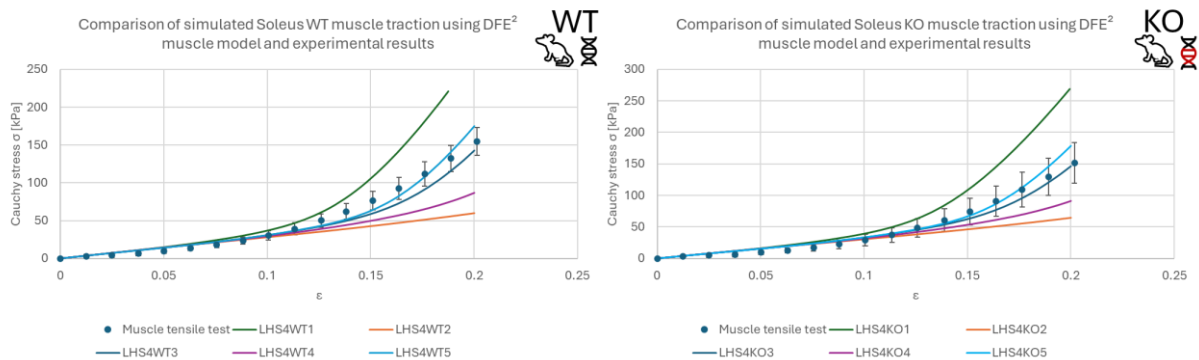
Figure 84. Macroscopic behavior obtained for series exploring restricted parameter space with C10=200 kPa, in comparison with the experimental data.

5.3.4. Comparison between genotypes

Parameters sets fitting to the experimental data from one genotype also fit the other experimental data, as muscles from both genotypes display a similar experimental mechanical behavior with no significant statistical difference between them. The goodness of fit is computed on the mean mechanical behavior; however a parameter set is considered as "*fitting*" if the macroscale mechanical behavior is comprised between the experimental bounds (Figure 85).
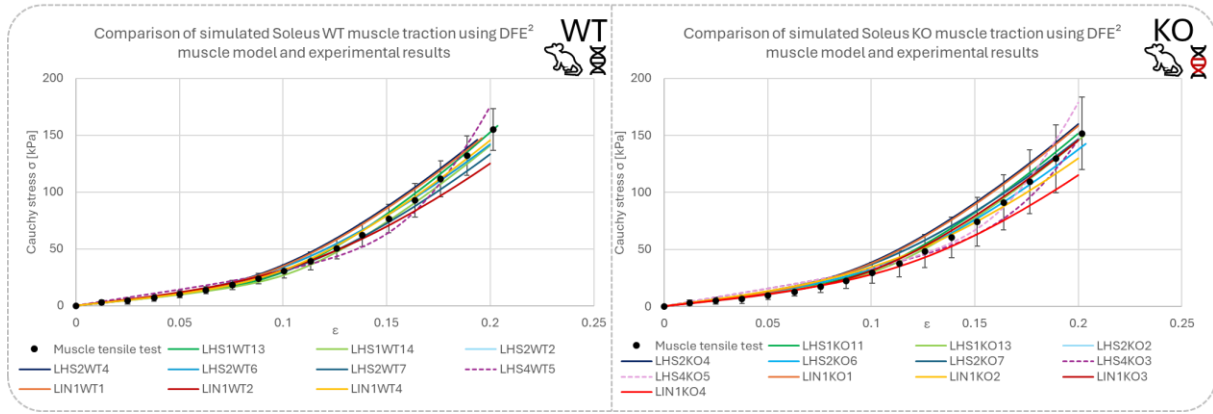
Figure 85. Macroscopic behavior obtained for parameter sets fitting the experimental data. Several parameter sets enable the fit of experimental data for each genotype. Our results highlight parameter redundancy. Whatever the parameter set is, better fit was systematically obtained for Klf10 KO with lower parameter k1 compared to WT soleus.

As previously seen, the soleus KO muscle seems softer than the soleus WT muscle. More precisely, using a dataset fitting to the WT experimental data, it was observed that by lowering parameter k_1 by 40%, a similar goodness of fit was obtained on the KO model (highlighted in bold in Table 29). Thus, pairs of previously defined parameter sets were created (Table 29), where only the k_1 value differed by a proportion of 40%. The observation was repeated: the error measure difference is below 2 points for each pair. Since parameters k_1 and k_2 are linked, similar tests could be conducted on parameter k_2. However, the conclusion would still point towards an alteration of collagen fiber-related mechanical properties between genotypes. This is our final list of acceptable parameter sets.

Table 29. Summary of the parameter sets fitting to the experimental data

Reference of the parameter set	C_{10} [kPa]	k_1 [kPa]	k_2 [-]	θ [°]	Total RMSE WT [kPa]	Total RMSE KO [kPa]
Pairs of datasets varying parameter k1 by 40%						
LHS1-SET15	36	5	100	55	8.11	13.9
LHS1-SET14	36	3	100	55	9.82	7.91
LHS2-SET2	36	47.7	57.6	70	11.5	17.3
LHS2-SET7	36	28.6	57.6	70	13.4	12.0
LHS2-SET13	36	25.1	80	55	14.2	27.1
LHS2-SET15	36	15.1	80	55	7.53	15.6
LHS2-SET14	36	65.3	40	55	20.7	18
LHS2-SET16	36	39.2	40	55	31.5	23.2
Additional (unpaired) datasets						
LHS2-SET4	36	28.6	79.7	64	30.5	29.0
LHS2-SET6	36	47.7	57.6	55	10.6	16.8
LHS3-SET3	200	8.13	30.3	57	26.8	19.4
LHS3-SET5	200	3.89	41.1	69	22.2	24.4

Since the numerical and experimental mechanical behaviors corresponding to these 12 datasets have already been compared, they will not be presented again here. Most of these parameter sets are comprised within the experimental uncertainty bounds for both the WT and the KO model (Figure 86).

135
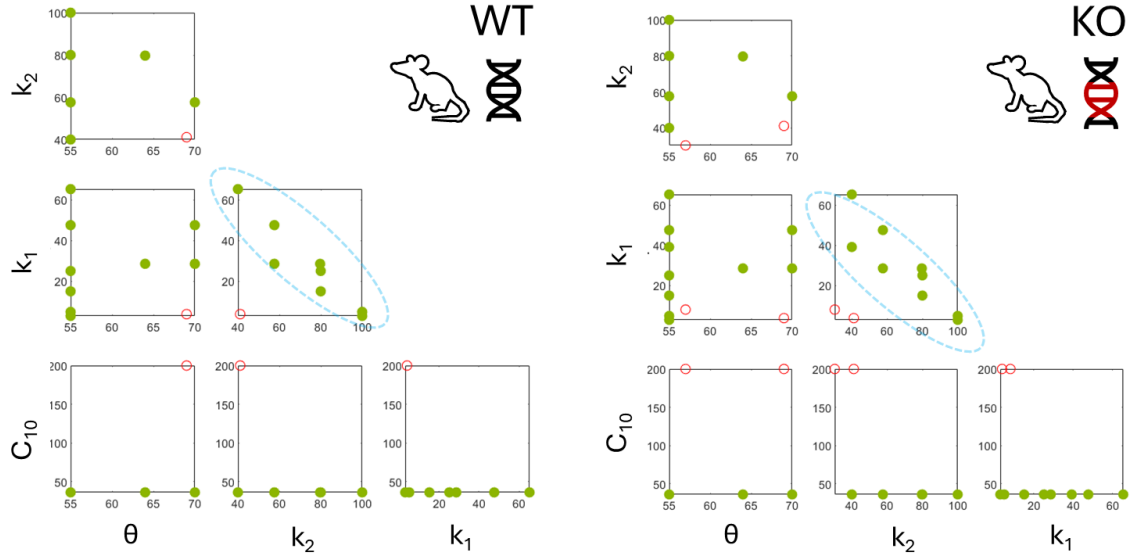
Figure 86. Matrix plot of the parameters fitting to WT and KO experimental data and highlight of a possible relationship between k_1 and k_2 (blue circle). Green dots: C_{10} = 36 kPa; red dots: C_{10} = 200 kPa.

5.3.5. Microscale analysis of the stress field

Until now, we have focused exclusively on establishing and evaluating these parameter sets, considering only the macroscopic mechanical behavior of the muscle, whether WT or Klf10 KO, while taking into account the combined influence of slow and fast muscle fibers as well as the transition from the microscopic to the macroscopic scale. Although the resulting macroscopic behavior is similar for all parameter sets, one can wonder whether the distribution of microscopic stresses follows the same tendency. Can the difference between parameter C_{10} = 36 kPa and C_{10} = 200 kPa be reflected in the microscopic stress extrema or spatial repartition?
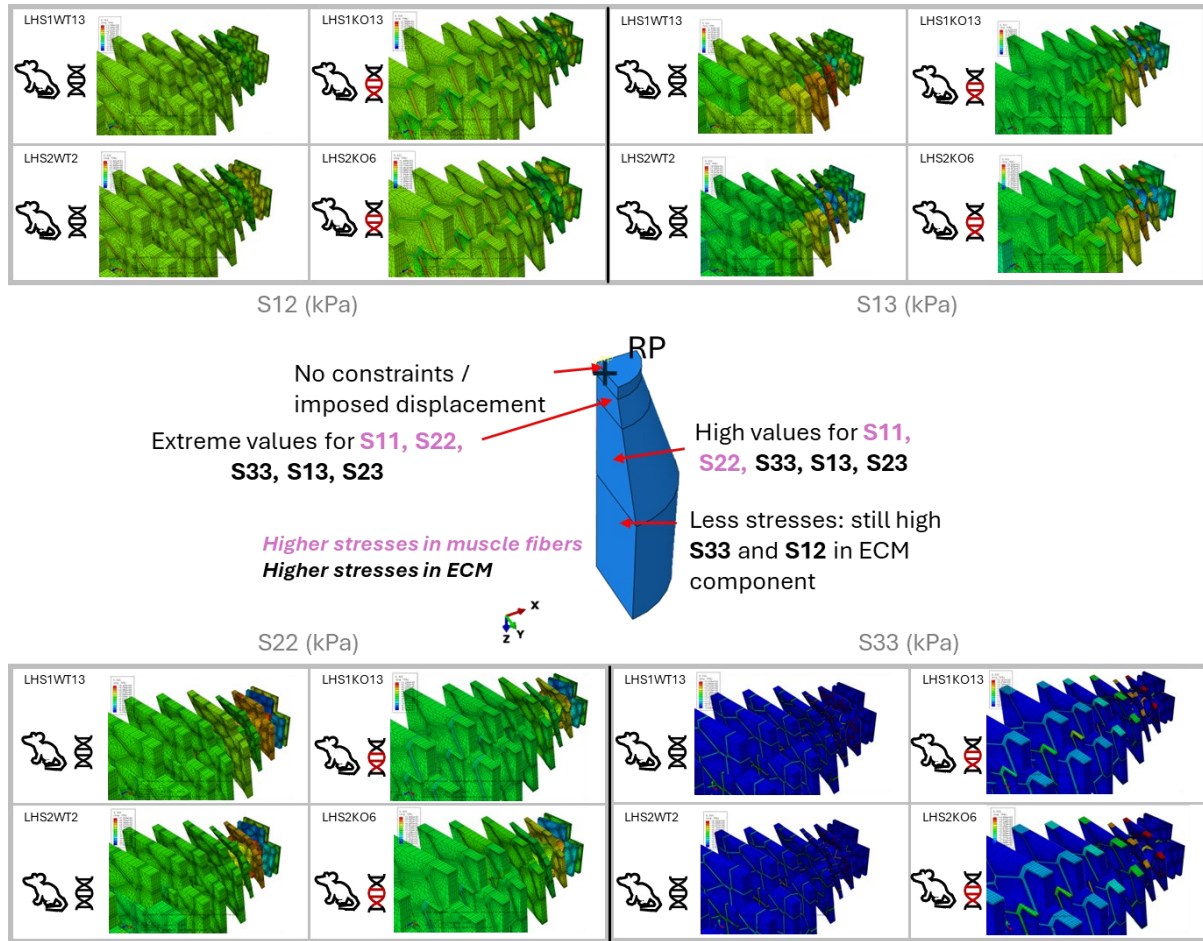
Figure 87. Stress field overview: region wise localization of stresses and components bearing those stresses.

The microscopic stress field components extrema and spatial distribution were extracted for several parameter sets (Figure 87). No tendency can be seen from the extremum values (some example of maximum and minimum Cauchy stress values are detailed for some simulations in Table 30), which all display a similar magnitude for both genotypes. Furthermore, the spatial repartition of stresses follows a similar pattern on all the studied geometries. However, it is interesting to note that within this repeatable pattern, the ECM contains the major part of the axial stress and all shear stresses, which is coherent with its functioning through shear deformations.

Table 30. Microscopic maximum and minimum values of the Cauchy stress tensor (in kPa) for different fitting parameter sets for the tensile simulations. Values obtained at 20% deformation on both WT and KO models.

Reference of the parameter set	S_{11} MIN	S_{11} MAX	S_{22} MIN	S_{22} MAX	S_{33} MIN	S_{33} MAX	S_{12} MIN	S_{12} MAX	S_{13} MIN	S_{13} MAX	S_{23} MIN	S_{23} MAX
LHS1-SET13 for WT soleus muscle	-98.4	84.8	-10.0	8.11	-99.5	5560.	-27.6	17.9	-84.0	75.0	-86.4	66.3
LHS1-SET13 for KO soleus muscle	-95.4	101.0	-97.9	116.0	-97.8	5770.	-25.9	18.1	-71.1	102.0	-78.3	101.0
LHS2-SET2 for WT soleus muscle	-79.1	79.4	-79.0	75.3	-80.1	5020.	-27.1	16.2	-57.9	86.6	-60.6	82.4
LHS2-SET6 for KO soleus muscle	-93.2	94.0	-95.6	107.0	-95.5	5000.	-24.0	16.5	-60.7	89.0	-66.9	89.0

For all datasets studied, the stress pattern seems repeatable; however, higher stresses are observed with higher values of C_{10}.

5.3.6. Effect of the geometry

All the results introduced previously have been generated using 1 set of geometries. We took the parameter sets fitting to experimental data using geometry *set 1* and simulated muscle uniaxial tensile behavior again using geometry *set 2* (Table 31).
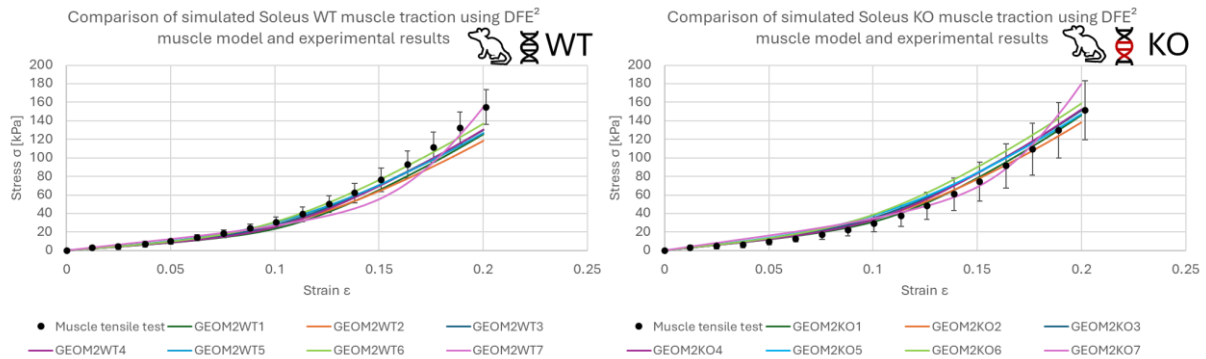
Figure 88. Macroscopic behavior obtained for geometry dependency investigation, in comparison with the experimental data.

Results shown on Figure 88 display very good agreement with the previous data for KO soleus muscle. However, the agreement with the previous data for soleus WT muscle is not very good, with the new geometry displaying less rigid behavior using the same parameters. This can be explained by the Fiber Volume Fraction (FVF) which is higher in the second set of WT geometry, therefore there is less ECM in the RVE. As ECM is the main load bearing component in large deformations, we observe higher error (typically above 10 kPa) starting from 16% deformation (Table 31) and the simulation does not fit the experimental bounds anymore. The influence of FVF is very important in skeletal muscle modeling, therefore this effect is expected. However, the simulated response still is of the same magnitude as the experimental data, and our previous conclusions still hold: KO soleus displays a less stiff response that WT soleus, which is expressed especially in the collagen fiber related parameters.

Table 31. Mechanical parameters and total error results for the second set of geometry, for both WT and KO models.

Small error KO [kPa]	Medium error KO (kPa]	Large error KO [kPa]	Total error KO [kPa]	Small error WT [kPa]	Medium error WT [kPa]	Large error WT [kPa]	Total error WT [kPa]	C10 [kPa]	k1 [kPa]	k2 [-]	theta [°]
1.03	3.93	1.98	6,94	2.04	6.38	17.60	26.02	36	3	100	55
2.08	5.61	5.01	12.70	0.97	5.02	22.43	28.42	36	28.6	57.6	70
1.76	8.12	7.12	17.01	1.43	2.41	13.25	17.09	36	15.1	80	55
1.27	6.69	7.16	15.12	1.94	3.73	12.66	18.33	36	5	100	55
2.76	9.79	6.15	18.70	0.57	1.56	15.50	17.63	36	47.6	57.6	70
2.30	12.08	13.55	27.92	1.10	1.56	7.54	10.21	36	25.1	80	55
6.68	3.43	15.73	25.84	3.48	9.63	13.13	26.24	200	3.89	41.1	69

5.4. Discussions

Using detailed analysis and these multiscale numerical models, along with an original approach that combines numerical modeling and experimental biomechanics, we were able to accurately replicate experimental tensile curves obtained by our team at the macroscopic (whole muscle) and microscopic (fiber) scales by analyzing experimentally missing and currently unknown parameters (on ECM), by obtaining robust parameter sets. Furthermore, we were also able to study and interpret the influences of each of the four ECM parameters concerned and analyze their interconnections, both in the WT and KO cases.

The results introduced so far in this chapter seem to indicate that the model is not much sensitive to variations in parameter θ, *i.e.* to the (double) orientation of the collagen fibers in the ECM, while the other parameters are linked by relations. For the different parameter sets allowing to replicate experimental behavior for WT and KO soleus muscles (Figure 89 A and B, respectively), no significant difference in the macroscopic global stress response can be exhibited. This opens further discussion on which parameter set is closest to the actual ECM mechanical properties.

-    **Parameter θ** represents the orientation of collagen fibers. However, this orientation is not fixed during muscle extension but rather evolves in the considered range. The insensitivity of the model to this parameter may reflect either a flaw in the model or the evolution of collagen fiber arrangement through extension. It is important to note, however, that we have considered here the behavior in extension and that this microscopic parameter could play a much more important role in the macroscopic mechanical response to shear in muscle tissue. This constitutes a first avenue for future investigation in the continuation of this thesis work.

-    **Parameter C_{10}** is related to the shear modulus in the proteoglycan matrix. However, it seems linked to parameters k_1 and k_2. The literature on experiments regarding murine ECM (Lanzl et al., 2024; Lloyd et al., 2022), as well as our own AFM results, tend to indicate that this value is located around 40 kPa. This correlates with the literature on multiscale models representing collagen fiber reinforced ECM (Bleiler et al., 2019; He et al., 2022; Kuravi et al., 2021a; Kuravi et al., 2021b; Spyrou, 2020; Spyrou et al., 2017, 2019). It is difficult to compare all the behaviors of hyperelastic models in the literature with ours, but we can already compare the shear modulus values (Figure 90). Therefore, most simulations were run using this order of magnitude for C_{10}. Interestingly, this is the same order of magnitude as parameter C_{10} for the muscle fibers, suggesting a continuum in the mechanical properties of ground matrices within the muscle. However, fitting parameter sets were found using a value of 200 kPa, which is also within our preliminary experimental results range.
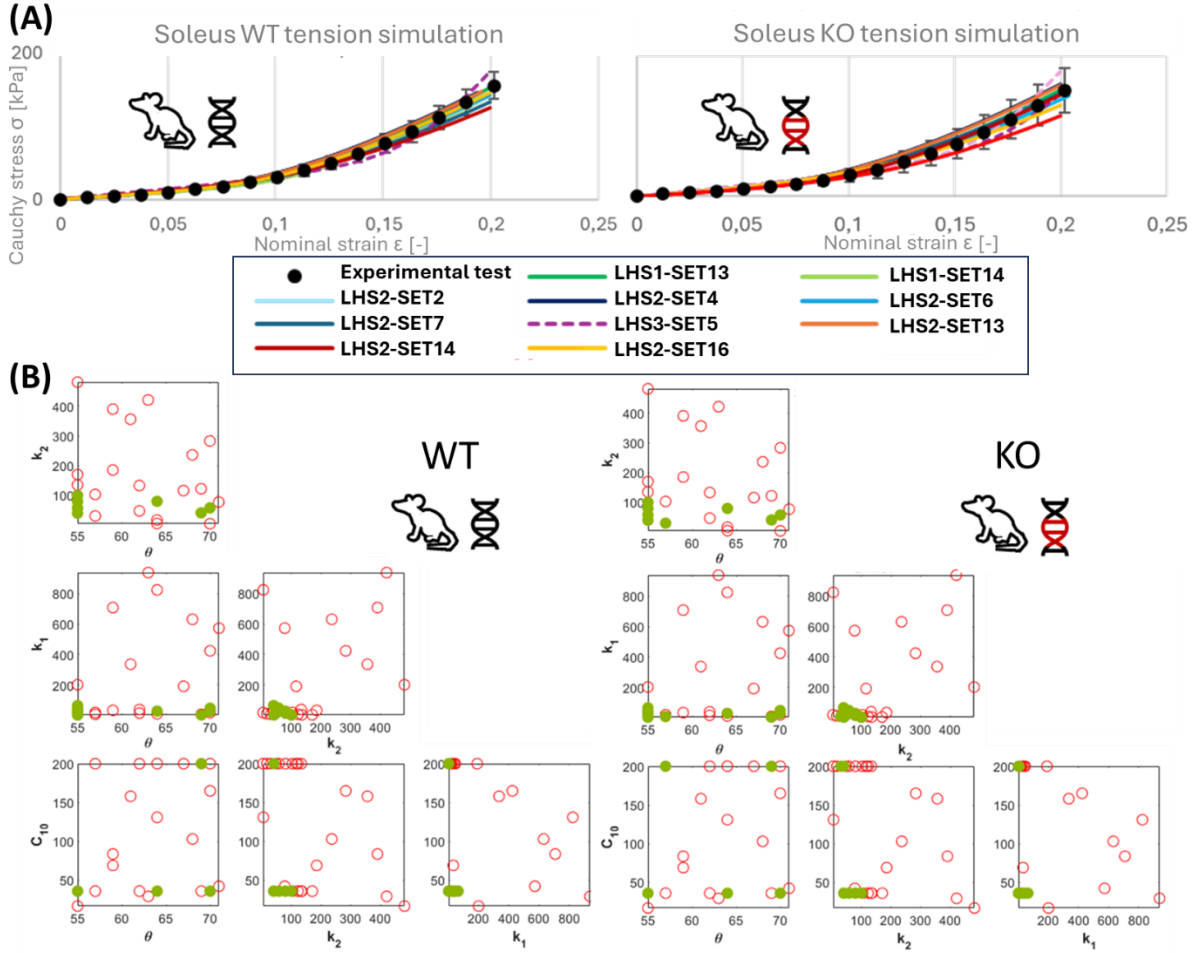
Figure 89. (A) Macroscopic response for the ECM sets of parameters that are in agreement with the experimental data for the WT (left) and Klf10 KO (right) data. (B) Overview of all parameter sets evaluated for the WT (left) and Klf10 KO (right) models. Green points correspond to parameter sets fitting to experimental data (sets exposed in (A)), which macroscopic behavior is plotted against the experimental data.

- **Parameter k_2** controls collagen fibers' exponential behavior. Thus, small variation of k_2 can be source of great variations of the values of the stiffness matrix. This causes strong differences in ECM mechanical behavior but also changes the magnitude of the values stored in the stiffness matrix. As a FE simulation first and foremost consists in solving a linear system with many degrees of freedom, it involves large storage capacities. In this case, values with a high magnitude, especially mixed with values of low magnitude representing different materials or directions, can lead to information loss due to limited storage. Therefore, this parameter is the most strongly correlated to simulation divergence. Nevertheless, numerical considerations do not provide any information on the actual ECM mechanical properties.

- **Parameter k_1** linearly modulates the amplitude of the responses of the collagen fibers. It can be interpreted in different ways: it can be seen either as an indicator of collagen fiber quantity within the ECM or as an indicator of collagen fiber stiffness. The literature is filled of contradictions regarding values of parameters k_1 and k_2, so that not even an order of magnitude can be estimated.
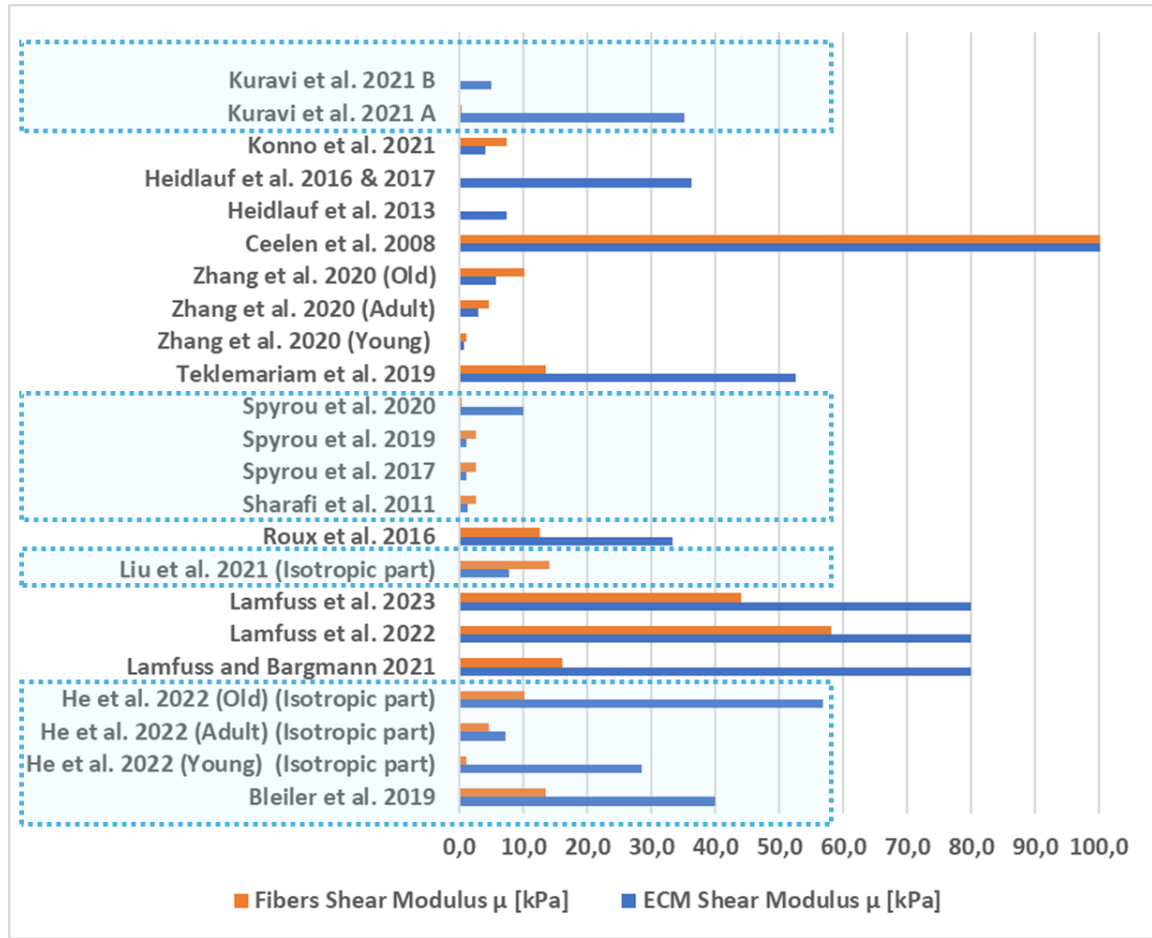
Figure 90. Values for microscopic (muscular fiber and endomysium from the ECM) shear moduli in numerical multiscale modeling of skeletal muscle from the literature compared to our final model. Models considering anisotropic ECM are highlighted in blue box.

Although the same parameter sets fit both WT and KO experimental behaviors, decreasing parameter k_1 by 40% allows a better fit of experimental mean behavior. Since parameters k_1 and k_2 are linked, we can only hypothesize the collagen fiber density or the collagen fiber mechanical properties may be altered in the KO muscle. However, these conclusions are based on a model comprising many parameters. Many biases were introduced in the model, although they are present for both genotypes.

The major bias in our approach is related to all the choices to obtain model size reduction, which means simplified muscle geometry and especially the use of C3D8R elements. The model results are then dependent on the hyperparameter regulating the hourglass stiffness. Moreover, for the same reasons, we restricted the RVE size around 20,000 elements. One can wonder whether the mesh density and RVE dimensions affect the results, and especially the local observation on Cauchy stress tensorial fields. The influence of other choices such as relying on one user to segment microscopic cross-sections (both regarding the RVE generation and the ECM width segmentation) would be very interesting to investigate. However, as mentioned earlier, we introduced the exact same bias for both genotypes, so the difference in mechanical parameters between them remains interpretable.

Another limitation is actually the periodicity assumption, because it limits the components present in the macroscale model. Indeed, the skeletal muscle is surrounded by a layer of epimysium, which also contains a fibrillar collagen network and therefore contributes to the mechanical properties of the whole muscle. If this component were included in the model, then the microscopic periodicity

141

assumption would not hold true. Further adaptation is needed to ensure the energy equilibrium and the deformation continuity at the interface. It is still possible to use a FE² method in that case, and even the DFE² method, but that requires to work on the boundary between the muscle and the epimysium to include domain adaptation (Liu et al., 2023). For the same reason, representing the fascicles surrounded by epimysium at the mesoscale would also require domain adaptation. Nevertheless, one can also formulate the hypothesis that the mechanical properties would not vary much by adding domain adaptation. In the literature, multiscale models have been using the microscopic periodicity assumption without adaptation at the border with other macroscale components (He et al., 2022) or used another homogenization method to add another component (Sahani et al., 2024).

Finally, this study solely focuses on uniaxial tension following the muscle's main orientation. Although we exhibited through this approach that ECM accounts for more than half of the mechanical stress in large deformations (Gillies et al., 2011), we did not consider other solicitations. Indeed, in our experimental study described in chapter 2, we exhibited differences in muscle shear properties that might be linked to ECM; thus it would be interesting to simulate shear solicitation of the skeletal muscle as well.

5.5. Conclusions

In this chapter, our model replicated experimental uniaxial tension tests on whole muscles. Solution parameter sets are not unique, and cannot provide exact value of mechanical properties for either genotype, but rather indicate their order of magnitude and potential variations. However, our analysis has shown a decrease in Soleus KO collagen-related mechanical properties k_1 and k_2, which allows us to attest that the mechanical properties of the ECM are well affected by the Klf10 gene. More specifically we formulate the two following hypothesis: (i) the genetic deletion affects the collagen fiber density; (ii) the genetic deletion affects the collagen fiber mechanical properties.

Our original approach and our model exhibit many limitations, especially due to the different strategies employed to reduce the model's size. Although the same strategy has been applied to both genotypes, biases related to RVE dimensions and the macroscale model mesh could strongly influence the results described here and should be addressed in future works. Moreover, no evaluation of the model under different solicitations was performed due to the lack of experimental data, another important aspect to be addressed in future works.

However, the analysis of the microscale stress field revealed that the ECM is bearing most of the axial and shear stresses, thus highlighting the importance of this component's contribution to the whole muscle mechanics. These conclusions are in good agreement with the functions of ECM described in chapter 1, and especially lateral force transmission through shear. To the best of our knowledge, no such analysis has been performed using a multiscale skeletal muscle model yet.

Discussions, perspectives and conclusions

The complexity of the skeletal muscle mechanical properties arises from the contribution of various microconstituents arranged in a hierarchical structure comprising several scales. A link can be established between the state of health of the muscle and its mechanical properties, the latter becoming markers of interest for the study of altered states of health. Although skeletal muscles contain many components, a few of them contribute to most of the resulting mechanical properties: especially, across the different scales, the extracellular matrix (ECM), divided in three different components that are the endomysium (microscopic scale), perimysium (mesoscopic scale) and epimysium (macroscopic scale) recently got under the spotlight for its significant contribution to skeletal muscle mechanical behavior. However, the isolated mechanical properties of these components are difficult to retrieve experimentally (Binder-Markey et al., 2021), resulting in usage of innovative methods like multiscale modeling to compute them indirectly (Loumeaud et al., 2024).

In this PhD, we evaluate the effect of the Klf10 genetic deletion on murine skeletal muscles mechanical properties. Previous *ex vivo* studies revealed both an influence of the gene on the mechanical properties of isolated muscle fibers (microscopic scale) and an absence of significant influence on the overall muscle mechanical properties (Tatarenko et al., 2024). This suggests the existence of a potential compensation mechanism, possibly in the form of an alteration of the ECM components. Hence, two research axes were developed in this thesis: firstly, the investigation of *in vivo* mechanical properties of whole muscles using Magnetic Resonance Elastography (MRE) as a first attempt to observe effects of the genetic deletion *in vivo*, independently of *ex vivo* experimental conditions; and secondly the indirect investigation of ECM mechanical properties though multiscale numerical modeling coupled to *ex vivo* experimental results.

The first contribution of this PhD thesis is the establishment of an MRE protocol for the study of *in vivo* murine skeletal muscle (Loumeaud al., 2025). We demonstrated that this protocol was repeatable. The protocol was applied to two genetically different cohorts of mice, in two different positions (flexion, extension) for three different excitation frequencies. The results highlighted a difference in extensor muscles rigidity in the extended position for Klf10 KO mice. This opens the way to more experiments to be performed with the developed protocol. Additionally, even though this aspect was not developed within this manuscript, we would like to highlight that our repeatability and reproducibility measures using this protocol add credit to our experimental results and this offers a guarantee when sharing the protocol and setup to scientific collaborators, as these aspects are scarcely studied in the literature. Moreover, both the experimental setup and protocol are adaptable to a wide variety of organs, allowing us to investigate the effect of Klf10 gene in different organs such as the liver in the future. Current developments also involve different organs or biomechanical materials such as hemostatic sponges or phantoms, highlighting the interest of our developments for the scientific community.

However, the main focus of this thesis was the development of the multiscale model. Considering the available experimental data, many choices are articulated around the idea of separating geometrical and mechanical effects of the Klf10 gene at the microscopic scale. Indeed, the available data about microscopic geometry and structure are sufficient to generate a genotype-specific microscale geometry (Kammoun et al., 2016, 2017). As a result, fewer parameters need to be identified; moreover, most of those parameters are associated with interpretable mechanical

properties. To build such a geometry, an original periodic geometry generation pipeline was developed, incorporating probabilistic distributions regarding the different components' geometry and features facilitating numerical implementation. This geometry contains three components at the microscopic scale: muscle fibers (slow, fast), endomysium, and a transition layer which can be used in many ways. The transition layer can help reduce numerical instabilities within the simulation by using a gradient of mechanical properties; however, it can be modified to more accurately represent the link between ECM and muscle fibers (costameres), containing transmembrane proteins. These proteins are involved in pathological pathways such as Duchenne Muscular Dystrophy (DMD), in which their density significantly decreases (Virgilio et al., 2015). Interestingly, this component is not always represented in multiscale models investigating DMD (Sahani et al., 2024). If further analyses on Klf10 KO muscles reveal an effect on this component, the model can be adapted to modify the contribution of transmembrane proteins. Moreover, such a transition material has also been the subject of publication in the context of RVE generation for industrially manufactured fiber reinforced composites (Riaño & Joliff, 2019) as it represents physical effects of the manufacturing process localized around the fibers. This indicates that our geometry generation pipeline can contribute not only to larger investigation of skeletal muscle disorders, but also to different fields using similar tools to conduct their research.

To represent the different component's mechanical behavior, we chose the HGO model (Holzapfel et al., 2000) as this model is adapted to fiber reinforced material. We adapted an existing user subroutine (Castillo-Méndez & Ortiz, 2022a) by including a second fiber family for the ECM material and by encoding localization of transition layer integration points within the final model. This last contribution is what makes it possible to compute a gradient of mechanical properties or to model transmembrane proteins as it provides a vector pointing from the muscle fiber boundary to the ECM at the current integration point. This method also provides the type of associated muscle fiber, so the transition layer behavior can be made dependent on the muscle fiber type. This enables the modelling of muscle fiber-dependent conditions.

To link our microscale RVE with the macroscale muscle geometry, an existing method called Direct Finite Element Square (DFE[2]) (Tan et al., 2020) was adapted for our geometry and benchmarked for hyperelastic materials in large deformations. The main motivations behind the choice of this method were the use of a complex geometry for the RVE, which proved to be incompatible with analytical homogenization methods, and the need for localization, as to provide access to the microscopic stress fields. The latter allows us to assess whether a certain geometry undergoes significantly higher constraints, or if the stress distribution patterns are different. Depending on the results, this method can help detect microscopic lesions in the biological material. Again, the developed approach is not specific to skeletal muscle and can be adapted to any material. Using this approach, we compared simulations of uniaxial extension of soleus muscle for both genotypes (Pouletaut et al., 2023). An encouraging first result was the ability of the model to provide a good fit to the experimental data. Surprisingly, several relationships were found between the 4 model parameters, resulting in many different datasets as solutions. Some redundancy was expected, such as the relationship between parameter C_{10} representing the proteoglycan matrix within the ECM, and parameters k_1 and k_2 representing the collagen fiber reinforcement. Parameters k_1 and k_2 are controlling the linear and exponential variations of the collagen mechanical properties respectively. However, the linear tendency observed between those parameters is surprising, considering the exponential formulation of the behavior law. Additionally, the literature about these parameters is scarce and very heterogeneous and therefore does not provide any indication about which parameter sets might be closer to ground truth. We tried discriminating these parameter sets by analyzing the microscopic scale stress fields; however, the results are fairly homogeneous. Thus, no conclusion can be drawn about the absolute values of mechanical parameters for the ECM. Surprisingly, the collagen fiber orientation

parameter θ showed no significant effect on the resulting mechanical behavior, in contrast to previous results obtained using a different approach that did not discriminate between geometrical and mechanical contribution, nor did it provide localization (Tatarenko, 2023). We can then conclude that the modeling approach we use has a significant effect on the resulting parameters and the interpretations that can be drawn. We should then be very careful about conclusions drawn from multiscale modeling and focus on formulating hypotheses to be confirmed with experimental protocols.

Nevertheless, the numerical results highlighted that the major stress-bearing structure is the collagen fibers contained in the ECM, and we showed that their mechanical behavior is softer in Klf10 KO muscles. These results suggest two hypotheses: either the collagen fiber density is lowered in Klf10 KO soleus muscles, or the collagen fibers mechanical properties are altered. This could correlate to our *in vivo* observations, as ECM functions through shear deformations (Lieber & Binder-Markey, 2021). Very interestingly, our analysis also showed that the muscle fibers mechanical behavior is neglectable compared to the ECM mechanical contribution for uniaxial extension of the skeletal muscle. This means that the compensation mechanism we were investigating does not exist as the ECM bears most of the load at the macroscale. Therefore, a healthy ECM displaying the same mechanical and structural characteristics could be contained in both genotypes. However, we highlighted differences in the ECM mechanical parameters when fitting our model to mean experimental data on soleus muscles from both genetic backgrounds, opening the way for new research on the effect of Klf10 genetic deletion on ECM.

Our approach was the first step towards identifying specific pathways and components affected by the genetic deletion, allowing us to choose appropriate protocols for further investigation without sacrificing animals at this stage. We showed that the results shift attention to the collagen fibers contained in the ECM. Following this indirect investigation of ECM, direct characterization experiments in collaboration with the Mayo Clinic and the Cochin Institute (*CNRS, Inserm, Paris*) will focus on the study of collagen. Scanning Electron Microscopy (Tateya et al., 2007), performed at the Mayo Clinic, will provide acquisitions of the ECM, from which structural, textural parameters and collagen density can be estimated. Immunohistochemical analyses and multiphoton microscopy at the Cochin Institute will focus on quantifying collagen quantity in function of the type, on histological cross sections. Such measurements can provide information on structural parameters that can be fixed in the simulation, thus restricting the parameter space.

As first short-term perspective, we have performed additional *in vivo* experiments on murine hindlimbs to increase the statistical power of our analysis and be able to evaluate the significance of our findings.

A second short-term perspective is to apply our model to the EDL muscle, to see if any similar conclusions can be drawn. However, with the current state of the model, the RVE consists in fibers parallel to the muscle axis, which holds true for the soleus, but is wrong for the EDL, which is why the soleus was prioritized during this PhD. In the EDL, the pennation angle is around 10° (Chleboun et al., 1997). Therefore, it could be of interest to first modify the geometry generation algorithm to incorporate this orientation within the RVE. This can be achieved through generation of a bigger RVE that would be cut using a suitably orientated bounding box.

Another perspective for the model is to modify the UMAT to include active skeletal muscle behavior. Indeed, active experimental data for both muscles and muscle fibers has been acquired and published (Kammoun et al., 2021) and can be implemented in the model. Moreover, as the ECM is a passive component, these datasets can actually be used for validation of the parameter sets identified

during this PhD. For this purpose, additional parameters can be passed to the UMAT and additional stress dependent on the current activation/ simulation time can be summed to the passive Cauchy stress (Spyrou et al., 2019).

With this notion of activation, we introduce the notion of time within the model. Although most active multiscale models of skeletal muscle are hyperelastic and only consider time indirectly (He et al., 2022; Konno et al., 2021; Spyrou et al., 2017, 2019; Teklemariam et al., 2019), the experimental data showcases a viscous behavior (Tatarenko et al., 2024), which we have been neglecting during this PhD. To take full advantage of the experimental data at our disposal, we can consider extending the model to a viscohyperelastic behavior and expanding the experimental datasets to include tests at different speeds. The DFE^2 method has now been benchmarked for both hyperelastic anisotropic and viscoelastic behaviors (Tan et al., 2020; Zhi et al., 2021; Zhi, Yang, et al., 2023), but the combination of both is yet to be tested. This would not induce any changes in the geometry or the scale transition algorithm, but constitute a fundamental modification of the UMAT, as the equations to compute stresses for such a material are much more complex than for a hyperelastic material, hence the scarcity of viscohyperelastic biomechanical models in the literature. This would overall constitute a very original and very useful contribution to the project and the scientific literature in general.

Many limitations were also introduced in the model and will be discussed here. Firstly, the segmentation of ECM used to generate the RVE results in about 90% fiber volume fraction (FVF) whereas healthy skeletal muscles display a FVF rather around 95%. Therefore, manual user segmentation should be refined and performed by several users. However, there is a possibility that this effect does not arise from the initial segmentation but rather from the method used to generate the ECM width. Indeed, the ECM visible on histological cross-sections is a mix of two layers of ECM which are endomysium and perimysium and do not play the same mechanical role. The current segmentation does not distinguish between endomysium and perimysium, therefore introducing a bias in the model. Endomysium is present all-around muscle fibers while perimysium delineates bundles of muscle fibers. Indeed, the thicker layer of perimysium separates a bundle of about 20 fibers at some positions within the histological cross-section. Visually, continuous, thicker ECM lines are present on the image, without the possibility to clearly distinguish them from endomysium. The current segmentation of ECM does not account for perimysium and draws random values of ECM width for each edge separating two Voronoi cells, from measurements that include both components, independently of the values chosen for neighboring edges. Instead of drawing values for a distribution for each edge, an implementation using graph theory to trace perimysium paths between the muscle fibers could lead to a better representation, and additional width can be added along those paths. To separate both components in the original segmentation, one can filter the measurements based on thresholds from the literature.

Similarly, no epimysium is represented around the skeletal muscle, although being present during the experiment. Therefore, its effects are blended into the identified ECM parameters. However, the epimysium does not fulfill the same functional role as the perimysium or the endomysium and does not exhibit a similar structure. The orientation of collagen fibers within the epimysium is orthogonal to the muscle's axis (Purslow, 2020; Sahani et al., 2022). For this reason, the bias introduced by its absence in the model might be very complex. However, as the epimysium is being located on the periphery of skeletal muscle, it is much more accessible for many imaging methods such as AFM, microscopy, SEM, optical elastography; these methods would even allow us to investigate directly the effect of the Klf10 genetic deletion on the epimysium instead of using an indirect method such as multiscale modeling; the resulting observations could then be implemented in a refined model to focus on the investigation of endomysium.

Another limitation regarding the first step of geometry generation is again user dependency. The segmentation is performed by one user which provides the seeds for the Voronoi diagram generation. However, an optimal position for seed location is actually retrievable through segmentation of the cell's edges. This method was developed by Honda and colleagues (Honda, 1978, 1983) and shown to be appliable to many biological tissues. A preliminary implementation was encoded; however the first results show that the method can diverge, and the seed can be found outside of the actual segmented fiber. Therefore, further reflection and refinement are needed before implementing this method within the geometry generation pipeline. We can suggest defining not an optimal point but rather an optimal area to place this point, which could help the algorithm to converge more easily.

RVE depth choices were made to reduce the model size. However, many RVE in the literature are cubic. This choice certainly greatly influence the response of our model and this effect should be investigated. However, in a sense, the flat RVE that we use in the model is closer to the assumption of locally parallel muscle fibers. Indeed, the real geometry presents wavy muscle fibers and intrafascicularly terminating muscle fibers (Kohn et al., 2021; Kuravi et al., 2021a), hence the fusiform shape of skeletal muscles. Intrafascicularly terminating fibers have already been investigated using multiscale models and shows the stress repartition is distributed through the ECM component (Kuravi et al., 2021a; Kuravi et al., 2021b). This highlights the importance of ECM's function in lateral force transmission. Such geometry could be generated within the geometry generation algorithm by considering successive planes instead of one 2D image. The continuity between the planes could be ensured by using Bézier curves (Farin, 1983) and these would also allow the introduction of intrafascicularly terminating muscle fibers within our RVE. Methods then exist in Abaqus to link the associated components on the different planes. The encoding of this geometry would be in itself a consequent work, and a non negligible difficulty would be to maintain the periodicity of both the geometry and the mesh. Fortunately, the inherent properties of Bézier curves allows the user to position symmetrical control points around and within the RVE volume, enforcing the curve to be both symmetrical and smooth.

Another criticizable choice related to model size is the dimension of the transition layer component, which was chosen similar to the ECM mean width to facilitate part meshing and avoid very dense mesh in this region. However, as ECM is shown to be the main load-bearing component, we can hypothesize that this choice did not have a large influence on the results. Nevertheless, dependency to this parameter could be investigated in the future.

As shown through the microscopic stress analysis, the macroscopic skeletal muscle fusiform shape has a great influence on the results. Indeed, the out-of-plane shear stress extremum values are concentrated in the volumes where muscle cross-sectional area is decreasing. This is a logical consequence of the macroscale geometry and this effect was of course expected. Therefore, using a segmentation from anatomical MRI acquisitions to retrieve the real muscle shape, and fitting a fusiform envelope on that shape can help reducing the bias introduced by the generic shape used in this thesis.

Microscopic stress analysis is also rendered difficult because of the volume scaling approach in DFE^2, which is efficient but makes the RVEs overlap. It requires hiding the different instances to visualize correctly the fields and is a tedious task. Implementing energy scaling in the UMAT (Zhi, Yang, et al., 2023) does not modify the results, but it would greatly improve the visuals and the readability of tensorial field results. Preliminary works regarding this aspect have started but remain to be developed.

In conclusion, an innovative *in vivo* experimental protocol and an original skeletal muscle multiscale numerical model were developed during this PhD. Both developments open the way for new research projects, in the context of Klf10 genetic deletion study but also in a variety of different applications. Focusing on the Klf10 gene investigation, we presented here a hyperelastic anisotropic numerical model based on our own experimental data able to (i) take into account the microstructure specific to each genotype, (ii) decouple structural and mechanical properties, (iii) provide an insight on the stress repartitions within the muscle components and (iv) simulate uniaxial tensile tests performed on whole muscles. The effected work highlighted differences in mechanical properties between the genotypes and provided hypotheses to be tested through other methods, especially regarding collagen fibers within the skeletal muscles. In this model, the strongest limitations have been introduced by our strategies to reduce the model size, thus new strategies to overcome those limits are being studied and should be the first objective in future works. These future works can also focus on expanding and including more of our group's experimental data regarding the viscous and active behavior of skeletal muscle. Finally, new experimental methods could expand our current experimental dataset and lead to evaluation of our model using different solicitations.

Valorization

Honours and awards

Presentation and Poster Prize of the MSII 2023 Doctoral School

Best junior presentation in session Biomaterials - Imaging - Robotics of 12th days of the Fédération de Médecine Translationelle de Strasbourg (FMTS), June 2025, Strasbourg, France.

International peer-reviewed journal

Loumeaud, A., Pouletaut, P., Bensamoun, S.F., George, D., Chatelin, S. Study of the Klf10 gene effect on murine soleus muscle through a multiscale mechanical model. In Writing.

Loumeaud, A., Po, C., De Cauwer, A., Teboul, M., Delaunay, F., Pouletaut, P., George, D., Bensamoun, S.F., Chatelin, S. Magnetic Resonance Elastography for the study of Klf10 gene effect on murine skeletal muscles. In Writing.

Dufour, N., **Loumeaud, A.,** Legrand, M., Martins Seromenho, E., Chatelin, S., Gennisson, J.-L., Nahas, A. Noise Correlation inspired method : a versatile tool for shear wave elastography using magnetic resonance, ultrasound and optical imaging. In Writing.

Loumeaud, A., Pouletaut, P., Bensamoun, S. F., George, D., & Chatelin, S. (2025). An original approach to generate periodic Representative Volume Elements with anisotropic heterogeneous microstructure: Application to skeletal muscle. Journal of Biomechanics, 191, 112897. https://doi.org/10.1016/j.jbiomech.2025.112897

Loumeaud, A., Pouletaut, P., Bensamoun, S.F., George, D., Chatelin, S. (2024). Multiscale mechanical modeling of skeletal muscle: a systemic review of the literature. Journal of Medical and Biological Engineering, 44(3), 337-356. DOI: https://doi.org/10.1007/s40846-024-00879-3

Ngo, H.H.P., Andrade, R. Brum, J.,Benech, N., Chatelin, S., **Loumeaud, A.**, Frappart, T. Fraschini, C., Nordez, A., Gennisson, J.-L. (2024). In plane quantification of in vivo muscle elastic anisotropy factor by steered ultrasound pushing beams. Physics in Medicine & Biology, 2024, vol. 69, no 4, p. 045013. DOI https://doi.org/10.1088/1361-6560/ad21a0

Ngo, H.H.P., Andrade, R.J., Lancelot, J., **Loumeaud, A.**, Cornu, C., Nordez, A., Chatelin, S., Gennisson, J.-L. (2024). Unravelling anisotropic nonlinear shear elasticity in muscles: towards a non-invasive assessment of stress in living organisms. Journal of the mechanical behavior of biomedical materials, vol. 150, p. 106325. DOI https://doi.org/10.1016/j.jmbbm.2023.106325

International congresses with peer-reviewed proceedings

Loumeaud, A., Pouletaut, P., Bensamoun, S. F., George, D., Chatelin, S. An original approach for multiscale modeling of the skeletal muscle. Submitted in: 20th Symposium on Computer Methods in Biomechanics and Biomedical Engineering (CMBBE), Sept 2025, Barcelona, Spain.

Loumeaud, A., Pouletaut, P., Bensamoun, S. F., George, D., Chatelin, S. Multiscale modeling of the skeletal muscle: an original approach of periodic representative volume elements. 30th Congress of the European Society of Biomechanics (ESB), July 2025, Zurich, Switzerland.

Loumeaud, A., Po, C., Wach, B., Bensamoun, S. F., Pagé, G., Doblas, S., Garteiser, P., Grenier, D., Tse Ve Koon, K., Beuf, O., Sango-Solanas, P., Chatelin, S. An original piezoelectric actuator design with dedicated sequences for mouse multi-organ magnetic resonance elastography (MRE) at 7T. International Tissue Elasticity Conference (ITEC), Oct 2024, Lyon, France.

Ngo, H.H.P., Andrade, R.J., Cornu, C., **Loumeaud, A.**, Frappart, T., Fraschini, C., Nordez, A., Chatelin, S., Gennisson, J.-L. Quanfication of nonlinear shear moduli in transversely isotropic medium: preliminary study ex vivo and in vivo on muscles, IEEE International Ultrasonics Symposium (IUS), Oct 2023, Montreal, Canada.

National congress with peer-reviewed proceedings

Loumeaud, A., Po, C., Wach, B., Bensamoun, S.F., Pagé, G., Doblas, S., Garteiser, P., Grenier, D., Tse Ve Koon, K., Beuf, O., Sango-Solanas, P., Chatelin, S. (2024, October). 49ème congrès de la Société de Biomécanique. Preclinical multi-organ Magnetic Resonance Elastography (MRE) at 7T: an original piezoelectric actuator design with dedicated sequences. Published in: Multidisciplinary Biomechanics Journal, 2024, vol. 1, p. 205-207, DOI: https://doi.org/10.46298/mbj.14507

Chakouch, M., Tatarenko, Y., **Loumeaud, A.**, Josse, A., George, D., Pouletaut, P., Bensamoun, S.F. & Chatelin, S. (2024, October). 49e congrès de la Société de Biomécanique. Multiscale mechanical constitutive equation of the passive properties of murine skeletal muscle: application to the influence of the Klf10 gene on the extra cellular matrix. Published in: Multidisciplinary Biomechanics Journal, 2024, vol. 1, p. 353-355, DOI: https://doi.org/10.46298/mbj.14541

Local & national congress without peer-reviewed proceedings

Loumeaud, A., Po, C., De Cauwer, A., Teboul, M., Delaunay, F., Pouletaut, P., George, D., Bensamoun, S.F., Chatelin, S. Couplage de la modélisation numérique multi échelles et de l'élastographie par IRM pour l'étude de l'impact du gène klf10 sur la matrice extracellulaire du muscle squelettique murin. 12th days of the Fédération de Médecine Translationelle de Strasbourg (FMTS), June 2025, Strasbourg, France.

Loumeaud, A., Po, C., Pagé, G., Garteiser, P., Vappou, J., Wach, B., George, D., Bensamoun, S.F., Chatelin, S. Development of preclinical MRI elastography at 7T: an original approach for the non-invasive mechanical characterization of mouse organs. 10th days of the Fédération de Médecine Translationelle de Strasbourg (FMTS), June 2023, Strasbourg, France.

Andrade, R.J., Ngo, H.H.P., Brum, J., Benech, N., Chatelin, S., **Loumeaud, A.**, Frappart, T., Fraschini, C., Magot, A., Péréon, Y., Nordez, A., Gennisson, J.-L. Noninvasive quantification of elastic anisotropy factor by steered ultrasound pushing beams: towards a novel imaging biomarker of muscle health, 20èmes Journées de la Société Française de Myologie (SFM), Nov 2023, La Baule, France.

Chatelin, S., **Loumeaud, A.**, Wach, B., Po, C., Nahas, A. MRESAT - Magnetic Resonance Elastography for Small Animal Translational research, Journée du hub Grand Est France Life Imaging, Sept 2024, Nancy, France (Best scientific presentation award)

Loumeaud, A., Bensamoun, S.F., George, D., Chatelin, S. Multiscale mechanical homogenized model for skeletal muscle coupling imaging, modeling and genetic expression. Annual ITI HealthTech days, Dec 2023, Strasbourg, France.

Fundings

151

Résumé long en français

Introduction

La connaissance de la structure et du fonctionnement des muscles squelettiques présente un intérêt particulier pour la recherche en biomécanique. Le tissu musculaire constitue la majeure partie de la masse corporelle humaine, et ses propriétés biomécaniques reflètent son état de santé et certaines caractéristiques, telles que l'âge. Les propriétés biomécaniques peuvent être étudiées *ex vivo* ou *in vivo*, allant de la palpation par un professionnel de santé à l'utilisation d'outils mathématiques pour prédire la réponse musculaire. Le choix de l'outil ou de la méthodologie dépend principalement des composants ciblés. En effet, un aspect essentiel du muscle squelettique réside dans sa structure hiérarchique, répartie à différentes échelles. L'échelle macroscopique désigne le muscle dans son ensemble, tandis qu'à l'échelle mésoscopique, ce muscle se divise en plusieurs faisceaux, chacun contenant à son tour des fibres musculaires à l'échelle microscopique. Cette description succincte n'est pas représentative de la diversité des composants contenus à chaque échelle dans le muscle squelettique, qui contribuent chacun à leur manière à la structure et au fonctionnement globaux de l'organe.

La recherche biomécanique étudie principalement la structure et les propriétés mécaniques de divers tissus. L'organe qui nous intéresse présente un comportement viscohyperélastique anisotrope spécifique à l'échelle macroscopique en raison de sa structure hiérarchique. Diverses méthodes ont été utilisées pour mener des études sur les muscles squelettiques, mais elles ont tendance à se complexifier à mesure que l'échelle et la taille des composants diminuent. À des échelles plus petites, il devient de plus en plus difficile d'isoler et de manipuler des composants individuels, à condition que des expériences *ex vivo* soient possibles. Les résultats sont fortement dépendants des conditions expérimentales.

Les méthodes relatives aux expériences *in vivo* ont connu des développements récents, mais restent rares. Dans ce contexte, les méthodes numériques combinant des modèles mathématiques et des données expérimentales constituent un bon compromis pour obtenir des informations sur les composants présentant des difficultés inhérentes aux méthodes *in vivo* et *ex vivo*. En particulier, une nouvelle famille de méthodes numériques appelées modèles multi-échelles est de plus en plus utilisée dans la littérature. Elles consistent à mettre en œuvre plusieurs échelles du muscle squelettique et des composants associés dans le même modèle mathématique, en tirant parti de la pertinence des

153

données expérimentales à plus grande échelle pour obtenir des informations à plus petite échelle, par exemple grâce à l'identification des paramètres.

Dans la littérature, cette abondance de données expérimentales s'applique à tout le muscle, mais aussi à des composants tels que les fibres musculaires et les myofibrilles, qui ont été largement étudiés chez plusieurs espèces. Bien que les muscles squelettiques contiennent de nombreux composants, seuls quelques-uns d'entre eux contribuent à la plupart des propriétés mécaniques qui en résultent : en particulier, à différentes échelles, la matrice extracellulaire (MEC), divisée en trois composants différents qui sont l'endomysium (échelle microscopique), le périmysium (échelle mésoscopique) et l'épimysium (échelle macroscopique). Récemment, l'intérêt de la communauté scientifique s'est tourné vers la MEC, car il est prouvé que ce composant contribue non seulement de manière importante aux propriétés mécaniques des muscles squelettiques, mais qu'il est également impliqué dans des troubles pathologiques tels que la dystrophie musculaire de Duchenne (DMD). Cependant, ce composant est particulièrement difficile à isoler car sa fraction volumique dans le muscle squelettique est faible (moins de 10 %) et il présente un lien continu avec d'autres composants tels que les fibres musculaires. Ainsi, deux axes de recherche clés ont récemment émergé dans la littérature : la caractérisation expérimentale de la MEC, souvent en combinaison avec une digestion chimique du muscle ; et l'utilisation de la modélisation multi-échelle pour récupérer indirectement des informations sur la MEC à partir de données expérimentales à l'échelle du muscle entier.

Le gène Klf10 (Krüppel-like factor 10), découvert pour son implication dans l'ostéoporose humaine, participe à la régulation de l'homéostasie métabolique dans divers organes. Plus précisément, il joue le rôle de régulateur transcriptionnel circadien du métabolisme énergétique dans le foie et des découvertes récentes suggèrent un rôle similaire dans le muscle squelettique. En effet, des études *ex vivo* récentes sur des modèles animaux murins ont démontré l'effet du gène Klf10 sur les propriétés mécaniques passives et actives du muscle squelettique strié. Des variations significatives des propriétés mécaniques passives et actives des fibres musculaires à l'échelle microscopique ont été induites par la délétion génétique chez les animaux. À la même échelle, des variations significatives de la structure ont été observées. Cependant, à différentes échelles, comme l'échelle submicronique contenant les myofibrilles et également à l'échelle macroscopique, aucune variation significative des propriétés mécaniques n'a été observée. Ces résultats suggèrent l'existence d'un mécanisme de compensation entre les échelles. L'hypothèse a été émise que la délétion génétique pourrait également affecter la MEC.

Compte tenu des méthodes susmentionnées pour étudier la MEC, il a été décidé de développer une approche de modélisation multi-échelle qui est désormais décrite dans cette thèse de doctorat. La thèse se concentre sur deux méthodes distinctes pour étudier l'effet de la délétion du gène Klf10 dans les muscles squelettiques de souris :

Mesures mécaniques *in vivo* du muscle squelettique murin. Les effets du gène Klf10 sur les différentes échelles du muscle squelettique ont été observés exclusivement *ex vivo* et n'ont jamais été confirmés *in vivo*. Par conséquent, un biais peut être introduit si le changement observé dans les propriétés mécaniques à l'échelle microscopique résulte uniquement d'une sensibilité accrue à un élément du protocole de test. Cette observation constitue l'un des deux principaux défis scientifiques abordés dans cette thèse. Outre l'analyse de modélisation multi-échelle ciblant spécifiquement la MEC, nous élargissons l'ensemble de données expérimentales *ex vivo* existant avec des mesures *in vivo* à l'échelle macroscopique. À cette fin, nous utilisons une méthode d'imagerie basée sur l'imagerie par résonance magnétique (IRM), appelée élastographie par résonance magnétique (MRE). La MRE nous permet d'obtenir des cartes représentant la variation de la propagation des ondes mécaniques dans les tissus, qui sont liées à la variation des propriétés mécaniques. Bien que la MRE soit largement utilisée dans la recherche clinique sur les patients humains, elle présente des défis supplémentaires spécifiques pour les espèces plus petites telles que les rongeurs. Par conséquent, très peu de dispositifs expérimentaux ont été développés pour la MRE chez les petits animaux.

Dans cette thèse, les travaux connexes comprennent le développement d'un protocole MRE pour l'étude du squelette murin dans deux positions distinctes, permettant d'isoler les contributions mécaniques des muscles fléchisseurs et extenseurs des membres postérieurs. Ce protocole a ensuite été appliqué à deux cohortes de souris présentant des génotypes différents, afin d'étudier *in vivo* les implications de la délétion génétique Klf10 sur la rigidité des muscles squelettiques pour les petites déformations.

Modélisation numérique multi-échelle du muscle squelettique murin. Afin d'étudier les propriétés mécaniques de la MEC dans les muscles squelettiques *ex vivo*, nous avons développé un modèle numérique multi-échelle original. Ce nouveau modèle vise à surmonter les limites actuelles de la littérature grâce à un algorithme innovant de génération d'éléments de volume représentatifs (RVE) combiné à une méthode « Direct Finite Element Square » (DFE²) pour assurer la transition entre les échelles. L'algorithme de génération de RVE fournit une géométrie personnalisée tenant compte des variations structurelles induites par la délétion génétique, découplant ainsi ces effets des paramètres mécaniques à identifier. La géométrie intègre des données probabilistes issues de données expérimentales d'imagerie *ex vivo* antérieures concernant le type de fibres musculaires (lentes,

rapides) ainsi qu'une représentation probabiliste de la géométrie de la MEC, divisée en deux composants : l'endomysium et son interface avec les fibres musculaires. En outre, la méthode choisie pour passer d'une échelle à l'autre permet non seulement de passer d'une échelle microscopique (fibres musculaires) à une échelle macroscopique (muscle), mais aussi de descendre à une échelle microscopique pour effectuer des recherches sur la géométrie à cette dernière échelle.

À travers la reproduction numérique d'essais d'extension uniaxiale expérimentaux, à l'échelle microscopique et macroscopique, les paramètres mécaniques associés à la MEC sont identifiés et fournissent des informations sur l'influence *ex vivo* de la délétion génétique Klf10 et mettent en évidence les effets sur les fibres de collagène au sein de la MEC.

Le premier chapitre de ce manuscrit vise à décrire la structure hiérarchique du muscle squelettique et les fonctions complexes de ses principaux composants. En parcourant les différentes échelles, nous présentons les méthodes biomécaniques, tant expérimentales que numériques, qui peuvent être utilisées pour étudier les propriétés biomécaniques du muscle squelettique. Une attention particulière est accordée au composant MEC.

Le deuxième chapitre détaille la caractérisation expérimentale *in vivo* du muscle squelettique murin. Après une brève présentation du dispositif expérimental, nous décrivons le protocole et le processus de post-traitement, ainsi que les résultats des tests expérimentaux.

La méthode de transition d'échelle numérique, présentée ci-dessus sous le nom de méthode DFE², est au centre du chapitre 3. L'adaptation de la méthode à la géométrie macroscopique du muscle squelettique et au matériau anisotrope hyperélastique, ainsi que l'analyse comparative et l'optimisation de la simulation sont présentées.

En changeant d'échelle, le chapitre 4 offre un aperçu de l'algorithme développé pour la conception de la géométrie microscopique du muscle squelettique à partir de coupes histologiques et de distributions probabilistes liées aux différents composants. Il décrit la génération d'éléments de volume représentatifs périodiques dans le logiciel EF, ainsi que les différentes stratégies adoptées pour réduire les artefacts numériques à l'échelle microscopique.

Résultant de la combinaison des développements présentés dans les chapitres 3 et 4, le modèle musculaire squelettique multi-échelle et son application à l'expression génétique Klf10 sont présentés dans le chapitre 5. L'étude du muscle soléaire chez des animaux sains et génétiquement modifiés et les conclusions sont présentées, ainsi que les limites posées par notre modèle actuel. Ce

chapitre ouvre la voie à une discussion scientifique sur les perspectives permettant de dépasser les limites actuelles, ainsi que sur l'intérêt de nos travaux pour la communauté scientifique.

Contexte scientifique

Le muscle squelettique est une structure hiérarchique avec des composants spécifiques à chaque échelle. Certains de ceux-ci influencent la réponse mécanique globale du muscle, qui se traduit par un comportement viscohyperélastique anisotrope non linéaire à l'échelle macroscopique. Ce comportement est directement lié à différentes caractéristiques physio-pathologiques, comme son âge ou la présence d'une atteinte musculaire.

Dans cette thèse, nous nous intéressons particulièrement aux échelle macroscopique (muscle entier) et microscopique (contenant fibres musculaires et la matrice extracellulaire – MEC). Plus particulièrement, nous nous intéressons au muscle squelettique de souris, dont l'étude présente des difficultés additionnelles de par sa taille.

Déjà impliqué dans la régulation de l'homéostasie métabolique dans divers organes, le gène Klf10 (Krüppel-like factor 10) est un régulateur transcriptionnel circadien du métabolisme énergétique dans le foie et de récents résultats suggèrent un rôle similaire dans le muscle squelettique (Baroukh et al., 2022). Des études récentes *ex vivo* sur modèle animal murin ont mis en évidence l'effet du gène Klf10 sur les propriétés mécaniques passives et actives des muscles striés squelettiques (Kammoun et al., 2021). Il a été également montré que Klf10 affecte de manière significative les propriétés mécaniques passives de composants spécifiques à l'échelle microscopique (fibre), sans variation notable aux échelles macroscopique (muscle) et submicronique (myofibrille), ce qui suggère un rôle clé dans la régulation de la matrice extracellulaire (MEC) (Tatarenko et al., 2024). Ce contexte à donné lieu à l'identification de deux verrous scientifiques majeurs, développés successivement ci-après. En utilisant des données histologiques et biomécaniques acquises par notre groupe (Kammoun et al., 2016, 2017; Tatarenko et al., 2024), aux deux échelles mentionnées précédemment, nous pouvons identifier les paramètres structuraux et mécaniques de la MEC, dans le cas d'un animal sain et d'un animal affecté par la délétion génétique Klf10-KO.

Résumé du chapitre 1

Ce premier chapitre nous permet de comprendre la structure et la fonction des muscles squelettiques, en mettant l'accent sur les composants responsables des propriétés mécaniques. La structure du muscle squelettique est hiérarchique et peut être divisée en différentes échelles, à savoir : l'échelle macroscopique, l'échelle mésoscopique, l'échelle microscopique et l'échelle submicronique.

De nombreuses méthodes expérimentales ont été développées pour étudier cette structure hiérarchique, mais aussi sa fonction à travers l'étude des propriétés mécaniques à différentes échelles. Bien que la plupart des études soient réalisées *ex vivo* et donc soumises à des changements *post mortem* dus à la rigidité cadavérique, certaines méthodes permettent de dépasser ces limites en utilisant des investigations *in vivo* du muscle squelettique dans son environnement physiologique. De plus, certaines méthodes expérimentales ciblent des composants spécifiques pouvant être impliqués dans des processus pathologiques, tels que la matrice extracellulaire (MEC). Dans le cas particulier de la MEC, les méthodes de caractérisation expérimentale sont rares et difficiles à mettre en œuvre ; c'est pourquoi différentes approches ont été développées, basées sur la modélisation numérique multi-échelle. Les modèles numériques multi-échelles du muscle squelettique se sont développés de manière croissante ces dernières années. Ils sont basés sur des méthodes dites d'homogénéisation qui relient différentes échelles. Beaucoup de ces modèles sont utilisés comme outils pour étudier la MEC dans différentes conditions : santé, vieillissement et conditions pathologiques telles que la Myopathie de Duchenne ou la paralysie cérébrale.

Dans cette thèse, nous étudions l'impact du gène Klf10 sur le muscle squelettique à l'aide d'un modèle murin. Dans ce modèle, des expériences antérieures ont montré des altérations dépendantes du muscle dans le métabolisme musculaire, ainsi que des altérations structurelles et fonctionnelles à l'échelle microscopique dans les fibres musculaires *ex vivo*. Il est intéressant de noter que ces altérations ne sont pas observées à des échelles plus grandes, telles que l'échelle macroscopique, ce qui suggère l'existence d'un mécanisme de compensation dû à un autre composant. Compte tenu de la structure du muscle squelettique, la MEC est le premier candidat pour ce mécanisme.

Nous proposons donc d'étudier l'impact du gène Klf10 dans la MEC du muscle squelettique de la souris. Pour ce faire, nous proposons d'utiliser des outils de modélisation multi-échelles, avec le développement d'un nouveau modèle de muscle squelettique reliant les échelles macroscopique et microscopique. Ce modèle devrait inclure des paramètres interprétables liés à la structure et à la fonction de la MEC et fournir des informations sur un mécanisme de compensation potentiel. Dans cet exposé, nous présentons le développement d'un modèle mécanique hyperélastique passif basé sur des expériences *ex vivo*, intégrant ainsi une partie des données expérimentales décrites dans la section ci-dessus. De plus, nous proposons de compléter l'ensemble de données expérimentales existant sur la caractérisation du muscle squelettique de souris à l'aide de l'élastographie par résonance magnétique afin d'étudier les propriétés mécaniques de cisaillement *in vivo* à l'échelle macroscopique. Compte tenu du rôle central de la déformation par cisaillement dans la fonction de la MEC, cette

méthode offre une occasion unique d'étudier les adaptations compensatoires possibles dans ce composant.

Résumé du chapitre 2

Les effets de Klf10 sur les différentes échelles du muscle squelettique ont été observés exclusivement *ex vivo* et n'ont à ce jour jamais été confirmés *in vivo*. Ce constat constitue le premier verrou scientifique majeur auquel s'attaque ce travail de thèse. Il s'agit donc d'étendre l'analyse mécanique du muscle squelettique via des protocoles expérimentaux *in vivo* novateurs, et d'en extraire les conclusions quant à l'influence *in vivo* du gène Klf10 sur la biomécanique du muscle squelettique murin. L'élastographie par résonance magnétique (ERM) est une méthode d'imagerie basée sur l'IRM permettant de cartographier des propriétés mécaniques *in vivo* (Muthupillai et al., 1995). Bien que largement utilisé en clinique, l'ERM a donné lieu à très peu de dispositifs adaptés au petit rongeur. Un dispositif novateur d'ERM du petit animal à 7T a été développé pour le muscle squelettique de souris (Loumeaud, Po, et al., 2025).

Le protocole consiste en positionner un système piézoélectrique sur la patte arrière de l'animal, dans 2 positions différentes : patte allongée et patte repliée. Le protocole a été appliqué à 2 cohortes de souris : les muscles squelettiques de la patte ont été étudiés dans les 2 positions ce qui a permis l'étude séparée des muscles fléchisseurs et extenseurs de la patte par rapport à l'articulation de la cheville. Des cartographies de module de cisaillement en petites déformations pour 3 valeurs de fréquences d'excitation différentes (800, 1000 et 1200 Hz) ont été obtenues. L'application de ce protocole à des cohortes de souris témoins et présentant une déficience du gène Klf10 a permis, en collaboration avec l'Institut de Biologie Valrose (Université Nice Côte d'Azur, CNRS, Inserm, UMR 7277 - U1091) et le département de biochimie et de biologie moléculaire de la Mayo Clinic (Rochester, MN, USA), de mettre en évidence *in vivo* une implication significative du gène à l'étude sur la rigidité d'une partie des muscles squelettiques des membres antérieurs. Des expériences complémentaires réalisées en juin 2025 permettrons de compléter ces observations.

Résumé du chapitre 3

Les outils actuels permettant d'évaluer les propriétés mécaniques de la MEC musculaire restent extrêmement limités, ce qui freine la compréhension de son rôle fonctionnel et de son rapport

au gène Klf10. La modélisation par éléments finis de ces composants à différentes échelles (Kuravi et al., 2021; Sahani et al., 2024) est une méthode efficace pour investiguer le comportement, qui permet de s'affranchir des limites posées par l'expérimentation (Binder-Markey et al., 2021). Dans ce contexte, la modélisation numérique du muscle squelettique apparaît comme une approche essentielle pour solutionner le second verrou scientifique majeur à l'origine de ce travail de thèse : le manque de données expérimentales sur la MEC, sur les mécanismes impliqués et sur la prédiction de la réponse musculaire d'une façon générale, et tout particulièrement en lien avec l'expression du gène Klf10. Bien que cette modélisation reste complexe, en raison de la structure hiérarchique du muscle combinant de nombreux composants à différentes échelles, elle constitue un levier majeur pour progresser dans l'analyse de sa réponse mécanique globale du muscle strié squelettique (Loumeaud et al., 2024).

Nous avons développé une approche originale de modélisation multiéchelles par éléments finis, reposant sur une génération périodique d'éléments de volume représentatifs (VER) et la méthode « Direct Finite Element Square » DFE[2] (Loumeaud, Pouletaut, et al., 2025; Tan et al., 2020). Ceci nous a permis d'intégrer des paramètres de distribution des fibres musculaires lentes et rapides (Kammoun et al., 2017), géométriques, mécaniques (Tatarenko et al., 2024), tout en prenant en compte l'organisation et les propriétés mécaniques de la MEC dans le cas d'un génotype sain et d'un génotype musculaire altéré par l'inhibition du gène Klf10.

Dans ce chapitre, nous présentons l'adaptation d'une méthode numérique multi-échelle (Tan et al., 2020) à une géométrie de muscle squelettique et à un matériau anisotrope hyperélastique. Nous fournissons une évaluation de la méthode pour les matériaux hyperélastiques soumis à de grandes déformations. Nous étudions également l'effet des conditions aux limites, des paramètres du solveur et des stratégies de maillage sur la convergence du modèle. Les résultats fournissent un aperçu des capacités et des limites de notre stratégie de modélisation, caractérisant ainsi le biais que nous introduisons en raison de nos choix de modélisation.

La méthode développée combine deux échelles différentes d'un matériau multi-échelle dans la même simulation, fournissant ainsi des informations à la fois à l'échelle macroscopique (homogénéisation) et à l'échelle microscopique (localisation). Elle est adaptée à la géométrie des muscles squelettiques aux deux échelles : l'échelle macro peut contenir une géométrie musculaire fusiforme, tandis que l'échelle micro peut être représentative d'un échantillon de muscle squelettique. En particulier, le modèle à l'échelle macro a été adapté pour simuler une expérience de tension uniaxiale. De plus, la méthode a été validée pour le comportement des matériaux hyperélastiques anisotropes. Des stratégies de réduction de la taille des modèles et des stratégies de convergence ont été mises en œuvre et testées sur des modèles musculaires DFE² simplifiés. La méthode développée

répond à nos deux objectifs principaux : le découplage des propriétés structurelles et mécaniques à l'échelle microscopique, et la nécessité d'une localisation. Dans ce chapitre, seule l'échelle macroscopique a été adaptée au muscle squelettique ; par conséquent, il est nécessaire de développer un RVE à l'échelle microscopique représentatif des propriétés structurelles du muscle squelettique de souris, avant de le combiner avec la méthode DFE² telle qu'elle a été développée ici. C'est sur cet aspect que nous nous concentrerons dans le chapitre suivant, avec une définition précise du RVE, de sa géométrie, de la distribution de ses constituants et de la mise en œuvre des lois de comportement via une approche de transition originale. Dans le dernier chapitre, nous comparerons les aspects macroscopiques discutés ici avec l'application du modèle global qui en résulte.

Résumé du chapitre 4

L'algorithme de génération de géométrie original présenté dans ce chapitre peut produire une géométrie musculaire spécifique au patient (Sahani et al., 2024 ; Virgilio et al., 2015) ou générique (Konno et al., 2021), selon quelques paramètres d'entrée. Cette fonctionnalité permet d'étudier différents phénotypes musculaires. De plus, la géométrie obtenue contient un composant supplémentaire entre les fibres et la MEC qui n'est généralement pas représenté dans les modèles musculaires (Loumeaud et al., 2024 ; Virgilio et al., 2015), bien qu'il soit impliqué dans les voies pathologiques (Sahani et al., 2022 ; Virgilio et al., 2015).

Cet algorithme permet la génération périodique en 3D d'un RVE du muscle squelettique à l'échelle microscopique, compatible avec l'approche DFE² présentée au chapitre 3. Il comprend des fonctionnalités personnalisées qui permettent la représentation de différents phénotypes musculaires, tout en offrant des fonctionnalités permettant de résoudre les problèmes numériques. Tous les composants sont modélisés par une loi de comportement HGO (Holzapfel et al., 2000) qui permet de représenter des matériaux renforcés de fibres et fournit des paramètres physiques structurels et interprétables. Sur la base de ces résultats, l'étape suivante (chapitre 5) consiste à assembler cette RVE dans le modèle musculaire DFE² et à l'appliquer pour contrôler les géométries et les propriétés mécaniques des muscles Klf10 KO sur la base de nos propres expériences (Kammoun et al., 2016, 2017 ; Tatarenko et al., 2024).

Résumé du chapitre 5

Dans ce chapitre, notre modèle a reproduit des essais expérimentaux de traction uniaxiale sur des muscles entiers. Nous avons d'abord reproduit des essais de traction sur fibre isolée, ce qui nous

a permis d'identifier les paramètres mécaniques des fibres rapides et lentes contenues dans le VER. Grâce à la reproduction numérique d'essais expérimentaux de tractions musculaires sur le muscle soléaire, nous avons identifié plusieurs sets de paramètres mécaniques et structuraux liés à la MEC. Les ensembles de paramètres de la solution ne sont pas uniques et ne peuvent fournir la valeur exacte des propriétés mécaniques pour l'un ou l'autre génotype, mais indiquent plutôt leur ordre de grandeur et leurs variations potentielles. Cependant, notre analyse a montré une diminution des propriétés mécaniques liées au collagène du muscle soléaire KO, ce qui nous permet d'attester que les propriétés mécaniques de la MEC sont fortement influencées par le gène Klf10. Plus précisément, nous formulons les deux hypothèses suivantes : (i) la délétion génétique affecte la densité des fibres de collagène ; (ii) la délétion génétique affecte les propriétés mécaniques des fibres de collagène.

Nous avons mis en évidence que le comportement mécanique musculaire dépend de l'expression du gène Klf10, et supposons que son influence s'exerce principalement sur la densité ou les propriétés mécaniques des fibres de collagènes de la MEC qui présentent environ une diminution d'environ 40% de leur rigidité dans le cas Klf10-KO.

Pour tester ces hypothèses, des protocoles d'imagerie par Microscopie à Balayage Electronique (MEB) en collaboration avec la Mayo Clinic et d'immunohistologie en collaboration avec Cochin ciblant l'étude du collagène dans les muscles murins ont été mis en place et des données préliminaires déjà acquises. Nous appliquerons ensuite le modèle à un autre muscle squelettique de souris : l'Extensor Digitorum Longus (EDL).

Notre approche originale et notre modèle présentent de nombreuses limites, notamment en raison des différentes stratégies utilisées pour réduire la taille du modèle. Bien que la même stratégie ait été appliquée aux deux génotypes, les biais liés aux dimensions du RVE et au maillage du modèle à grande échelle pourraient fortement influencer les résultats décrits ici et devraient être pris en compte dans les travaux futurs. De plus, aucune évaluation du modèle sous différentes sollicitations n'a été effectuée en raison du manque de données expérimentales, autre aspect important à prendre en compte dans les travaux futurs.

Cependant, l'analyse du champ de contraintes à échelle microscopique a révélé que la MEC supporte la plupart des contraintes axiales et de cisaillement, soulignant ainsi l'importance de la contribution de ce composant à la mécanique globale du muscle. Ces conclusions concordent avec les fonctions de la MEC décrites au chapitre 1, et en particulier la transmission des forces latérales par cisaillement. À notre connaissance, aucune analyse de ce type n'a encore été réalisée à l'aide d'un modèle de muscle squelettique à plusieurs échelles.

Conclusions & perspectives

La complexité des propriétés mécaniques du muscle squelettique résulte de la contribution de divers microconstituants organisés selon une structure hiérarchique comprenant plusieurs échelles. Un lien peut être établi entre l'état de santé du muscle et ses propriétés mécaniques, ces dernières devenant des marqueurs intéressants pour l'étude des états de santé altérés. Bien que les muscles squelettiques contiennent de nombreux composants, seuls quelques-uns d'entre eux contribuent à la plupart des propriétés mécaniques qui en résultent : en particulier, à travers les différentes échelles, la matrice extracellulaire (MEC), divisée en trois composants différents que sont l'endomysium (échelle microscopique), le périmysium (échelle mésoscopique) et l'épimysium (échelle macroscopique), a récemment été mise en avant pour sa contribution significative au comportement mécanique des muscles squelettiques. Cependant, les propriétés mécaniques isolées de ces composants sont difficiles à obtenir expérimentalement (Binder-Markey et al., 2021), ce qui conduit à l'utilisation de méthodes innovantes telles que la modélisation multi-échelle pour les calculer indirectement (Loumeaud et al., 2024).

Dans cette thèse, nous évaluons l'effet de la délétion génétique Klf10 sur les propriétés mécaniques des muscles squelettiques murins. Des études *ex vivo* antérieures ont révélé à la fois une influence du gène sur les propriétés mécaniques des fibres musculaires isolées (à l'échelle microscopique) et une absence d'influence significative sur les propriétés mécaniques globales du muscle (Tatarenko et al., 2024). Cela suggère l'existence d'un mécanisme de compensation potentiel, peut-être sous la forme d'une altération des composants de la MEC. Deux axes de recherche ont donc été développés dans cette thèse : premièrement, l'étude des propriétés mécaniques *in vivo* de muscles entiers à l'aide de l'élastographie par résonance magnétique (MRE) afin d'observer pour la première fois les effets de la délétion génétique *in vivo*, indépendamment des conditions expérimentales *ex vivo* ; et deuxièmement, l'étude indirecte des propriétés mécaniques de la MEC à l'aide d'une modélisation numérique multi-échelle couplée aux résultats expérimentaux *ex vivo*.

La première contribution de cette thèse de doctorat est le développement d'un protocole MRE pour l'étude *in vivo* du muscle squelettique murin (Loumeaud et al., 2025). Nous avons démontré que ce protocole était reproductible. Le protocole a été appliqué à deux cohortes de souris génétiquement différentes, dans deux positions différentes (flexion, extension) pour trois fréquences d'excitation différentes. Les résultats ont mis en évidence une différence de rigidité des muscles extenseurs en position d'extension chez les souris Klf10 KO. Cela ouvre la voie à d'autres expériences à réaliser avec le protocole développé. De plus, même si cet aspect n'a pas été développé dans le présent manuscrit, nous tenons à souligner que nos mesures de répétabilité et de reproductibilité à l'aide de ce protocole

renforcent la crédibilité de nos résultats expérimentaux et offrent une garantie lors du partage du protocole et de la configuration avec des collaborateurs scientifiques, car ces aspects sont rarement étudiés dans la littérature. De plus, le dispositif expérimental et le protocole sont adaptables à une grande variété d'organes, ce qui nous permettra à l'avenir d'étudier l'effet du gène Klf10 dans différents organes tels que le foie. Les développements actuels concernent également différents organes ou matériaux biomécaniques tels que les éponges hémostatiques ou les fantômes, ce qui souligne l'intérêt de nos développements pour la communauté scientifique.

Cependant, cette thèse s'est principalement concentrée sur le développement du modèle multi-échelle. Compte tenu des données expérimentales disponibles, de nombreux choix s'articulent autour de l'idée de séparer les effets géométriques et mécaniques du gène Klf10 à l'échelle microscopique. En effet, les données disponibles sur la géométrie et la structure microscopiques sont suffisantes pour générer une géométrie micro-échelle spécifique au génotype (Kammoun et al., 2016, 2017). Il en résulte que moins de paramètres doivent être identifiés ; de plus, la plupart de ces paramètres sont associés à des propriétés mécaniques interprétables. Pour construire une telle géométrie, un pipeline original de génération de géométrie périodique a été développé, intégrant des distributions probabilistes concernant la géométrie et les caractéristiques des différents composants, ce qui facilite la mise en œuvre numérique. Cette géométrie contient trois composants à l'échelle microscopique : les fibres musculaires (lentes, rapides), l'endomysium et une zone de transition qui peut être utilisée de nombreuses façons. La zone de transition peut contribuer à réduire les instabilités numériques au sein de la simulation en utilisant un gradient de propriétés mécaniques ; cependant, elle peut être modifiée pour représenter plus précisément le lien entre la MEC et les fibres musculaires (costamères), contenant des protéines transmembranaires. Ces protéines sont impliquées dans des voies pathologiques telles que la dystrophie musculaire de Duchenne (DMD), dans laquelle leur densité diminue considérablement (Virgilio et al., 2015). Il est intéressant de noter que cette composante n'est pas toujours représentée dans les modèles multi-échelles étudiant la DMD (Sahani et al., 2024). Si des analyses plus approfondies sur les muscles Klf10 KO révèlent un effet sur cette composante, le modèle pourra être adapté afin de modifier la contribution des protéines transmembranaires. De plus, un tel matériau de transition a également fait l'objet d'une publication dans le contexte de la génération de RVE pour les composites renforcés de fibres fabriqués industriellement (Riaño & Joliff, 2019), car il représente les effets physiques du processus de fabrication localisés autour des fibres. Cela indique que notre pipeline de génération de géométrie peut contribuer non seulement à une étude plus large des troubles musculaires squelettiques, mais aussi à différents domaines utilisant des outils similaires pour mener leurs recherches.

Pour représenter le comportement mécanique des différents composants, nous avons choisi le modèle HGO (Holzapfel et al., 2000), car ce modèle est adapté aux matériaux renforcés de fibres. Nous avons adapté une subroutine (UMAT) existante (Castillo-Méndez & Ortiz, 2022a) en incluant une deuxième famille de fibres pour le matériau ECM et en codant la localisation des points d'intégration de la zone de transition dans le modèle final. Cette dernière contribution permet de calculer un gradient de propriétés mécaniques ou de modéliser des protéines transmembranaires, car elle fournit un vecteur pointant de la frontière de la fibre musculaire vers l'ECM au point d'intégration actuel. Cette méthode fournit également le type de fibre musculaire associée, de sorte que le comportement de la couche de transition peut être rendu dépendant du type de fibre musculaire. Cela permet de modéliser des conditions dépendantes des fibres musculaires.

Afin de relier notre RVE à l'échelle microscopique à la géométrie musculaire à l'échelle macroscopique, une méthode existante appelée Direct Finite Element Square (DFE²) (Tan et al., 2020) a été adaptée à notre géométrie et évaluée pour les matériaux hyperélastiques soumis à de grandes déformations. Les principales motivations derrière le choix de cette méthode étaient l'utilisation d'une géométrie complexe pour le RVE, qui s'est avérée incompatible avec les méthodes d'homogénéisation analytiques, et la nécessité d'une localisation, afin de permettre l'accès aux champs de contraintes microscopiques. Cette dernière nous permet d'évaluer si une certaine géométrie subit des contraintes nettement plus élevées ou si les modèles de répartition des contraintes sont différents. En fonction des résultats, cette méthode peut aider à détecter des lésions microscopiques dans le matériau biologique. Là encore, l'approche développée n'est pas spécifique au muscle squelettique et peut être adaptée à n'importe quel matériau. À l'aide de cette approche, nous avons comparé les simulations d'extension uniaxiale du muscle soléaire pour les deux génotypes (Pouletaut et al., 2023).

Un premier résultat encourageant a été la capacité du modèle à fournir un bon accord avec les données expérimentales. Étonnamment, plusieurs relations ont été trouvées entre les 4 paramètres du modèle, ce qui a donné lieu à de nombreux ensembles de données différents comme solutions.

De plus, la littérature sur ces paramètres est rare et très hétérogène et ne fournit donc aucune indication sur les ensembles de paramètres qui pourraient être les plus proches de la réalité. Nous avons essayé de distinguer ces ensembles de paramètres en analysant les champs de contrainte à l'échelle microscopique, mais les résultats sont assez homogènes. Il n'est donc pas possible de tirer de conclusion quant aux valeurs absolues des paramètres mécaniques de la MEC. Étonnamment, le paramètre d'orientation des fibres de collagène θ n'a pas eu d'effet significatif sur le comportement mécanique obtenu, contrairement aux résultats précédents obtenus à l'aide d'une approche différente qui ne faisait pas la distinction entre la contribution géométrique et mécanique et ne fournissait pas

de localisation (Tatarenko, 2023). Nous pouvons donc conclure que l'approche de modélisation que nous utilisons a un effet significatif sur les paramètres obtenus et les interprétations qui peuvent en être tirées. Nous devons donc être très prudents quant aux conclusions tirées de la modélisation multi-échelle et nous concentrer sur la formulation d'hypothèses à confirmer par des protocoles expérimentaux.

Néanmoins, les résultats numériques ont mis en évidence que la principale structure supportant les contraintes est constituée par les fibres de collagène contenues dans la MEC, et nous avons montré que leur comportement mécanique est plus souple dans les muscles Klf10 KO. Ces résultats suggèrent deux hypothèses : soit la densité des fibres de collagène est réduite dans les muscles soléaires Klf10 KO, soit les propriétés mécaniques des fibres de collagène sont altérées. Cela pourrait correspondre à nos observations *in vivo*, car la MEC fonctionne par déformations de cisaillement (Lieber & Binder-Markey, 2021). Il est très intéressant de noter que notre analyse a également montré que le comportement mécanique des fibres musculaires est négligeable par rapport à la contribution mécanique de la MEC pour l'extension uniaxiale du muscle squelettique. Cela signifie que le mécanisme de compensation que nous étudiions n'existe pas, car la MEC supporte la majeure partie de la charge à l'échelle macroscopique. Par conséquent, une MEC saine présentant les mêmes caractéristiques mécaniques et structurelles pourrait être présente dans les deux génotypes. Cependant, nous avons mis en évidence des différences dans les paramètres mécaniques de la MEC lorsque nous avons ajusté notre modèle aux données expérimentales moyennes sur les muscles soléaires des deux origines génétiques, ouvrant la voie à de nouvelles recherches sur l'effet de la délétion génétique Klf10 sur la MEC.

Notre approche a constitué la première étape vers l'identification des voies et des composants spécifiques affectés par la délétion génétique, ce qui nous a permis de choisir les protocoles appropriés pour poursuivre nos recherches sans sacrifier d'animaux à ce stade. Nous avons montré que les résultats détournaient l'attention vers les fibres de collagène contenues dans la MEC. À la suite de cette étude indirecte de la MEC, des expériences de caractérisation directe menées en collaboration avec la clinique Mayo et l'Institut Cochin (CNRS, Inserm, Paris) se concentreront sur l'étude du collagène. La microscopie électronique à balayage (Tateya et al., 2007), réalisée à la Mayo Clinic, permettra d'acquérir des images de la MEC, à partir desquelles il sera possible d'estimer les paramètres structurels et texturaux ainsi que la densité du collagène. Les analyses immunohistochimiques et la microscopie multiphotonique à l'Institut Cochin se concentreront sur la quantification de la quantité de collagène en fonction du type, sur des coupes histologiques. Ces mesures peuvent fournir des

166

informations sur les paramètres structurels qui peuvent être fixés dans la simulation, limitant ainsi l'espace des paramètres.

Dans une première perspective à court terme, nous avons réalisé des expériences *in vivo* supplémentaires sur les membres postérieurs de souris afin d'augmenter la puissance statistique de notre analyse et d'être en mesure d'évaluer la signification de nos résultats.

Une deuxième perspective à court terme consiste à appliquer notre modèle au muscle EDL, afin de voir si des conclusions similaires peuvent être tirées. Cependant, dans l'état actuel du modèle, le RVE est constitué de fibres parallèles à l'axe musculaire, ce qui est vrai pour le soléaire, mais faux pour l'EDL, raison pour laquelle le soléaire a été privilégié dans le cadre de cette thèse. Dans l'EDL, l'angle de pennation est d'environ 10° (Chleboun et al., 1997). Il pourrait donc être intéressant de modifier d'abord l'algorithme de génération de la géométrie afin d'intégrer cette orientation dans le RVE. Cela peut être réalisé en générant un RVE plus grand qui serait découpé à l'aide d'une bounding box correctement orientée.

Une autre perspective pour le modèle consiste à modifier la UMAT afin d'inclure le comportement actif des muscles squelettiques. En effet, des données expérimentales actives pour les muscles et les fibres musculaires ont été acquises et publiées (Kammoun et al., 2021) et peuvent être implémentées dans le modèle. De plus, comme l'ECM est un composant passif, ces ensembles de données peuvent en fait être utilisés pour valider les ensembles de paramètres identifiés au cours de cette thèse. À cette fin, des paramètres supplémentaires peuvent être transmis à la UMAT et une contrainte supplémentaire dépendant du temps d'activation/de simulation actuel peut être ajoutée à la contrainte passive de Cauchy (Spyrou et al., 2019).

Avec cette notion d'activation, nous introduisons la notion de temps dans le modèle. Bien que la plupart des modèles multiscalaires actifs du muscle squelettique soient hyperélastiques et ne prennent en compte le temps qu'indirectement (He et al., 2022 ; Konno et al., 2021 ; Spyrou et al., 2017, 2019 ; Teklemariam et al., 2019), les données expérimentales montrent un comportement visqueux (Tatarenko et al., 2024), que nous avons négligé au cours de cette thèse. Afin de tirer pleinement parti des données expérimentales à notre disposition, nous pouvons envisager d'étendre le modèle à un comportement viscohyperélastique et d'élargir les ensembles de données expérimentales pour inclure des tests à différentes vitesses. La méthode DFE² a désormais été évaluée pour les comportements hyperélastiques anisotropes et viscoélastiques (Tan et al., 2020 ; Zhi et al., 2021 ; Zhi, Yang, et al., 2023), mais la combinaison des deux n'a pas encore été testée. Cela n'entraînerait aucun changement dans la géométrie ou l'algorithme de transition d'échelle, mais

constituerait une modification fondamentale de l'UMAT, car les équations permettant de calculer les contraintes pour un tel matériau sont beaucoup plus complexes que pour un matériau hyperélastique, d'où la rareté des modèles biomécaniques viscohyperélastiques dans la littérature. Cela constituerait globalement une contribution très originale et très utile au projet et à la littérature scientifique en général.

Pour conclure, au-delà des outils novateurs expérimentaux (dispositif ERM petit animal à 7T adaptable à de multiples organes) et numériques (approche multiéchelle originale tant à l'échelle microscopique par son VER que par la transition vers l'échelle macroscopique par la méthode DFE²) développés, cette thèse a mis en évidence non seulement la possibilité d'investiguer *in vivo* le muscle squelettique, mais également de déduire par la modélisation numérique les propriétés de la MEC musculaire, encore largement méconnue. Plus encore, le lien et les effets du gène Klf10 ont pu être clairement identifiés au travers des différentes échelles musculaires, constituant un pas majeur dans la compréhension des effets de ce gènes non seulement sur la biomécanique et les caractéristiques musculaires, mais plus largement sur l'homéostasie métabolique impliquée.

Finalement, les outils développés ne sont pas spécifiques à notre application, et peuvent être utilisés dans d'autres contexte comme l'étude des maladies musculaires telles que la myopathie de Duchenne, ou bien la caractérisation multiéchelles de matériaux renforcés de fibres longues.

Appendix A : Experimental characterization of the extracellular matrix

Annex 1. Experimental methods applied to ECM in non-murine species. T1: composition characterization. T2: structure characterization. T3: mechanical properties characterization. Scales: (1) macroscopic, (2) mesoscopic, (3) microscopic

Study	Type + Technique	ECM Structures	Species	Dim.	Scale
Purslow 1989	Light microscopy (T2)	Perimysium, perimysial collagen cables	Ox	2D	2
Purslow 1989	High angle X-ray diffraction (T1)	Collagen	Ox	2D	2
Trotter 1990	SEM micrographs (T2)	Endomysium	Cat	2D	3
Trotter 1990	TEM micrographs (T2)	Endomysium	Cat	2D	3
Trotter & Purslow 1992	SEM micrographs (T2)	Endomysium	Cat	2D	3
Trotter & Purslow 1992	TEM micrographs (T2)	Endomysium	Cat	2D	3
Purslow & Trotter 1994	SEM micrographs (T2)	Endomysium, endomysial collagen fibers	Ox	2D	3
Smith *et al.* 2021	High performance liquid chromatography (HPLC) (T1)	Collagen cross links, collagen content	Human	0D	2
Smith *et al.* 2021	Absorbance measurements (T1)	Proteoglycan and glycosaminoglycan content	Human	0D	2
Smith *et al.* 2021	TEM micrographs for stereological analysis (T2)	ECM components volume fraction	Human	3D	2,3
Smith *et al.* 2021	Transcriptional analysis from GEO datasets (T1)	Genes related to ECM expression	Human	0D	5
Sanden *et al.* 2021	Polarized fluorescence microscopy (T1, T2), staining (WGA, HE, Picrosirius red) (T1)	Collagen fibers, fibers thickness in perimysium	Chicken	2D	2
Sanden *et al.* 2021	FTIR microspectroscopy (T1)	Collagen triple helix structure, collagen cross link maturity	Chicken	2D	2
Sanden *et al.* 2021	Polarized FTIR imaging (T1, T2)	Collagen fiber orientation	Chicken	2D	2
Kuravi *et al.* 2021B	Biaxial testing on decellularized ECM (T3)	Stress-strain behavior	Pork	3D	1
Kohn *et al.* 2021	Picrosirius red staining + light microscopy on fresh and decellularized muscle cross-sections (T1,T2)	Endomysium and perimysium	Pork	3D	3
Kohn *et al.* 2021	Tension and compression experiments on fresh and decellularized muscle samples with different fibre orientation (0 °, 45 °, 90 °) (T3)	Endomysium and perimysium stress-strain behavior	Pork	3D	1

Study	Type + Technique	ECM Structures	Muscles	Dim.	Scale
Wheatley *et al.* **2023**	SEM micrographs (T2) + mechanical uniaxial tensile testing (T3)	Epimysium thickness, waviness ratio, stress strain behavior	Pork	2D	1

Annex 2. Experimental methods applied to murine ECM. T1: composition characterization. T2: structure characterization. T3: mechanical properties characterization. Scales: (1) macroscopic, (2) mesoscopic, (3) microscopic, (4) submicron, (5) nanoscopic. Muscle abbreviations: Extensor Digitorum Longus (EDL), Soleus (SO), Tibialis Anterior (TA) Rectus Femoris (RF), semimembranosus (SM), and Lateral Gastrocnemius (LG)

Study	Type + Technique	ECM Structures	Muscles	Dim.	Scale
Smith & Barton 2014	Light microscopy (T2) + picrosirius red staining (T1)	ECM/collagen	EDL, SO, diaphragm	2D	3
Smith & Barton 2014	Hydroxyproline assay (T1)	collagen	EDL, SO, diaphragm	0D	1
Smith & Barton 2014	Active and passive mechanical tests (T3)	Whole muscle ECM	EDL, SO, diaphragm	3D	1
Wood *et al.* **2014**	Light microscopy (T2) + picrosirius red staining (T1)	ECM/collagen	TA	2D	3
Wood *et al.* **2014**	Fluorescence microscopy (T1, T2)	ECM/collagen	TA	2D	3
Wood *et al.* **2014**	Polarized light microscopy (T2) + picrosirius red staining (T1)	ECM orientation	TA	2D	3
Wood *et al.* **2014**	Hydroxyproline assay (T1) + other assays (T1)	Collagen + AGEs content	TA	0D	1
Wood *et al.* **2014**	Uniaxial tension on muscle fibers and fiber bundles (T3)	Whole muscle ECM	TA	3D	2,3
Stearns-Reider *et al.* **2017**	Second harmonic generation microscopy (SHG) imaging (T1, T2)	Elastin and collagen orientation	Gastrocnemius	3D	2
Stearns-Reider *et al.* **2017**	Light microscopy (T2) + Herovici (collagen III) and Verhoeff van Gieson (elastin) staining (T1)	Collagen III and elastin content	Gastrocnemius	2D	1
Stearns-Reider *et al.* **2017**	Biaxial mechanical testing (T3)	Whole muscle ECM	Gastrocnemius	3D	1
Gillies *et al.* **2017**	Scanning Electron Microscopy (T2)	Perimysial cables, collagen fibers	EDL	2D	3
Gillies *et al.* **2017**	Confocal microscopy (T2) + fluorescence (T1) + uniaxial stretch (T3)	Perimysial cables, type I collagen	EDL	2D	3
Gillies *et al.* **2017**	TEM (T2) for stereology analysis (T1 + T2)	Quantity and CSA of perimysial cables, components volume fraction	EDL	3D	3
Gillies *et al.* **2014, 2017**	Serial block face scanning electron microscopy (SBEM) (T2)	Perimysial cables	EDL	3D	3
DiMario 2018	Immunostaining + fluorescence microscopy (T2)	Laminin	Diaphragm + TA	2D	3
DiMario 2018	Hydroxyproline assay (T1)	Collagen content	Diaphragm + TA	0D	1
DiMario 2018	Grip strength (T3)	Whole muscle ECM	Diaphragm + TA	3D	1

Binder-Markey *et al.* **2020**	Hydroxyproline assay (T1)	Collagen content	RF, SM, TA, LG	0D	1
Binder-Markey *et al.* **2020**	Light microscopy (T2) + picrosirius red staining (T1)	ECM/collagen	RF, SM, TA, LG	2D	1
Lofaro *et al.* **2021**	Mass spectroscopy (T1)	Collagens, glycoproteins, proteoglycans, ECM regulators	Gastrocnemius	0D	1
Lofaro *et al.* **2021**	TEM (T2)	Basement membrane and endomysium thickness, size and tortuosity of perimysial collagen bundles	Gastrocnemius	2D	2, 3
Lofaro *et al.* **2021**	Fluorescence microscopy (T1, T2)	collagen VI, laminin, collagen I	Gastrocnemius	2D	2, 3
Sahani *et al.* **2021**	scanning electron microscopy (SEM) (T2)	collagen fiber direction, alignment, and straightness	diaphragm	2D	1
Brashear *et al.* **2021, 2022**	Active test: isometric contraction; Passive test: stress-relaxation (T3)	Whole muscle ECM	SO, EDL	3D	1
Brashear *et al.* **2021, 2022**	Hydroxyproline assay (T1)	Collagen content	SO, EDL	0D	1
Brashear *et al.* **2021**	Polarized light microscopy (T2) + picrosirius red staining (T1)	ECM orientation	SO, EDL	2D	2
Brashear *et al.* **2021, 2022**	Second harmonic generation microscopy (SHG) at 870 and 830 nm (T2)	Collagen fibers, sarcomeres orientation	SO, EDL	3D	2
Olesen *et al.* **2022**	Lateral force transmission (T3)	Whole muscle ECM	SO	3D	1
Olesen *et al.* **2022**	Stretch-release test (T3)	Whole muscle ECM	Gastrocnemius, plantaris, SO	3D	1
Olesen *et al.* **2022**	Polarized light microscopy (T2) + picrosirius red staining (T1)	ECM orientation	Gastrocnemius, plantaris, SO	2D	2
Olesen *et al.* **2022**	Fluorometry (T1)	Hydroxyproline content Advanced glycation end- products (AGEs)	Gastrocnemius	0D	1
Wohlgemuth *et al.* **2023, 2024**	Hydroxyproline assay + collagen solubility protocol (T1)	Collagen content and cross-linking	SO, EDL, diaphragm	0D	1
Wohlgemuth *et al.* **2023**	Fluorescence microscopy (T2) + immunostaining (T1)	Cellular components	TA	2D	3
Wohlgemuth *et al.* **2023, 2024**	Polarized light microscopy (T2) + picrosirius red staining (T1)	Collagen	SO, EDL, diaphragm	2D	3
Wohlgemuth *et al.* **2023, 2024**	Stretch relaxation tests on whole muscle intact, after decellularization or after collagenase (T3)	Whole muscle ECM	SO, EDL, diaphragm	3D	1
Danesini *et al.* **2024**	Mechanical uniaxial testing of fiber bindles in presence or absence of	Lateral force transmission through endomysium	EDL	3D	3

	incision in the endomysium (T3)	

Appendix B : Multiscale skeletal muscle models

Annex 3. Characteristics of skeletal muscle multiscale models published in the literature in chronological order. It includes 11 entries for each model, which are (1) the reference of the model, (2) a short description of the model, (3) indications about the isotropic part of the model concerning the extracellular matrix, (4) indications about the anisotropic part of the model concerning the extracellular matrix, (5) indications about the isotropic part of the model concerning the muscle fiber, (6) indications about the anisotropic part of the model concerning the muscle fiber, (7) the modeled constituents, (8) the scale transition method, (9) the reference for the experimental datasets used for identification of the model, (10) the FE solver used, and (11) the reference for the experimental datasets used for validation of the model.

Studies	Description	ECM Law & Parameters		Fibers Law & Parameters		Components	Scale transition	Study used for identification	FE solver	Study used for validation
		Isotropic part	Anisotropic part	Isotropic part	Anisotropic part					
Ceelen et al. 2008	Chemo-mechanical model of hypoxia in muscles due to muscle compression	Neo-Hookean		Neo-Hookean		ECM, Fibers, Capillaries	Averaged results	Bosboom et al. (2001) Damage : Labbe et al. (1987)		
Röhrle et al. 2008, 2012		Passive Mooney-Rivlin (1st order)			Passive & active normalized force length relationships	Fibers, ground matrix, sarcomeres	Concurrent numerical homogenization	Shorten et al. (2007)	Open CMISS	
Sharafi & Blemker 2010	3-scale model to study variations of the microstructure		Model of Blemker et al. (2005)		Model of Blemker et al. (2005)	Fibers, ECM, fascicles	Periodic homogenization		Matlab	
Sharafi et al. 2011	Study of force transmission in a realistic fascicle geometry		Model of Blemker et al. (2005)		Model of Blemker et al. (2005)	Fibers, ECM	Periodic homogenization	parameters taken from the literature	Matlab, NIKE3D	
Gindre et al. 2013	tension compression model		Force generated by wavy collagen helices		Wormlike chain model of titin	ECM, Fiber, Titin, Collagen	Homogenization: Voigt / mixture law	parameters taken from the literature	Matlab	Takaza et al. (2013), Calvo et al. (2010), Morrow et al. (2010), Nie et al. (2011), Yamada (1970), Martins et al. (1998), Van Loocke et al.

										(2006), Grieve and Armstrong (1988), Vannah and Childress (1993), Zheng et al. (1999)
Heidlauf et al. 2013		Passive Mooney-Rivlin (1rst order)		Passive Mooney-Rivlin (1rst order)	Passive part model of Markert et al. () + active part model of Röhrle et al. (2012)	ECM, Fast & slow fibers, Sarcomeres	Concurrent numerical homogenization	Shorten et al. (2007)	Open CMISS	
Virgilio et al. 2015	Study of Duchenne Muscular Dystrophy with AI generated geometry		Model of Blemker et al. (2005)		Model of Blemker et al. (2005)	Fibers, ECM, fat, dystrophin	Averaged results		NIKE3D	
Roux et al. 2016	Discrete Element Method	Hookean at microscopic scale + accounting for collagen toe region, Ogden at macroscopic scale		Hookean at microscopic scale, Ogden at macroscopic scale		ECM, Collagen Fibers, Tendons, Epimysium	Identification	Matscheke et al. 2013 Regev et al. 2011	GranOO	
Heidlauf et al. 2016, 2017, Schmid et al. 2019	Model based on sliding-filament & cross-bridge theory	Passive Mooney-Rivlin (1rst order)		Passive Mooney-Rivlin (1rst order)	Model of Heidlauf et al. (2016) + active contribution of actin-titin interaction	ECM, Fast & slow fibers, Sarcomeres Titin	Concurrent numerical homogenization	Shorten et al. (2007)	Open CMISS	
Spyrou et al. 2017	Homogenized muscle model	Neo-Hookean	Gindre et al. (2013)	Neo-Hookean	Active part: normalized weibull distribution (Ehret 2011) and hyperbolic function Böl et al. (2008), Van Leeuwen et al. (1997) Passive part: linear fonction Blemker et al. (2005)	Fibers, ECM	Analytical homogenization + numerical periodic homogenization	parameters taken from the literature	ABAQUS	Hawkins & Bey 1994
Marcucci et al. 2017	Passive 3D FE model based on Hill model				Hill model, using quadratic and exponential	Fibers	Averaged results	Botinelli et al. 1996, He et al. 2000	ABAQUS	

					formulations for the elements					
Marcucci et al. 2019	Passive 3D Hill model with separate contributions of muscle fibers and ECM	Isotropic element in parallel to the Hill model, with exponential behavior			Hill model, using quadratic and exponential formulations for the elements	Fibers, ECM	Averaged results	Own experiments	ABAQUS	
Bleiler et al. 2019	Description of the passive behaviour of skeletal muscle tissue	Neo-Hookean	Lanir et al. 1983	Neo-Hookean	-	Fibers, ECM	Voigt-type homogenization	Holzapfel et Weizsäcker 1998, Holzapfel et al. 2005, Purslow & Trotter 1994, Light & Champion 1984, Light et al. 1985, Mohammadkhah et al. 2018	Open CMISS	Hawkins & Bey 1994, Morrow et al. 2010, Calvo et al. 2010, Takaza et al. 2013
Spyrou et al. 2019		Neo-Hookean	Gindre et al. (2013)	Neo-Hookean	Active part: normalized weibull distribution (Ehret 2011) and hyperbolic function Böl et al. (2008), Van Leeuwen et al. (1997) Passive part: linear fonction Blemker et al. (2005)	Fibers, ECM	Analytical homogenization + numerical periodic homogenization	Hawkins & Bey 1994	ABAQUS	Morrow et al. 2010
Teklemariam et al. 2019	model of motor unit remodeling with age	Mooney-Rivlin (2nd order)		Yeoh model	Second order polynomial (passive) + active stress in fiber direction	Fibers, ECM, tendon	Averaged results	Bosboom et al. 2001; Chi et al. 2010; Prado et al. 2005	Comsol Multiphysics	

Reference	Model	Col3	Col4	Col5	Col6	Components	Method	Col9	Software	Col11
Carriou et al. 2019	Hill-inspired model detailing the electromechanical behavior of the muscle based on the Huxley formulation					Motor Unit contractile elements repeated in parallel to constitute the muscle, including calcium dynamics for activation	Averaged results	Benoussaad et al. 2013		Benoussaad et al. 2013
Spyrou et al. 2020	Muscle fibers, intramuscular connective tissue (IMCT), intramuscular fat (IMF)	Neo-Hookean IMCT	Lanir et al. 1983, Gasser et al. 2006	Neo-Hookean	standard reinforcement model Lopez-Pamies et al. 2010			Böl et al. 2019, van der Rijt et al. 2006, Holzapfel et al. 2005, Purslow 1989, Purslow & Trotter 1994, Gefen et Dilmoney 2007	ABAQUS	Morrow et al. 2010
Zhang et al. 2020	Young, Adult & Old models	cubic polynomial hyperelastic model		Mooney-Rivlin (2nd order)	Model of Blemker et al. 2005	Fibers, ECM	Averaged results	Parameters from the literature		Hawkins & Bey 1994, Morrow et al. 2010 Calvo et al. 2010
Roux et al. 2021	Discrete element model of active muscle	Hookean at microscopic scale, Ogden at macroscopic scale		Hookean at microscopic scale, Ogden at macroscopic scale + force length relationship as parabolic curve (Winter et al. 2010, Mohammed et al. 2016)		Fibers, ECM, tendon	Averaged results	Matscheke et al. 2013 Regev et al. 2011 Winters & Stark 1988 Gordon et al. 1966 Winters et al. 2011	GranOO	
Lamfuss & Bargmann 2021	Fascicle modeling, effect of pennation angle	Endomysium Ogden (1rst order)		Passive part: Neo Hookean	Active part: Heidlauf & Röhrle 2013	Fibers, ECM	Numerical homogenization	Haug et al. 2018, Meyer et Lieber 2011; Kammoun et al. 2019, Schneidereit et al. 2018		

| Reference	Model	Matrix model	Collagen/fiber model	Fiber model	Active/passive formulation	Constituents	Homogenization	Parameters source	Software	Validation
Liu et al. 2022	Model to study shear loading	Neo-Hookean	Type I collagen model with exponential + polynomial formulations	Neo-Hookean	Exponential + polynomial formulations	Fibers, ECM	Numerical periodic homogenization	Smith et al. 2011, Böl et al. 2019, own experiments	ABAQUS	Morrow et al. 2010, own experiments
Konno et al. 2021	Model to study cerebral palsy	Yeoh model	Simo et al. 1992	Yeoh model	Simo et al. 1992 + polynomial passive part + trigonometric active part	ECM, Fibers (Active & passive)	Voigt-type homogenization	Gillies et al. 2011, Winters et al. 2011, Mohammadkhah et al. 2016	Deal II	Takaza et al. 2013, Mohammadkhah et al. 2016
Kuravi et al. 2021 a	Constitutive model of the extracellular matrix	Rubin & Bodner, 2002	Holzapfel et al. 2015	Neo-Hookean	Exponential Holzapfel 2000	ECM, Fibers, Collagen	Numerical periodic homogenization	Böl et al. 2019	ABAQUS	Van Loocke et al. 2006, Böl et al. 2012, Böl et al. 2019
Kuravi et al. 2021 b	Constitutive model of the extracellular matrix	Rubin & Bodner, 2002	Holzapfel et al. 2015 + contributions for shear modeling	Neo-Hookean	Exponential Holzapfel 2000	ECM, Fibers, Collagen	Numerical periodic homogenization	Böl et al. 2019, Kohn et al. 2021	ABAQUS	Own experiments
He et al. 2022	Young, Adult & Old models	Mooney-Rivlin (3rd order)	Lanir et al. 1983, Bleiler et al. 2019, Spyrou et al. 2019, exponential formulation for collagen helices	Mooney-Rivlin (2nd order)	Exponential passive part + Polynomial active part	ECM, Fibers, Tendons	Numerical periodic homogenization	Spyrou et al. 2019 Zhang et al. 2020	ABAQUS	Calvo et al. 2010
Terzolo et al. 2022	Model of human vocal folds	Neo-hookean	Orgeas et al. 1998	Neo-hookean	Orgeas et al. 1998 + repulsive interactions between myofibrils	Fibers, ECM, myofibrils, collagen	Caillerie et al. 2006	Cochereau et al. 2020		
Lamfuss et al. 2022	Model of damage initiation & rupture of activated muscle fibers resulting from eccentric contractions	Endomysium Ogden (1rst order)		Passive part: Neo Hookean	Active part: Heidlauf & Röhrle 2013 + titin force enhancement (Cankaya et al. 2021) + anisotropic damage model	Fibers, ECM	Numerical homogenization	Haug et al. 2018, Meyer et Lieber 2011; Meyer et al. 2011, Schneidereit et al. 2018,		

	formation of microcracks							Cankaya et al. 2021		
Lamfuss et al. 2023	Model of thermal treatments	Endomysium Ogden (1rst order) Thermomechanical & thermal energies	-	Passive part: Neo Hookean with thermomechanical & thermal parts	Active part: Force length relationship (zuurbier 1995) Thermomechanical & thermal energies, endothermal contribution due to cross-bridge cycling	Fibers, ECM	Numerical homogenization	Erdman & Gos 1990, Okamoto & Saeki 1964, Werner & Buse 1988, Briese 1998, Mcintosch & Anserson 2010, Mutungi & Ranatunga 1998, Segal et al. 1986, Ranatunga 1994, Bershitsky & Tsaturyan 1989, Ried et al. 1999		
Sahani et al. 2024	Model of Duchenne Muscular Dystrophy in mice	-	Angular Integration model of Ateshian et al. 2009, power law based on ellipsoidal collagen fiber distribution	Model of Blemker et al. 2005	Model of Blemker et al. 2005	ECM (endomysium, epimysium), Fibers	Periodic homogenization then Voigt homogenization to include epimysium	Sahani et al. 2022, Wohlgemuth et al. 2023, Morrow et al. 2010, Zajac et al. 1989, own experiments	FeBio	own experiments

Spadoni et al. 2024	Active 3D FE model of a young and old human muscle fiber bundle	Endomysium Neo-hookean			Hill model, using quadratic and exponential formulations for the elements	Fibers, ECM	Averaged results	Gollapudi et al. 2009, Sharafi et al. 2011	ABAQUS	

Appendix C: MRI Physics

Annex 4. Illustration of MRI physics using two complementary perspectives: a macroscopic view showing the evolution of the net magnetization vector throughout an imaging sequence. The mouse is divided into two imaging slices, and the sequence is broken down into six key steps: (1) Pre-MRI state: The mouse has not yet entered the MRI scanner; (2) Magnetization alignment in the MRI field; (3) Slice selection via magnetic field gradient; (4) Excitation of the selected slice; (5) Relaxation phase; (6) Return to equilibrium.
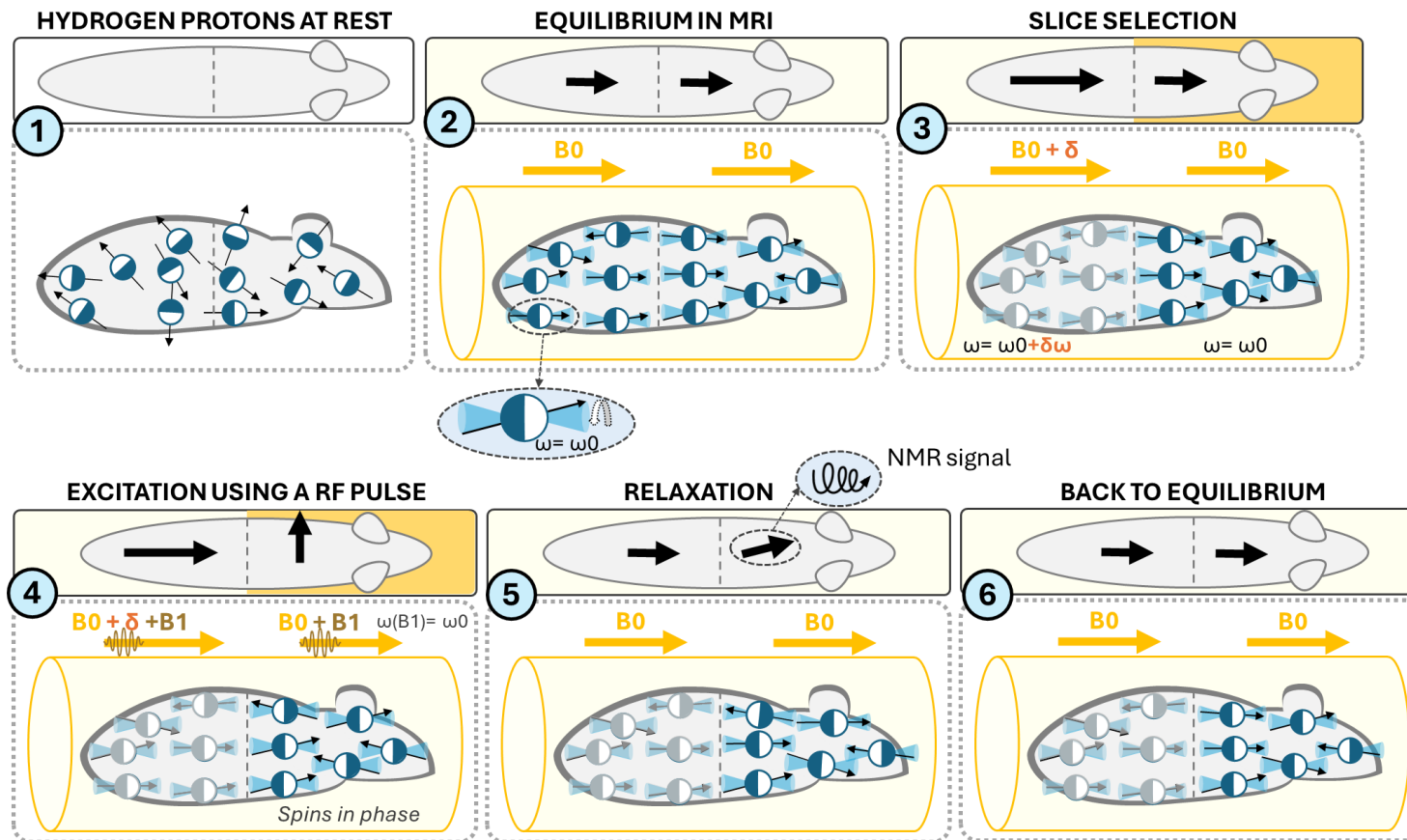
References

Abbott, B. C., & Aubert, X. M. (1952). The force exerted by active striated muscle during and after change of length. *The Journal of Physiology*, *117*(1), 77–77.

Abdel Rahman, R., George, D., Baumgartner, D., Nierenberger, M., Remond, Y., & Ahzi, S. (2012). An asymptotic method for the prediction of the anisotropic effective elastic properties of the cortical vein: Superior sagittal sinus junction embedded within a homogenized cell element. *Journal of Mechanics of Materials and Structures*, *7*(6), 593–611.

Affagard, J.-S., Feissel, P., & Bensamoun, S. F. (2015). Identification of hyperelastic properties of passive thigh muscle under compression with an inverse method from a displacement field measurement. *Journal of Biomechanics*, *48*(15), 4081–4086. https://doi.org/10.1016/j.jbiomech.2015.10.007

Afzal, A., Kim, K.-Y., & Seo, J. (2017). Effects of Latin hypercube sampling on surrogate modeling and optimization. *International Journal of Fluid Machinery and Systems*, *10*(3), 240–253.

Agoras, M., Lopez-Pamies, O., & Ponte Castañeda, P. (2009). A general hyperelastic model for incompressible fiber-reinforced elastomers. *Journal of the Mechanics and Physics of Solids*, *57*(2), 268–286. https://doi.org/10.1016/j.jmps.2008.10.014

Ameye, L., & Young, M. F. (2002). Mice deficient in small leucine-rich proteoglycans: Novel in vivo models for osteoporosis, osteoarthritis, Ehlers-Danlos syndrome, muscular dystrophy, and corneal diseases. *Glycobiology*, *12*(9), 107R-116R.

B. Boashash. (1992). Estimating and interpreting the instantaneous frequency of a signal. I. Fundamentals. *Proceedings of the IEEE*, *80*(4), 520–538. https://doi.org/10.1109/5.135376

Bargmann, S., Klusemann, B., Markmann, J., Schnabel, J. E., Schneider, K., Soyarslan, C., & Wilmers, J. (2018). Generation of 3D representative volume elements for heterogeneous materials: A review. *Progress in Materials Science*, *96*, 322–384. https://doi.org/10.1016/j.pmatsci.2018.02.003

Baroukh, N., Canteleux, N., Lefèvre, A., Dupuy, C., Martias, C., Presset, A., Subramaniam, M., Hawse, J., Emond, P., Pouletaut, P., Hawse, J. R., Morandat, S., Bensamoun, S. F., & Nadal-Desbarats, L. (2022). *Serum and Soleus Metabolomics Signature of Klf10 Knockout Mice to Identify Potential Biomarkers*. https://doi.org/10.3390/metabo12060556ï

Bendall, J. R. (1967). The elastin content of various muscles of beef animals. *Journal of the Science of Food and Agriculture*, *18*(12), 553–558. https://doi.org/10.1002/jsfa.2740181201

Bensamoun, S. F., Tsubone, T., Subramaniam, M., Hawse, J. R., Boumediene, E., Spelsberg, T. C., An, K.-N., & Amadio, P. C. (2006). Age-dependent changes in the mechanical properties of tail tendons in TGF-β inducible early gene-1 knockout mice. *Journal of Applied Physiology*, *101*(5), 1419–1424.

Binder-Markey, B. I., Sychowski, D., & Lieber, R. L. (2021). *Systematic Review of Skeletal Muscle Passive Mechanics Experimental Methodology*.

Birk, D. E., & Bruckner, P. (2005). Collagen suprastructures. *Topics in Current Chemistry*, *247*, 185–205. https://doi.org/10.1007/b103823

Bleiler, C., Castañeda, P. P., & Röhrle, O. (2021). Tangent second-order homogenisation estimates for incompressible hyperelastic composites with fibrous microstructures and anisotropic phases. *Journal of the Mechanics and Physics of Solids*, *147*, 104251–104251.

Bleiler, C., Ponte Castañeda, P., & Röhrle, O. (2019). A microstructurally-based, multi-scale, continuum-mechanical model for the passive behaviour of skeletal muscle tissue. *Journal of the Mechanical Behavior of Biomedical Materials*, *97*, 171–186. https://doi.org/10.1016/j.jmbbm.2019.05.012

Blemker, S. S., & Delp, S. L. (2005). Three-dimensional representation of complex muscle architectures and geometries. *Annals of Biomedical Engineering*, *33*(5), 661–673. https://doi.org/10.1007/s10439-005-1433-7

Blok, L. J., Grossmann, M. E., Perry, J. E., & Tindall, D. J. (1995). Characterization of an early growth response gene, which encodes a zinc finger transcription factor, potentially involved in cell cycle regulation. *Molecular Endocrinology*, *9*(11), 1610–1620. https://doi.org/10.1210/mend.9.11.8584037

Böl, M., Ehret, A. E., Leichsenring, K., Weichert, C., & Kruse, R. (2014). On the anisotropy of skeletal muscle tissue under compression. *Acta Biomaterialia*, *10*(7), 3225–3234. https://doi.org/10.1016/j.actbio.2014.03.003

Böl, M., Iyer, R., Dittmann, J., Garcés-Schröder, M., & Dietzel, A. (2019). Investigating the passive mechanical behaviour of skeletal muscle fibres: Micromechanical experiments and Bayesian hierarchical modelling. *Acta Biomaterialia*, *92*, 277–289. https://doi.org/10.1016/j.actbio.2019.05.015

Böl, M., Leichsenring, K., Ernst, M., & Ehret, A. E. (2016). Long-term mechanical behaviour of skeletal muscle tissue in semi-confined compression experiments. *Journal of the Mechanical Behavior of Biomedical Materials*, *63*, 115–124. https://doi.org/10.1016/j.jmbbm.2016.06.012

Bowman, A. W., & Azzalini, A. (1997). *Applied smoothing techniques for data analysis: The kernel approach with S-Plus illustrations* (Vol. 18). OUP Oxford.

Brashear, S. E., Wohlgemuth, R. P., Gonzalez, G., & Smith, L. R. (2021). Passive stiffness of fibrotic skeletal muscle in mdx mice relates to collagen architecture. *Journal of Physiology*, *599*(3), 943–962. https://doi.org/10.1113/JP280656

Brashear, S. E., Wohlgemuth, R. P., Hu, L. Y., Jbeily, E. H., Christiansen, B. A., & Smith, L. R. (2022). Collagen cross-links scale with passive stiffness in dystrophic mouse muscles, but are not altered with administration of a lysyl oxidase inhibitor. *PLoS ONE*, *17*(10 October). https://doi.org/10.1371/journal.pone.0271776

Brun, M., Lopez-Pamies, O., & Ponte Castañeda, P. (2007). Homogenization estimates for fiber-reinforced elastomers with periodic microstructures. *International Journal of Solids and Structures*, *44*(18), 5953–5979. https://doi.org/10.1016/j.ijsolstr.2007.02.003

Brynnel, A., Hernandez, Y., Kiss, B., Lindqvist, J., Adler, M., Kolb, J., Van der Pijl, R., Gohlke, J., Strom, J., & Smith, J. (2018). Downsizing the molecular spring of the giant protein titin reveals that skeletal muscle titin determines passive stiffness and drives longitudinal hypertrophy. *Elife*, *7*, e40532–e40532.

Buck, D., Smith III, J. E., Chung, C. S., Ono, Y., Sorimachi, H., Labeit, S., & Granzier, H. L. (2014). Removal of immunoglobulin-like domains from titin's spring segment alters titin splicing in mouse skeletal muscle and causes myopathy. *Journal of General Physiology*, *143*(2), 215–230.

Caillerie, D., Mourad, A., & Raoult, A. (2006). Discrete homogenization in graphene sheet modeling. *Journal of Elasticity*, *84*(1), 33–68.

Camman, M., Joanne, P., Brun, J., Marcellan, A., Dumont, J., Agbulut, O., & Hélary, C. (2023). Anisotropic dense collagen hydrogels with two ranges of porosity to mimic the skeletal muscle extracellular matrix. *Biomaterials Advances*, *144*, 213219.

Caralt, M., Uzarski, J. S., Iacob, S., Obergfell, K. P., Berg, N., Bijonowski, B. M., Kiefer, K. M., Ward, H. H., Wandinger-Ness, A., & Miller, W. M. (2015). Optimization and critical evaluation of decellularization strategies to develop renal extracellular matrix scaffolds as biological templates for organ engineering and transplantation. *American Journal of Transplantation*, *15*(1), 64–75.

Carlson, B. (2022). Chapter 1—Mature skeletal muscle—An overview. In B. Carlson (Ed.), *Muscle Biology* (pp. 1–33). Academic Press. https://doi.org/10.1016/B978-0-12-820278-4.00004-9

Carriou, V., Boudaoud, S., Laforet, J., Mendes, A., Canon, F., & Guiraud, D. (2019). Multiscale Hill-type modeling of the mechanical muscle behavior driven by the neural drive in isometric conditions. *Computers in Biology and Medicine*, *115*, 103480–103480.

Castillo-Méndez, C., & Ortiz, A. (2022a). Numerical simulation data and FORTRAN code to compare the stress response of two transversely isotropic hyperelastic models in ABAQUS. *Data in Brief*, *41*, 107853. https://doi.org/10.1016/j.dib.2022.107853

Castillo-Méndez, C., & Ortiz, A. (2022b). Role of anisotropic invariants in numerically modeling soft biological tissues as transversely isotropic hyperelastic materials: A comparative study. *International Journal of Non-Linear Mechanics*, *138*. https://doi.org/10.1016/j.ijnonlinmec.2021.103833

Ceelen, K. K., Oomens, C. W. J., & Baaijens, F. P. T. (2008). Microstructural analysis of deformation-induced hypoxic damage in skeletal muscle. *Biomechanics and Modeling in Mechanobiology*, *7*(4), 277–284. https://doi.org/10.1007/s10237-007-0097-7

Chagnon, G., Rebouah, M., Favier, D., Chagnon, G., Rebouah, M., & Favier, D. (2015). Hyperelastic Energy Densities for Soft Biological Tissues: A Review. *Hyperelastic Energy Densities for Soft Biological Tissues: A Review. Journal of Elasticity*, *120*(2), 129–160. https://doi.org/10.1007/s10659-014-9508-zï

Chakouch, M., Tatarenko, Y., Loumeaud, A., Josse, A., George, D., Pouletaut, P., Bensamoun, S. F., & Chatelin, S. (2025). Multiscale mechanical constitutive equation of the passive properties of murine skeletal muscle: Application to the influence of the Klf10 gene on the extra cellular matrix. *Multidisciplinary Biomechanics Journal*, *1*(Musculoskeletal biomechanics), 353–355. https://doi.org/10.46298/mbj.14541

Chin, L., Kennedy, B. F., Kennedy, K. M., Wijesinghe, P., Pinniger, G. J., Terrill, J. R., McLaughlin, R. A., & Sampson, D. D. (2014). Three-dimensional optical coherence micro-elastography of skeletal muscle tissue. *Biomedical Optics Express*, *5*(9), 3090–3102.

Chleboun, G., Patel, T., & Lieber, R. (1997). Skeletal muscle architecture and fiber-type distribution with the multiple bellies of the mouse extensor digitorum longus muscle. *Cells Tissues Organs*, *159*(2–3), 147–154.

Cooper, B. J., & Valentine, B. A. (2015). Muscle and Tendon. In *Jubb, Kennedy & Palmer's Pathology of Domestic Animals: Sixth Edition* (Vol. 1, pp. 164–249). Elsevier Inc. https://doi.org/10.1016/B978-0-7020-5317-7.00003-5

Criscione, J. C., Douglas, A. S., & Hunter, W. C. (2001). Physically based strain invariant set for materials exhibiting transversely isotropic behavior. *Journal of the Mechanics and Physics of Solids*, *49*(4), 871–897.

Csapo, R., Gumpenberger, M., & Wessner, B. (2020). Skeletal Muscle Extracellular Matrix – What Do We Know About Its Composition, Regulation, and Physiological Roles? A Narrative Review. *Frontiers in Physiology*, *11*. https://doi.org/10.3389/fphys.2020.00253

Danesini, P. C., Heim, M., Tomalka, A., Siebert, T., & Ates, F. (2024). Endomysium determines active and passive force production in muscle fibers. *Journal of Biomechanics*, *168*, 112134. https://doi.org/10.1016/j.jbiomech.2024.112134

deBotton, G., Hariton, I., & Socolsky, E. A. (2006). Neo-Hookean fiber-reinforced composites in finite elasticity. *Journal of the Mechanics and Physics of Solids*, *54*(3), 533–559. https://doi.org/10.1016/j.jmps.2005.10.001

DiMario, J. X. (2018). KLF10 Gene Expression Modulates Fibrosis in Dystrophic Skeletal Muscle. *American Journal of Pathology*, *188*(5), 1263–1275. https://doi.org/10.1016/j.ajpath.2018.01.014

Drago, A., & Pindera, M. J. (2007). Micro-macromechanical analysis of heterogeneous materials: Macroscopically homogeneous vs periodic microstructures. *Composites Science and Technology*, *67*(6), 1243–1263. https://doi.org/10.1016/j.compscitech.2006.02.031

Dupres, V., Pouletaut, P., Chakouch, M., Josse, A., Hawse, J. R., & Bensamoun, S. F. (2025). Age-Related Changes in Longitudinal and Transversal Elastic Properties of Murine Skeletal Muscle Fibers. *IRBM*, *46*(5), 100908. https://doi.org/10.1016/j.irbm.2025.100908

Dutov, P., Antipova, O., Varma, S., Orgel, J. P. R. O., & Schieber, J. D. (2016). Measurement of elastic modulus of collagen type i single fiber. *PLoS ONE*, *11*(1). https://doi.org/10.1371/journal.pone.0145711

Eshelby, J. D. (1959). *The Elastic Field Outside an Ellipsoidal Inclusion* (Source: Proceedings of the Royal Society of London. Series A, Mathematical and Physical Sciences, Vol. 252, Issue 1271, pp. 561–569).

Farin, G. (1983). Algorithms for rational Bézier curves. *Computer-Aided Design*, *15*(2), 73–77.

Gasser, T. C., Ogden, R. W., & Holzapfel, G. A. (2006). Hyperelastic modelling of arterial layers with distributed collagen fibre orientations. *Journal of the Royal Society Interface*, *3*(6), 15–35. https://doi.org/10.1098/rsif.2005.0073

Geers, M. G. D., Kouznetsova, V. G., & Brekelmans, W. A. M. (2010). Multi-scale computational homogenization: Trends and challenges. *Fourth International Conference on Advanced COmputational Methods in ENgineering (ACOMEN 2008)*, *234*(7), 2175–2182. https://doi.org/10.1016/j.cam.2009.08.077

Gelse, K., Pöschl, E., & Aigner, T. (2003). Collagens—Structure, function, and biosynthesis. *Advanced Drug Delivery Reviews*, *55*(12), 1531–1546. https://doi.org/10.1016/j.addr.2003.08.002

Gillies, A. R., Chapman, M. A., Bushong, E. A., Deerinck, T. J., Ellisman, M. H., & Lieber, R. L. (2017). High resolution three-dimensional reconstruction of fibrotic skeletal muscle extracellular matrix. *Journal of Physiology*, *595*(4), 1159–1171. https://doi.org/10.1113/JP273376

Gillies, A. R., & Lieber, R. L. (2011). Structure and function of the skeletal muscle extracellular matrix. *Muscle and Nerve*, *44*(3), 318–331. https://doi.org/10.1002/mus.22094

Gillies, A. R., Smith, L. R., Lieber, R. L., & Varghese, S. (2011). Method for decellularizing skeletal muscle without detergents or proteolytic enzymes. *Tissue Engineering - Part C: Methods*, *17*(4), 383–389. https://doi.org/10.1089/ten.tec.2010.0438

Gindre, J., Takaza, M., Moerman, K. M., & Simms, C. K. (2013). A structural model of passive skeletal muscle shows two reinforcement processes in resisting deformation. *Journal of the Mechanical Behavior of Biomedical Materials*, *22*, 84–94. https://doi.org/10.1016/j.jmbbm.2013.02.007

Grounds, M. D., Sorokin, L., & White, J. (2005). Strength at the extracellular matrix–muscle interface. *Scandinavian Journal of Medicine & Science in Sports*, *15*(6), 381–391. https://doi.org/10.1111/j.1600-0838.2005.00467.x

Gumez, L., Bensamoun, S. F., Doucet, J., Haddad, O., Hawse, J. R., Subramaniam, M., Spelsberg, T. C., & Pichon, C. (2010). Molecular structure of tail tendon fibers in TIEG1 knockout mice using synchrotron diffraction technology. *Journal of Applied Physiology*, *108*(6), 1706–1710. https://doi.org/10.1152/japplphysiol.00356.2010

H. Knutsson, C. . -F. Westin, & G. Granlund. (1994). Local multiscale frequency and bandwidth estimation. *Proceedings of 1st International Conference on Image Processing*, *1*, 36–40 vol.1. https://doi.org/10.1109/ICIP.1994.413270

Hashin, Z., & Shtrikman, S. (1962). A variational approach to the theory of the elastic behaviour of polycrystals. *Journal of the Mechanics and Physics of Solids*, *10*(4), 343–352.

Hashin, Z., & Shtrikman, S. (1963). A variational approach to the theory of the elastic behaviour of multiphase materials. *Journal of the Mechanics and Physics of Solids*, *11*(2), 127–140.

185

He, X., Taneja, K., Chen, J. S., Lee, C. H., Hodgson, J., Malis, V., Sinha, U., & Sinha, S. (2022). Multiscale modeling of passive material influences on deformation and force output of skeletal muscles. *International Journal for Numerical Methods in Biomedical Engineering*, *38*(4). https://doi.org/10.1002/cnm.3571

Heidlauf, T., Klotz, T., Rode, C., Altan, E., Bleiler, C., Siebert, T., & Röhrle, O. (2016). A multi-scale continuum model of skeletal muscle mechanics predicting force enhancement based on actin–titin interaction. *Biomechanics and Modeling in Mechanobiology*, *15*(6), 1423–1437. https://doi.org/10.1007/s10237-016-0772-7

Heidlauf, T., Klotz, T., Rode, C., Siebert, T., & Röhrle, O. (2017). A continuum-mechanical skeletal muscle model including actin-titin interaction predicts stable contractions on the descending limb of the force-length relation. *PLoS Computational Biology*, *13*(10). https://doi.org/10.1371/journal.pcbi.1005773

Herzog, W. (2017). Skeletal muscle mechanics: Questions, problems and possible solutions Daniel P Ferris. *Journal of NeuroEngineering and Rehabilitation*, *14*(1). https://doi.org/10.1186/s12984-017-0310-6

Herzog, W. (2018). The multiple roles of titin in muscle contraction and force production. *Biophysical Reviews*, *10*, 1187–1199.

Hill, A. V. (1938). The heat of shortening and the dynamic constants of muscle. *Proceedings of the Royal Society of London. Series B-Biological Sciences*, *126*(843), 136–195.

Hill, R. (1963). Elastic properties of reinforced solids: Some theoretical principles. *Journal of the Mechanics and Physics of Solids*, *11*(5), 357–372. https://doi.org/10.1016/0022-5096(63)90036-X

Hill, R. (1967). The essential structure of constitutive laws for metal composites and polycrystals. *Journal of the Mechanics and Physics of Solids*, *15*(2), 79–95. https://doi.org/10.1016/0022-5096(67)90018-X

Hill, R. J. (1965). A self-consistent mechanics of composite materials. *Journal of the Mechanics and Physics of Solids*, *13*(4), 213–222. https://doi.org/10.1016/0022-5096(65)90010-4ï

Holzapfel, G. A., Gasser, T. C., & Ogden, R. W. (2000). A new constitutive framework for arterial wall mechanics and a comparative study of material models. *Journal of Elasticity and the Physical Science of Solids*, *61*, 1–48.

Holzapfel, G. A., & Ogden, R. W. (2015). On the tension-compression switch in soft fibrous solids. *European Journal of Mechanics, A/Solids*, *49*, 561–569. https://doi.org/10.1016/j.euromechsol.2014.09.005

Holzapfel, G. A., & Ogden, R. W. (2017). On Fiber Dispersion Models: Exclusion of Compressed Fibers and Spurious Model Comparisons. *Journal of Elasticity*, *129*(1–2), 49–68. https://doi.org/10.1007/s10659-016-9605-2

Holzapfel, G. A., & Ogden, R. W. (2020). An arterial constitutive model accounting for collagen content and cross-linking. *Journal of the Mechanics and Physics of Solids*, *136*. https://doi.org/10.1016/j.jmps.2019.103682

Holzapfel, G. A., Ogden, R. W., & Sherifova, S. (2019). On fibre dispersion modelling of soft biological tissues: A review. *Proceedings of the Royal Society A: Mathematical, Physical and Engineering Sciences*, *475*(2224). https://doi.org/10.1098/rspa.2018.0736

Honda, H. (1978). Description of cellular patterns by Dirichlet domains: The two-dimensional case. *Journal of Theoretical Biology*, *72*(3), 523–543. https://doi.org/10.1016/0022-5193(78)90315-6

Honda, H. (1983). Geometrical Models for Cells in Tissues. *International Review of Cytology*, *81*(C), 191–248. https://doi.org/10.1016/S0074-7696(08)62339-6

Hu, W., Cheng, H., Wang, S., Cheng, H., Cheng, Y., Zhang, K., & Liang, B. (2024). A coupled FEM-FFT concurrent multiscale method for the deformation simulation of CFRPs laminate. *Composite Structures*, *342*, 118246. https://doi.org/10.1016/j.compstruct.2024.118246

Humphrey, J. D., Dufresne, E. R., & Schwartz, M. A. (2014). Mechanotransduction and extracellular matrix homeostasis. *Nature Reviews Molecular Cell Biology*, *15*(12), 802–812. https://doi.org/10.1038/nrm3896

Huxley, A. F. (1957). Muscle structure and theories of contraction. *Progress in Biophysics and Biophysical Chemistry*, *7*, 255–318.

Huxley, H. E. (1969). The Mechanism of Muscular Contraction: Recent structural studies suggest a revealing model for cross-bridge action at variable filament spacing. *Science*, *164*(3886), 1356–1366.

Jain, A. (2019). Micro and mesomechanics of fibre reinforced composites using mean field homogenization formulations: A review. *Materials Today Communications*, *21*. https://doi.org/10.1016/j.mtcomm.2019.100552

Järvinen, T. A. H., Józsa, L., Kannus, P., Järvinen, T. L. N., & Järvinen, M. (2002). Organization and distribution of intramuscular connective tissue in normal and immobilized skeletal muscles. *Journal of Muscle Research & Cell Motility*, *23*(3), 245–254. https://doi.org/10.1023/A:1020904518336

Jorgenson, K. W., Phillips, S. M., & Hornberger, T. A. (2020). Identifying the Structural Adaptations that Drive the Mechanical Load-Induced Growth of Skeletal Muscle: A Scoping Review. *Cells*, *9*(7). https://doi.org/10.3390/cells9071658

Kailash, K. A., Hawes, J. Z., Cocciolone, A. J., Bersi, M. R., Mecham, R. P., & Wagenseil, J. E. (2024). Constitutive modeling of mouse arteries suggests changes in directional coupling and extracellular matrix remodeling that depend on artery type, age, sex, and elastin amounts. *Journal of Biomechanical Engineering*, *146*(6).

Kalamkarov, A. L., Andrianov, I. V., & Danishevs' kyy, V. V. (2009). *Asymptotic homogenization of composite materials and structures*.

Kammoun, M., Meme, S., Meme, W., Subramaniam, M., Hawse, J. R., Canon, F., & Bensamoun, S. F. (2017). Impact of TIEG1 on the structural properties of fast- and slow-twitch skeletal muscle. *Muscle and Nerve*, *55*(3), 410–416. https://doi.org/10.1002/mus.25252

Kammoun, M., Piquereau, J., Nadal-Desbarats, L., Même, S., Beuvin, M., Bonne, G., Veksler, V., Le Fur, Y., Pouletaut, P., Même, W., Szeremeta, F., Constans, J. M., Bruinsma, E. S., Nelson Holte, M. H., Najafova, Z., Johnsen, S. A., Subramaniam, M., Hawse, J. R., & Bensamoun, S. F. (2020). Novel role of Tieg1 in muscle metabolism and mitochondrial oxidative capacities. *Acta Physiologica*, *228*(3). https://doi.org/10.1111/apha.13394

Kammoun, M., Pouletaut, P., Canon, F., Subramaniam, M., Hawse, J. R., Vayssade, M., & Bensamoun, S. F. (2016). Impact of TIEG1 deletion on the passive mechanical properties of fast and slow twitch skeletal muscles in female mice. *PLoS ONE*, *11*(10). https://doi.org/10.1371/journal.pone.0164566

Kammoun, M., Pouletaut, P., Morandat, S., Subramaniam, M., Hawse, J. R., & Bensamoun, S. F. (2021). Krüppel-like factor 10 regulates the contractile properties of skeletal muscle fibers in mice. *Muscle & Nerve*, *64*(6), 765–769.

Kammoun, M., Ternifi, R., Dupres, V., Pouletaut, P., Même, S., Même, W., Szeremeta, F., Landoulsi, J., Constans, J. M., Lafont, F., Subramaniam, M., Hawse, J. R., & Bensamoun, S. F. (2019). Development of a novel multiphysical approach for the characterization of mechanical properties of musculotendinous tissues. *Scientific Reports*, *9*(1). https://doi.org/10.1038/s41598-019-44053-1

Kohn, S., Leichsenring, K., Kuravi, R., Ehret, A. E., & Böl, M. (2021). Direct measurement of the direction-dependent mechanical behaviour of skeletal muscle extracellular matrix. *Acta Biomaterialia*, *122*, 249–262. https://doi.org/10.1016/j.actbio.2020.12.050

Konno, R. N. (2022). *Skeletal muscle and cerebral palsy: Morphological consequences on muscle mechanics*.

Konno, R. N., Nigam, N., & Wakeling, J. M. (2021). Modelling extracellular matrix and cellular contributions to whole muscle mechanics. *PLoS ONE*, *16*(4 April 2021). https://doi.org/10.1371/journal.pone.0249601

Kotz, N. J., & Balakrishnan, N. (1993). *Continuous Univariate Distributions. Vol. 1, Hoboken*.

Kovanen, V. (2002). *Intramuscular Extracellular Matrix: Complex Environment of Muscle Cells* (Exerc. Sport Sci. Rev, Vol. 30, Issue 1, pp. 20–25). www.acsm-essr.org

Kuravi, R., Leichsenring, K., Böl, M., & Ehret, A. E. (2021). 3D finite element models from serial section histology of skeletal muscle tissue – The role of micro-architecture on mechanical behaviour. *Journal of the Mechanical Behavior of Biomedical Materials*, *113*. https://doi.org/10.1016/j.jmbbm.2020.104109

Kuravi, R., Leichsenring, K., Trostorf, R., Morales-Orcajo, E., Böl, M., & Ehret, A. E. (2021). Predicting muscle tissue response from calibrated component models and histology-based finite element models. *Journal of the Mechanical Behavior of Biomedical Materials*, *117*. https://doi.org/10.1016/j.jmbbm.2021.104375

Lagarias, J. C., Reeds, J. A., Wright, M. H., & Wright, P. E. (1998). Convergence properties of the Nelder—Mead simplex method in low dimensions. *SIAM Journal on Optimization*, *9*(1), 112–147.

Lahellec, N., Mazerolle, F., & Michel, J. C. (2004). Second-order estimate of the macroscopic behavior of periodic hyperelastic composites: Theory and experimental validation. *Journal of the Mechanics and Physics of Solids*, *52*(1), 27–49. https://doi.org/10.1016/S0022-5096(03)00104-2

Lamsfuss, J., & Bargmann, S. (2021). Skeletal muscle: Modeling the mechanical behavior by taking the hierarchical microstructure into account. *Journal of the Mechanical Behavior of Biomedical Materials*, *122*. https://doi.org/10.1016/j.jmbbm.2021.104670

Lamsfuss, J., & Bargmann, S. (2022a). Computational modeling of damage in the hierarchical microstructure of skeletal muscles. *Journal of the Mechanical Behavior of Biomedical Materials*, *134*. https://doi.org/10.1016/j.jmbbm.2022.105386

Lamsfuss, J., & Bargmann, S. (2022b). Python codes to generate skeletal muscle models on each hierarchical level. *Software Impacts*, *14*. https://doi.org/10.1016/j.simpa.2022.100437

Lamsfuss, J., & Bargmann, S. (2023). Mechanisms of thermal treatments in trigger points of the skeletal muscle: Computational microstructural modeling. *European Journal of Mechanics / A Solids*, *99*, 104906–104906. https://doi.org/10.1016/j.simpa

Lanir, Y. (1983). Constitutive equations for fibrous connective tissues. *Journal of Biomechanics*, *16*(1), 1–12.

Lanzl, F., Peldschus, S., Holzapfel, G. A., Duddeck, F., & Sommer, G. (2024). A Microstructural Material Model for Adipose Tissue Under Blunt Impact Considering Different Types of Loading. *Available at SSRN 5067578*.

Lauzeral, N., Borzacchiello, D., Kugler, M., George, D., Rémond, Y., Hostettler, A., & Chinesta, F. (2019). Shape parametrization of bio-mechanical finite element models based on medical images. *Computer Methods in Biomechanics and Biomedical Engineering: Imaging & Visualization*, *7*(5–6), 480–489. https://doi.org/10.1080/21681163.2018.1447400

Li, H., Chen, L., Zhi, G., Meng, L., Lian, H., Liu, Z., Yu, T., & Li, P. (2024). A direct FE2 method for concurrent multilevel modeling of piezoelectric materials and structures. *Computer Methods in Applied Mechanics and Engineering*, *420*, 116696. https://doi.org/10.1016/j.cma.2023.116696

Lieber, R. L., & Binder-Markey, B. I. (2021). Biochemical and structural basis of the passive mechanical properties of whole skeletal muscle. *Journal of Physiology*, *599*(16), 3809–3823. https://doi.org/10.1113/JP280867

Lieber, R. L., & Meyer, G. (2023). Structure-Function relationships in the skeletal muscle extracellular matrix. *Journal of Biomechanics*, *152*. https://doi.org/10.1016/j.jbiomech.2023.111593

Linke, W. A. (2023). Stretching the story of titin and muscle function. *Journal of Biomechanics*, 111553–111553.

Liu, F., Wang, M., & Ma, Y. (2022). Multiscale modeling of skeletal muscle to explore its passive mechanical properties and experiments verification. *Mathematical Biosciences and Engineering*, *19*(2), 1251–1279. https://doi.org/10.3934/mbe.2022058

Liu, K., Meng, L., Zhao, A., Wang, Z., Chen, L., & Li, P. (2023). A hybrid direct FE2 method for modeling of multiscale materials and structures with strain localization. *Computer Methods in Applied Mechanics and Engineering*, *412*, 116080. https://doi.org/10.1016/j.cma.2023.116080

Liu, M., Yue, Y., Harper, S. Q., Grange, R. W., Chamberlain, J. S., & Duan, D. (2005). Adeno-associated virus-mediated microdystrophin expression protects young mdx muscle from contraction-induced injury. *Molecular Therapy*, *11*(2), 245–256.

Lloyd, E. M., Hepburn, M. S., Li, J., Mowla, A., Hwang, Y., Choi, Y. S., Grounds, M. D., & Kennedy, B. F. (2022). Three-dimensional mechanical characterization of murine skeletal muscle using quantitative micro-elastography. *Biomedical Optics Express*, *13*(11), 5879–5899.

Lloyd, E. M., Pinniger, G. J., Murphy, R. M., & Grounds, M. D. (2023). Slow or fast: Implications of myofibre type and associated differences for manifestation of neuromuscular disorders. *Acta Physiologica*, *238*(4), e14012. https://doi.org/10.1111/apha.14012

Lofaro, F. D., Cisterna, B., Lacavalla, M. A., Boschi, F., Malatesta, M., Quaglino, D., Zancanaro, C., & Boraldi, F. (2021). Age-Related Changes in the Matrisome of the Mouse Skeletal Muscle. *International Journal of Molecular Sciences*, *22*(19). https://doi.org/10.3390/ijms221910564

López Jiménez, F. (2014). Modeling of soft composites under three-dimensional loading. *Composites Part B: Engineering*, *59*, 173–180. https://doi.org/10.1016/j.compositesb.2013.11.020

Lopez-Pamies, O., & Idiart, M. I. (2010). Fiber-reinforced hyperelastic solids: A realizable homogenization constitutive theory. *Journal of Engineering Mathematics*, *68*(1), 57–83. https://doi.org/10.1007/s10665-009-9359-y

Loumeaud, A. (2022). *Development of a piezoelectric vibration system for 7T magnetic resonance elastography of mouse muscle* [Master Thesis].

Loumeaud, A., Po, C., Wach, B., Bensamoun, S. F., Pagé, G., Doblas, S., Garteiser, P., Grenier, D., Koon, K. T. V., & Beuf, O. (2025). Preclinical multi-organ Magnetic Resonance Elastography (MRE) at 7T: an original piezoelectric actuator design with dedicated sequences. *Multidisciplinary Biomechanics Journal*, *1*(Magnetic Resonance Elastography). https://doi.org/10.46298/mbj.14507

Loumeaud, A., Pouletaut, P., Bensamoun, S. F., George, D., & Chatelin, S. (2024). Multiscale Mechanical Modeling of Skeletal Muscle: A Systemic Review of the Literature. *Journal of Medical and Biological Engineering*, *44*(3), 337–356. https://doi.org/10.1007/s40846-024-00879-3

Loumeaud, A., Pouletaut, P., Bensamoun, S. F., George, D., & Chatelin, S. (2025). An original approach to generate periodic Representative Volume Elements with anisotropic heterogeneous microstructure: Application to skeletal muscle. *Journal of Biomechanics*, *191*, 112897. https://doi.org/10.1016/j.jbiomech.2025.112897

MacLennan, D. H., & Holland, P. C. (1975). Calcium transport in sarcoplasmic reticulum. *Annual Review of Biophysics and Bioengineering*, *4*(1), 377–404.

Mandel, J. (1973). Equations constitutives et directeurs dans les milieux plastiques et viscoplastiques. *International Journal of Solids and Structures*, *9*(6), 725–740.

Manduca, A., Oliphant, T. E., Dresner, M. A., Mahowald, J. L., Kruse, S. A., Amromin, E., Felmlee, J. P., Greenleaf, J. F., & Ehman, R. L. (2001). Magnetic resonance elastography: Non-invasive mapping of tissue elasticity. *Medical Image Analysis*, *5*(4), 237–254. https://doi.org/10.1016/S1361-8415(00)00039-6

Marcucci, L., Bondì, M., Randazzo, G., Reggiani, C., Natali, A. N., & Pavan, P. G. (2019). Fibre and extracellular matrix contributions to passive forces in human skeletal muscles: An experimental based constitutive law for numerical modelling of the passive element in the classical Hill-type three element model. *PLoS ONE*, *14*(11). https://doi.org/10.1371/journal.pone.0224232

Marcucci, L., Reggiani, C., Natali, A. N., & Pavan, P. G. (2017). From single muscle fiber to whole muscle mechanics: A finite element model of a muscle bundle with fast and slow fibers. *Biomechanics and Modeling in Mechanobiology*, *16*(6), 1833–1843. https://doi.org/10.1007/s10237-017-0922-6

Martins-Bach, A. B., Bachasson, D., Araujo, E. C., Soustelle, L., Loureiro de Sousa, P., Fromes, Y., & Carlier, P. G. (2021). Non-invasive assessment of skeletal muscle fibrosis in mice using nuclear magnetic resonance imaging and ultrasound shear wave elastography. *Scientific Reports*, *11*(1), 284.

Mele, A., Fonzino, A., Rana, F., Camerino, G. M., De Bellis, M., Conte, E., Giustino, A., Conte Camerino, D., & Desaphy, J.-F. (2016). In vivo longitudinal study of rodent skeletal muscle atrophy using ultrasonography. *Scientific Reports*, *6*(1), 20061.

Méndez, J. (1960). Density and composition of mammalian muscle. *Metabolism*, *9*, 184–188.

Meyer, G. A., & Lieber, R. L. (2011). Elucidation of extracellular matrix mechanics from muscle fibers and fiber bundles. *Journal of Biomechanics*, *44*(4), 771–773. https://doi.org/10.1016/j.jbiomech.2010.10.044

Michel, J.-C., Moulinec, H., & Suquet, P. (1999). Effective properties of composite materials with periodic microstructure: A computational approach. *Computer Methods in Applied Mechanics and Engineering*, *172*(1–4), 109–143.

Mohammadkhah, M., Murphy, P., & Simms, C. K. (2016). The in vitro passive elastic response of chicken pectoralis muscle to applied tensile and compressive deformation. *Journal of the Mechanical Behavior of Biomedical Materials*, *62*, 468–480.

Mori, T., & Tanaka, K. (1973). Average stress in matrix and average elastic energy of materials with misfitting inclusions. *Acta Metallurgica*, *21*(5), 571–574.

Morrow, D. A., Haut Donahue, T. L., Odegard, G. M., & Kaufman, K. R. (2010). Transversely isotropic tensile material properties of skeletal muscle tissue. *Journal of the Mechanical Behavior of Biomedical Materials*, *3*(1), 124–129. https://doi.org/10.1016/j.jmbbm.2009.03.004

Muiznieks, L. D., & Keeley, F. W. (2013). Molecular assembly and mechanical properties of the extracellular matrix: A fibrous protein perspective. *Biochimica et Biophysica Acta - Molecular Basis of Disease*, *1832*(7), 866–875. https://doi.org/10.1016/j.bbadis.2012.11.022

Mukund, K., & Subramaniam, S. (2020). Skeletal muscle: A review of molecular structure and function, in health and disease. *Wiley Interdisciplinary Reviews: Systems Biology and Medicine*, *12*(1). https://doi.org/10.1002/wsbm.1462

Muthupillai, R., Lomas, D. J., Rossman, P. J., Greenleaf, J. F., Manduca, A., & Ehman, R. L. (1995). Magnetic Resonance Elastography by Direct Visualization of Propagating Acoustic Strain Waves. *Science*, *269*(5232), 1854–1857. https://doi.org/10.1126/science.7569924

Nelissen, J. L., de Graaf, L., Traa, W. A., Schreurs, T. J. L., Moerman, K. M., Nederveen, A. J., Sinkus, R., Oomens, C. W. J., Nicolay, K., & Strijkers, G. J. (2017). A MRI-Compatible Combined Mechanical Loading and MR Elastography Setup to Study Deformation-Induced Skeletal Muscle Damage in Rats. *PLOS ONE*, *12*(1), e0169864. https://doi.org/10.1371/journal.pone.0169864

Nelissen, J. L., Sinkus, R., Nicolay, K., Nederveen, A. J., Oomens, C. W., & Strijkers, G. J. (2019). Magnetic resonance elastography of skeletal muscle deep tissue injury. *NMR in Biomedicine*, *32*(6), e4087.

Nierenberger, M. (2013). *Mécanique multiéchelles des parois vasculaires: Expérimentation, imagerie, modélisation* (Issue 2013STRAD013) [Theses, Université de Strasbourg]. https://theses.hal.science/tel-00966831

Olesen, A. T., Malchow-Møller, L., Bendixen, R. D., Kjær, M., Mackey, A. L., Magnusson, S. P., & Svensson, R. B. (2022). Intramuscular connective tissue content and mechanical properties: Influence of aging and physical activity in mice. *Experimental Gerontology*, *166*, 111893. https://doi.org/10.1016/j.exger.2022.111893

Omairey, S. L., Dunning, P. D., & Sriramula, S. (2019). Development of an ABAQUS plugin tool for periodic RVE homogenisation. *Engineering with Computers*, *35*(2), 567–577. https://doi.org/10.1007/s00366-018-0616-4

Oukfif, H., Tikarrouchine, E., Louar, M.-A., Chatzigeorgiou, G., & Meraghni, F. (2024). Multi-scale FE2 investigation of non linear rate dependent 3D composite structures accounting for fiber–matrix damage. *Composite Structures*, *334*, 117960. https://doi.org/10.1016/j.compstruct.2024.117960

Passerieux, E., Rossignol, R., Chopard, A., Carnino, A., Marini, J. F., Letellier, T., & Delage, J. P. (2006). Structural organization of the perimysium in bovine skeletal muscle: Junctional plates and associated intracellular subdomains. *Journal of Structural Biology*, *154*(2), 206–216. https://doi.org/10.1016/j.jsb.2006.01.002

Passerieux, E., Rossignol, R., Letellier, T., & Delage, J. P. (2007). Physical continuity of the perimysium from myofibers to tendons: Involvement in lateral force transmission in skeletal muscle. *Journal of Structural Biology*, *159*(1), 19–28. https://doi.org/10.1016/j.jsb.2007.01.022

Pavan, P., Monti, E., Bondí, M., Fan, C., Stecco, C., Narici, M., Reggiani, C., & Marcucci, L. (2020). Alterations of extracellular matrix mechanical properties contribute to age-related functional impairment of human skeletal muscles. *International Journal of Molecular Sciences*, *21*(11), 3992.

Peter, A. K., Cheng, H., Ross, R. S., Knowlton, K. U., & Chen, J. (2011). The costamere bridges sarcomeres to the sarcolemma in striated muscle. *Progress in Pediatric Cardiology*, *31*(2), 83–88. https://doi.org/10.1016/j.ppedcard.2011.02.003

Potier-Ferry, M. (2024). Asymptotic numerical method for hyperelasticity and elastoplasticity: A review. *Proceedings of the Royal Society A*, *480*(2285), 20230714.

Pouletaut, P., Li, M., Kammoun, M., Subramaniam, M., Hawse, J., Joumaa, V., Herzog, W., & Bensamoun, S. (2021). Loss of KLF10 expression does not affect the passive properties of single myofibrils. *Computer Methods in Biomechanics and Biomedical Engineering*, *24*(sup1), S158.

Pouletaut, P., Tatarenko, Y., Chakouch, M. K., Li, M., Joumaa, V., Hawse, J. R., Herzog, W., Chatelin, S., & Bensamoun, S. F. (2023). Multiscale Passive Mechanical Characterization of Rodent Skeletal Muscle. *IRBM*, *44*(6), 100800. https://doi.org/10.1016/j.irbm.2023.100800

Powers, J. D., Malingen, S. A., Regnier, M., & Daniel, T. L. (2021). The sliding filament theory since Andrew Huxley: Multiscale and multidisciplinary muscle research. *Annual Review of Biophysics*, *50*, 373–400.

Prado, L. G., Makarenko, I., Andresen, C., Krüger, M., Opitz, C. A., & Linke, W. A. (2005). Isoform diversity of giant proteins in relation to passive and active contractile properties of rabbit skeletal muscles. *Journal of General Physiology*, *126*(5), 461–480. https://doi.org/10.1085/jgp.200509364

Purslow, P. (1999). *The intramuscular connective tissue matrix and cell-matrix interactions in relation to meat toughness*. 210–219.

Purslow, P. P. (1989). Strain-induced reorientation of an intramuscular connective tissue network: Implications for passive muscle elasticity. *Journal of Biomechanics*, *22*(1), 21–31.

Purslow, P. P. (2002). *The structure and functional significance of variations in the connective tissue within muscle* (Comparative Biochemistry and Physiology Part A, Vol. 133, pp. 947–966).

Purslow, P. P. (2010). Muscle fascia and force transmission. *Journal of Bodywork and Movement Therapies*, *14*(4), 411–417. https://doi.org/10.1016/j.jbmt.2010.01.005

Purslow, P. P. (2020). The Structure and Role of Intramuscular Connective Tissue in Muscle Function. *Frontiers in Physiology*, *11*. https://doi.org/10.3389/fphys.2020.00495

Purslow, P. P., & Delage, J.-P. (2022). *General anatomy of the muscle fasciae*.

Purslow, P. P., & Trotter, J. A. (1994). *The morphology and mechanical properties endomysium in series-fibred muscles: Variations with muscle length of* (Journal of Muscle Research and Cell Motility, Vol. 15, pp. 299–308).

Qin, E. C., Jugé, L., Lambert, S. A., Paradis, V., Sinkus, R., & Bilston, L. E. (2014). In vivo anisotropic mechanical properties of dystrophic skeletal muscles measured by anisotropic MR elastographic imaging: The mdx mouse model of muscular dystrophy. *Radiology*, *273*(3), 726–735.

Rajamannan, N. M., Subramaniam, M., Abraham, T. P., Vasile, V. C., Ackerman, M. J., Monroe, D. G., Chew, T., & Spelsberg, T. C. (2007). TGFβ inducible early gene-1 (TIEG1) and cardiac hypertrophy: Discovery and characterization of a novel signaling pathway. *Journal of Cellular Biochemistry*, *100*(2), 315–325.

Raju, B., Hiremath, S. R., & Roy Mahapatra, D. (2018). A review of micromechanics based models for effective elastic properties of reinforced polymer matrix composites. *Composite Structures*, *204*, 607–619. https://doi.org/10.1016/j.compstruct.2018.07.125

Raju, K., Tay, T. E., & Tan, V. B. C. (2021). A review of the FE2 method for composites. *Multiscale and Multidisciplinary Modeling, Experiments and Design*, *4*(1). https://doi.org/10.1007/s41939-020-00087-x

Reinholz, M. M., An, M.-W., Johnsen, S. A., Subramaniam, M., Suman, V. J., Ingle, J. N., Roche, P. C., & Spelsberg, T. C. (2004). Differential Gene Expression of TGFβ Inducible Early Gene (TIEG), Smad7, Smad2 and Bard1 in Normal and Malignant Breast Tissue. *Breast Cancer Research and Treatment*, *86*(1), 75–88. https://doi.org/10.1023/B:BREA.0000032926.74216.7d

Reuß, A. (1929). Berechnung der fließgrenze von mischkristallen auf grund der plastizitätsbedingung für einkristalle. *ZAMM - Journal of Applied Mathematics and Mechanics/Zeitschrift Für Angewandte Mathematik Und Mechanik*, *9*(1), 49–58.

Reyna, W. E., Pichika, R., Ludvig, D., & Perreault, E. J. (2020). Efficiency of skeletal muscle decellularization methods and their effects on the extracellular matrix. *Journal of Biomechanics*, *110*. https://doi.org/10.1016/j.jbiomech.2020.109961

Riaño, L., & Joliff, Y. (2019). An ABAQUS™ plug-in for the geometry generation of Representative Volume Elements with randomly distributed fibers and interphases. *Composite Structures*, *209*, 644–651. https://doi.org/10.1016/j.compstruct.2018.10.096

Roberts, T. J., Eng, C. M., Sleboda, D. A., Holt, N. C., Brainerd, E. L., Stover, K. K., Marsh, R. L., & Azizi, E. (2019). The multi-scale, three-dimensional nature of skeletal muscle contraction. *Physiology*, *34*(6), 402–408. https://doi.org/10.1152/physiol.00023.2019

Röhrle, O., Davidson, J. B., & Pullan, A. J. (2008). Bridging scales: A three-dimensional electromechanical finite element model of skeletal muscle. *SIAM Journal on Scientific Computing*, *30*(6), 2882–2904. https://doi.org/10.1137/070691504

Röhrle, O., Davidson, J. B., & Pullan, A. J. (2012). A physiologically based, multi-scale model of skeletal muscle structure and function. *Frontiers in Physiology*, *3 SEP*. https://doi.org/10.3389/fphys.2012.00358

Roux, A., Haen, T. X., Iordanoff, I., & Laporte, S. (2023). Model of calf muscle tear during a simulated eccentric contraction, comparison between ex-vivo experiments and discrete element model. *Journal of the Mechanical Behavior of Biomedical Materials*, *142*. https://doi.org/10.1016/j.jmbbm.2023.105823

Roux, A., Laporte, S., Lecompte, J., Gras, L.-L., Roux, A., Laporte, S., Lecompte, J., Gras, L., & Iordanoff, I. (2016). Influence of muscle-tendon complex geometrical parameters on modeling passive stretch behavior with the Discrete Element Method. Influence of muscle-tendon complex geometrical parameters on modeling passive stretch behavior with the Discrete Element Method. *Journal of Biomechanics*, *49*(2), 252–258. https://doi.org/10.1016/j.jbiomech.2015.12.006ï

Roux, A., Lecompte, J., Iordanoff, I., & Laporte, S. (2021). Modeling of muscular activation of the muscle-tendon complex using discrete element method. *Computer Methods in Biomechanics and Biomedical Engineering*, *24*(11), 1184–1194. https://doi.org/10.1080/10255842.2020.1870039

Rowe, J., Chen, Q., Domire, Z. J., McCullough, M. B., Sieck, G., Zhan, W. Z., & An, K. N. (2010). Effect of collagen digestion on the passive elastic properties of diaphragm muscle in rat. *Medical Engineering and Physics*, *32*(1), 90–94. https://doi.org/10.1016/j.medengphy.2009.11.002

Sahani, R., Hixson, K., & Blemker, S. S. (2024). It's more than the amount that counts: Implications of collagen organization on passive muscle tissue properties revealed with micromechanical models and experiments. *Journal of the Royal Society Interface*, *21*(211), 20230478–20230478.

Sahani, R., Wallace, C. H., Jones, B. K., & Blemker, S. S. (2022). Diaphragm muscle fibrosis involves changes in collagen organization with mechanical implications in Duchenne muscular dystrophy. *Journal of Applied Physiology*, *132*(3), 653–672.

Sanchez-Palencia, E. (2006). Homogenization method for the study of composite media. In *Asymptotic Analysis II— Surveys and New Trends* (pp. 192–214). Springer.

Sanden, K. W., Böcker, U., Ofstad, R., Pedersen, M. E., Høst, V., Afseth, N. K., Rønning, S. B., & Pleshko, N. (2021). Characterization of collagen structure in normal, wooden breast and spaghetti meat chicken fillets by ftir microspectroscopy and histology. *Foods*, *10*(3). https://doi.org/10.3390/foods10030548

Sanes, J. R. (2003). The basement membrane/basal lamina of skeletal muscle. *Journal of Biological Chemistry*, *278*(15), 12601–12604. https://doi.org/10.1074/jbc.R200027200

Sango Solanas, P., Tse Ve Koon, K., Ratiney, H., Millioz, F., Caussy, C., & Beuf, O. (2021). Harmonic wideband simultaneous dual-frequency MR Elastography. *NMR in Biomedicine*, *34*(2), e4442.

Schmid, L., Klotz, T., Siebert, T., & Röhrle, O. (2019). Characterization of Electromechanical Delay Based on a Biophysical Multi-Scale Skeletal Muscle Model. *Frontiers in Physiology*, *10*. https://doi.org/10.3389/fphys.2019.01270

Schmidt, H., Alber, T., Wehner, T., Blakytny, R., & Wilke, H.-J. (2009). Discretization error when using finite element models: Analysis and evaluation of an underestimated problem. *Journal of Biomechanics*, *42*(12), 1926–1934. https://doi.org/10.1016/j.jbiomech.2009.05.005

Schüler, S. C., Liu, Y., Dumontier, S., Grandbois, M., Le Moal, E., Cornelison, D., & Bentzinger, C. F. (2022). Extracellular matrix: Brick and mortar in the skeletal muscle stem cell niche. *Frontiers in Cell and Developmental Biology*, *10*, 1056523.

Sharafi, B., & Blemker, S. S. (2010). A micromechanical model of skeletal muscle to explore the effects of fiber and fascicle geometry. *Journal of Biomechanics*, *43*(16), 3207–3213. https://doi.org/10.1016/j.jbiomech.2010.07.020

Sharafi, B., & Blemker, S. S. (2011). A mathematical model of force transmission from intrafascicularly terminating muscle fibers. *Journal of Biomechanics*, *44*(11), 2031–2039. https://doi.org/10.1016/j.jbiomech.2011.04.038

Shields, M. D., & Zhang, J. (2016). The generalization of Latin hypercube sampling. *Reliability Engineering & System Safety*, *148*, 96–108.

Sigrist, R. M., Liau, J., El Kaffas, A., Chammas, M. C., & Willmann, J. K. (2017). Ultrasound elastography: Review of techniques and clinical applications. *Theranostics*, *7*(5), 1303.

Silverman, B. (1986). Kernel density estimation technique for statistics and data analysis. *Monographs on Statistics and Applied Probability*, *26*.

Singh Dhari, R., Hall, W., Asthana, A., & Javanbakht, Z. (2023). Direct FE2 analysis of additively manufactured parts with voids. *Materials Today: Proceedings*. https://doi.org/10.1016/j.matpr.2023.05.124

Sleboda, D. A., Stover, K. K., & Roberts, T. J. (2020). Diversity of extracellular matrix morphology in vertebrate skeletal muscle. *Journal of Morphology*, *281*(2), 160–169. https://doi.org/10.1002/jmor.21088

Smith, G. F., & Rivlin, R. S. (1997). The strain-energy function for anisotropic elastic materials. *Collected Papers of RS Rivlin: Volume I and II*, 541–559.

Smith, L. R., & Barton, E. R. (2014). Collagen content does not alter the passive mechanical properties of fibrotic skeletal muscle in mdx mice. *American Journal of Physiology-Cell Physiology*, *306*(10), C889–C898.

Smith, L. R., Pichika, R., Meza, R. C., Gillies, A. R., Baliki, M. N., Chambers, H. G., & Lieber, R. L. (2021). Contribution of extracellular matrix components to the stiffness of skeletal muscle contractures in patients with cerebral palsy. *Connective Tissue Research*, *62*(3), 287–298. https://doi.org/10.1080/03008207.2019.1694011

Spadoni, S., Todros, S., Reggiani, C., Marcucci, L., & Pavan, P. G. (2024). The role of the extracellular matrix in the reduction of lateral force transmission in muscle bundles: A finite element analysis. *Computers in Biology and Medicine*, *175*, 108488. https://doi.org/10.1016/j.compbiomed.2024.108488

Spyrou, L. A. (2020). A computational multiscale modeling framework for investigating the mechanical properties of meat. *Food Structure*, *26*. https://doi.org/10.1016/j.foostr.2020.100161

Spyrou, L. A., Agoras, M., & Danas, K. (2017). A homogenization model of the Voigt type for skeletal muscle. *Journal of Theoretical Biology*, *414*, 50–61. https://doi.org/10.1016/j.jtbi.2016.11.018

Spyrou, L. A., Brisard, S., & Danas, K. (2019). Multiscale modeling of skeletal muscle tissues based on analytical and numerical homogenization. *Journal of the Mechanical Behavior of Biomedical Materials*, *92*, 97–117. https://doi.org/10.1016/j.jmbbm.2018.12.030

Stearns-Reider, K. M., D'Amore, A., Beezhold, K., Rothrauff, B., Cavalli, L., Wagner, W. R., Vorp, D. A., Tsamis, A., Shinde, S., & Zhang, C. (2017). Aging of the skeletal muscle extracellular matrix drives a stem cell fibrogenic conversion. *Aging Cell*, *16*(3), 518–528.

Stein, M. (1987). Large sample properties of simulations using Latin hypercube sampling. *Technometrics*, *29*(2), 143–151.

Subramaniam, M., Gorny ,Genevieve, Johnsen ,Steven A., Monroe ,David G., Evans ,Glenda L., Fraser ,Daniel G., Rickard ,David J., Rasmussen ,Kay, van Deursen ,Jan M. A., Turner ,Russell T., Oursler ,Merry Jo, & and Spelsberg, T. C. (2005). TIEG1 Null Mouse-Derived Osteoblasts Are Defective in Mineralization and in Support of Osteoclast Differentiation In Vitro. *Molecular and Cellular Biology*, *25*(3), 1191–1199. https://doi.org/10.1128/MCB.25.3.1191-1199.2005

Subramaniam, M., Harris, S. A., Oursler, M. J., Rasmussen, K., Riggs, B. L., & Spelsberg, T. C. (1995). Identification of a novel TGF-β-regulated gene encoding a putative zinc finger protein in human osteoblasts. *Nucleic Acids Research*, *23*(23), 4907–4912. https://doi.org/10.1093/nar/23.23.4907

Subramaniam, M., Hawse, J. R., Rajamannan, N. M., Ingle, J. N., & Spelsberg, T. C. (2010). Functional role of KLF10 in multiple disease processes. *Biofactors*, *36*(1), 8–18.

Sun, B. (2021). The mechanics of fibrillar collagen extracellular matrix. *Cell Reports Physical Science*, *2*(8). https://doi.org/10.1016/j.xcrp.2021.100515

Suwankanit, K., Shimizu, M., Suzuki, K., & Kaneda, M. (2023). Usefulness of ultrasound shear wave elastography for detection of quadriceps contracture in immobilized rats. *Animals*, *14*(1), 76.

Takaza, M., Moerman, K. M., Gindre, J., Lyons, G., & Simms, C. K. (2013). The anisotropic mechanical behaviour of passive skeletal muscle tissue subjected to large tensile strain. *Journal of the Mechanical Behavior of Biomedical Materials*, *17*, 209–220. https://doi.org/10.1016/j.jmbbm.2012.09.001

Tan, V. B. C., Raju, K., & Lee, H. P. (2020). Direct FE2 for concurrent multilevel modelling of heterogeneous structures. *Computer Methods in Applied Mechanics and Engineering*, *360*, 112694.

Tatarenko, Y. (2023). *Modélisation multi-échelle des propriétés mécaniques passives du muscle squelettique murin: Application à l'étude de l'expression du gène Klf10*. https://theses.hal.science/tel-04513626v1

Tatarenko, Y., Li, M., Pouletaut, P., Kammoun, M., Hawse, J. R., Joumaa, V., Herzog, W., Chatelin, S., & Bensamoun, S. F. (2024). Multiscale analysis of Klf10's impact on the passive mechanical properties of murine skeletal muscle. *Journal of the Mechanical Behavior of Biomedical Materials*, *150*, 106298. https://doi.org/10.1016/j.jmbbm.2023.106298

Tatarenko, Y., Pouletaut, P., Chatelin, S., & Bensamoun, S. F. (2022). Passive and active mechanical tests at different scales of the skeletal muscle: A literature review. *State of the Art in Bioengineering*, *2*(1).

Tateya, T., Tateya, I., & Bless, D. M. (2007). *Immuno-Scanning Electron Microscopy of Collagen Types I and III in Human Vocal Fold Lamina Propria* (Rhinology & Laryngology, Vol. 116, Issue 2, pp. 156–159).

Teklemariam, A., Hodson-Tole, E., Reeves, N. D., & Cooper, G. (2019). A micromechanical muscle model for determining the impact of motor unit fiber clustering on force transmission in aging skeletal muscle. *Biomechanics and Modeling in Mechanobiology*, *18*(5), 1401–1413. https://doi.org/10.1007/s10237-019-01152-2

Ternifi, R., Kammoun, M., Pouletaut, P., Subramaniam, M., Hawse, J. R., & Bensamoun, S. F. (2020). Ultrasound image processing to estimate the structural and functional properties of mouse skeletal muscle. *Biomedical Signal Processing and Control*, *56*, 101735. https://doi.org/10.1016/j.bspc.2019.101735

Terzolo, A., Bailly, L., Orgéas, L., Cochereau, T., & Henrich Bernardoni, N. (2022). A micro-mechanical model for the fibrous tissues of vocal folds. *Journal of the Mechanical Behavior of Biomedical Materials*, *128*. https://doi.org/10.1016/j.jmbbm.2022.105118

Tian, L., Wang, Z., Liu, Y., Eickhoff, J. C., Eliceiri, K. W., & Chesler, N. C. (2016). Validation of an arterial constitutive model accounting for collagen content and crosslinking. *Acta Biomaterialia*, *31*, 276–287. https://doi.org/10.1016/j.actbio.2015.11.058

Toscano, A. E., Ferraz, K. M., Castro, R. M. de, & Canon, F. (2010). Passive stiffness of rat skeletal muscle undernourished during fetal development. *Clinics*, *65*, 1363–1369.

Trotter, J. A. (1990). Interfiber tension transmission in series-fibered muscles of the cat hindlimb. *Journal of Morphology*, *206*(3), 351–361.

Trotter, J. A., & Purslow, P. P. (1992). *Functional Morphology of the Endomysium in Series Fibered Muscles* (JOURNAL OF MORPHOLOGY, Vol. 212, pp. 109–122).

Virgilio, K. M., Martin, K. S., Peirce, S. M., & Blemker, S. S. (2015). Multiscale models of skeletal muscle reveal the complex effects of muscular dystrophy on tissue mechanics and damage susceptibility. *Interface Focus*, *5*(2). https://doi.org/10.1098/rsfs.2014.0080

Voigt, W. (1889). Ueber die Beziehung zwischen den beiden Elasticitätsconstanten isotroper Körper. *Annalen Der Physik*, *274*(12), 573–587.

Walter, F., Seydewitz, R., Mitterbach, P., Siebert, T., & Böl, M. (2023). On a three–dimensional model for the description of the passive characteristics of skeletal muscle tissue. *Biomechanics and Modeling in Mechanobiology*, *22*(5), 1499–1514. https://doi.org/10.1007/s10237-022-01664-4

Wang, M. N., & Liu, F. J. (2020). A compressible anisotropic hyperelastic model with I 5 and I 7 strain invariants. *Computer Methods in Biomechanics and Biomedical Engineering*, 1–10. https://doi.org/10.1080/10255842.2020.1795839

Ward, S. R., Winters, T. M., O'Connor, S. M., & Lieber, R. L. (2020). Non-linear Scaling of Passive Mechanical Properties in Fibers, Bundles, Fascicles and Whole Rabbit Muscles. *Frontiers in Physiology*, *11*. https://doi.org/10.3389/fphys.2020.00211

Weber, I. T., Harrison, R. W., & Iozzo, R. V. (1996). Model structure of decorin and implications for collagen fibrillogenesis. *Journal of Biological Chemistry*, *271*(50), 31767–31770.

Wisdom, K. M., Delp, S. L., & Kuhl, E. (2015). Use it or lose it: Multiscale skeletal muscle adaptation to mechanical stimuli. *Biomechanics and Modeling in Mechanobiology*, *14*(2), 195–215. https://doi.org/10.1007/s10237-014-0607-3

Wohlgemuth, R. P., Feitzinger, R. M., Henricson, K. E., Dinh, D. T., Brashear, S. E., & Smith, L. R. (2023). The extracellular matrix of dystrophic mouse diaphragm accounts for the majority of its passive stiffness and is resistant to collagenase digestion. *Matrix Biology Plus*, *18*. https://doi.org/10.1016/j.mbplus.2023.100131

Wohlgemuth, R. P., Sriram, S., Henricson, K. E., Dinh, D. T., Brashear, S. E., & Smith, L. R. (2024). Strain-dependent dynamic re-alignment of collagen fibers in skeletal muscle extracellular matrix. *Acta Biomaterialia*, *187*, 227–241.

Wood, L. K., Kayupov, E., Gumucio, J. P., Mendias, C. L., Claflin, D. R., & Brooks, S. V. (2014). Intrinsic stiffness of extracellular matrix increases with age in skeletal muscles of mice. *Journal of Applied Physiology*, *117*(4), 363–369.

Xu, J., Li, P., Poh, L. H., Zhang, Y., & Tan, V. B. C. (2022). Direct FE2 for concurrent multilevel modeling of heterogeneous thin plate structures. *Computer Methods in Applied Mechanics and Engineering*, *392*, 114658. https://doi.org/10.1016/j.cma.2022.114658

Zhang, Y., Chen, J. S., He, Q., He, X., Basava, R. R., Hodgson, J., Sinha, U., & Sinha, S. (2020). Microstructural analysis of skeletal muscle force generation during aging. *International Journal for Numerical Methods in Biomedical Engineering*, *36*(1). https://doi.org/10.1002/cnm.3295

Zhi, J., Leong, K. H., Yeoh, K. M., Tay, T.-E., & Tan, V. B. C. (2023). Multiscale modeling of laminated thin-shell structures with Direct FE2. *Computer Methods in Applied Mechanics and Engineering*, *407*, 115942. https://doi.org/10.1016/j.cma.2023.115942

Zhi, J., Raju, K., Tay, T.-E., & Tan, V. B. C. (2021). Transient multi-scale analysis with micro-inertia effects using Direct FE^2 method. *Computational Mechanics*, *67*(6), 1645–1660.

Zhi, J., Yang, B., Li, Y., Tay, T.-E., & Tan, V. B. C. (2023). Multiscale thermo-mechanical analysis of cure-induced deformation in composite laminates using Direct FE2. *Composites Part A: Applied Science and Manufacturing*, *173*, 107704. https://doi.org/10.1016/j.compositesa.2023.107704

Aude LOUMEAUD

Coupling multiscale numerical modeling and MRI elastography to investigate the impact of the Klf10 gene on the extracellular matrix of murine skeletal muscle

Résumé

La délétion génétique Klf10 provoque des maladies osseuses et cardiaques chez les patients humains. Ce gène est fortement exprimé dans les muscles squelettiques et des études ont montré ses effets sur les propriétés structurelles et fonctionnelles des fibres musculaires à l'échelle microscopique. À l'aide d'un modèle murin, l'implication du gène Klf10 dans les propriétés fonctionnelles des muscles squelettiques a été étudiée à l'aide de deux approches : (1) des mesures des propriétés mécaniques *in vivo* par élastographie IRM (ERM) et (2) une modélisation numérique multi-échelle des propriétés mécaniques passives *ex vivo*. Un effet du génotype sur les propriétés mécaniques *in vivo* des membres postérieurs de souris a été mis en évidence à l'aide de l'ERM. De plus, les résultats numériques suggèrent qu'un composant musculaire appelé matrice extracellulaire (MEC) semble être affecté par la délétion génétique. En effet, la contribution des fibres de collagène contenues dans la MEC à la force musculaire diminue lorsque le gène Klf10 est inhibé. Des études futures se concentreront sur la quantification de la teneur en collagène et de la structure de ce composant.

Mots clés : Muscle squelettique, gène Klf10, modélisation multiéchelles, Elastographie par Résonance Magnétique, Matrice Extracellulaire

Abstract

The Klf10 genetic deletion causes bone and heart diseases in human patients. This gene is strongly expressed in skeletal muscles and effects on structural and functional properties of muscle fibers at the microscopic scale have been shown in previous studies. Using a mouse model of this condition, the Klf10 gene's implication in skeletal muscle functional properties was investigated using 2 approaches: (1) *in vivo* mechanical properties measurements using Magnetic Resonance Elastography (MRE) and (2) numerical multiscale Finite Element (FE) modeling of the *ex vivo* passive mechanical properties. An effect of the genotype on the *in vivo* mechanical properties of mouse hindlimbs could be highlighted using MRE. Moreover, numerical results suggest that a muscle component named ExtraCellular Matrix (ECM) seems to be affected by the genetic deletion. More precisely, contribution of the collagen fibers contained in ECM to muscle strength decreases when the Klf10 gene is inhibited. Further studies will focus on quantifying collagen content and structure in this component.

Keywords : Skeletal muscle, Klf10 gene, Multiscale modeling, Magnetic Resonance Elastography, Extracellular Matrix